High-Resolution Observations of Active Galactic Nuclei in the Southern Hemisphere

Hochauflösende Beobachtungen Aktiver Galaxienkerne am Südhimmel

Der Naturwissenschaftlichen Fakultät
der Friedrich-Alexander-Universität Erlangen-Nürnberg
zur Erlangung des Doktorgrades Dr. rer. nat.
vorgelegt von

Cornelia Müller

aus Nürnberg

Als Dissertation genehmigt
von der Naturwissenschaftlichen Fakultät
der Friedrich-Alexander-Universität Erlangen-Nürnberg

Tag der mündlichen Prüfung:	1. September 2014
Vorsitzender des Promotionsorgans:	Prof. Dr. J. Barth
Erstgutachter:	Prof. Dr. J. Wilms (FAU Erlangen-Nürnberg)
	Prof. Dr. M. Kadler (Universität Würzburg)
Zweitgutachter:	Prof. Dr. A. Marscher (Boston University)
Drittgutachter:	Prof. Dr. M. Brüggen (Universität Hamburg)

The monochrome picture on the title page shows the Astronomical Institute of the Friedrich-Alexander University of Erlangen-Nuremberg, the Dr. Karl Remeis Observatory in Bamberg, Germany, which celebrates 125 years of existence in 2014.

Zusammenfassung

Diese Arbeit beschäftigt sich mit der detaillierten Analyse von extragalaktischen Jets, mit dem Ziel, die Physik dieser Objekte besser zu verstehen. Dazu werden hochauflösende Aufnahmen mit simultanen Multiwellenlängenbeobachtungen, die das ganze elektromagnetische Spektrum abdecken, kombiniert. Jets sind hochrelativistische, astrophysikalische Quellen. Sie gehören zu den leuchtkräftigsten Objekten im Universum und können bis in den Gammastrahlungsbereich extrem hell sein. Nach heutigem Stand der Forschung sind Jets stark gebündelte Materieströme, die aufgrund von Masseakkretion auf ein supermassives Schwarzes Loch im aktiven Kern einer Galaxie (englisch: 'active galactic nucleus' oder AGN) entstehen.

Dank umfangreicher Multiwellenlängenbeobachtungen lässt sich ein einheitliches Gesamtbild eines AGN-Jets konstruieren, jedoch sind die Emissions- und Enstehungsprozesse noch nicht vollständig verstanden. Das typische Breitbandspektrum einer Jetquelle hat die Form eines Doppelhöckers. Bei niedrigen Energien lässt sich diese spektrale Form durch Synchrotronstrahlung erklären, doch die zugrunde liegenden Prozesse im Röntgen- bis Gammastrahlungsbereich sind noch nicht eindeutig geklärt. So existieren noch viele offene Fragen zur Physik von AGN, bezüglich der Emissionsmechanismen und des Aufbaus, der Enstehung und Beschleunigung von Jets. Um weitere Informationen zu erhalten und den Parameterraum bestehender Emissionsmodelle besser einschränken zu können, untersuche ich in dieser Arbeit die innersten Bereiche (kleiner als ein Parsec) und die spektralen Charakteristiken bei hohen Energien von extragalaktischen Jets. Dabei konzentriere ich mich auf Quellen am Südhimmel, die im Rahmen des Projekts TANAMI (*Tracking Active Galactic Nuclei with Austral Milliarcsecond Interferometry*) regelmäßig beobachtet werden. Dieses Beobachtungsprogramm ergänzt hochauflösende Aufnahmen, die mit Hilfe von Radiointerferometrie gemacht werden, mit simultanen Multiwellenlängenbeobachtungen.

Radiointerferometrische Beobachtungen auf langen Basislinien (englisch: 'Very Long Baseline Interferometry' oder kurz VLBI) können ein räumliches Auflösungsvermögen von weniger als einer Millibogensekunde erzielen. Mit dieser Technik lassen sich die schärfsten, am höchsten aufgelösten Bilder aufnehmen und somit die Morphologie, Oberflächenhelligkeit und Spektrum des innersten Teils des Jets sehr genau studieren. Regelmäßige VLBI-Beobachtungen erlauben die zeitliche Entwicklung der Jets abzubilden und somit die Jetkinematik und mögliche Wechselwirkungen mit dem umgebenden Medium zu studieren. Die detaillierten Untersuchungen der kleinskaligen Struktur wird durch regelmäßige Multiwellenlängenbeobachtungen ergänzt, um zeitgleich spektrale Informationen zu erhalten. Diese kombinierten Beobachtungen sind deshalb entscheidend, da Korrelationen zwischen der Aktivität im Hochenergiebereich und Änderungen der Jetstruktur Aufschluss über den Entstehungsort und -mechanismus der hochenergetischen Photonen geben können. Bezieht man des Weiteren noch die Suche nach extragalaktischen Neutrinoquellen in die Nachforschungen mit ein, spricht man von Multimessenger-Astronomie. Dies kann dabei helfen, die genaue Zusammensetzung von Jets aus Leptonen und möglicherweise Hadronen zu entschlüsseln.

Das TANAMI-Sample besteht aus 75 der hellsten extragalaktischen Jets am Südhimmel im Deklinationsbereich südlich von $-30°$. Hochauflösende Radiobeobachtungen aller Quellen werden mit (quasi-)simultanen Multiwellenlängenbeobachtungen kombiniert, insbesondere vom *Fermi*-Weltraumteleskop im Gammabereich. Ungefähr dreiviertel aller TANAMI-Quellen sind bei diesen hohen Energien detektiert. Somit ist dies ein ideales Sample, um die Gammastrahlungsquellen mit den nicht detektierten Jets zu vergleichen und nach möglichen Unterschieden in den kleinskaligen Strukturen ($\lesssim 1\,\mathrm{pc}$) zu suchen.

Die Studie des gesamten TANAMI-Samples ergibt, dass die im Gammabereich hellen Jets stärker durch ihre kompakte Kernemission dominiert sind und höhere Helligkeitstemperaturen haben. Dies

bestätigt vorangegangene Beobachtungen. Allerdings zeigt sich für die Quasare im Sample, dass deren Morphologie keine starke Korrelation zwischen der Kompaktheit und dem Gammastrahlungsfluss aufweist. Darüber hinaus sind die Werte der Helligkeitstemperatur der Quasare vergleichsweise breiter verteilt. Dieses Ergebnis lässt darauf schließen, dass es möglicherweise Untergruppen von Quasaren mit verschiedenen spektralen Eigenschaften gibt.

Die Gammastrahlungsvariabilität der TANAMI-Quellen geht zusätzlich in die Kandidatenauswahl möglicher Neutrinoquellen für eine Punktquellensuche mit dem Neutrinoteleskop ANTARES ein. Könnten AGN als Neutrinoquellen bestätigt werden, würde das den Parameterraum von Emissionsmodellen ungemein einschränken und könnte Jets als Beschleuniger kosmischer Strahlung identifizieren. Unter Berücksichtigung der präzisen Quellposition und Informationen zur zeitlichen Variabilität kann die Sensitivität des Neutrinoteleskops signifikant erhöht werden. Dazu wird eine Selektion für die Punktquellensuche erarbeitet und präsentiert, die explizit nur TANAMI-Quellen mit hellen und kurzen Strahlungsausbrüchen auswählt. Diese Studie ebnet den Weg für zukünftige Projekte zur Suche nach extragalaktischen Neutrinos mit Hilfe von Multimessenger-Astronomie.

Die Studie des TANAMI-Samples liefert ein tieferes Verständnis und allgemeines Bild der Jet-Eigenschaften, doch detailliertere Informationen können besser mit Analysen einzelner Quellen erworben werden. Zu diesem Zweck werden VLBI- und Multiwellenlängenbeobachtungen zweier besonderer TANAMI-Quellen, nämlich PMN J1603−4904 und Centaurus A, analysiert und diskutiert.

Wie für die meisten der neu entdeckten, extragalaktischen Gammastrahlungsquellen am Südhimmel, waren auch für PMN J1603−4904 keine VLBI-Informationen verfügbar bevor die Quelle ins TANAMI-Beobachtungsprogramm aufgenommen wurde. Dieses Objekt gehört zu den hellsten extragalaktischen Gammastrahlungsquellen am Himmel und war ursprünglich als Blazar klassifiziert. Die hoch aufgelösten Bilder der TANAMI-Beobachtungen zeigen eine symmetrische Morphologie mit der hellsten, kompaktesten Komponente im Zentrum der Emissionsregion und einer Ausdehnung von wenigen Millibogensekunden. Diese Struktur und diverse ungewöhnliche spektrale Eigenschaften sind sehr untypische Charakteristiken für einen Blazar. Multiwellenlängenbeobachtungen zeigen unter anderem eine unerwartet prominente Emission im Infrarotbereich und eine dünne Eisenlinie im Röntgenspektrum. Letztere erlaubt die erste Messung der Rotverschiebung der Quelle. Da diese Eigenschaften schwierig mit der Klassifikation als Blazar in Einklang zu bringen sind, wird eine alternative Klassifikation als junge, im Gammabereich helle Radiogalaxie mit möglicher starker Sternentstehungsrate betrachtet. Würde PMN J1603−4904 als ein solches Objekt bestätigt werden, wäre es das erste dieser Klasse. Da es nur wenige Gammastrahlungsquellen gibt, deren Jets unter einem großen Winkel zur Sichtlinie gesehen werden, würde PMN J1603−4904 diese Quellgruppe erweitern. Diese Jets stellen eine Herausforderung für die derzeitigen Emissionsmodelle dar, die die Gammastrahlung mit Hilfe von hohen Dopplerfaktoren erklären. Daher kann die Erforschung dieser Objekte dazu beitragen, die Emissionregionen und -mechanismen von hochenergetischen Photonen in Jets besser zu verstehen.

Centaurus A gehört genau zu dieser Gruppe der im Gammabereich detektierten Radiogalaxien und ist darüber hinaus bei einer Entfernung von nur 3.8 Mpc der nächste AGN. VLBI-Beobachtungen mit TANAMI erlauben die derzeit besten Aufnahmen dieser Quelle mit einer Auflösung von ~ 0.02 pc. Die Ergebnisse dieser Studie des innersten Parsecs eines extragalaktischen Jets wird in dieser Arbeit vorgestellt und ausführlich diskutiert. Die komplexe Kinematik zeigt eine nach außen zunehmende Beschleunigung des Jetflusses und kann am besten durch ein Modell aus einem schnellen, dichten Jetinneren, umhüllt von einer langsameren, dünneren Schicht beschrieben werden. Die Beobachtungen zeigen eine lokale Unterbrechung der Strömung, die mit einem Rückgang der Jethelligkeit und einem Aufweiten des Jets einhergeht, was durch die Kollision des Jets mit einem Stern erklärt werden. Multiwellenlängenbeobachtungen der letzten Jahre ergeben

eine mögliche Korrelation zwischen erhöhter Röntgenemission und Jetaktivität, die Hinweis auf eine gemeinsame Emissionregion geben kann.

Zusammenfassend lässt sich sagen, dass im Rahmen des TANAMI-Beobachtungsprogramms die Emissions- und Entstehungsmechanismen extragalaktischer Jets studiert werden. Dabei geht diese Arbeit insbesonders auf die Forschungsergebnisse zweier spezieller Quellen ein, um weitere Erkenntnisse über die Physik von Jets zu gewinnen.

Abstract

In this work, high-resolution observations combined with multiwavelength monitoring of extragalactic jets are presented, aiming at a better understanding of these objects. Jets are extremely bright, highly relativistic astrophysical sources emitting light across the electromagnetic spectrum. According to our current knowledge, jets of Active Galactic Nuclei (AGN) are well collimated material outflows emerging from the center of AGN due to accretion onto a supermassive black hole. These objects belong to the most powerful and persistent sources in the Universe.

Extensive multiwavelength studies established a consistent overall picture of AGN jets, but the underlying emission and formation processes are still not completely understood. A typical broadband spectral energy distribution shows a double-humped shape, which is well explained by synchrotron radiation of relativistic electrons in the lower energy regime, but the physical processes from the X-ray to γ-ray bands are still heavily discussed. Open questions concerning AGN physics involve the emission mechanism, jet composition, formation and acceleration. In order to gain more information and to constrain theoretical models, I investigate the parsec-scale and high-energy properties of extragalactic jets in this work. I focus on the sample of the monitoring program TANAMI (*Tracking Active Galactic Nuclei with Austral Milliarcsecond Interferometry*), which regularly observes extragalactic jets in the Southern Hemisphere using Very Long Baseline Interferometry (VLBI) radio observations complemented by multiwavelength monitoring.

VLBI measurements obtain the best insight into this enigmatic objects, resolving structures down to scales of less than a milliarcsecond (mas). With this technique the (sub-)parsec scale morphology, surface brightness and spectral distribution of the jets can be studied in great detail. VLBI monitoring allows the investigation of jet kinematics and interaction with the ambient medium. These high-resolution radio images are combined with multiwavelength monitoring from radio to γ-rays in order to simultaneously study spectral and structural changes. Correlations of high energy activity with variations within the jet give crucial information on production sites and mechanisms of the high energy photons. In addition, multimessenger astronomy, i.e., the search for extragalactic neutrinos from AGN, aims at investigating the possible hadronic constitution of jets.

The TANAMI sample consists of 75 of the brightest extragalactic jets south of -30° declination. High-resolution radio monitoring is complemented by (quasi-)simultaneous multiwavelength monitoring, in particular by the *Fermi* Gamma-ray Space Telescope. About three-quarters of all sources are detected by *Fermi*, making this an ideal sample to study possible differences in the parsec-scale properties of γ-ray faint and loud objects.

The TANAMI sample study shows that the γ-ray bright sources are more core dominated and have higher brightness temperatures, confirming previous findings. For the quasars in the sample, however, the situation is not that clear: their mas-scale morphologies do not show a clear correlation of compactness with γ-ray flux density and their brightness temperatures are more broadly distributed. This result indicates the existence of possible sub-types of quasars, which might explain why some of these powerful radio sources are high energy emitters while others are not.

The γ-ray variability of the TANAMI jets is used to select possible neutrino emitters for a point source search with the neutrino telescope ANTARES. Confirming AGN as neutrino sources would tremendously help to constrain parameters of jet emission models as well as to identify jets as cosmic ray accelerators. The sensitivity of ANTARES for point source searches can be significantly enhanced by taking the precise source position and additional time information into account. Therefore, a method was developed to select only sources which exhibit short and bright flares over four years of *Fermi* monitoring in the γ-rays. This work paves the way for future multimessenger projects to search for extragalactic neutrinos.

The presented sample study yields a better, overall understanding and picture of extragalactic jet properties, while more detailed information are best acquired with individual source studies. For this purpose, I discuss the VLBI observations, complemented by multiwavelength data, of two particular sources of the TANAMI sample, namely PMN J1603−4904 and Centaurus A.

Like for most of the newly detected γ-ray bright extragalactic jets in the Southern Hemisphere, no VLBI information has been available for PMN J1603−4904 before it was added to the TANAMI sample. This object is one of the brightest γ-ray sources in the sky and was initially classified as a blazar. TANAMI observations revealed a symmetric mas-scale morphology, with the brightest, most compact feature at the center. This appearance along with unusual broadband properties are very atypical for a blazar. Multiwavelength observations reveal among other things an excess in the infrared, and an iron line in the sensitive X-ray spectrum, which allows the first redshift measurement of the spectrum. As these features challenge the classification as a blazar, an alternative explanation as a young radio source with possible starburst contribution in the host galaxy is considered. If confirmed, PMN J1603−4904 would be the first object in this class and would add to the group of jet sources with high inclination angles, of which only few are detected in γ-rays. These sources challenge current models which attempt to explain the high-energy emission with high Doppler beaming factors. The investigation of these sources can help to determine the emission regions and mechanism of the highly energetic photons in jets.

Centaurus A belongs to this group of objects of γ-ray bright radio galaxies and, more important, it is the closest AGN, such that VLBI observations with TANAMI probe jet features of ~ 0.02 pc in size and jet physics can be studied in unrivaled detail. I present these high-resolution observations, revealing complex jet dynamics and a potential connection between increased hard X-ray flux and higher jet activity. The study of the jet kinematics gives a consistent picture of the innermost parsec of the jet: a spine-sheath like structure fits best to the observed downstream acceleration of the flow. A disturbance causing a widening of the jet flow can be explained by an interaction of the jet and a star. Multiwavelength monitoring yields a possible correlation of higher X-ray emission and increasing jet activity, which could indicate a common emission origin.

In conclusion, in the framework of the TANAMI monitoring program the emission and formation mechanisms of extragalactic jets are studied. Therefore, this work focuses on the comprehensive study of two special sources with the goal to gain better knowledge of the whole sample.

Contents

A curious straight ray lies in a gap in the nebulosity in p.a. 20°, apparently connected with the nucleus by a thin line of matter...

(H. D. Curtis, 1918, about M 87)

1. Relativistic extragalactic jets

They appear as straight objects, are bright across the whole electromagnetic spectrum, emerge from the central engine of active galactic nuclei (AGN), and outshine their host galaxies: relativistic extragalactic jets. AGN jets are highly relativistic, well collimated outflows of matter, which are formed in the vicinity of a central galactic supermassive black hole (SMBH). AGN constitute the most powerful sources in the Universe, producing tremendous luminosities in volumes of less than a cubic parsec.

This thesis presents the analysis of very high-resolution observations of a subsample of extragalactic jets in the Southern Hemisphere, concentrating on two particular jets with striking properties at (sub-)parsec scales. Multiwavelength studies are performed to further investigate the emission and formation mechanism of these enigmatic objects.

The structure of this work as follows, an introduction to this topic, a brief history about the beginning of AGN research is given in Sect. 1.1. In Section 1.2, general properties and different appearances and activity stages of AGN are discussed, in order to lead over to the physics of relativistic jets (Sect. 1.3). In Chapter 2 the multiwavelength observations and the corresponding analysis methods are presented. The observations presented here were performed in the framework of the monitoring program TANAMI at radio frequencies (Ch. 3), with a close connection to γ-ray observations with the *Fermi* Large Area Telescope (Sect. 2.2) and multimessenger astronomy with the neutrino telescope ANTARES (Ch. 4). In Chapter 5 the parsec-scale properties with respect to γ-ray loudness of the TANAMI sample are presented. The main focus will be laid on the high-resolution study in the radio, accompanied by multiwavelength observations, of the γ-ray loud sources PMN J1603−4904 and Centaurus A (Ch. 6 and 7), discussing in detail the results and implications.

1.1. Discovery and history

The first observation of an extragalactic jet was performed by the Lick observatory astronomer H. D. Curtis in 1918 who detected a “curious straight ray” in the elliptical galaxy M 87 in the Virgo Cluster, the sight of an extended feature, probably similar to the optical (amateur) image shown in Fig. 1.1. Further investigations of this puzzling object were possible due to the development of a new branch of astronomy: Karl Jansky’s discovery of radio waves from the Milky Way opened a new “window” to the Universe (Jansky, 1933). After World War II, the advanced techniques in radio astronomy (see Sect. 2.1.2) allowed the identification of the brightest radio sources in the sky with known optical counterparts (Baade & Minkowski, 1954). The higher angular resolution achieved at radio wavelengths resulted in the detection of extended radio emission in these objects, later identified with jets ending in hot spots and lobes (e.g., Ryle et al., 1965). Jets are highly relativistic

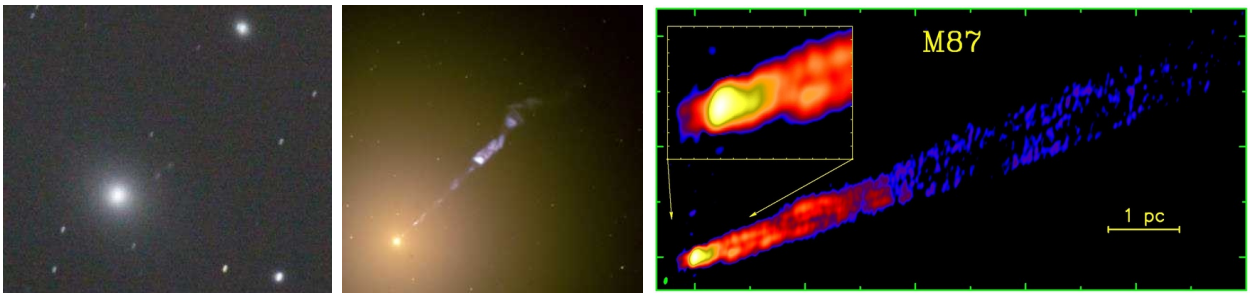

Figure 1.1.: Views of the M 87 jet. *Left:* Optical image of M 87 taken with a f/4.9 Newtonian Reflector and 30 s exposure on the Plains of San Agustin, New Mexico, April 6th, 2013, (© M. Gorski, K. Obenberger). This amateur image already reveals a faint, straight extension of the bright elliptical galaxy to the north-west. *Middle:* With the Hubble space telescope the *"curious straight ray"* can be further resolved and imaged in detail (Credit: NASA & The Hubble Heritage Team). *Right:* The jet is emitting light across the whole electromagnetic spectrum (see Sect. 1.3.1). At radio wavelengths and with interferometric techniques using the Very Long Baseline Array (see Sect. 2.1.2) the sharpest images of AGN jets can be obtained. In M 87, this technique reveals structure of less than 1 pc in size (at a distance of ∼16 Mpc; Credit: MPIfR, Kovalev et al., 2007).

objects, being extremely powerful accelerators and emitting light across the whole electromagnetic spectrum (see Sect. 1.3.1). According to the current scientific knowledge, these powerful and luminous sources are formed due to mass accretion onto a SMBH of $10^6 - 10^9$ solar masses in the center of a galaxy ("active galactic nucleus"). Part of the infalling matter is accelerated and ejected, forming a highly relativistic, symmetric jet-counterjet-system. This process covers an enormous range of linear scales; the jet is launched close to the AGN on scales of a few Schwarzschild radii (sub-parsec scales), while the jets and lobes can span several kilo-parsecs. It is still not fully understood how jets form. They appear as persistent sources, while the younger versions of the powerful radio galaxies open the possibility to study the evolution of these objects. The composition of jets – leptonic or hadronic – and the underlying emission mechanisms to produce the observed broadband emission from radio wavelengths to TeV energies are a major topic of current research and requires further investigations and comparisons to theoretical models (see Sect. 1.3.5).

The illustration in Fig. 1.2 summarizes the main properties of an extragalactic jet and presents a first outline of this thesis: shown is a multiwavelength composite of Centaurus A (Cen A) combined with a close-up of the innermost region of the radio-loud active galaxy. It exhibits prominent radio jets and lobes, which are also detected in the X-rays and γ-rays. Cen A is the closest active galaxy at a distance of only 3.8 Mpc (Harris et al., 2010), with the result that one can resolve the source down to the inner few light days. Hence, it is the perfect laboratory to actually probe jets from kpc-scales almost down to the launching point in the vicinity of the SMBH. In the optical the elliptical host galaxy NGC 5128 has a prominent dust lane. Beyond that, the extension of the giant radio lobes is $\sim 10^\circ$ on the sky (comparable to ∼20 times the size of the full moon). Due to its proximity this radio galaxy is indeed a particular case, however it features properties, e.g. the broadband emission from radio to γ-rays, in common with a large sample of extragalactic jets. The detailed investigation of Centaurus A gives crucial information on the physics of jets in general. As part of this work very high-resolution radio observations of Cen A have been analyzed, resulting in this best-ever[1] snapshot of the jet-counterjet system of Centaurus A at the highest possible resolution (Fig. 1.2). It displays in unprecedented detail the innermost region of an AGN.

[1] `http://www.nasa-usa.de/topics/universe/features/radio-particle-jets.html`

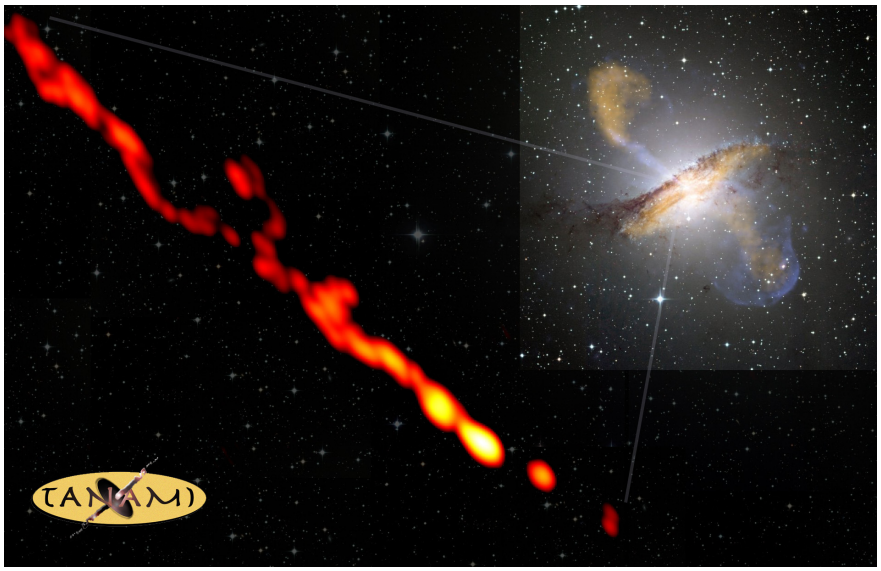

Figure 1.2.: Multiwavelength composite (upper right corner) of the elliptical galaxy NGC 5128, the host of the radio source Centaurus A. Shown are the optical image overlaid by a radio and X-ray image showing the kiloparsec-scale radio lobes (Credit: ESO/WFI; MPIfR/ESO/APEX/A. Weiss et al.; NASA/CXC/CfA/R. Kraft et al.). The zoom-in displays the observations by TANAMI with Very Long Baseline Interferometry (see Ch. 3) providing the best-resolved radio image of an extragalactic jet, displaying the inner parsec of the AGN. With an angular resolution of less than 1 milli-arcsecond, this image reveals features of the jet of sizes of a few light-days across (NASA/ESO/MPIfR/TANAMI and Müller et al., 2011, more details see Ch. 7).

1.2. Active Galactic Nuclei

The term *active galactic nucleus* (AGN) refers to a galactic central region being overall distinctly brighter than "normal galaxies". The main characteristic of an AGN is its high luminosity, which cannot be explained by stellar emission from the host galaxy. Such a galaxy is labeled as "active", when producing powerful, non-thermal broadband emission contrary to non-active galaxies, which are dominated by thermal emission from stars. In the following a brief introduction to AGN phenomenology and evolution is given; more detailed information can be found in Krolik (1999) and Boettcher et al. (2012).

1.2.1. AGN phenomenology and unification

Broadband observations reveal various AGN types with a large variety of spectral and structural features of different strength. Based on these individual properties, the sources are classified following (in general) optical classification schemes (see below and e.g., Seyfert, 1943). However, observations show that they have common characteristic features, such that different classes can be assembled in one unification scheme (Urry & Padovani, 1995).

The most catching general property is the high luminosity ($L \sim 10^{42} \ldots 10^{48}\,\mathrm{erg\,s^{-1}}$) of the galaxy center compared to the overall brightness of the host (or another normal) galaxy. The broadband spectrum can be described by a power law, indicating non-thermal emission. AGN show variability across the whole electromagnetic spectrum on various time scales, from hours to months (Wagner & Witzel, 1995; Ciaramella et al., 2004; Abdo et al., 2010a).

Table 1.1.: Unification scheme (after, e.g., Urry & Padovani, 1995)

inclination angle ↓		**radio-quiet**	**radio-loud**
	Type 1	Seyfert 1 radio-quiet quasar	BL Lac radio-loud quasar
	Type 2	Seyfert 2 radio-quiet quasar	NLRG (FR I & II) radio-loud quasar

The central engine that powers an AGN is the SMBH of the galaxy, accreting material. Accretion on a compact object is the only mechanism to release this amount of energy within $< 1\,\mathrm{kpc}$[3] (Shakura & Sunyaev, 1973). The accreted material fuels the whole system: gas and dust orbiting the central SMBH form an accretion disk, continuously dissipating energy, hence loosing angular momentum through friction and radiation. The spectrum of a thin accretion disk can be described by a (stretched) black body emission with a radial temperature dependence. There is observational evidence that the amount of accretion regulates the activity of the AGN, i.e, a turning-on of the engine when more material falls onto the black hole (see also Sect. 1.2.2 and Di Matteo et al., 2005; Schawinski et al., 2007).

Multiwavelength observations over the last decades revealed the different appearances of AGN. There is an apparent dichotomy in radio-loud and radio-quiet[2] objects, which can be explained by the presence of a powerful radio jet. Only a minority of $\sim 10\%$ are radio-loud. The commonly adopted classification scheme is based on optical observations. Due to the compact, extremely luminous appearance of these objects, they were called "quasi-stellar objects" (QSOs) or "quasi-stellar radio sources" (Quasars), when identified with a radio source.

Seyfert galaxies: Seyfert (1943) first discovered the bright emission lines of quasars. Today following his studies radio-quiet AGN showing strong emission lines are classified as Seyfert galaxies. Sources showing mainly broad emission lines, indicating high velocities up to $10^4\,\mathrm{km\,s^{-1}}$ of the emitting material, are classified as *Seyfert Type 1* galaxies, while narrow (forbidden) lines define the *Seyfert Type 2*. The hosts of Seyfert galaxies are spiral galaxies. Similar optical spectral features show so called *LINERs* (Low-Ionization Nuclear Emission Region) but with a weaker continuum, i.e., the spectrum is dominated by strong emission lines from low-ionization states. All of these objects belong to the radio-weak sub-class of AGN (see Table 1.1).

Quasars: The brightest objects are classified as *quasars* showing Seyfert-like optical spectra. All objects which can not be associated with an optical counterpart belong to this class, without distinguishing between radio loud or quiet. Quasars are typically the most distant objects. Depending on the power law index of their continuum emission, they are called flat-spectrum quasars (FSRQs) or compact steep spectrum sources (CSS).

Radio Galaxies: Radio-loud AGN are classified mainly based on their properties in the radio band rather than on the optical emission features. Radio galaxies, i.e., active galaxies exhibiting powerful

[2]The term "radio-quiet" is somewhat misleading, because these objects do show faint radio emission (e.g., Panessa & Giroletti, 2013).

radio jets, are associated with elliptical hosts. They can be seen as the radio-loud complement to Seyferts and the optical classification can be also adopted, leading to *Broad/Narrow Line Radio Galaxies* (BLRG/NLRG). Based on their appearance in the radio showing two-sided radio jets, they are divided into *Fanaroff-Riley Type I* and *Type II* (FR I and FR II, Fanaroff & Riley, 1974). This classification scheme distinguishes sources with a bright core and low power jets as FR I types, and in total more luminous sources exhibiting bright lobes and hot spots as FR II types.

Blazars: If no host galaxy is detected, the radio-loud sources are classified as *BL Lac objects* or *flat spectrum radio-quasars*, making up the class of *blazars*. Typically no emission lines in the optical spectrum are detected. Their broadband spectrum is dominated by non-thermal emission. Blazars are the most luminous sources among AGN, emitting light across the spectrum up to the highest energies. They are highly variable and often strongly polarized. With interferometric techniques (see Sect. 2.1.2) the innermost regions can be resolved, revealing highly relativistic jets (see Ch. 5).

Unification: Table 1.1 summarizes the various AGN classes (for a more detailed discussion, see Véron-Cetty & Véron, 2000). The ordering is based on the inclination angle, which is the angle between the line of sight and the jet axis, according to the concept of the *unified model* of AGN (Lawrence, 1987; Antonucci, 1993; Urry & Padovani, 1995). Due to the similarity of spectral features detected in the different object classes, an intrinsic similarity is suggested. Using the unification scheme the variety of optical appearances can be explained with an orientation and projection effect: assuming all of these sources have the same components in common, the observed spectrum, image and other particular source characteristics depend mainly on the viewing angle.

In Figure 1.3 a sketch of the unified model components is shown. According to that model a prototype AGN is composed of a SMBH with a mass of $M \sim 10^{7-8} M_{\odot}$ surrounded by an accretion disk ($r \sim 10^{-3}$ pc). In the same plane, colder material is forming a dust torus around this central engine ($r \sim 1 - 10$ pc). Perpendicular to this plane of accretion disk and torus, a radio-loud AGN exhibits collimated jets of relativistically outflowing material. Long term X-ray monitoring of AGN recently showed that AGN tori are clumpy structures, i.e., time variant absorption due to eclipse events along the line of sight is observed (Markowitz et al., 2014; Rothschild et al., 2011; Rivers et al., 2011). At $r \sim 0.01 - 0.1$ pc the broad line region (BLR) of a dense and fast rotating medium is formed followed further out by the narrow line region (NLR, $r \sim 100 - 1000$ pc) of low density medium. Note that this unified model is strongly debated, since observations indicate that changes or extensions are required (e.g., Bianchi et al., 2012).

In the radio-loud case, the jet inclination angle strongly affects the appearance of the whole system. Due to boosting effects (see Sect. 1.3.3), the highly relativistic outflows of blazars are seen as one-sided jets. The boosted emission of the jet can outshine the whole emission of the system, such that the other components are not detected.

1.2.2. AGN evolution and feedback

The luminosity functions and number counts of AGN reveal that the number density of AGN peaks at redshift $z \sim 2$ and declines to the present ("AGN downsizing", Hasinger et al., 2005; Richards et al., 2006; Rigby et al., 2011), as opposed to the expectations of a hierarchical growth in a cold dark matter universe (Springel et al., 2005). This contradiction is a first indication that the galaxy evolution is regulated by some processes. Observations show that the evolution of AGN are closely related to the growth of their host galaxies (e.g., Ferrarese & Merritt, 2000; Gültekin et al., 2009). The mass of the central SMBH is correlated with the stellar mass and velocity dispersion in the

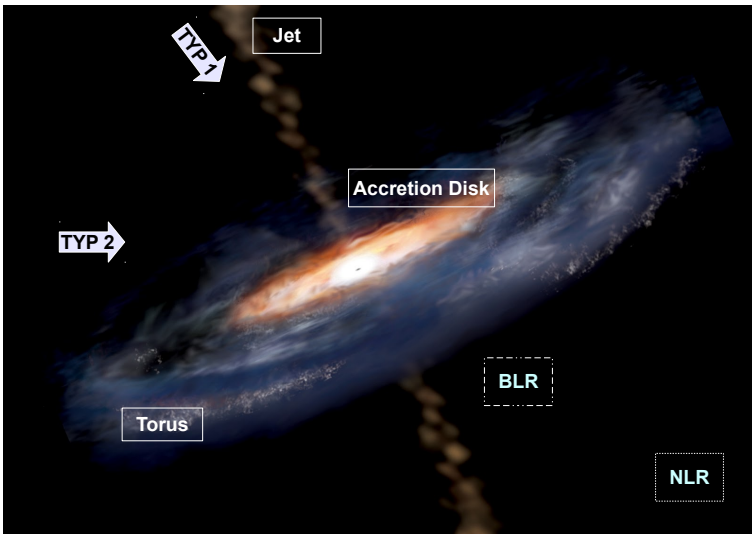

Figure 1.3: Artist impression of a radio-loud AGN. The components of the unification model are labeled (see Sect. 1.2.1). Type 1 sources are characterized by a small angle between the jet axis and the line of sight, while Type 2 sources are seen edge-on (Credit: Aurore Simonnet).

galactic bulge, i.e., more massive SMBHs are found in larger galaxies. Due to the large amount of gas in early formed galaxies and/or due to galaxy mergers, the accretion onto the central SMBH can "turn-on" AGN activity (Di Matteo et al., 2005). There is evidence that jets regulate this evolution (see Ch. 12 in Boettcher et al., 2012, and references therein). This mechanism is called *AGN feedback*, directly linking the formation of jets in the vicinity of the SMBH to the large scale evolution of the surrounding host (see Fabian, 2012). A detailed review on galaxy formation within the cosmological framework is given by Benson (2010, and references therein). Here, it is important to note the close relation between (early) star formation and black hole growth. Current models include a so called "radio mode" in which powerful jets from the AGN inject energy into the galaxy, heating the gas and terminating star formation. Observations by Page et al. (2012) confirm these predictions showing that the star formation is suppressed in highly luminous X-ray AGN.

1.3. Physics of relativistic jets

One major aim of this work is to further investigate the spectral and structural properties of extragalactic jets. Multiwavelength observations provide useful information for a better understanding of the underlying physics of these powerful objects. In this section, facts on jet properties known from observations and simulations are summarized (see Boettcher et al., 2012, for more information). I will complete the Chapter with an outline of open questions, focussing on the topics which are addressed by this work.

1.3.1. Broadband emission and variability

Multiwavelength observations show that the broadband emission in AGN jets is dominated by synchrotron radiation and the inverse Compton mechanism. In the following the theoretical background of these processes is summarized to lead over to the description of the broadband spectrum (see also Rybicki & Lightman, 1979). In Sect. 1.3.5 the modeling of the observed spectra is presented.

Low frequency emission

Synchrotron emission or *magnetobremsstrahlung* as the physical process of the radio emission of jets is very well established, first suggested by Alfvén & Herlofson (1950). In contrast to thermal emission, it can well explain the high degree of polarization observed from jets (e.g., Homan et al., 2002; Hovatta et al., 2010).

Charged particles moving in a magnetic field are influenced by the Lorentz force, emitting electromagnetic radiation. In the case of highly relativistic velocities, they produce characteristic synchrotron radiation. For a single particle of mass m, energy E, and moving with velocity $\beta = v/c$ in a magnetic field B, the emitted power is given by

$$P = \frac{1}{6\pi}\sigma_{\mathrm{T}} c \beta^2 \left(\frac{E}{mc^2}\right)^2 B^2 \quad , \tag{1.1}$$

with the Thomson cross section σ_{T}. It is clear that the synchrotron emission dominates for lighter particles of the same energy. Due to relativistic beaming effects, the dipole emission of a single particle in its rest frame is transformed to an emission cone with an opening angle $\propto \gamma^{-1}$ (with the Lorentz factor γ). When this cone points towards the observer, a short pulse is detected.

The averaged power of a (non-thermal) electron population with a power law velocity distribution yields the superposition of all individual electron spectra (with a characteristic frequency ν), an overall power law spectrum

$$P_\nu \propto \nu^{\frac{-(p-1)}{2}} \quad , \tag{1.2}$$

with the *spectral index* $\alpha = \frac{1-p}{2}$ for the index p of the particle energy distribution.

Synchrotron emission can lead to *Synchrotron self-absorption* effects when low energy photons are absorbed by their synchrotron emitting parent electrons. The resulting spectral shape strongly depends on the photon energy. The absorption coefficient a can be expressed as (detailed derivation in Boettcher et al., 2012)

$$a = -\frac{(p+2)}{18\pi m \nu^2}\left(\frac{3q}{4\pi mc}\right)^{\frac{p-2}{2}}\left(\frac{q^2}{mc^2}\right) B^{\frac{p+2}{2}} \nu^{-\frac{p+4}{2}} \tag{1.3}$$

for a power law distribution of particles (mass m, charge q) in a magnetic field B. This expression shows that the opacity increases for decreasing frequency. Below a critical frequency (the synchrotron self-absorption frequency), where the optical depth (or thickness) is $\tau_\nu = 1$, the spectrum changes from $S_\nu \propto \nu^{\frac{-(p-1)}{2}}$ at higher frequencies to $S_\nu \propto B^{-\frac{1}{2}}\nu^{\frac{5}{2}}$ at lower frequencies.

With radio observations at highest possible angular resolution (see Sect. 2.1.2), the synchrotron self-absorption mechanism in extragalactic jets can be imaged in detail. So called spectral index images display the optically thin (spectral index $\alpha \leq -0.5$) and optically thick ($\alpha \geq -0.5$) regions along the jet (see Sect. 3.3 and 7.3.3 for more details). The innermost regions of jets clearly show the effect of synchrotron self-absorption. Moreover, the spectral indices can indicate additional contribution of external absorption due to steeper indices of $\alpha \leq -2.5$ (e.g., by the torus, Kadler et al., 2004). The "core" of the jet is then referring to the brightest feature (typically the unresolved, upstream end) in a radio image, coincident with the $\tau = 1$-surface but not necessarily equal to the nucleus of the object. Images at different radio frequencies probe therefore different parts along the jet, since the jet is more opaque at lower frequencies (also known as the "core shift", e.g., Sokolovsky et al., 2011a).

High frequency emission

Compton scattering (Compton, 1923) describes the process of an inelastic scattering interaction of a photon with a charged particle (mostly an electron), resulting in an energy loss of the photon and, hence, in an increase of its wavelength. In the case of *inverse Compton scattering*, low-energy photons are up-scattered by relativistic electrons, which lose energy as a consequence. This mechanism is important in astronomical sources containing a large amount of hot electron gas, such as in the vicinity of galactic or supermassive black holes. Thermal comptonization, i.e. Compton scattering of photons with electrons in a thermal distribution, can yield a cooling of the electron gas when the photons gain energy and vice versa (Rybicki & Lightman, 1979). The resulting spectral shape can be approximated by a power law with an exponential cut-off (see also Dermer & Schlickeiser, 1993). The Compton losses can lead to the so called Compton catastrophe, when an efficient amplification causes a rapid down-cooling of the electrons (Kellermann & Pauliny-Toth, 1969), resulting in a theoretical limiting maximum brightness temperature of $T_{\mathrm{B}} \sim 10^{12}$ K of jets.

Inverse Compton scattering in AGN can involve different types of photon fields. In the special case of Synchrotron-Self-Compton (SSC) emission, the synchrotron photons are up-scattered by the same electrons which emitted them (e.g., Marscher & Gear, 1985; Dermer et al., 1997). For external photon fields, the seed photons are emitted by a different parent population (External Compton emission, e.g., Dermer & Schlickeiser, 2002; Meyer et al., 2012).

Hadronic emission processes play an important role and interactions with hadrons should be considered, since relativistic jets are promising candidates for ultra-high-energy cosmic rays (UHECRs) with energies greater than 10^{18} eV. Note that it is still under investigation if the jet material is composed of leptons and hadrons (see Sect. 1.3.5). At very high energies protons can reach the threshold for secondary particle production (Mannheim & Biermann, 1992; Mannheim, 1993). *Photon-proton interactions* result in the production of an electromagnetic pair cascade and can explain the high-frequency spectrum. The principle interactions are the photo-meson production $p + \gamma \rightarrow p + \pi^0$ (with a subsequent π^0 cascade), $p + \gamma \rightarrow n + \pi^+$, and the electron-positron pair production via the Bethe-Heitler process $p + \gamma \rightarrow p + e^+ + e^-$ (Bethe & Heitler, 1934). The neutrino production is an inevitable result of hadronic interaction processes, due to pion decay and therefore, their detection would be a substantive evidence for protons and ions in AGN jets (see Sect. 3.4).

In Sect. 1.3.5 theoretical models are presented trying to differentiate which of these processes dominates the observed broadband blazar spectra.

Broadband spectral energy distribution

Extragalactic jet sources are found to be bright throughout the electromagnetic spectrum up to TeV energies (e.g., Dermer et al., 1992; Fossati et al., 1998; Ghisellini et al., 1998). The different radiating components, i.e., the accretion disk, the torus, the broad/narrow line region, and the innermost jet, make up the overall spectrum. Due to orientation and relativistic beaming effects (see Sect. 1.2.1 and 1.3.3), emission of these different components appears with varying strength in the resulting broadband spectrum. However, in radio-loud objects the synchrotron (and associated inverse Compton) emission from the jet is clearly dominating. Despite the highest angular resolution of today's telescopes, these components in the vicinity of the central SMBHs still remain spatially unresolved. Spectral and temporal information help to disentangle the various contributions. Multiwavelength observations yield broadband spectra and long term variability information to study the emission mechanism(s) and correlation of different spectral components.

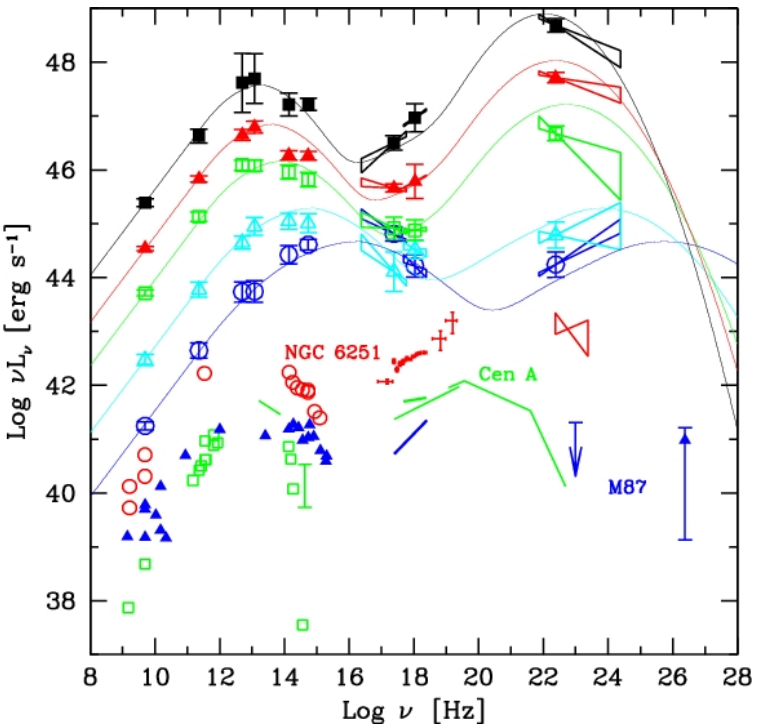

Figure 1.4: The blazar sequence after Fossati et al. (1998). The broadband SEDs of blazars show a correlation between bolometric luminosity and peak frequencies. Non-blazar sources – as for example the radio galaxies M 87, Cen A (see Ch. 7) and NGC 6251 – show a remarkably similar spectral shape. Image taken from Ghisellini et al. (2005).

The broadband spectral energy distribution (SED) of jet sources shows a double-humped shape in νF_ν representation peaking in the optical and in the hard X-rays or γ-rays (e.g., Chang, 2010). It is well established that the low energy peak is due to synchrotron radiation of relativistic electrons (Blandford & Königl, 1979). However, it is still under consideration which emission processes (synchrotron self-Compton up-scattering and/or Compton scattering with external photons, Königl, 1981; Sikora et al., 1994) and which different effects of jet composition (leptons, hadrons or both, Mücke et al., 2003) can explain the observed high energy broadband emission (see Sect. 1.3.5).

Studying a complete sample of blazar SEDs, Fossati et al. (1998) found a correlation between the source luminosity and the shape of the broadband SED (see Fig. 1.4 and also Ghisellini et al., 1998). Less luminous sources are found to have higher (synchrotron) peak frequencies than more luminous ones. Furthermore the two peaks are correlated. The double-humped shape is shifted in frequency depending on the source bolometric luminosity, the brighter the source the lower the synchrotron peak frequency. Broadband studies of non-blazar sources, e.g., the radio galaxy Centaurus A (Ghisellini et al., 2005; Abdo et al., 2010e, and see Ch. 7) reveal a very "blazar-like" SED shape suggesting that the underlying emission mechanism is similar.

However, the mechanisms causing the observed blazar sequence are still under debate, spanning discussions on selection effects (missing luminous, high-peaked objects, e.g., Finke, 2013), to the proposal of two distinct population according to the FR I/II dichotomy (Meyer et al., 2011).

Broadband variability

Blazars are characterized by their high variability throughout the spectrum, showing correlations within different wavebands. The variability timescales range from of short variations (hours to days) to longer active phases of weeks to months (see also Urry, 1996, for a review), depending on the observing frequency. This flaring behaviour of jet sources is often accompanied with a change in the polarization angle (indicating highly ordered magnetic fields, e.g., Abdo et al., 2010f) and/or jet ejection events.

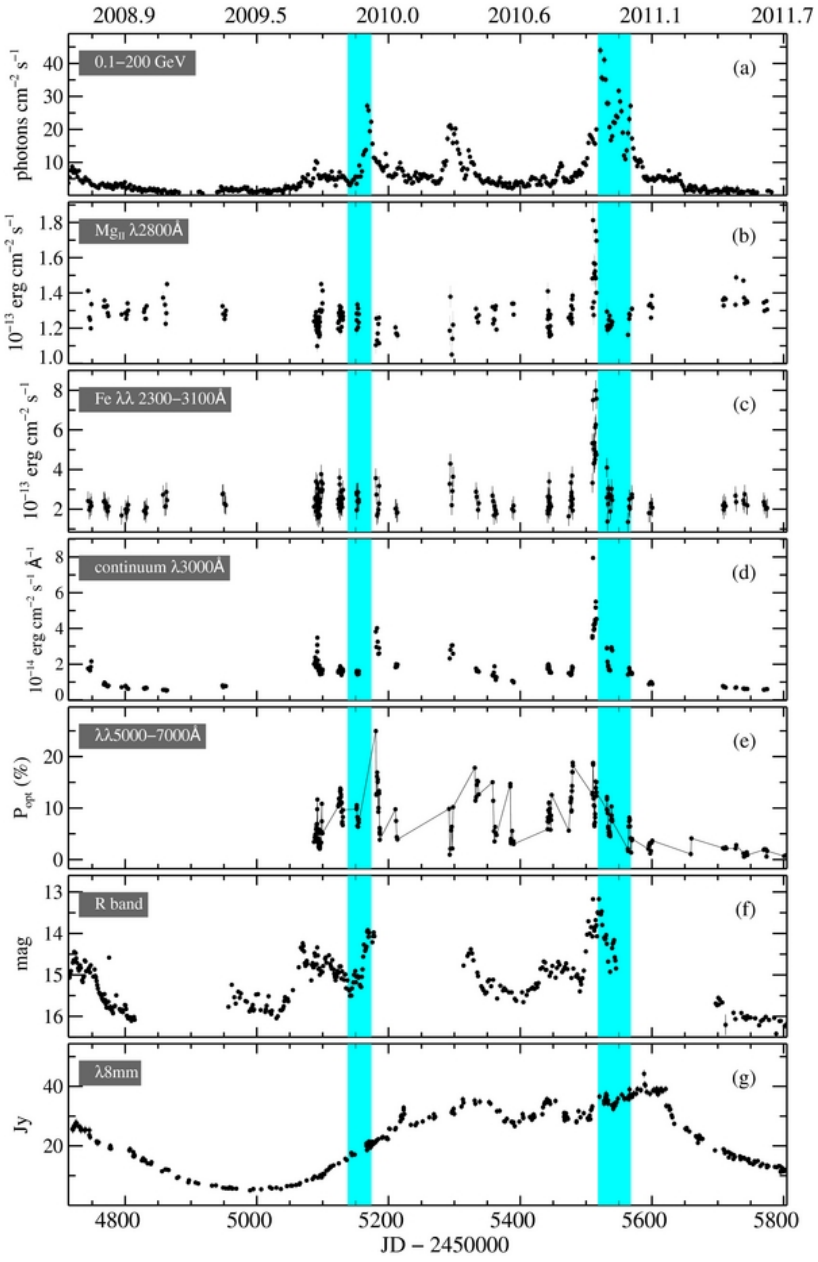

Figure 1.5: Multiwavelength variability of blazars. As an example, the simultaneous radio to γ-ray light curves of the highly variable flat spectrum radio quasar 3C 454 are shown. The blue shaded vertical stripes indicate the ejection times of newly emerged components from the core (see León-Tavares et al., 2013, and references therein). Correlation studies aim to pin down the origin of the γ-ray emission, discussing possible production sites close to the black hole (e.g., Tavecchio et al., 2010) or further downstream the jet involving EC mechanism (Jorstad et al., 2010). Figure from León-Tavares et al. (2013).

The study of the multiwavelength variability and the relationship between the bands is crucial for understanding the underlying emission mechanism. Simultaneous (long-term) monitoring of blazars give information on the origin of the high energy emission, the cause of the flares and the structure of the jets themselves.

The inter-band correlation is still a matter of debate. Some sources show correlated emission pattern in the optical and γ-rays (see Fig. 1.5), while the radio and X-rays lack an obvious correlation (see, e.g., the multi-waveband variability results on PKS 1510–089 Marscher et al., 2010). Note that there are instances where such correlations are not present or even "orphan flares" occur (e.g., Neronov et al., 2012). The lack of correlation with the radio emission might be due to the fact that the observed high-energy flare is produced within a region which is optically thick in the radio (see also Sect. 7.7).

The combination of high angular resolution radio observations and multiwavelength monitoring gives a better understanding of the relation between high-energy flares and structural changes within the jet ("jet ejections"). However, as the jets are optically thick where the outburst potentially occurs, correlation studies are not straightforward. Very Long Baseline Interferometry (VLBI, see Sect. 2.1.2) and polarimetry are powerful tools to study the connections of the ejection of (superluminal) jet knots and the (rapid) increase of high-energy emission. In principle, the association of an outburst with jet ejection times or the change in polarization of radio knots with optical flares, allows the localization of the activity along the jet via the corresponding time lags (Marscher, 2008; Jorstad, 2008, see Fig. 1.8). Such analysis suggests that occurrence of high-energy flares can be explained by shocks propagating down the jet. As these disturbances travel along a spiral streamline in a helical magnetic field, they pass the acceleration and collimation zone and the upstream standing (conical) shock, generating high-energy flares (Marscher et al., 2008; Marscher, 2009). Furthermore, VLBI to X-ray monitoring indicate jet ejections follow a dip in the X-ray light curves which can be explained by a jet-accretion disk interaction (Marscher et al., 2002; Marscher, 2006; Tombesi et al., 2012).

First high-resolution monitoring of γ-ray bright blazars detected by *CGRO*/EGRET (Hartman et al., 1999) revealed that these sources have faster apparent proper motions (see Sect. 1.3.3) indicating larger relativistic beaming factors (Jorstad et al., 2001b). Correlation studies of the γ-ray to radio flux, jet ejections and polarization changes during high-energy flares already suggested that the flares are connected to superluminal jet knots (Jorstad et al., 2001a) and that γ-ray bright sources tend to have larger brightness temperatures and opening angles (Taylor et al., 2007). Based on these studies and triggered by the launch of the Gamma-ray Space Telescope *Fermi* (see Sect. 2.2), comprehensive multiwavelength campaigns aim nowadays at investigating the mechanism causing the broadband variability of extragalactic jets.

Multiwavelength campaigns

Monitoring campaigns with simultaneous observations from the radio to the γ-rays of individual (exceptional) and of samples of extragalactic jets allow detailed investgations of their physics. As introduced above, the optimum output is achieved by connecting VLBI observations at high angular resolution with simultaneous multiwavelength monitoring. This gives information on the evolution of the parsec-scale jet morphology along with the flux variability via correlation studies. Simultaneous broadband spectra of different activity phases (flaring versus quiescence, see Fig. 1.6) provide insight in spectral changes and hence, information on the contribution of individual emission components to the flare.

With the launch of *Fermi* in 2008 (see Sect. 2.2), a new era of broadband studies has been started. Thanks to the continuous monitoring of the whole sky at γ-ray energies, variability studies of large source samples is now possible, much less unbiased and restricted to particular bright and active sources.

Ongoing sub-milliarcsecond monitoring at 15 GHz of total flux density and linear polarization by the *MOJAVE* program (Kellermann et al., 1998, 2004; Lister & Homan, 2005; Lister et al., 2009a) provide jet kinematics and an important database for inter-band correlation studies on the Northern Hemisphere. The resulting long-term evolution of jets revealed that γ-ray bright jets have generally higher radio flux densities (Kovalev et al., 2009), larger opening angles (Pushkarev et al., 2009), and higher Doppler factors (Savolainen et al., 2010). It was found that jet proper motion is not simply a ballistic motion in a constant direction. Instead, significant acceleration along and perpendicular to the observed component motions and changes of the jet position angle are measured (Homan et al., 2009; Lister et al., 2013). In addition, total and polarized intensity

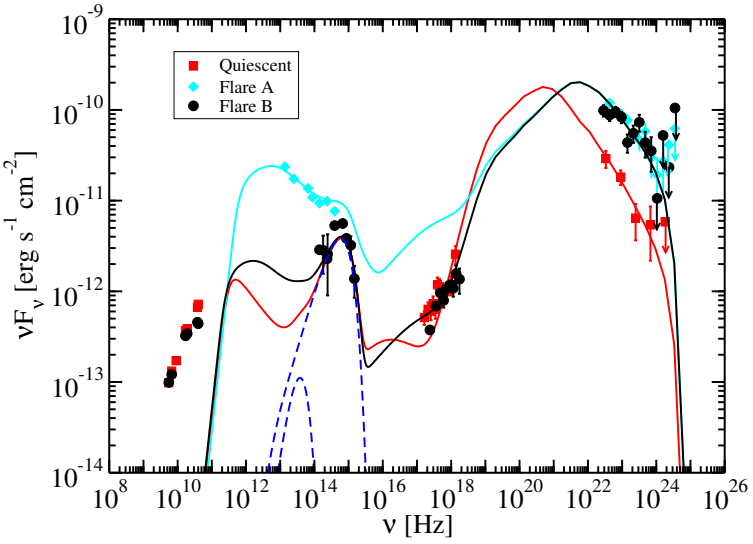

Figure 1.6: Quasi-simultaneous spectral energy distributions of PKS 2142–75 measured during two active γ-ray periods (blue and black points) and a quiescent (red) γ-ray period on 2011 December (Dutka et al., 2013). Such studies allow to identify the source parameters which change or stay constant during a flare, providing crucial insight into the emission mechanism. Figure from Dutka et al. (2013).

monitoring at 43 GHz[3] (i.e., generally further upstream the jet, closer to the launching region) reveal a close connection between γ-ray flares and jet ejection events (Marscher et al., 2012), further challenging emission models to explain short intra-day variability.

The high-resolution imaging is complemented by polarimetry measurements in the *VLBA Imaging and Polarimetry Survey* (VIPS, Taylor et al., 2007) and the *5 GHz Caltech-Jodrell Bank Flat-Spectrum Survey* (CJF, Taylor et al., 1996; Britzen et al., 2007, 2008) comprising an enormous database to perform statistical studies.

On the Southern Hemisphere the *TANAMI* program (Ojha et al., 2010) combines VLBI monitoring with multiwavelength observations to continuously study extragalactic jets during low as well as active phases (see Ch. 3 for more details).

1.3.2. Formation and structure

Observations of various astrophysical systems, like X-ray binaries or young stars, show clear evidence that their high luminosity is due to accretion onto a compact object. Similarly, the multiwavelength information of AGN suggests the presence of an accreting supermassive black hole as the central engine. Accretion onto a black hole releases large amounts of energy and provides the power for collimation of jets. Material falling onto a black hole is forced to assemble an accretion disk due to conservation of angular momentum. For trapped matter to be accreted, angular momentum needs to be transferred outwards via friction and radiation. The “fuel” can consist of gas from the interstellar medium or from tidally disrupted stars close to the central SMBH.

Seminal work by (Blandford & Znajek, 1977), had led to the understanding that the energy of rotating, accreting black holes powers the launching of jets. In this general picture the magnetic field close to the BH is locked to the accretion disk and hence, due to space-time rotation, the magnetic field lines are twisted to form a helical field perpendicular to the disk. The extraction of energy from the spinning black hole leads to the formation of jets – accelerated plasma along the rotational axis (Blandford & Payne, 1982). Most recent numerical simulations are based on this picture. As an example, Fig. 1.7 shows the results of general-relativistic, magneto-hydrodynamic (GRMHD) simulations of an accreting black hole (Tchekhovskoy et al., 2011). A powerful, collimated jet-counterjet system is formed, resulting from a turbulent accretion onto an extremely

[3] `http://www.bu.edu/blazars/VLBAproject.html`

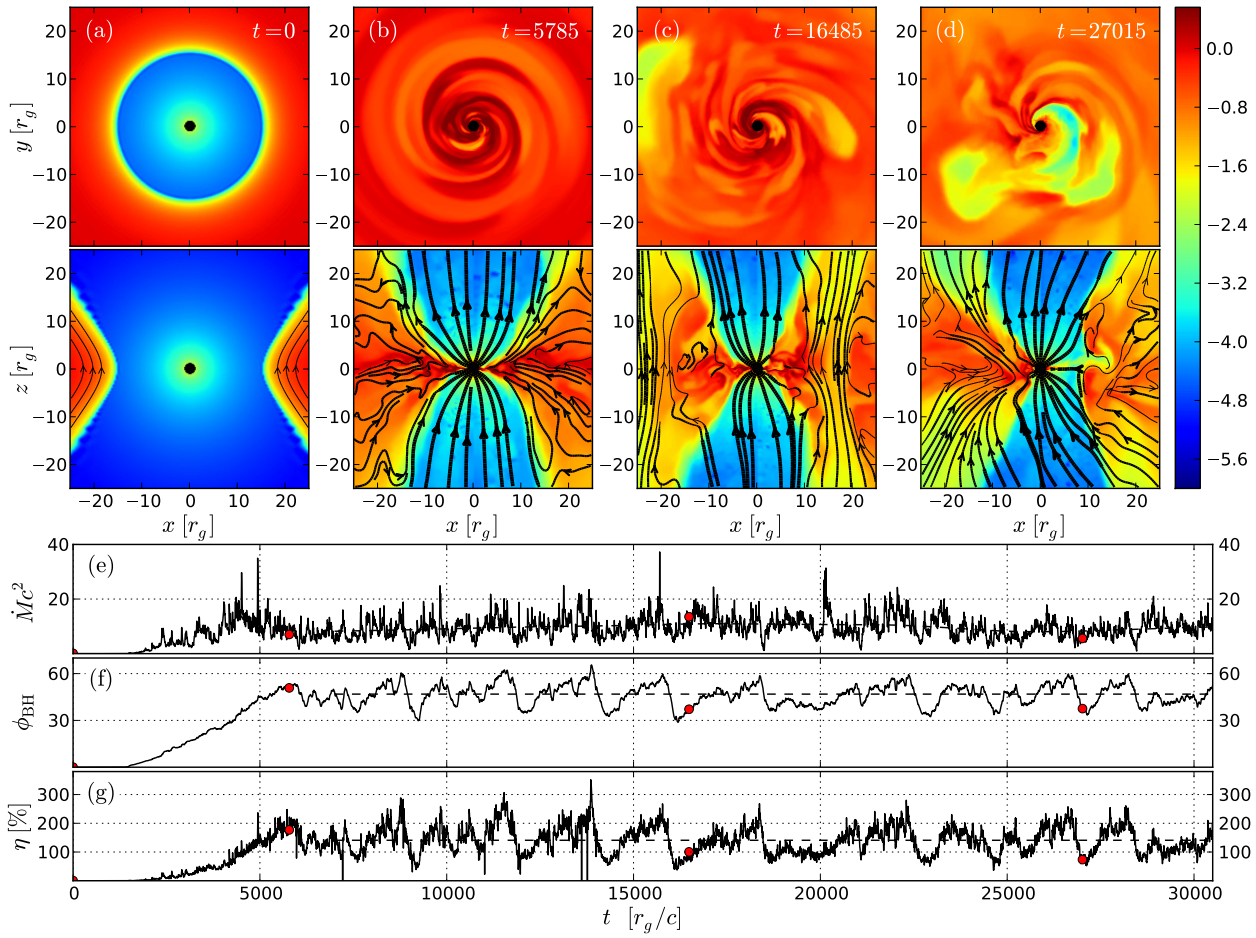

Figure 1.7.: GRMHD simulation for a spinning black hole (spin parameter $a = 0.99$, Tchekhovskoy et al., 2011). Shown is the time evolution of the turbulent accretion (*panel a-d*, top and edge-on snapshots, respectively), where the color scale represents the fluid frame rest mass density, the filled black circle indicate the BH horizon, and the black lines show the magnetic field lines in the image plane. *Panel e to g:* time evolution of the rest mass accretion rate, of the large-scale magnetic flux, and of the energy outflow efficiency, respectively. Figure taken from Tchekhovskoy et al. (2011).

spinning black hole. After the jet has launched the plasma is collimated, accelerating particles up to their highest energies.

High resolution radio observations reveal that AGN jets are already highly collimated at sub-parsec scales (Kovalev et al., 2007; Müller et al., 2011). Remarkably, the jets extend and stay collimated up to scales which are ten orders of magnitude larger than the size of the SMBH. The process to confine the jet is not fully understood, though there is evidence that the magnetic field and the ambient pressure are the confining components while the acceleration of the plasma can be explained by the adiabatic expansion (see Lyubarsky, 2011, and references therein).

Shocks and instabilities

Figure 1.8 shows an illustration of an AGN jet indicating the basic physical components which make up such a system and the broadband emission. This picture is based on observations and simulations described above. On top of the collimated and accelerated plasma outflow, due to enhanced mass-injection into the jet, shocks can evolve and propagate downstream (first proposed

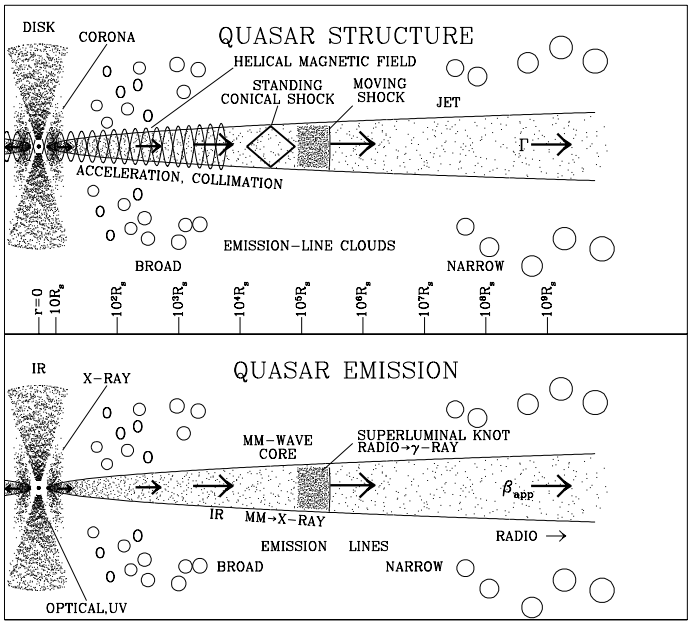

Figure 1.8: AGN jet model showing physical structure (*top*) and origin of electromagnetic radiation (*bottom*) with logarithmic length scale. Figure from Marscher (2009).

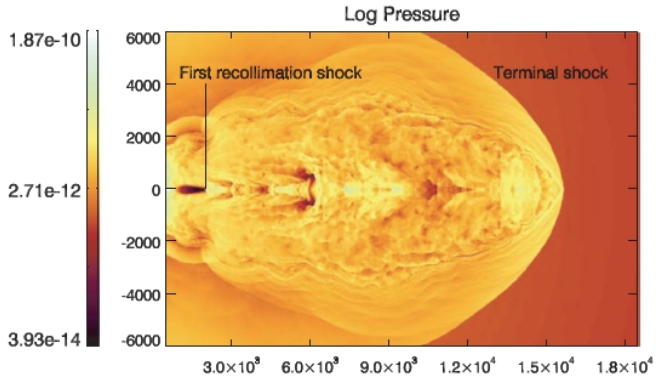

Figure 1.9: Relativistic numerical simulation of an expanding jet. Due to expansion the overpressured jet becomes underpressured and recollimates, resulting in *"subsequent oscillations around pressure equilibrium and generation of standing shocks"* (Perucho & Martí, 2007). Shown is the logarithm of the pressure (in Pa), coordinates are in parsecs. The location of the first recollimation shock and the terminal shock are indicated. The terminal or bow shock is formed where the jet hits the ambient medium. Figure from Perucho & Martí (2007).

by Blandford & Rees, 1978). These traveling shocks can explain the bright, moving jet knots with apparent superluminal velocities (see below). In this local pressure maximum, the particle density and energy is expected to increase, such that shocks are particle acceleration sites within a jet.

The cause of shock formation is the perturbation of the jet flow, i.e., inhomogeneous injection of plasma or entrainment of or interaction with material from the environment. The propagation of a perturbation along the jet results in the formation of a shock front. When passing through it particles gain energy (Fermi, 1949).

Standing shocks can be explained as recollimation shocks, occurring when the pressure equilibrium between the jet and the ambient medium levels out at these points (Perucho & Martí, 2007; Gomez et al., 1995). Figure 1.9 shows the result of a numerical simulation of an overpressured jet. Its expansion leads to a density, temperature and pressure decrease. Simultaneously, the jet plasma is accelerated and the jet becomes overpressured again. This dynamical behavior results in an oscillating expansion region followed by a recollimation shock.

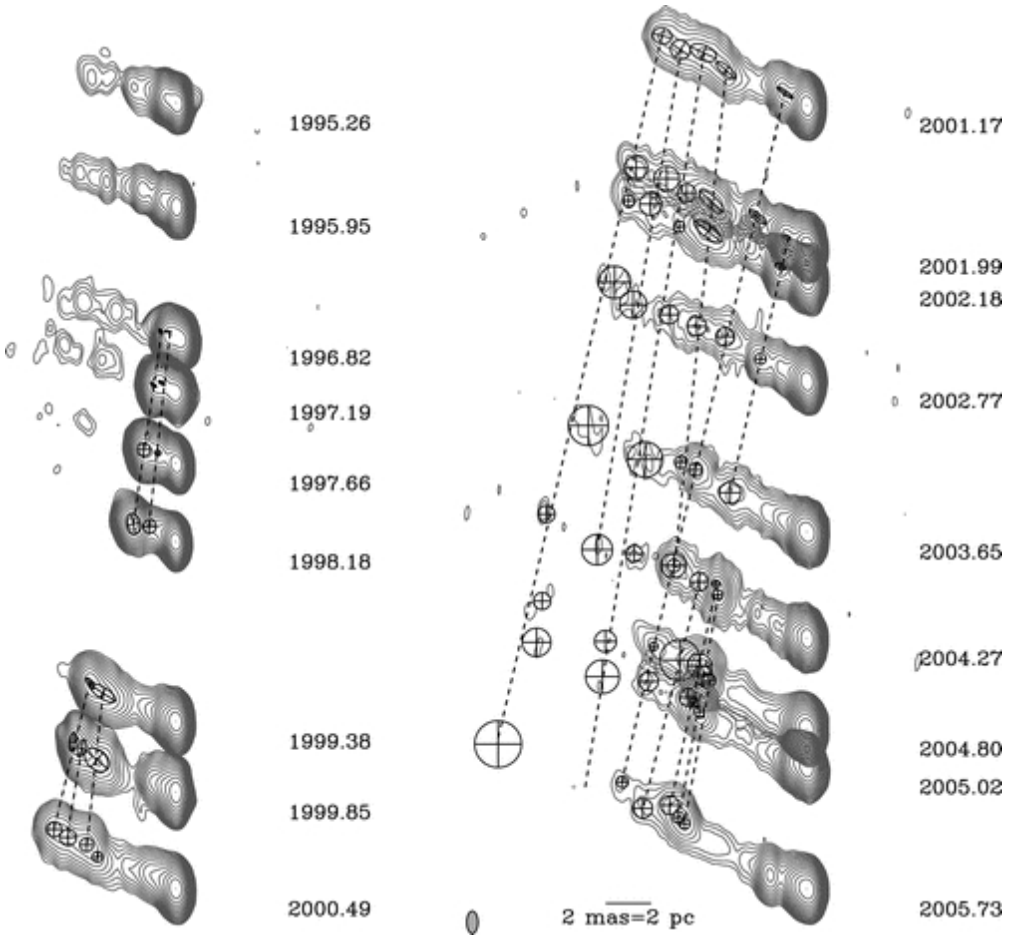

Figure 1.10.: Jet kinematics of 3C 111. High angular resolution observations at 15 GHz obtain an apparent jet velocity of $\sim 5c$, which is known as "superluminal motion". Figure from Kadler et al. (2008).

1.3.3. Relativistic effects

After the first detection of superluminal motion in an AGN jet by Gubbay et al. (1969), this phenomenon has been found in most of the monitored extragalactic jets (e.g., Cohen et al., 1977; Jorstad et al., 2001b; Kellermann et al., 2004) and is a clear evidence that jets are highly relativistic. As an example, the kinematic of 3C 111 is shown in Fig. 1.10, revealing an apparent motion of the bright jet components of $\sim 5c$.

Superluminal motion is easily explained by a projection effect and the constant and finite speed of light (see Fig. 1.11). Consider a moving bright jet feature propagating with speed v along a jet, which has a small angle θ to the line of sight. Two distinct light signals emitted by this jet feature while traveling a certain distance are considered in the following. The observer detects the signals separated by

$$\Delta t_{\mathrm{obs}} = \left(1 - \frac{v}{c}\cos\theta\right)\Delta t_{\mathrm{emit}} \quad . \tag{1.4}$$

As the feature moves downstream the jet, the observed distance is $\Delta x = v\Delta t_{\mathrm{emit}}\sin\theta$, which leads to an observed velocity of

$$v_{\mathrm{app}} = \frac{v\sin\theta}{1 - \frac{v}{c}\cos\theta} \quad . \tag{1.5}$$

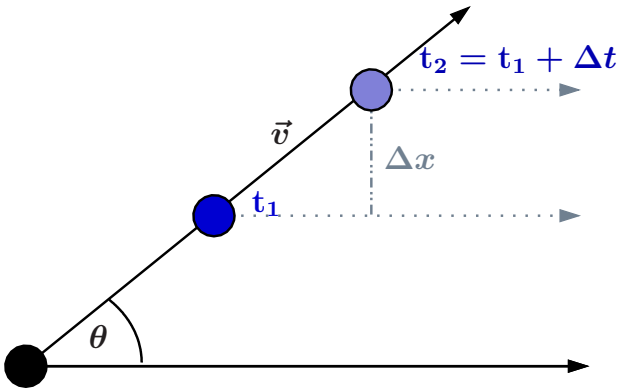

Figure 1.11: Sketch to illustrate the projection effect of superluminal motion. A bright emission feature propagates along the jet with velocity v, close to the line of sight under the inclination angle θ. The observer takes projected images of this system. See text for further explanations.

The apparent velocity $\beta_{\rm app} = v_{\rm app}/c$ strongly depends on the jet inclination angle. For small θ, it can reach $v_{app} > c$. To determine the real speed, this angle must be known.

Since jets are highly relativistic, further effects need to be taken into account. The Doppler factor D is an important quantity for the study of jets. It is defined as

$$D = \frac{\nu_{\rm obs}}{\nu_{\rm em}} = \frac{\sqrt{1-\beta^2}}{1-\beta\cos\theta} = \frac{1}{\gamma(1-\beta\cos\theta)} \tag{1.6}$$

strongly depending on the inclination angle (see Fig. 1.12). Doppler boosting is the effect of increased/decreased observed flux density due to emission of an approaching/receding emitting feature moving at relativistic speed and on a path close to the line of sight. Spherical emission of a relativistically moving feature is transformed into a "boosting cone" with an opening angle γ^{-1}. It can be shown that for the flux density S_ν at frequency ν the quantity $S_\nu \nu^{-3}$ is Lorentz invariant (see Ch. 4.9 in Rybicki & Lightman, 1979). Therefore, the observed intensity of a relativistically moving jet with a power law spectrum ($S \sim \nu^\alpha$) is (Lind & Blandford, 1985)

$$S(\nu_{\rm obs}) = D^{3-\alpha} S(\nu_{\rm em}) \quad . \tag{1.7}$$

This effect is clearly seen in VLBI images of extragalactic jets (see, e.g., Fig. 1.10) and known as "jet one-sidedness" and leads to the definition of the "counterjet" as the receding (fainter) jet.

Using the jet and counterjet surface brightness, the Eq. 1.6 and 1.7 give the following relation

$$R = \frac{S_{\rm approach}}{S_{\rm depart}} = \left(\frac{1+\beta\cos\theta}{1-\beta\cos\theta}\right)^{i-\alpha} \quad , \tag{1.8}$$

with $i = 2$ for a smooth jet and $i = 3$ for a spherical emission feature. This relation allows the estimation of the jet inclination angle (see also Sect. 6.4.2 and 7.6.1).

1.3.4. Jet kinematics

Sample studies of AGN jets reveal that the overall jet flow follows a preexisting channel, although individual components can move differentially (see, e.g., Fig. 1.10 and Kellermann et al., 2004; Lister et al., 2009b). The kinematics of particular jet features can then be described by a characteristic speed primarily in the direction of the established jet, although bends and twists can cause changes in the motion vectors or surface brightness due to Doppler boosting. Kellermann et al. (2004) report on faster speeds at higher observing frequencies, suggesting that observations at different frequencies sample different parts of the jet. These results can be explained assuming

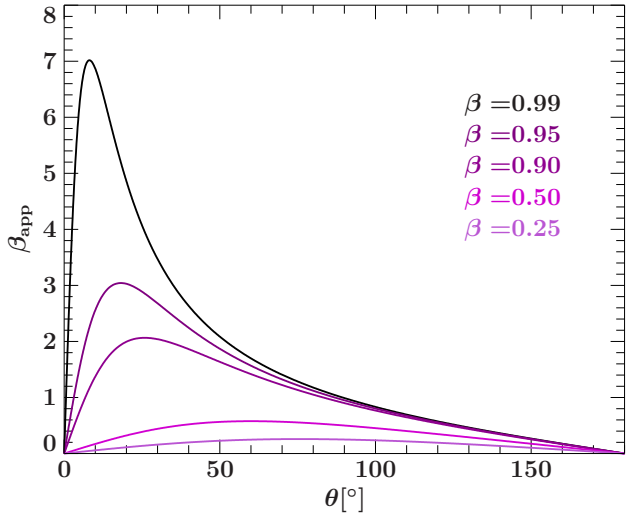

Figure 1.12: Observed apparent speed $\beta_{\rm app}$ as a function of inclination angle and for different intrinsic $\beta = v/c$.

a spine-sheath like structure (Ghisellini et al., 2005; Tavecchio & Ghisellini, 2008; Perucho et al., 2006).

Significant acceleration of components has been measured in a number of AGN jets (Homan et al., 2009; Lister et al., 2013), both parallel and perpendicular relative to the jet, although it is hard to distinguish whether parallel acceleration is due to a change in the Lorentz factor Γ or a change in the angle to the line of sight. Overall, a positive acceleration trend is found closer to the jet base at ≤ 15 pc, while deceleration occurs further out. Recent studies by Piner et al. (2012) and Lister et al. (2013) showed that non-ballistic behavior, i.e., non-radial motion and acceleration, is very common in blazar jets. These authors found a general trend of increasing speed down the jet for BL Lac objects and radio galaxies. Orientation effects cannot fully account for these speed changes (see also Sect. 7.6.1). Further high-resolution investigations are required to understand the kinematical behavior of extragalactic jet. In Section 7.5, I therefore present the kinematic study of the inner parsec of Cen A.

1.3.5. Blazar emission models

The previous sections described the results of observations (and simulations) on extragalactic jets, revealing powerful, highly relativistic plasma outflows radiating light across the whole electromagnetic spectrum. In order to get information on the mechanism and location of the emission and the particle composition of the jets, physical models to describe the broadband SED and variability are required.

Two distinct emission humps are seen in blazar SEDs (see Sect. 1.3.1), allowing the subclassification into low-, intermediate- and high-peaked objects, defined by the frequency of the low energy component (Fossati et al., 1998). The strong variability observed in blazars is often correlated with a change in the spectral shape. Such correlated variability provides important insight into the underlying physics.

The basis of jet emission models is the description of the broadband emission with synchrotron and inverse Compton emission (see Sect. 1.3.1 and Boettcher, 2010). It is contentious which photon fields are involved, where is the emission origin of the observed radiation and what is the composition of the jets.

The fast variability (down to a few minutes), the high bolometric luminosity, and the relativistic motion in jets indicate that the non-thermal broadband emission is produced in a region of less

than a light-day in size. Hence, single-zone synchrotron models have been favored, though they are difficult to reconcile with "orphan" high energy flares, requiring multiple-component models (e.g., Krawczynski et al., 2004). The low energy hump in the SED is well explained by synchrotron emission of relativistic electrons. For the high energy hump, however, there are two main approaches: leptonic and hadronic models.

Leptonic Models

With Synchrotron Self-Compton (SSC) models, the SED is described by the synchrotron emission of relativistic electrons, which also serve to scatter the photons to higher energies via the inverse Compton effect, resulting in the high-energy hump (Marscher & Gear, 1985).

Leptonic models can also involve external radiation fields (Dermer et al., 1992; Dermer & Schlickeiser, 1993; Sikora et al., 1994; Ghisellini & Tavecchio, 2008), such as photons from the accretion disk, the jet itself, the torus or the BLR.

In general, leptonic models are able to successfully describe the SEDs and spectral variability of blazars. However, the detection of very rapid flares displays problems for simple one-zone models (Dermer & Lott, 2012, and references therein). Moreover, VLBI observations reveal multiple emission sites of high energy photons (e.g., Müller et al., 2011) and requires more sophisticated models taking the source geometry into account (Richter & Spanier, 2013). Multi-zone models like the spine-sheath scenario by Tavecchio & Ghisellini (2008) or the decelerating jet model by Georganopoulos & Kazanas (2003a) attempt to include the differential motion within the jet.

Shock-in-jet models are powerful to explain the variability and the correlation between different frequency bands by simulating the radiation transfer and the dynamics of the electrons in shocks (Spada et al., 2001; Mimica et al., 2004; Böttcher & Dermer, 2010; Marscher, 2014).

(Lepto-)Hadronic Models

In hadronic models the low energy hump is also modeled with the synchrotron emission from a highly relativistic electron population, but the high energy emission is attributed to an additional hadronic component. Part of the kinetic jet power can be transferred to accelerate protons, inducing pion production through photon-proton interactions and subsequent production of an electromagnetic particle cascade (Mannheim & Biermann, 1992; Mannheim, 1993). The accelerations of protons to these high energies requires strong magnetic fields of several tens of Gauss (Boettcher, 2010; Mücke et al., 2003).

1.4. Outline of this thesis

This introduction to extragalactic jets covers of course just parts of the topic and much more could be said on these interesting objects. Further explanations, however, would go beyond the scope of this work and can instead be found in the textbooks by Krolik (1999), Beckmann & Shrader (2012) and Boettcher et al. (2012).

I have shown so far that the physics of these powerful objects is best revealed by simultaneous, long term studies throughout the electromagnetic spectrum. For a deeper understanding, it is crucial to obtain information on the structural evolution on parsec-scales as well as to monitor the broadband spectrum during different activity stages. This observational approach yields the optimum conditions to test jet emission and formation models.

Extensive multiwavelength studies result in a consistent overall picture of AGN jets, though they also give rise to questions. Main topics, which will be addressed in this work, include the emission mechanisms and origin of the X-ray and γ-ray photons. Why are some jets γ-ray bright, while others, though powerful in the radio, are not? What is the composition of jets, leptons or hadrons or a mixture of both? Furthermore, the collimation and formation of jets is yet to be solved. What happens during the interaction of the jet with its environment? What causes the high-energy flares, are they produced downstream or close to the base of the jet?

My aim is to contribute to a better understanding of these issues. To this end, I have analyzed high angular resolution observations in the radio and simultaneous multiwavelength monitoring of a sample of extragalactic jets in the Southern Hemisphere – the TANAMI sample. Chapter 2 presents the instruments and methods to analyze these observations, which have been performed in the framework of the TANAMI program (Ch. 3). In Chapter 4, I present the γ-ray variability analysis of the TANAMI sample in the context of extragalactic neutrino search with ANTARES. The milliarcsecond scale properties with respect to the γ-ray loudness of all sources are discussed in Chapter 5.

The main part of this thesis covers the detailed study of two exceptional objects of this sample: PMN J1603−4904 (Ch. 6) and Centaurus A (Ch. 7). The former shows unusual multiwavelength properties, which are difficult to reconcile with typical blazar characteristics, but open room for a possible classification as a young radio galaxy. Since it is one of the brightest γ-ray sources in the sky, detailed investigations are important to understand the underlying emission mechanism. The latter is the closest radio galaxy, so that the reported observations resolve the jet down to scales of a few light days. The jet propagation and emission can be studied with unprecedented detail providing valuable information for theoretical models. These highly resolved images in combination with multiwavelength monitoring give the deepest insight into an AGN jet ever and allow me to constrain the emission origin of high energy photons. With respect to blazars, the study of the radio to γ-ray emission of these specific sources provides decisive information on AGN physics and their interaction with their host galaxy in general.

The development of the telescope, together with increased knowledge of things, brought men to see that the earth is not what man had once thought it to be.

(Joseph F. Rutherford)

2. Multiwavelength observations and data analysis

Since extragalactic jets are broadband emitters, the optimum study of the physics of these extreme objects requires high-resolution and simultaneous multiwavelength observations. The following sections describe the main observational techniques and corresponding data analysis which were applied to the studies presented in this thesis (see Chapters 4 to 7). For the X-ray analysis of *XMM-Newton* and *Suzaku* data presented in Sect. 6.2.4, I refer to the detailed introduction by Hanke (2011) and Fürst (2011).

2.1. Radio observations and analysis

The serendipitous detection of Galactic radio waves by Karl Jansky (1933) paved the way for a new branch of astronomy: with radio observations scientists started to reveal the optically invisible space. Nowadays radio interferometry achieves the highest angular resolutions of astronomical observations down to less than a milliarcsecond (see Sect. 2.1.2). With radio interferometers it is possible to resolve the most distant objects in the universe, e.g., to investigate the parsec-scale structure of extragalactic jets (Sect. 1) up to high redshifts. The following introduction is based on the textbooks by Thompson et al. (2001) and by Burke & Graham-Smith (2002).

2.1.1. Radio telescopes and single-dish observations

A radio telescope consists of a receiving antenna, a sensitive receiver, and a recording system. The angular resolution of an antenna is determined by the diffraction pattern and can be expressed by the basic approximation derived from the Rayleigh criterion

$$\sin(\theta) \approx 1.22\frac{\lambda}{D} \quad , \tag{2.1}$$

where θ is the angular resolution, D the diameter of the aperture and λ the observing wavelength. In order to achieve the highest possible resolution, one must either increase the diameter of the antenna or observe at smaller wavelengths. The observable (radio) wavelengths range from several tens of meters to the (sub-)millimeter regime, depending on the "radio window" of the atmosphere, weather conditions and of course the science case. For mm/cm wavelengths, radio antennas are parabolic reflectors (see Fig. 2.1) where the incoming wavefront is reflected and focused on the receiving device. The typical diameters of such "dishes" are of a few meters, while the construction

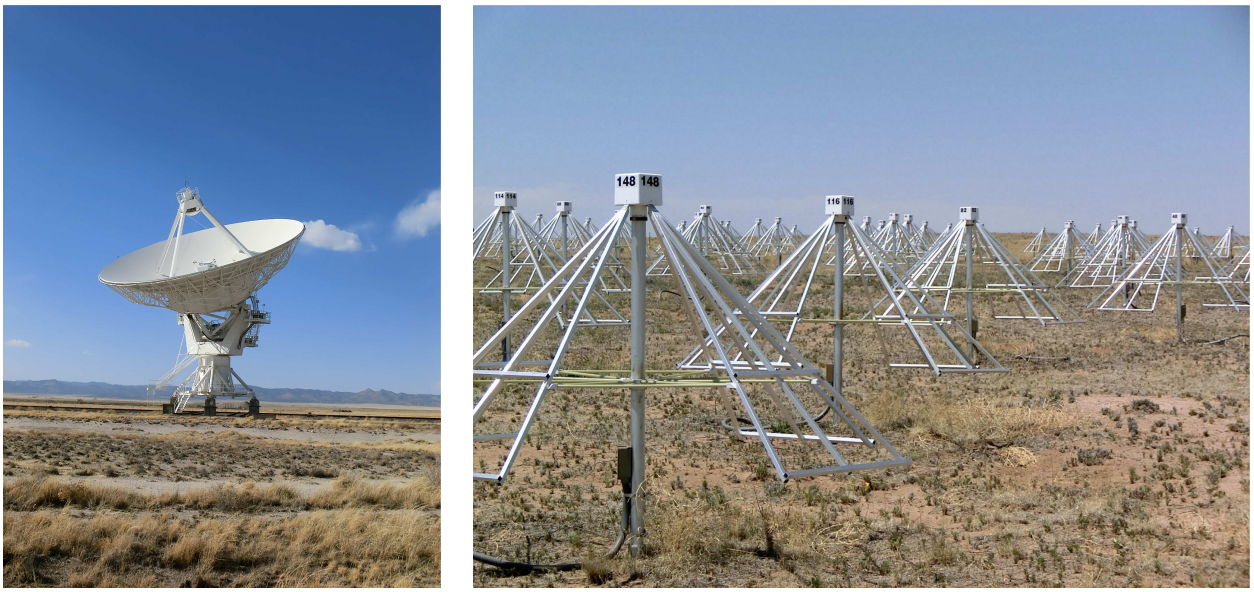

Figure 2.1.: Antenna types in the desert of New Mexico, USA. *Left:* parabolic reflector of the Jansky Very Large Array (JVLA) with a diameter of $D = 25\,\mathrm{m}$. *Right:* dipole antennae of the Long Wavelength Array (LWA, Ellingson et al., 2009).

and operation of large antennas is physically limited by their weight[1]. For the study of radio emission at longer wavelengths, different types of antennas are more suitable, like dipoles with certain designs (see Fig. 2.1). Due to radio interference, mainly disturbances by man-made radio signals, the telescope sites are often chosen to be far away from civilized areas (e.g., in the desert of New Mexico or at the South Pole). The effects of interference become worse when the observing frequency is higher and the cosmic radio signals become weaker. Moreover, at higher frequencies, observational conditions are constrained by the weather and the atmosphere.

The reception pattern of a single antenna consists of the main beam and the side lobes. The full width at half maximum (FWHM) of the main beam is defining the angular resolution.The reception pattern is described by the Fourier transform of the aperture distribution. The incoming wavefront is detected at the antenna feed, typically a waveguide horn. The radiation is transfered to a sensitive receiver and converted into an electric signal. The sensitivity of an antenna strongly depends on the size of the effective area. The antenna temperature T_A (in Kelvin) is the output quantity of a radio telescope. It is defined as the corresponding temperature of a hypothetical resistor at the receiver input generating the same output noise power per frequency bandwidth.

Observations with one single antenna are also called “single dish observations”. For most of the radio telescopes observing at mm/cm-wavelengths, their diameter is not large enough to resolve most astronomical objects[2]. Hence, single dish observations are more suited to observe the overall (unresolved) emission of a source, to obtain a spectrum or a light curve. With the knowledge of the source properties from higher resolved observations, together with these single-dish information, one can make statements on the regions dominating the observed emission (see, e.g., Sect. 6.3.5).

[1]The largest steerable antenna is the Green Bank Telescope (GBT) in Virginia, USA, with a diameter of $\sim 101\,\mathrm{m}$, followed by the 100 m radio telescope in Effelsberg (Germany).

[2]There are, however, some exceptions, where middle-sized telescopes are already able to resolve the extended emission with single pointings, like the Sun with an angular extension of $d \sim 0.^\circ5$ or the closest active galaxy Centaurus A with $d \sim 10^\circ$ (see Ch. 7)

Figure 2.2: Jansky Very Large Array (JVLA, Perley et al., 2011) on the Plains of San Agustin (New Mexico, USA). On Y-shaped tracks, 27 single antennas with a reflector diameters of $D = 25\,\mathrm{m}$ are connected to operate as a radio interferometer with a maximum extent of 36 km.

2.1.2. Very Long Baseline Interferometry

To enhance angular resolution and sensitivity of a radio telescope, a larger reflector is required. The technique of radio interferometry - connecting individual telescopes to an array - allows us to construct telescopes with diameters as large as the size of the Earth. This section introduces the concept of radio interferometry focussing on the methods and observational techniques used for the analysis presented in this work (see Ch. 5 to 7). More detailed information can be found in Thompson et al. (2001), Burke & Graham-Smith (2002) and Müller (2010).

Theory of VLBI

The basic concept of a radio interferometer involves the combination of two or more antennas, operating together as a large telescope of the size of the largest antenna spacing ("baseline"). Using Fourier transform techniques, the image of the source brightness distribution can be reconstructed. Such a setup can tremendously increase the angular resolution of the observing instruments. Figure 2.2 shows one of the most prominent examples of radio interferometers, the Jansky Very Large Array (JVLA, Condon et al., 1998) in New Mexico, USA. All 27 antennas in a Y-shaped configuration are connected to operate as one single telescope with a maximal extent of 36 km.

If further extending baselines to several hundreds of kilometers, i.e., unconnected telescopes on different continents are used, one refers to as *Very Long Baseline Interferometry (VLBI)* (see Fig. 2.3). In this case, the observations of each antenna are recorded and the exact observation time is measured by an atomic clock ("maser"). The outputs of every telescope pair are correlated offline for further data analysis. Therefore, the most important difference between connected interferometry and VLBI is to satisfy the following requirements: a precise clock at every station and the subsequent (offline) correlation of individual signals to get the "fringes", i.e., the interference pattern is synthesized afterwards (see below).

An interferometer is measuring the Fourier transform of the brightness distribution in the sky convolved with the reception pattern (or "the beam"), called the *Visibility* $V(u, v)$, a complex function in the spatial frequency domain (defined by the projected baseline coordinates u and v). It is an unnormalized complex quantity, which is measured in units of flux density. The phase of the complex visibility measures the fringe phase, containing information of resolved and asymmetric

sources. Depending on the array configuration (i.e., the baseline lengths and their orientations), the (u,v)-*coverage* describes the sampling in the Fourier space and hence, in turn after deconvolution and Fourier transformation, the quality of the reconstructed image. This sampling of Fourier components of the source brightness distribution is generally called *aperture synthesis*.

In two dimensions, the visibility function for a pair of telescopes (with baseline length b) is defined as

$$V(u,v) = \iint_{-\infty}^{\infty} A(x',y')I(x',y') \cdot e^{i2\pi(x'u+y'v)}\, dx'dy' \quad , \tag{2.2}$$

with the spatial frequencies $u = f \cdot b\cos\zeta/c$ and $v = f \cdot b\sin\zeta/c$ spanning the so called (u,v)-plane, with the observing frequency f, the zenith angle ζ, the function of the reception pattern $A(x,y)$, and the intensity distribution in the sky $I(x,y)$. The coordinates x and y span a 2D-space perpendicular to the line of sight in the plane of the source. During one integration period, such a single two-element interferometer measures the intensity distribution in the sky at one spatial frequency (i.e., one point in the (u,v)-plane). For multiple sampling, this spatial distribution can then be reconstructed via Fourier transform and deconvolution of the beam.

In general, radio interferometry takes advantage of the Earth's rotation to achieve multiple sampling and, thus, improvement of the (u,v)-coverage[3]. As the Earth rotates, the projected baseline lengths are changing. With this approach a better sampling of the visibility function in the spatial frequency domain, and hence more information about the surface brightness distribution of the source. This method is called *Earth rotation synthesis* (Ryle & Hewish, 1960; Ryle & Neville, 1962). By combining radio telescopes all over the world and observing the target for a certain amount of time, the (u,v)-plane can be suitably filled. Long distances, corresponding to small spatial frequencies, bring the highest resolution, while smaller baselines are sensitive to large scale structures. The better the (u,v)-sampling, the better the image reconstruction with fewer artefacts.

Ideally, an interferometer should continuously sample the entire spatial frequency domain in order to get a full, artefact- and errorless recovery of the real source intensity distribution. In practice, there will always be "holes" in the (u,v)-plane, adding unwanted components to the synthesized beam and thus causing spurious effects in the image. The amount of sampling by a specific array and observing configuration is given by the sampling function $W(u,v)$ expressing the limitations of reconstructing $I(x,y)$ as being a measure of the sensitivity to certain spatial frequencies comparable to the effective area of a single reflector. The response of an interferometer array is then given by

$$V_{\text{measured}}(u,v) = W(u,v)w(u,v)V(u,v) \quad , \tag{2.3}$$

with a given weighting factor $w(u,v)$ of the spatial frequencies. Applying such a weighting to the visibility data, e.g. natural[4] or uniform weighting, allows us to address more compact or extended structures by weighting particular spatial frequencies more or less. Uniform weighting achieves the highest resolution but a higher noise level, while natural weighting gives the best point source sensitivity but lower angular resolution. Similarly, "tapering" of the visibility data, i.e., weighting the visibility data by a Gaussian, one can further damp weight of high spatial frequencies increasing the detectability of extended source structures.

[3] Only in cases where the (u,v)-coverage is already sufficient, interferometric snapshot observations can achieve suitable images (e.g., in case of ALMA or the VLA).

[4] With "Natural weighting" or equal weighting well sampled regions of the (u,v)-plane get overall a higher weight than sparsely sampled ones, since a constant weight is given to all visibilities. "Uniform Weighting" is defined as weighting with the inversely proportional to the sampling density function within a given pixel size.

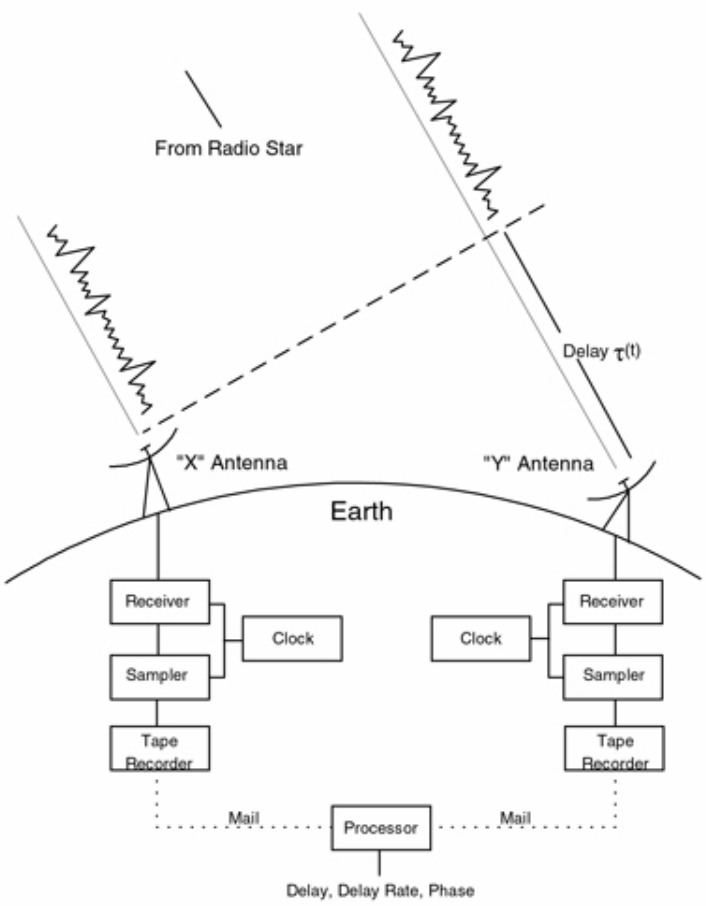

Figure 2.3: Basic illustration of VLBI measurements. Individual antennas are simultaneously observing a distant source. The signals are recorded (with an accurate time stamp) and correlated offline (Credit: A. Whitney).

Some examples of telescope arrays

In principle, every single radio telescope could be included in an interferometer array as long as an accurate clock is provided. There are a few telescope arrays, however, dedicated to radio interferometry. On the Northern Hemisphere, the JVLA (see Fig. 2.2) can be operated either as an independent interferometric array or, by phasing up all antennas, as a single telescope (Perley et al., 2011). As such it can be included in a global VLBI array (e.g., Parsley, 2004), for example in combination with the Very Long Baseline Array in North America VLBA[5] (VLBA, Napier, 1995) or the European VLBI Network[6] (EVN Paragi et al., 2005; Venturi, 2010) or the Global Millimeter VLBI Array[7] (GMVA, Krichbaum et al., 2008), where independent telescopes are participating for a few sessions per year to form this huge instrument. The only interferometer array built for VLBI is the Very Long Baseline Array[8] (VLBA, Napier, 1995) in North America.

On the Southern Hemisphere, the Long Baseline Array[9] (LBA, Norris, 1988) in Australia is a combination of individual telescopes originally not designed for VLBI observations (see Sect. 3.1). Recently, the Atacama Large Millimeter/sub-millimeter Array (ALMA, Wootten & Thompson, 2009) in Chile started operations to study the radio sky in unprecedented detail at millimeter wavelengths.

In space, the HALCA satellite of the VLBI Space Observatory Programme (VSOP, Hirabayashi

[5] www.vlba.nrao.edu
[6] http://www.evlbi.org/
[7] http://www3.mpifr-bonn.mpg.de/div/vlbi/globalmm
[8] www.vlba.nrao.edu
[9] http://www.atnf.csiro.au/vlbi

et al., 2000) had the first VLBI antenna on board. Since 2011, the radio space telescope RadioAstron[10] operates together with ground based antennas, extending the maximum baseline length to several Earth radii, which tremendously increases the angular resolution.

VLBI data calibration and reduction

At every station, the observational data are saved on disc and transported to the correlator[11]. After correlation, the data are loaded into *AIPS* (Astronomical Image Processing System; Greisen, 2003) for calibration and fringe fitting (see Diamond, 1995, for more details). The a-priori amplitude calibration accounts for instrumental or atmospheric effects at every station (documented in the observing log-files). The observational data of flux calibrators are used to determine the system temperatures, corresponding sensitivities and on-source noise (depending on the elevation) of each telescope, resulting in a set of transfer functions to reconstruct the true observed visibility amplitudes. The next step is the a-priori phase calibration and subsequent fringe fitting (Cotton, 1995). The output of the calibration and editing in *AIPS* is then stored in a *uv*-file in FITS format (Flexible Image Transport System, Wells et al., 1981), containing the calibrated data. These files can then be read into the interactively editing and hybrid mapping program `difmap` (Shepherd, 1997) for further data inspection and analysis of the visibility data[12], i.e., imaging (Fourier transform and deconvolution) via self-calibration[13].

Following Eq. 2.2, the process of image reconstruction consists of two steps: the Fourier transform of the visibilities and subsequent deconvolution of the synthesized beam and the intensity distribution of the source. Due to imperfect (u, v)-sampling of the true intensity distribution, the imaging procedure requires interpolating between measured visibilities. Within `difmap`, the `clean` algorithm (Högbom, 1974) is implemented to perform the deconvolution numerically.

With `clean`, a model for the source intensity distribution consisting of several point-source components is constructed to deconvolve the image. This procedure can be combined with self-calibration of the amplitudes and phases (preserving the closure phases) at incrementally shorter timescales to build up the optimum model to describe the measured visibilities. The final product is called "the clean image" of the source, which is the final model of the self-calibrated data convolved with the so called "clean beam", the synthesized beam approximated by a Gaussian to remove sidelobe effects.

The task `modelfit` in `DIFMAP` allows us to model the visibility data with 2D-functions, like Gaussian functions, to describe the source intensity distribution in a more simple way. These Gaussian model components are defined by their FWHM in two dimensions, i.e. their major and minor axis, the integrated flux density, the position, and, in case of an elliptical component, the orientation or position angle. The `modelfit`-algorithm is based on the Levenberg-Marquardt non-linear least squares minimization technique (Levenberg, 1944; Bevington & Robinson, 2003) by directly fitting the real and imaginary part of the visibility data points. In general, such a source model consisting of Gaussian components is constructed for the self-calibrated visibility data, the output of the imaging procedure. The result of model-fitting gives a simpler model with less components than the `clean`-model which can be used for studying the overall source structure and its time dependent behavior (see Sect. 6.3 and 7.5).

[10] `http://www.asc.rssi.ru/radioastron`

[11] For the EVN, also real-time transfer via optical fibre cables of the data to the correlator is possible, called "eVLBI", speeding up the data processing.

[12] Note that imaging of VLBI data can be performed in *AIPS* or in `difmap`.

[13] Due to phase self-calibration the absolute position information of the source is lost as long as no phase referencing observations is conducted.

Statistical error calculation

Within `difmap`, no uncertainties for the model fit parameters can be derived. Therefore, a new method of calculating the statistical errors was developed by C. Großberger and implemented on the computing cluster of the Dr. Remeis Observatory (for more details see Großberger, 2014). Using the *Interactive Spectral Interpretation System* (ISIS, Version 1.6.2-27, Houck & Denicola, 2000) with a direct link to `difmap`, the parameter values and their uncertainties in χ^2-statistics can be determined for each fit. With this method, an error calculation for each parameter can be performed (see Sect. 7.5 as an exemplary application).

Peculiarities of Southern Hemisphere VLBI observations

The Chapters 5 to 7 cover results of VLBI observations obtained with a VLBI array on the Southern Hemisphere. In contrast to the VLBA, which is a dedicated telescope array to VLBI observations, there is no such instrument to observe below $-30°$ declination. However, as mentioned above, interferometry works in principle with every array setup (telescope type, position, size) as long as the receiver (frequencies) are compatible. Some telescopes[14] (mainly) in Australia are jointly performing VLBI observations for some weeks per year, forming the Long Baseline Array (LBA), but additional antennas can in principle be added. More details on possible array setups are given in Sect. 3.1. Especially for Southern Hemisphere VLBI, there are some things to consider before analyzing the data (see also, e.g., Ojha et al., 2010):

- All telescopes were designed to operate as single-dish instruments. Therefore, they are all of different sizes, have different mounts, and elevation limits and receivers, and slew at distinctive speeds.
- The sensitivity of a VLBI array is dependent on the size of the individual telescopes, resulting in a higher baseline sensitivity for baselines involving a large antenna. It is recommendable to schedule an observation in a way that the source is visible to the largest antennas (Parkes and DSS45) during all scans.
- As the array was not designed as such, the telescope locations are partly in a north-south configuration not optimized for Earth rotation synthesis.
- The geography of the Southern Hemisphere prevents measurements at intermediate baseline lengths resulting in large gaps in the (u, v)-plane. Beam shapes can thus become quite elliptical, while the synthesized beam[15] can cause unwanted artefacts.
- Uniform weighting for an extended LBA array including smaller transoceanic antennas results in lower signal-to-noise ratios as the sensitivity at the long baselines are generally much lower.
- Calibration tables (e.g., flags or system temperature table) have to be created by the user.
- The LBA does not have operators. Therefore, each PI and his/her co-PIs is expected to observe from one of the telescopes for the entire length of a VLBI session which is typically about a week long.
- Performing LBA observations requires observers (members of the proposer's team) at each station. No staff as for the VLBA is available.

[14] The documentation on available telescopes is available at `http://www.atnf.csiro.au/vlbi/documentation`.

[15] The synthesized beam is also known as "dirty"beam, with respect to the "clean beam", which represents a Gaussian approximation to the synthesized beam to suppress the side-lobes.

2.2. Gamma-ray astronomy with the *Fermi* satellite

High energetic γ-ray photons emerge from extreme environments like the vicinity of a black hole. As opposed to charged particles (cosmic rays), γ-rays are not affected by magnetic fields and hence, the location of their production can be determined[16]. Therefore, investigations of their properties give valuable information on the ongoing physical processes, like particle acceleration in jets.

After the discovery of cosmic rays by Victor Hess in 1912, the existence of cosmic γ-rays, photons with energies in the MeV to TeV range, was predicted (see, e.g., Fazio, 1970, for a summary). Due to the shielding of the Earth's atmosphere[17], it is not possible to directly detect γ-rays on Earth. The first γ-ray telescope onboard a spacecraft, *Explorer 11* was launched in 1961, which yielded no detections. A few years later, however, an instrument on the OSO-3 satellite successfully detected photons with energies above ~ 50 MeV (Kraushaar et al., 1972).

Further exploratory missions with improved techniques brought detailed scientific insights and cleared the way for a new generation of γ-ray telescopes. The Energetic Gamma Ray Experiment Telescope (EGRET, Thompson et al., 1993) onboard the *Compton Gamma-Ray Observatory (CGRO)* enabled several major discoveries in the γ-ray regime (operating from 30 keV to 30 GeV) as highlighted by Gehrels & Shrader (2001). The all-sky map at these high energies shows that the γ-ray sky is quite diverse and highly variable and allowed the identification of blazars as high-energy emitters. The third EGRET catalog (Hartman et al., 1999) already showed that blazars constitute the largest subsample of γ-ray source, triggering the first multiwavelength campaigns to study the broadband emission of extragalactic jets (e.g., Jorstad et al., 2001b,a).

EGRET's findings raised further questions on the emission origin of γ-rays in AGN or the classification of most of the detected but unidentified sources. Therefore a succeeding instrument was required in order to further (and better) investigate the γ-ray sky: the *Fermi Gamma-ray Space Telescope* (Fig. 2.4), formerly GLAST (*Gamma Ray Large Area Space Telescope*, GLAST Facility Science Team et al., 1999), was launched in mid 2008. Its main instrument is the Large Area Telescope (LAT, see Sect. 2.2.1) with imaging properties superior to its predecessor. The secondary instrument is the Gamma-ray Burst Monitor (GBM, Meegan et al., 2009) with a much larger field of view than the LAT. With the GBM, gamma-ray bursts and fast transients can be studied from 10 keV up to 20 MeV (Abdo et al., 2009).

2.2.1. The *Fermi* Large Area Telescope

The *Fermi*/LAT is an imaging gamma-ray telescope observing in the energy range from ~ 20 MeV to ~ 300 GeV. It is a pair-conversion detector detecting the produced e^+e^--pairs of incident photons interacting with the detector material.

In the following a brief overview of the instrument is given, a more detailed technical description give Atwood et al. (2009) and the online science support center of the mission at `http://fermi.gsfc.nasa.gov/ssc/`.

[16] However, γ-rays can be absorbed by the extragalactic background light (EBL) and, thus, spectral measurements of distant sources are affected by this pair-conversion process ($\gamma + \gamma_{\mathrm{EBL}} \rightarrow e^+ + e^-$) leaving an imprint in the spectrum (e.g., H.E.S.S. Collaboration et al., 2013a; Ackermann et al., 2012b; Georganopoulos et al., 2010).

[17] Note that on Earth there is another, indirect method to detect γ-rays (in the TeV range): Cherenkov telescopes detect the "Cherenkov light" emitted by the cascade of secondary particles which originates from the interaction of highly energetic photons with the atmosphere.

Figure 2.4.: Schematic diagram of the *Fermi Gamma-ray Space Telescope* (left) and detailed close-up view of the Large Area Telescope (LAT, right, see Sect. 2.2.1) showing one of 16 towers covered by the anti-coincidence shield to reject the charged cosmic particle background. Each tower consists of a converter, a calorimeter and a data acquisition module (Credit: NASA).

Pair-conversion telescopes

The primary interaction in the energy range of *Fermi* is pair conversion. The LAT was constructed in a way, based on this process, that γ-rays can be easily distinguished from charged cosmic rays, producing a unique track in the detector. The *Fermi*/LAT is a pair-conversion telescope with a precision converter tracker and a calorimeter to measure the direction and the energy deposit of the γ-rays.

The basic setup of the *Fermi*/LAT is the following: The incident photons need to first pass through an anticoincidence detector (ACD), rejecting the charged cosmic particle background. Pair conversion requires heavy nuclei, such that the photons need to pass the conversion foils, a thin layer of high-Z material. The trajectories of the produced e^+e^--pairs are then detected by the converter tracker and their energies are measured in the calorimeter (Atwood et al., 2009). The LAT consists of 16 towers in a 4×4 array, each a converter, calorimeter and data acquisition module, covered by the anticoincidence shield (see Fig. 2.4).

Different event classes are provided for the data analysis of certain type(s) of the source(s) of interest. The events detected by the LAT are classified based on the probability that they result from photons and on the reconstruction probability, resulting in cuts based on various requirements given by the expected source properties and background events. There are currently three event classes (each with an own set of response functions), which are hierarchically nested, i.e., higher probability events are a subset of the less restricted event class. The “ultraclean class” has the highest requirements (lowest background rate), followed by the “clean class”, the “source class”, and finally the “transient class” with least restrictions. Depending on the science to be performed the suitable event class needs to be selected. For the analysis of AGN the “source class” is the best choice as the background rate is lower as for the “transient class” and it is optimized for point source studies.

Instrument operations and performance

With its very wide field of view (about 20% of the sky) and its large effective area of $> 8000\,\mathrm{cm}^2$ (energy dependent, see Fig. 14 and 15 in Atwood et al., 2009), the *Fermi*/LAT mainly operates in an all-sky scanning mode, monitoring each point in the sky every two orbits in approximately 3 hours, alternating between the Southern and Northern Hemisphere in each orbit. This approach results

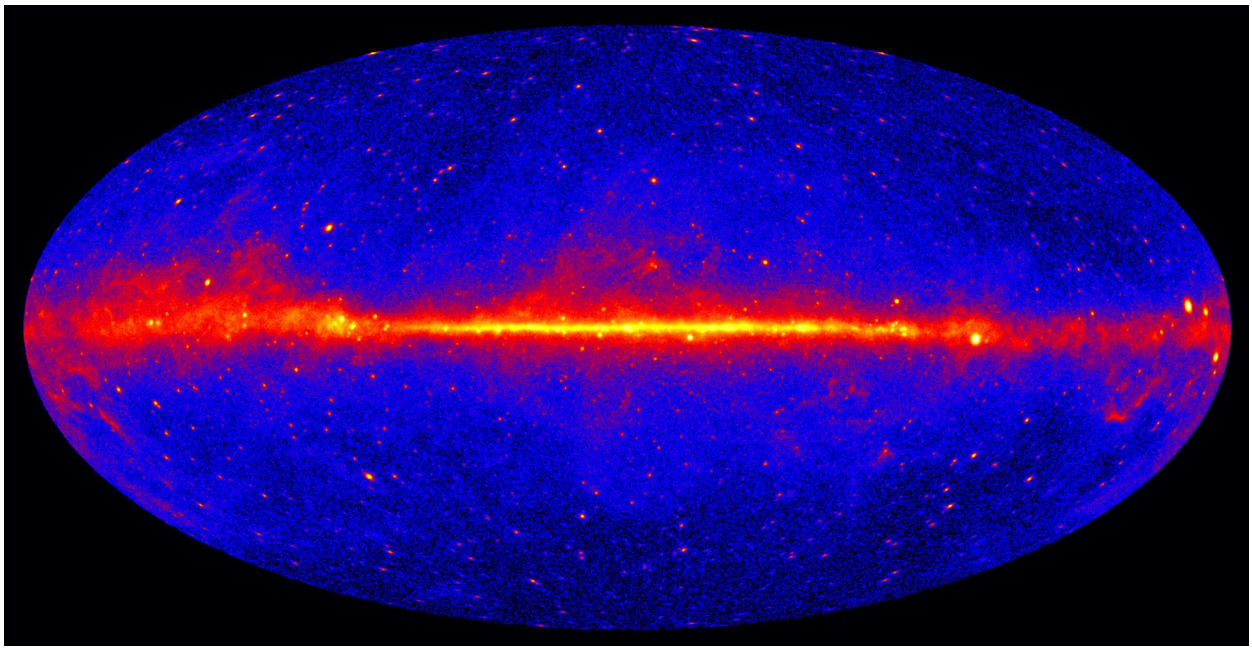

Figure 2.5.: All-sky survey (in Galactic coordinates) by *Fermi*/LAT after 5 years of operation. Shown are the all-sky data above 1 GeV, where lighter colors indicate enhanced γ-ray emission. The Galactic plane emission, composed of a diffuse component and point sources, is clearly dominating the γ-ray sky. Off the Galactic plane, most point sources can be identified with blazars or other types of AGN (see also Ch. 5). (Credit: NASA, Fermi/LAT Collaboration)

in a nearly uniform coverage of the entire sky and a continuous monitoring of single sources. The all-sky map in γ-rays after 5 years of operation is shown in Fig. 2.5. The angular resolution of the LAT is a function of energy and incident angle dependent (see also Fig. 17 and 18 in Atwood et al., 2009). The 68% containment radius for the reconstructed event of a single on-axis photon is $3.^{\circ}5$ at 100 MeV down to $< 0.^{\circ}15$ at > 10 GeV. The energy resolution is less than 10% (1σ, on-axis). The point-source sensitivity is depending on the total exposure. For a source at high galactic latitude, a 1-year exposure results in a point source sensitivity of $< 10^{-8}\mathrm{cm}^{-2}\mathrm{s}^{-1}$ (see Fig. 2 in Atwood et al., 2009).

Scientific highlights

After more than five years of operations *Fermi* has given an unprecedented view of the γ-ray sky, discovering hundreds of new γ-ray sources and resolving point sources. It would go beyond the scope of this thesis to discuss all[18] of the discoveries obtained by *Fermi*. In the following some results which are relevant for this work are briefly outlined.

Thanks to the large FoV and sensitivity, the all-sky monitoring with *Fermi*/LAT gives continuous information on the γ-ray sky. The observations revealed newly flaring sources and enabled the study of the dynamical time scales of already detected ones. *Fermi* observes a large amount of sources: point sources like galactic and supermassive black holes, neutron stars, gamma-ray bursts, starburst galaxies, the Sun and the Moon, and it made important observations of the diffuse galactic and extragalactic γ-ray emission.

[18] All publications by the *Fermi* Collaboration and related talks and reviews can be found at `http://www-glast.stanford.edu/cgi-bin/pubpub`

Results of the *Fermi*/LAT all-sky monitoring after one and two years are published in *Fermi* first and second source catalogs (1FGL and 2FGL, Abdo et al., 2010; Nolan et al., 2012). As by far the largest source class of γ-ray emitters are active galactic nuclei, corresponding catalogs 1LAC and 2LAC explicitly treat the properties of these sources (Abdo et al., 2010b; Ackermann et al., 2011). The First *Fermi*/LAT Catalog of Sources above 10 GeV (1FHL, Ackermann et al., 2013) covers three years of data and shows that about 76% of these hard-spectrum sources are AGN. This catalog paper also includes a candidate source list for which a detection at (higher) energies ($\geq 50 - 100$ GeV) with ground-based γ-ray observatories is expected[19].

The continuous observations of the variable γ-ray sky are controlled and quickly analyzed by the *Fermi Flare Advocates* (also known as Gamma-ray Sky Watcher, FA-GSW, Ciprini et al., 2013). This service provides daily information to the *Fermi* team members, as well as weekly information of variable sources (available online as the "Fermi Sky Blog"[20]). For special flaring events, flare advocates send alerts to inform external scientists and to coordinate multiwavelength campaigns. The monitoring data of a selection of bright and transient sources is automatically analyzed, to provide quick-look light curves for the public, known as *LAT Monitored Source List* (`http://fermi.gsfc.nasa.gov/ssc/data/access/lat/msl_lc/`).

2.2.2. Analysis of LAT-data

Fermi data and the analysis software, the *Fermi Science Tools* (FSTs), are publicly available at `http://fermi.gsfc.nasa.gov/ssc/data`. The software package facilitate the analysis of *Fermi* data, as for all analysis tasks specific functions are provided and also embedded in a *python* environment. The FSTs are continuously updated – information can be found in the online documentation. This web-portal also gives an extensive introduction to the analysis of *Fermi*/LAT data. Moreover, other publications on *Fermi* data provide detailed descriptions on the analysis pipeline, e.g. Böck (2012), Abdo et al. (2009), and Abdo et al. (2010b). In this section only a summary on the typical procedure will be given, focussing on the analysis of AGN. Although the event files give detailed information on the detected photons, it is not possible to directly obtain the desired source characteristics, for example position or flux. A more complex data reduction procedure is required considering instrumental effects, like the larger PSF at lower energies or the orientation of the (in motion) telescope.

The *Fermi*/LAT analysis is based on the maximum-likelihood method to get the best estimation of the source properties (location, spectrum, intensity) from the observed events. Given a particular input model, the likelihood $\mathscr{L}$ is the probability to obtain the measured data. In case of *Fermi*/LAT data the model consists of the source properties and the background information, i.e., the diffuse emission and the neighboring sources. Following Cash (1979) and assuming Poisson statistics, the likelihood is then

$$\mathscr{L} = \prod_{i=1}^{N} \frac{m_i^{n_i} \cdot e^{-m_i}}{n_i!} = e^{-N_{\mathrm{exp}}} \prod_{i=1}^{N} \frac{m_i^{n_i}}{n_i!} \quad , \tag{2.4}$$

where N = total number of counts, n_i are the detected counts in bin i, m_i is the number of expected counts in bin i predicted by the model (strongly depending on the input model), and N_{exp} total number of expected counts. The set of parameters of a particular model which maximizes Eq. 2.4 represents then the maximum likelihood estimate. To determine the significance of a detection, the

[19] One of the most promising candidates is the source PMN J1603−4904 with the highest flux above 50 GeV of all candidate sources. Its multiwavelength properties are discussed in detail in Ch. 6.

[20] `http://fermisky.blogspot.de/`

Fermi/LAT team commonly uses the test statistics

$$\mathrm{TS} = -2\ln\left(\frac{\mathscr{L}_{\mathrm{max},0}}{\mathscr{L}_{\mathrm{max}}}\right) \quad , \tag{2.5}$$

where $\mathscr{L}_{\mathrm{max},0}$ is the maximum likelihood for the data given the model without a source present in the model ("null hypothesis") and $\mathscr{L}_{\mathrm{max}}$ is the maximum likelihood with a source included in the model. TS gives a measure of the source significance, i.e. how (un)likely the detection occured by chance. According to Wilk's theorem (Wilks, 1938) TS is comparable to the χ^2 statistics (Mattox et al., 1996). Therefore, one can apply the simple estimation of $TS \approx \sqrt{\sigma}$ (in first-order approximation). As an example, a 5σ-detection ($\sim 99\%$) requires then a TS-value of TS$\gtrsim 25$ (see also, e.g., Abdo et al., 2010).

For *Fermi*/LAT data, the detection (localization), flux determination and spectral modeling of sources is accomplished by such a maximum likelihood optimization technique. Since computation time and memory scales with the number of photons and the type of sources, for some calculations, the binned analysis is more appropriate. Binning is performed in two dimensions, in energy and in position (pixel). For sources with lower photon rates, an unbinned analysis can be adopted, where each event is treated individually. To perform the likelihood analysis, the data need to be prepared and the input model, which depends on the type of the analysis and the desired output, need to be constructed.

The data access is possible via a ftp-server at `fermi.gsfc.nasa.gov/ssc/data/access`. Required are an event data file (containing the detection time, the reconstructed incident angle, the event class and estimated photon energy for each event), a corresponding spacecraft file (including the pointing and lifetime information of *Fermi*), the latest background models and instrument response functions (IRFs, depending on the event class) compatible with the latest version of the FSTs.

Fermi/LAT data are available from the start of observations (2008-08-04 00:00:00.000 UTC) to the latest observation run. Generally, the all-sky data are cut depending on the time range which should be analyzed and the good-time-intervals (GTI[21]), the event class, the energy range (between 100 MeV and 300 GeV), the region of interest (RoI) to be analyzed, and the zenith angle[22]. The latter two parameters are constrained in the following: Since the *Fermi*/LAT effective area becomes worse below 100 MeV, the *Fermi* team recommends to select energies above this value. The angular resolution is higher at $\gtrsim$ 1 GeV, the flux is better defined and the response is more stable (Abdo et al., 2010; Nolan et al., 2012), so that for spectral analysis the higher energy bands are better suited since the uncertainty in flux is lower. The PSF is a function of energy, hence, the definition of the RoI should consider the energy range to be analyzed. The RoI, centered at the position of the source, should have a radius large enough to pick up events several degrees away from the center, due to the large PSF. Therefore, the sky region to be analyzed might include further close-by sources represented by an additional ring of a few degrees around the RoI. To disentangle the contribution of each source in and close to the RoI, detailed *Fermi*/LAT analysis of one position in the sky always involves to model the whole sky simultaneously. In practice, to save computing time, typical RoIs have sizes of 10° to 20° and, as a compromise, only this fraction is modeled instead of the whole sky.

[21] The GTIs defined at which time the *Fermi*/LAT observation quality was "good" and the data are considered to be valid. For example, when passing the South Atlantic Anomaly (SAA) or during , no measurements are performed. The GTI information is saved in the spacecraft files.

[22] The *Fermi*/LAT team recommends a zenith angle cut of $\leq 100°$ to avoid contamination of the Earth's limb, which is a bright γ-ray source.

The source model flux density distribution $S(E, \hat{x}, t)$ includes the fluxes of all known γ-ray point sources[23] s_i and of the extended sources S_k, and the model of the galactic and extragalactic diffuse background emission $S_{\rm G}$ and $S_{\rm EG}$ (both assumed to be constant over the observed time range)

$$S(E, \hat{x}, t) = \sum_i s_i(E, t)\delta(x - \hat{x}) + S_{\rm G}(E, \hat{x}) + S_{\rm EG}(E, \hat{x}) + \sum_k S_k(E, \hat{x}, t) \tag{2.6}$$

for a particular fraction in the sky defined by the radius of the RoI. All model parameters, such as position, spectral model and corresponding parameter values, are saved in an XML-file, the input model. It is folded with the IRFs to obtain the predicted events which are then compared to the measured data as part of the likelihood analysis.

Depending on the type of analysis, this initial model can be modified to obtain the best representation of the source region to start with. The 2FGL catalog currently contains the best all-sky information and can be used as a reasonable input model for further analysis. Two types of *Fermi*/LAT analyses are summarized below, which are relevant for further discussion of results in Sect. 3.3 and 3.4.

In addition to the cuts on the data and the construction of the input model (before doing the likelihood fitting), the full *Fermi*/LAT analysis requires the calculation of an exposure map, specific for the region of interest. It is worth noting that the type of exposure map used for the likelihood analysis differs from the usual term, normally being integrals of the effective area over time. Here, the exposure is given by integrating over the total response of the RoI data-space in order to compute the predicted number of events within a given RoI

$$\varepsilon(E, \hat{x}) = \int_{\rm RoI} R(E', \hat{x}'; E, \hat{x}, t) d\hat{x}' dE' dt \quad , \tag{2.7}$$

where the primed parameters indicate the measured energies E' and directions $\hat{x}'$, respectively. Hence, for a given position on the sky, the exposure map gives the total exposure, i.e., area multiplied by time, producing counts in the RoI. For the likelihood analysis later, this exposure can then be used to calculate the expected number of events in the RoI.

The generation of such an exposure map requires the beforehand calculation of a so called *livetime cube*, which gives the amount of time that *Fermi*/LAT has observed a given position at any given inclination angle for the time range covered by the spacecraft file. Livetime cubes are additive and need only be created once per time range, as they cover the whole sky information, independent on source models. More detailed information on the *Fermi*/LAT analysis can be obtained from the *Fermi* Science Support Center.

Gamma-ray light curves of blazars

The standard way to obtain the time variability of a source, i.e., to derive its light curve, is to cut a certain time range into intervals n over which the flux density is assumed to be constant. A likelihood analysis is performed for every time bin resulting in n flux density points or upper limits, if the source flux is not significant over the length of the time interval.

For the variability analysis of blazars, the input model (Eq. 2.6) is typically constructed as follows. Since the spectral shape and the flux are strongly correlated and the uncertainties in flux can become very large when fitting both parameters (Abdo et al., 2010), the light curve analysis is based on the assumption that the spectral shape is constant (within this uncertainty) and therefore

[23] Typically, the spectral and spatial source models can be obtained from the results of one of the *Fermi* catalogs (Abdo et al., 2010; Nolan et al., 2012).

fixed. It is fixed for all sources in the RoI (including the one of interest) to the input value obtained from a long-term study, for example from the 2FGL-catalog (Nolan et al., 2012). Note that with such constraints one rather detects variability than characterizes the change of the spectral shape with time. However, blazar variability does not show a large change in spectral index, only by $< 0.2 - 0.3$, despite large variability in flux (Abdo et al., 2010a; Abdo et al., 2009). Moreover, such a spectral change can only significantly be detected in the brightest blazars. Abdo et al. (2010a) showed a much stronger and violent variability of the flux for the sources in the *LAT Bright AGN sample* (LBAS or 3-months list) than of their photon indices.

To further constrain the model parameters, only for the close neighbors (within default RoI of 7°) the amplitudes or prefactors are let free to vary. The starting conditions from the catalog are used. The sources outside the RoI and the diffuse components are assumed to be constant. The reason for this approach is that close sources can influence the determined flux of the source of interest due to the large PSF. The simultaneous modeling of their variability reduces such effects.

At the Dr. Remeis Observatory & ECAP data reduction and analysis scripts in *ISIS* (Houck & Denicola, 2000) and *python* were developed as part of this work[24]. The main objective for this development was the automatization of the light curve analysis on the "Remeis cluster", especially the processing of long time studies of large source samples (see Sect. 4.2). The scripts are based on the FSTs as well as on work by W. McConville (NASA/GSFC) and A. Schooley[25]. Furthermore the user contribution software by T. Johnson (Naval Research Lab) to create automatically source model XML files based on certain input criteria was implemented (`http://fermi.gsfc.nasa.gov/ssc/data/analysis/user`). The large advantage of this automatization is the flexibility in terms of input parameter, like energy range, time range, bin sizes etc., which allows the user to create light curves for every source from the all-sky *Fermi* data. An enormous decrease in computing time (note that every single time bin requires a full likelihood analysis) was the parallelization with the scheduling system *torque*[26], such that every fit can be performed on one of the cluster nodes.

Fitting γ-ray spectra of blazars

The *Fermi*/LAT energy range spans three orders of magnitude, so an accurate modeling of the source spectral energy distribution is possible. Most blazar spectra can be described by a simple power law $N(E) = N_0(E/E_0)^{-\Gamma}$, with N_0 being the prefactor, E_0 the reference energy, and Γ the spectral index. However, over the whole energy range, it was found for bright blazars[27] that the spectral shape does not follow this simple model, but rather exhibits a curvature (Abdo et al., 2010; Nolan et al., 2012). A broken power law model $N(E) = N_0(E/E_b)^{\Gamma_{1,2}}$ (γ_1 for $E < E_b$, γ_2 for $E > E_b$) with a break energy E_b, or a log-parabola $N(E) = N_0(E/E_b)^{(\alpha+\beta\ln(E/E_b))}$, with the spectral index α and the curvature β, which is more stable for moderately bright sources with a smaller number of free parameters than the broken power law model, often gives a better description. In order to determine whether a simple power law or a curved spectrum better fits the data, a likelihood analysis of the form $TS_{\text{curve}} = 2(\log \mathscr{L}_{\text{LogParabola}} - \log \mathscr{L}_{\text{Powerlaw}})$ is performed (Nolan et al., 2012).

With the all-sky information and the extensive spectral modeling performed for the 2FGL and 2LAC catalogs (Nolan et al., 2012; Ackermann et al., 2011), the spectral energy distribution for

[24] Here the P7V6 version of the LAT science data were used.

[25] A. Schooley performed a student summer project at the Remeis Observatory of three months duration in 2012 (Supervisor: C. Müller).

[26] `http://www.adaptivecomputing.com/products/open-source/torque/`

[27] Due to the larger flux uncertainties in the lower energy bands ($\lesssim 300$ MeV) and the correlation of spectral index and flux, a simple power law model could result in higher flux densities in this energy range.

each source in these catalogs can easily be obtained. Similar as for the light curve analysis, the input model is constructed based on the catalog information of the sources in the RoI and the near surroundings. For this type of analysis, though, the spectral index parameter for the source of interest is also left free. A typical spectral analysis includes first a likelihood fit for the whole energy range (for the data of the given time range) to get a suitable starting value to perform the fitting for energy sub-bands. This step-by-step fitting procedure also supports the convergence of the single energy band fits. The amount of bins should not be less then ~ 10 per energy decade, even for bright sources to ensure that the changes in effective area at lower energies are taken into account.

Similar to the automatization of the light curve analysis, scripts for the use on the "Remeis cluster" have been developed as part of this work in order to perform a larger amount of spectral fits for a large sample with the all-sky data and the 2FGL catalog information as inputs. The script to calculate a spectral energy distribution is based on the extension software to the FSTs provided by T. Johnson at `http://fermi.gsfc.nasa.gov/ssc/data/analysis/user`. The developed wrapper allows a flexible spectral modeling of sources, optimized for blazar analysis, via the specification of input parameters (like time and energy range, number of energy bins, etc.), and can thus be applied to analyze a large source sample (see Sect. 3.4).

Astronomy compels the soul to look upwards and leads us from this world to another.

(Plato)

3. The multiwavelength monitoring program TANAMI

Tracking Active Galactic Nuclei with Austral Milliarcsecond Interferometry is a VLBI monitoring program to study the parsec-scale structures and dynamics of extragalactic jets on the Southern Hemisphere[1]. The VLBI monitoring is supplemented by further multiwavelength observations from the radio to the γ-rays in order to investigate the broadband emission mechanism and the correlation of high energy emission with mas-scale changes in morphology of blazars.

The following introduction to the definition and characteristics of the program is based on the papers by Ojha et al. (2010) and Müller et al. (2009, 2010, 2011). Further information can be found in Böck (2012) and in Böck et al. (2014) with more details on the γ-ray properties of the TANAMI sources. In Section 3.1 the setup of the monitoring program and the sample definition is introduced. Section 3.2 addresses the gamma-ray properties of the sample and is complemented by the results of the first VLBI observations of a subset of newly added (γ-ray loud) sources in Chapter 5. The multiwavelength approach of the TANAMI program is discussed in Sect. 3.3, and the connection to multi-messenger astronomy in Sect. 3.4.

3.1. Concept and scientific goals

The centerpiece of TANAMI are the contemporaneous dual-frequency (8.4 GHz and 22.3 GHz) VLBI observations of extragalactic jets in the southern sky, which are regularly performed about twice a year since 2007[2], providing structural and spectral information at mas-scales of all sources. In addition, several associated multiwavelength observations allow us to study the broadband spectral behavior with time. Table 3.1 summarizes the multiwavelength observations related to TANAMI (see Sect. 3.3 for more details).

The sample was defined as a combination of a radio and γ-ray subsample (see below) in order to address the so called "radio-gamma-connection" seen in AGN jets, i.e. the connection of high energy emission and changes in the (sub-)parsec scales jet properties. With the detection of γ-ray emission of AGN jets in the EGRET era (Hartman et al., 1992) various models were considered in order to explain the broadband emission (see Sect. 1.3.5). TANAMI aims to investigate the emission and formation mechanism of AGN jets. The long term VLBI monitoring provides information on jet properties, like apparent speed, overall structure and changes with time (e.g., jet bends, knot

[1] `http://pulsar.sternwarte.uni-erlangen.de/tanami`

[2] The exact number of observations per source depend on the appropriate observing cadence. Details on the observing strategy can be found in Ojha et al. (2010).

Table 3.1.: TANAMI Associated Multiwavelength Observations

Waveband	Instrument	related Publications
5.5, 9, 17, 19, 38 & 40 GHz	ATCA (Project: C1730)	Stevens et al. (2012)
6.7 GHz	Ceduna	
6.7 GHz	Ceduna-Hobart-Interferometer (CHI)	Blanchard et al. (2012)
optical	Gemini South (GMOS)	
optical	*Rapid Eye Mount* (REM, INAF)	Nesci et al. (2013)
optical	*Swift*/UVOT	
0.5–10 keV	*Swift*/XRT	Krauß (2013)
0.5–10 keV	*XMM-Newton*	
0.5–12 keV	*Suzaku*/XIS	
3 keV–10 MeV	*INTEGRAL*	
100 MeV–300 GeV	*Fermi*/LAT	Böck et al. (2014)

ejection events), opening angles, inclination, and (specifically for TANAMI) the dual-frequency monitoring gives spatial spectral index distributions of individual jet features. The simultaneous broadband observations allow us to study the jet activity and spectral changes in order to check for intra-band correlations or of jet ejection events with high energy flares.

Such investigations are required to address the following key questions concerning jet physics:

- Are the parsec-scale structural changes (always) related to high-energy flaring and if yes, how and why?
- Where are the production sites of high energetic photons (X-rays and γ-rays) and how are they produced?
- Which photon fields are responsible for the inverse Compton hump seen in blazar SEDs?
- Are the γ-rays beamed with the same Lorentz factor as indicated by the apparent speed?
- What is the structure, the ingredients/content of the jet in blazars and radio galaxies?

Figure 3.1 summarizes the TANAMI setup and science goals emphasizing the "TANAMI-*Fermi*-connection" to face this ambitious list of open questions.

The TANAMI array

The TANAMI VLBI observations are made with the Australian Long Baseline Array (LBA), including the telescopes at NASA's Deep Space Network (DSN) located at Tidbinbilla, and the 26 m South-African Hartebeeshoeck antenna. Since 2009, the 9 m German Antarctic Receiving Station (GARS) in O'Higgins, Antarctica, and the 6 m Transportable Integrated Geodetic Observatory (TIGO) in Chile participate in the program. Since 2011, the Warkworth, Katherine and Yarragadee antennas are contributing to the TANAMI observations, further improving the (u, v)-coverage with additional intermediate-length baselines. The array properties displayed in Fig. 3.2 and summarized in Table 3.2. Figure 3.3 shows a typical TANAMI (u, v)-coverage for both observing frequencies.

This results in a typical angular resolution of about a few mas, down to less than 1 mas. The largest baselines are achieved with the transoceanic antennas Hartebeeshoeck, TIGO and O'Higgins antennas. Although intermediate-length baselines are rare, limiting the image quality, past imaging programs found that this constraint does not preclude good images as long as special care is taken in calibration and the imaging process (e.g., Ojha et al., 2005, and see Sect. 7.3.2).

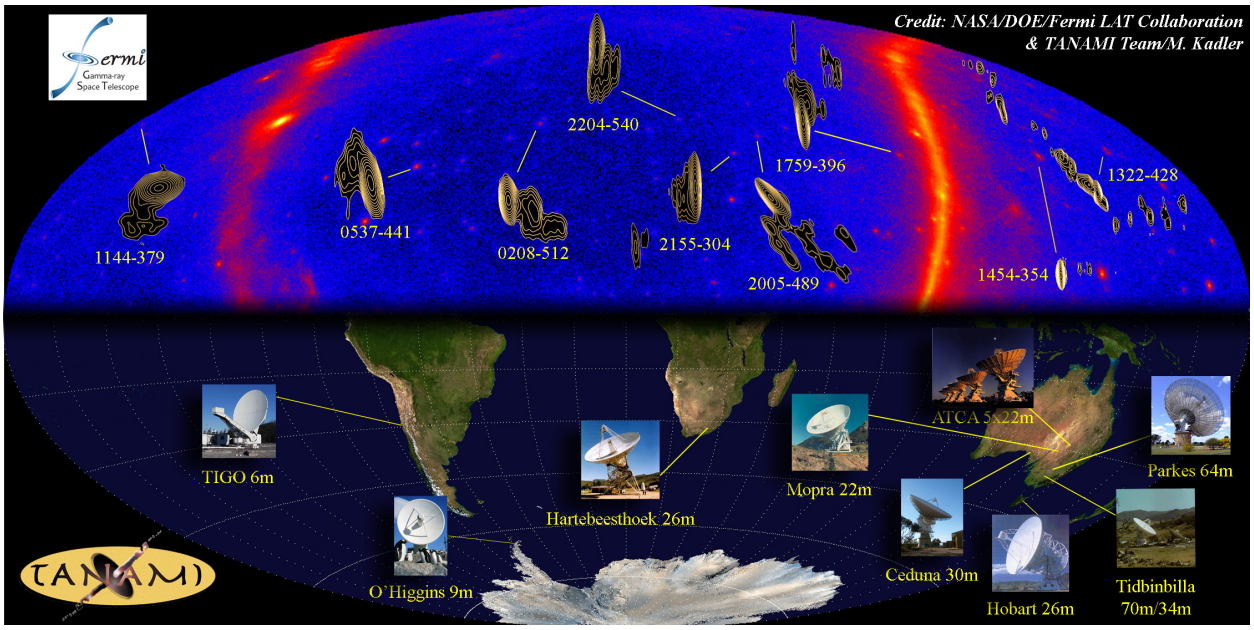

Figure 3.1.: Collage to illustrate the basic concept of the TANAMI program emphasizing the "TANAMI-*Fermi*-connection". With the Southern Hemisphere VLBI array (lower half of the plot) extragalactic jets are monitored on mas-scales. Blazars emit over the whole energy range up to γ-rays, where they can be continuously monitored with *Fermi*/LAT (and simultaneously to the TANAMI observations). The upper half of the collage displays the southern sky in γ-rays seen by *Fermi*/LAT (in celestial coordinates). The Milky Way and some distinct bright point sources, which can be associated with TANAMI sources, are clearly detected (Credit: NASA/FERMI & TANAMI/M.Kadler).

Data processing

The data are recorded on the LBADRs (Long Baseline Array Disk Recorders) and correlated on the DiFX software correlator at Curtin University in Perth, Western Australia (Deller et al., 2007). The inspection, initial editing and fringe fitting of the correlated data are performed using *AIPS* (National Radio Astronomy Observatory's Astronomical Image Processing System software, Fomalont, 1981). The amplitude calibration is done by using known flux values of prior observed sources. The imaging is performed applying standard methods in the program `difmap` (Shepherd, 1997), using the `clean` algorithm and making use of amplitude and phase self-calibration.

TANAMI sample definition

The TANAMI sample was defined as a hybrid sample of sources south of $-30°$ declination consisting of a radio selected flux-density limited subsample and a γ-ray selected subsample of known and candidate γ-ray sources based on results of CGRO/EGRET (Ojha et al., 2010).

All sources south of $\delta = -30°$ with a limiting radio flux density of $S_{5\ \mathrm{GHz}} > 2\,\mathrm{Jy}$ from the catalog of Stickel et al. (1994) and a flat radio spectrum ($\alpha > -0.5$, $S \sim \nu^{+\alpha}$) between 2.7 GHz and 5 GHz were included in the radio subsample, representing a Southern Hemisphere extension of the MOJAVE 1 sample (Lister et al., 2009a). The γ-ray selected subsample includes all known γ-ray blazars detected by EGRET south of $\delta = -30°$. The initial TANAMI sample consists of 43 extragalactic jets. The corresponding first epoch images are presented and discussed in Ojha et al. (2010).

With the launch of the *Fermi* Gamma-ray space telescope (see Sect. 2.2), newly detected γ-ray sources, associated with known radio-loud AGN have been added to the TANAMI sample (see

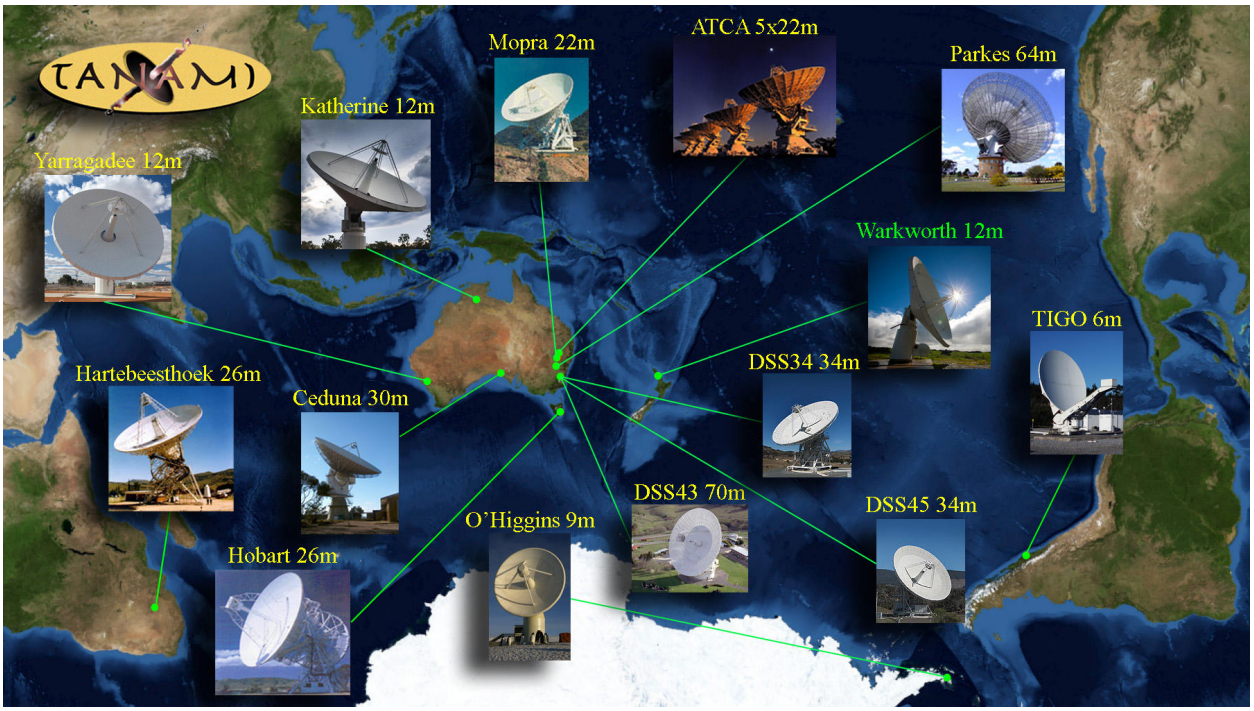

Figure 3.2.: The TANAMI array consists of antennas in the Southern Hemisphere (see Table 3.2 for details) combining the Long Baseline Array in Australia/South Africa with additional telescopes in Antarctica, Chile and New Zealand (Credit: TANAMI/J. Wilms/M. Kadler).

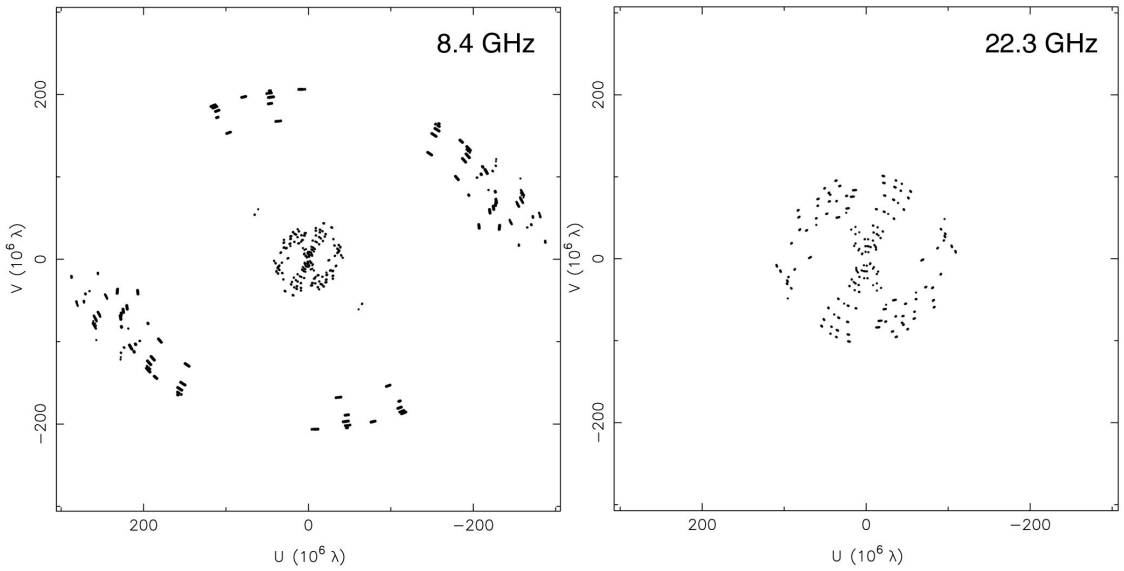

Figure 3.3.: Typical TANAMI (u, v)-coverage at 8.4 GHz and 22.3 GHz for a source at declination $\delta \sim -43°$. Note that most of the transoceanic telescopes are not equipped with 22.3 GHz receivers. Figure from Müller (2010).

Ch. 5 for more details). For most of these sources no high resolution VLBI observations have been obtained so far, i.e., TANAMI provides the first mas-scales information. In Table 5.1 all current sources of the TANAMI sample are listed, giving the affiliation to the initial sample.

Table 3.2.: The TANAMI array

Telescope Name	Diameter (meters)	Location
Parkes	64	Parkes, New South Wales, Australia
ATCA	5×22	Narrabri, New South Wales, Australia
Mopra	22	Coonabarabran, New South Wales, Australia
Hobart	26	Mt. Pleasant, Tasmania, Australia
Ceduna	30	Ceduna, South Australia
DSS43[a]	70	Tidbinbilla, Australia
DSS45[a]	34	Tidbinbilla, Australia
Hartebeesthoek[c]	26	Hartebeesthoek, South Africa
O'Higgins[b]	9	O'Higgins, Antarctica
TIGO[b]	6	Concepcion, Chile
Warkworth	12	Aukland, New Zealand
Katherine	12	Northern Territory, Australia
Yarragadee	12	Western Australia

Notes. [a]Operated by the Deep Space Network of the National Aeronautics and Space Administration
[b]Operated by Bundesamt für Kartographie und Geodäsie (BKG)
[c]Due to a major failure not available between Sept. 2008 and Sept. 2010. See Brand (2013) for a description of the data analysis pipeline for single-dish observations with Hartebeesthoek.

3.2. Gamma-ray properties of TANAMI sources

After one year of *Fermi*/LAT observations a fraction of 76% of the 75 TANAMI sources was associated with γ-ray emitters. Böck (2012) and Böck et al. (2014) discuss the γ-ray properties of 75 TANAMI sources based on 1-year *Fermi*/LAT data, including an upper limit calculation for the γ-ray quiet fraction. In this section, the results of the *Fermi* analysis and the conclusion are summarized, for more details on the γ-ray properties of the TANAMI sample see Böck et al. (2014) and Böck (2012).

Over 70% of the TANAMI sources had already been detected by the *Fermi*/LAT (Abdo et al., 2010; Abdo et al., 2010b). The detection rates for BL Lacs, quasars and radio galaxies are consistent with what was found in other samples (e.g., Lister et al., 2011). For those TANAMI sources not in the 1FGL catalog (Abdo et al., 2010), an upper limit analysis was performed. Three new γ-ray sources (PKS 2149−306, PKS 2326−477 and PKS 1505−495) were significantly detected by this analysis which was later confirmed with 2FGL (Nolan et al., 2012). The γ-ray luminosities of the undetected quasars are likely to be close to the determined upper limits, unless they are intrinsically fainter in γ-rays. Furthermore, the undetected sources have lower γ-ray to radio luminosity ratios and lower brightness temperatures which fits to the picture of Doppler boosting playing a dominant role in determining the γ-ray state of an AGN.

The γ-ray source characteristics raise issues which need to be investigated with the corresponding statistics and correlation study of the radio properties. This study is relevant to check for differences in the radio (e.g., morphology) which might explain the γ-ray loudness. A relation between γ-ray and radio flux was apparent (see Fig. 3.4). The brightness temperatures[3] of the radio cores (all quasars, one γ-ray faint quasar) were found to scale with the γ-ray luminosity

[3]The radio analysis on which these values are based on was performed as part of this work and are in detail discussed in Chapter 5.

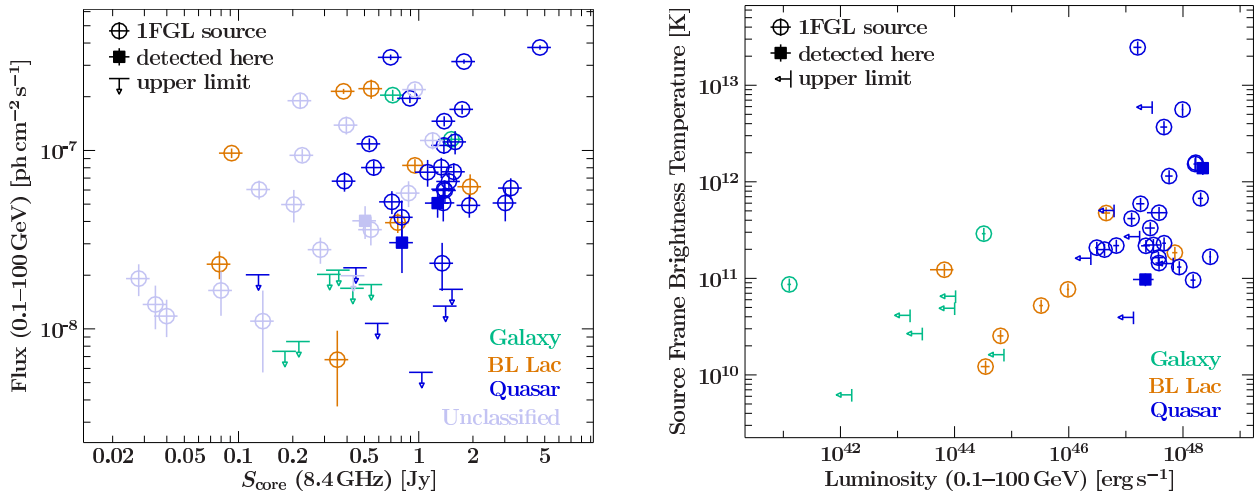

Figure 3.4.: *Left:* Relation between γ-ray and radio core flux density at 8.4 GHz. *Right:* Relation between γ-ray luminosity and brightness temperature of the radio core. Figures from Böck et al. (2014) and adapted from Böck (2012), respectively.

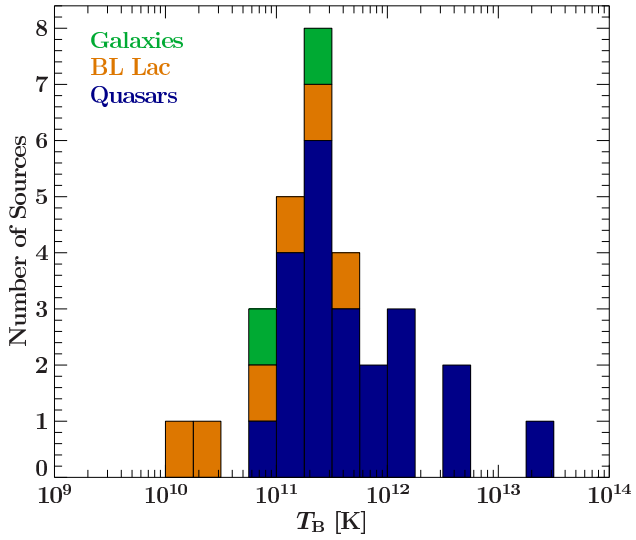

Figure 3.5: Brightness temperature distribution of TANAMI sample. Note that only the $T_{\rm B}$-values for sources with known redshift are shown. Figure from Böck et al. (2014).

($L_\gamma \sim L_{\rm radio}^{0.86\pm0.04}$, see Fig. 3.4 and 5.11). Some sources have brightness temperatures well above the inverse Compton limit ($T_{\rm B} \sim 10^{12}$ K, Kellermann & Pauliny-Toth, 1969) suggesting strong Doppler boosting.

The radio-γ-ray correlation study of Böck et al. (2014) is based on 8.4 GHz data of TANAMI observations (quasi-)simultaneous to the 1FGL time range. I present the milliarcsecond scale properties of the sample, in the context of the γ-ray bright/faint dichotomy, in Chapter 5. According to the TANAMI sample definition, newly detected γ-ray sources were added and (partly) observed at mas-scale resolution for the first time. Chapter 5 therefore includes the first-epoch images of this subset of TANAMI sources, completing and connecting to the list presented in Ojha et al. (2010).

3.3. Broadband spectral properties

With the multiwavelength setup described in Sect. 3.1, TANAMI aims to study the broadband emission behavior of jets at different source states (see Müller et al., 2013; Krauß et al., 2013, for further

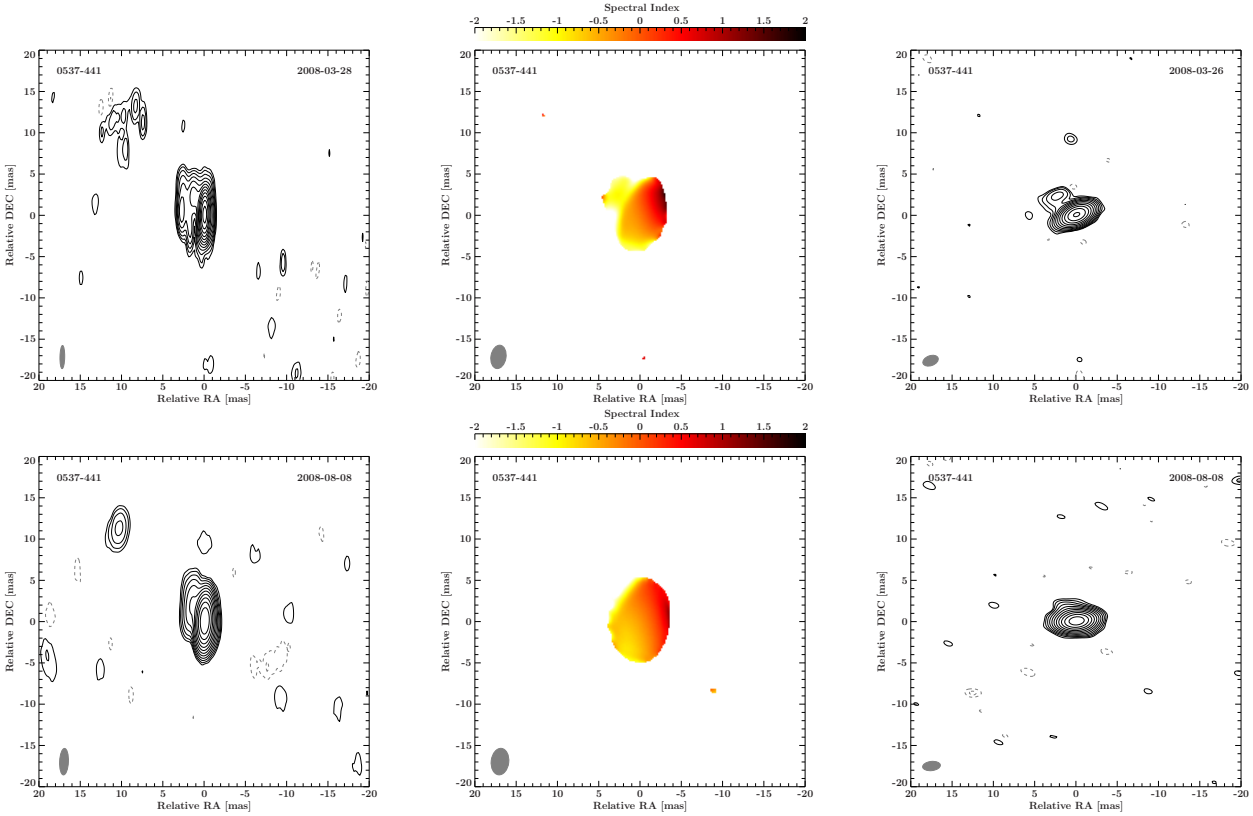

Figure 3.6.: Two simultaneous dual-frequency TANAMI observations of PKS 0537−441 in March 2008 (top) and August 2008 (bottom). The left and right panels show the 8.4 GHz and 22.3 GHz images, respectively, with the corresponding spectral index map in the middle panel. The color scale indicates the spectral index distribution: optically thick regions appear darker. Contours in the left and right panels are logarithmic, separated by a factor 2, with the lowest level set to the 3σ-noise-level. The spectral index is derived where the flux densities at 8 GHz and 22 GHz exceed both the 3σ-noise-level. To construct the spectral index map both images have been restored with a common beam represented by the gray ellipse in the lower left corner. Figures from Müller et al. (2013).

details). The VLBI monitoring provides insight into structural changes of the jets at milliarcsecond resolution. In addition, the frequent dual-frequency VLBI observations allow us to construct spectral index images for all sources[4] to monitor the evolution of the spectral index distribution along the jet. These observations can help to identify possible γ-ray production sites because the optically thick (with inverted to flat spectral indices) regions within the jet are expected to be the emission origin of high energy photons (see Sect. 7.3.4). In the following, to outline such analyses, the multiwavelength investigations of the blazar PKS 0537−441 are presented as representative example[5].

Figure 3.6 shows the contemporaneous 8.4 GHz, 22.3 GHz and corresponding spectral index image for two simultaneous TANAMI observations of PKS 0537−441. The spectral index images were constructed as follows. In order to reduce the effects of different (u, v)-sampling but, both images were restored with a common beam which represents the enclosing ellipse of the original beams. The spectral index for each pixel at position (x, y) in the map can be derived from the flux

[4]The analysis and discussion of the first-epoch 22.3 GHz TANAMI observations and corresponding spectral index images is in preparation for publication by the TANAMI team. First results are discussed in Trüstedt (2013) and Müller et al. (2012, 2013).

[5]The detailed study and interpretation of the data is in preparation for publication by the TANAMI team, led by F. Krauß.

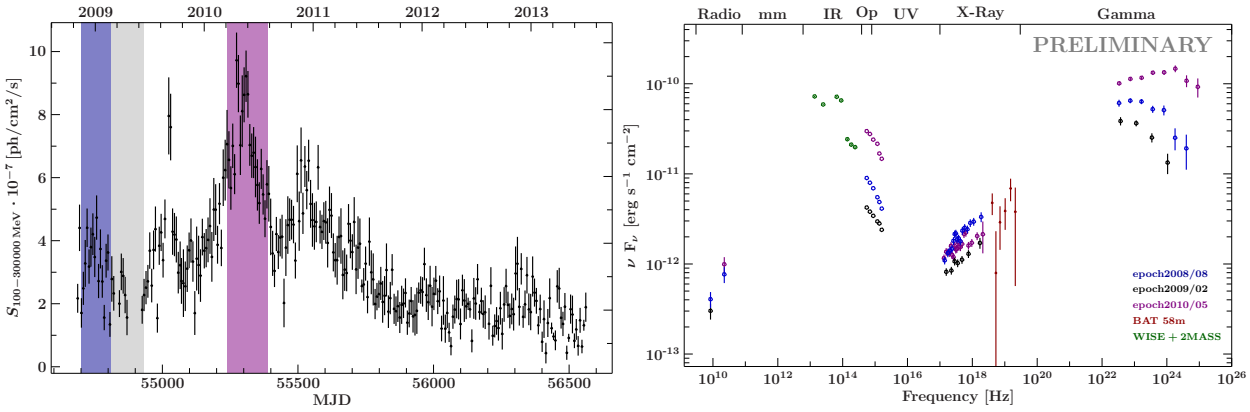

Figure 3.7.: Multiwavelength behaviour of PKS 0537−441. *Left:* Weekly binned γ-ray light curve from *Fermi*/LAT monitoring. Different activity phases – low, intermediate and high – are indicated by the gray, blue, purple shaded areas, respectively. *Right:* Broadband SED including simultaneous TANAMI, *Swift*/UVOT & XRT, *Fermi*/LAT, from *Swift*/BAT (58-month survey Baumgartner et al., 2010) and archival data from *WISE* (Wright et al., 2010) and 2MASS (Skrutskie et al., 2006). The colors correspond to the activity phases defined by the respective shaded areas in the light curve. Figures from Krauß et al. (2013).

density distribution at each frequency $S(x, y)$, assuming that the emission can be well described by a power law $S_\nu \propto \nu^{+\alpha}$, with

$$\alpha(x,y) = \frac{\log(S_{8.4\,\mathrm{GHz}}(x,y)) - \log(S_{22.3\,\mathrm{GHz}}(x,y))}{\log(8.4\,\mathrm{GHz}) - \log(22.3\,\mathrm{GHz})} \quad . \tag{3.1}$$

The spectral index is then derived where the flux densities at both frequencies exceed the 3σ-noise-level.

In order to test different jet emission models (see Sect. 1.3.5), this time dependent study of the spectral index distribution at high angular resolution is a powerful tool. In combination with simultaneous multiwavelength investigations of the sources at different activity states, this approach resolves the possible active regions. Changes in structure and in the spectrum of individual jet feature are monitored to test if those are correlated with flaring or quiescence source states. Figure 3.7 displays such a combined study for PKS 0537−441. *Fermi*/LAT monitoring provides a continuous γ-ray light curve allowing us to identify time ranges with low, intermediate and high variability. For these different activity phases, (quasi-)simultaneous spectral energy distributions are compiled from TANAMI related multiwavelength observations (see Sect. 3.1), clearly showing a change in the γ-ray spectrum.

The broadband SED can be parametrized with two logarithmic parabolas (see Sect. 6.3.5) in order to determine the shape of the synchrotron and Compton peak. More sophisticated SED models give information on the physical conditions of the jet (e.g., Dutka et al., 2013, for the TANAMI source PKS 2142−758).

3.4. Multimessenger astronomy

The composition of extragalactic jets is still under consideration. Both leptonic and hadronic emission models are tested to describe the observed broadband emission (see Sect. 1.3.5). The detection of neutrinos from an AGN, however, could turn the balance and would be a clear indicator for hadronic jet emission (Mannheim et al., 1992). Furthermore the origin and acceleration of cosmic rays is still unknown. Powerful extragalactic jets are a possible source and addressed by current

instruments including air shower or large scale neutrino detectors (see also Halzen & Hooper, 2002; Atoyan & Dermer, 2001, for reviews). These strongly collimated outflows are expected to accelerate particles to relativistic energies, such that the secondary neutrino flux can exceed the atmospheric background above 100 TeV (Mannheim, 1995).

Neutrinos are weakly interacting particles, and therefore, their travel path from the emission origin is hardly affected, even, escaping optically thick regions. In hadronic processes neutrinos are mainly produced via the charged pion $\pi^{\pm}$ decay chain

$$\begin{aligned} \pi^{+} &\rightarrow \mu^{+} + \nu_{\mu} \\ \pi^{-} &\rightarrow \mu^{-} + \bar{\nu_{\mu}} \end{aligned}$$

and the subsequent process

$$\begin{aligned} \mu^{+} &\rightarrow e^{+} + \nu_{e} + \bar{\nu_{\mu}} \\ \mu^{-} &\rightarrow e^{-} + \bar{\nu_{e}} + \nu_{\mu} \end{aligned}$$

with the charged muons $\mu^{\pm}$, the electron/positron $e^{\pm}$, and the corresponding neutrinos $\nu_{\mu,e}$ and anti-neutrinos $\bar{\nu_{\mu,e}}$. Neutrinos are a clear tracer for hadronic acceleration.

In order to discriminate between hadronic and leptonic emission processes in jets, TANAMI aims to extend the observations over the electromagnetic spectrum to the search for extragalactic neutrino candidates. Recently, the cubic-kilometer neutrino detector at the South Pole *IceCube* (Halzen & Klein, 2010) detected the first PeV-neutrinos. This is the first detection of an excess neutrino flux above the atmospheric background indicating an extraterrestrial emission origin (IceCube Collaboration, 2013). The reconstructed location of the first two events (with the nicknames “Ernie” and “Bert”) are positionally consistent with six[6] TANAMI blazars - the brightest extragalactic jets in this field. We study the multiwavelength and mas-scale properties of these sources addressing the question whether these PeV events could originate from extragalactic jets (Krauß et al., 2014).

This study displays a first step of multimessenger astronomy with extragalactic jets, the search for positional coincidence between high-energy neutrino events and possible emitters. The next step is the usage of time information in addition to the accurate source position provided by VLBI. In Chapter 4, I discuss such a study which is based on the γ-ray loud TANAMI subsample using the source position together with variability information from the γ-ray monitoring by *Fermi*/LAT.

[6]The sources PKS B0235−616, PKS B0302−623 and PKS B0308−611 are positionally consistent with the highest-energy neutrino event. The sources Swift J1656.3−3302, PMN 1802−3940 (1714−336) and PMN J1717−3342 (1759−396) are located in the field of the second highest-energy event (Krauß et al., 2014).

Neutrino – the "little neutral one" in Italian.

(Enrico Fermi)

4. Search with ANTARES for extragalactic neutrino candidates in the TANAMI sample

Since blazars are promising candidates for extragalactic neutrino emitters (see Sect. 3.4), and the TANAMI field coincides with the part of the sky where the neutrino detector ANTARES[1] is most sensitive, a close collaboration was initiated. In this Chapter, I will focus on the joint project to search for neutrinos from γ-ray loud TANAMI jets (see Ch. 5) using the time information of the *Fermi*/LAT γ-ray light curves. The aim of this analysis is to enhance the ANTARES sensitivity by reducing the background with the additional time information[2]. The analysis is independent of a specific emission model, but assumes a correlation of γ-ray and neutrino flux. Time periods of high jet activity, such as jet ejection events or γ-ray flares, are expected to correlate with an enhanced neutrino flux. Though the neutrino fluence (the integral of the flux density over time) is less for short time periods like flares compared to longer time ranges, the significance, however, increases as the background is reduced. As part of this thesis and as a major contribution to this project[3], methods for the source selection and calculation of the *Fermi*/LAT light curves were developed (see Sect. 2.2.2) in order to select a subsample of most promising candidates from the γ-ray loud TANAMI sample.

4.1. The ANTARES detector

In the deep Mediterranean sea, 30 km south of Toulon (France), a large water Cherenkov detector was constructed[4], called ANTARES. Figure 4.1 shows the principle method of (indirectly) detecting high-energy astrophysical (muon)[5] neutrinos. The Earth acts as part of the detector material: if the incoming muon neutrino weakly interacts with the medium, a muon is produced. These leptons from astrophysical neutrinos are highly energetic and emit Cherenkov light in the sea water. An array of photomultiplier tubes in glass spheres (optical modules) detects this radiation and allows

[1] *Astronomy with a Neutrino Telescope and Abyss Environment RESearch*, `http://antares.in2p3.fr/`

[2] A previous joint TANAMI-ANTARES study led by U. Fritsch (2014) incorporated only the accurate positions of TANAMI sources (see also Böck, 2012)

[3] The analysis is led by K. Fehn (2014) and a joint publication by the ANTARES Collaboration is in preparation.

[4] ANTARES was completed in May 2008. It is the predecessor of the future multi-cubic kilometer array in the Mediterranean sea, KM3NeT (e.g., Katz & Km3NeT Consortium, 2011).

[5] The main detection channel is the muon channel. ANTARES can also detect the secondary particles of other neutrino flavors, but the shorter ranges of these leptons result in a lower angular resolution and detection efficiency. Note that also the anti-particles are considered.

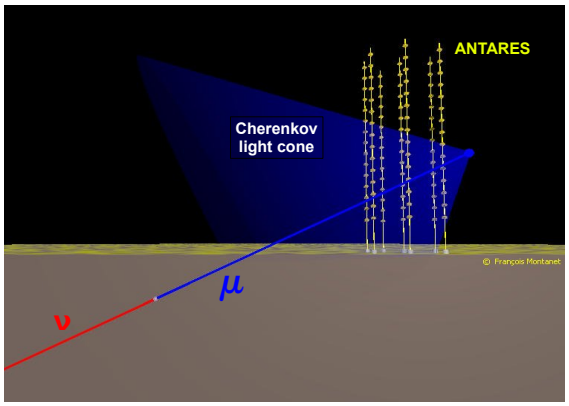

Figure 4.1: Principle of detection of high energy muon neutrinos in ANTARES. Due to the interaction with the Earth (material surrounding the telescope), the incoming neutrino creates a muon. In the sea water, the muon emits Cherenkov light which is detected by the photomultipliers. The muon track can be reconstructed by measuring the arrival times of the Cherenkov light at the optical modules at a known position. Image from Ageron et al. (2011).

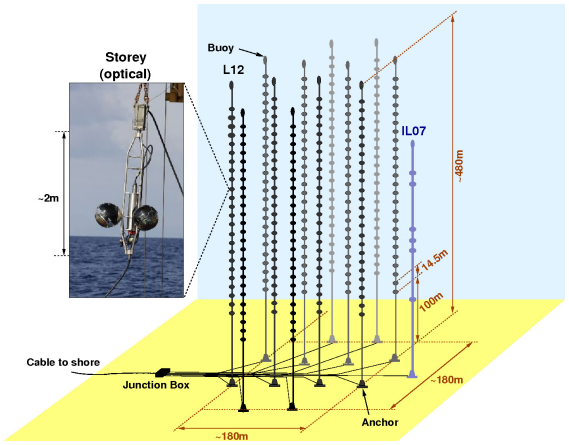

Figure 4.2: Scheme of the ANTARES detector. Shown are the 12 mooring lines at 2475 m depth, holding light sensors (photomultiplier tubes in optical modules). The detector is optimized for the detection of upwards-going high energy muon neutrinos by tracing the Cherenkov light cone from secondary charged particles. Image from Ageron et al. (2011).

the tracking of the path of the incoming muon (see Fig. 4.2). Details on the construction and detector performance are given in Ageron et al. (2011). Due to this detection method, the fields of view of ANTARES is mainly the Southern Hemisphere, in particular, the most sensitive region coincides with the part of the sky which is addressed by TANAMI.

The main particle background detected by ANTARES consists of muons and neutrinos from cosmic-ray air showers. It can significantly be reduced by considering only the upwards-going particles (see Fig. 4.2), hence ANTARES is a lot more sensitive to the southern sky. In order to distinguish between of atmospheric or cosmic signals, one uses additional information of potential source location, timing or energy criteria. The γ-ray light curves of particular TANAMI sources gives both, the direction and the time information. Constraining the predicted energy range, further background reduction can be achieved.

4.2. Candidate selection

The γ-ray loud subsample of TANAMI, consisting of 55 sources which have associated counterparts in the 2FGL catalog (see Table 4.1 and Nolan et al., 2012), was taken as input to perform this candidate search. Due to the overlap of the field of view of ANTARES and TANAMI, and due to the fact that TANAMI performs multiwavelength monitoring of the brightest extragalactic jets in the southern sky, it is reasonable to make a cut on this sample. The positional accuracy is given by the accurate VLBI positions of the sources. More important for this analysis is the accuracy in time: the sensitivity to detect neutrinos against the atmospheric background increases the shorter the time given interval. In order to select the time intervals where the sources are in a highly γ-ray

active states, the light curves for all 55 TANAMI sources were computed (see Fig. 4.3), following the method described in Sect. 2.2.2.

The full four years (April 8, 2008 to April 8, 2012) of *Fermi* data (P7V6) were used to perform this analysis, overlapping with ANTARES operations. As described in Sect. 2.2.1, the *Fermi*/LAT sensitivity is best between 1 GeV and 100 GeV. Therefore[6], the light curve analysis was performed for this energy range (with RoIs of 7°). The light curve binning was set to 14 days, a compromise between the requirement of very short time intervals for the ANTARES analysis, and the detection sensitivity of the *Fermi*/LAT for moderately bright sources (to avoid only upper limit bins). For the selection analysis described below, only the time intervals with detections are taken into account. The upper limit (for TS$\leq$ 9) bins were neglected. In addition, the averaged γ-ray flux density over four years $S_{4\,\mathrm{yrs}}$ and the corresponding photon index ($\Gamma_{4\,\mathrm{yrs}}$ for 1-100 GeV) was calculated to describe the long-term behavior of the sources (see Table 4.1). The Figures 4.3 to 4.7 show the resulting 4-year light curves with 2-weeks binning of all γ-ray sources associated with TANAMI objects.

Criterion: Variability

Highly variable sources suggest high activity and, hence, are promising candidates to search for extragalactic neutrinos, as the neutrino fluence is strongly time dependent. The root mean square (RMS) variability gives the measure of the variability. Calculating this value for all sources, neglecting the time intervals with upper limits, and applying a cut on RMS, the most variable sources can be selected (e.g., PKS 0426–380 or PKS 0537–441, known for their prominent variability).

This source selection has a big disadvantage concerning the aim of this analysis (see above): since it disregards the duration of each flare and the relative brightness (to the long term flux state), this selection is not ideal. The integration over bright, long flares gives indeed a higher neutrino fluence, but the ANTARES sensitivity is considerably improved when selection shorter time ranges.

Criterion: Short and bright flares

The goal of this study is to reduce the background and enhance the ANTARES sensitivity by defining as short as possible time intervals where a bright γ-ray flare occurred for a particular source. Therefore, it requires the selection of all sources showing bright, short γ-ray flares during 4-years of *Fermi*/LAT monitoring.

The selection was performed as follows (see also Figs. 4.3 to 4.7). For every source, only bins with flux density values above a certain threshold were considered. The threshold is defined as $S \geq S_{4\,\mathrm{yrs}} + 3\sigma$ based on the long-term flux behavior $S_{4\,\mathrm{yrs}}$. This cut gives the number of bins N at a high flux. The inverse of this number ($1/N$) defines the "short criterion", i.e., few bins of flux density level above this defined threshold. The ratio of the maximum flux density S_{max} to the averaged flux over 4 years $S_{4\,\mathrm{yrs}}$ provides the "bright criterion", for selecting only sources with a ratio of > 5. The combination of both criteria results in the selection of a subsample of sources, which show a substantial flux increase within a short time range. In Table 4.1 and Figs. 4.3 to 4.7 the selected sources are particularly marked. One can introduce a weighting factor defined by the product of $1/N$ and the ratio, to sort the selected sources by this combined criterion. See Table 4.1 for details on all sources.

[6]Note that an additional tradeoff had to be made, as the computing of the full energy range (100 MeV to 300 GeV) is very time consuming.

Table 4.1.: Gamma-ray properties (1-100 GeV) of TANAMI sources (MJD 54689.65 - 56131.65)

Name	2FGL Name	$S_{\max}$ $[\times 10^{-10}\mathrm{cm}^{-2}\mathrm{s}^{-1}]$	$S_{\max}/S_{4\,\mathrm{yrs}}$	$S_{4\,\mathrm{yrs}}$ $[\times 10^{-10}\mathrm{cm}^{-2}\mathrm{s}^{-1}]$	$\Gamma_{4\,\mathrm{yrs}}$ (1–100 GeV)	N	weight	short flare candidate
0047–579	2FGL J0049.7–5738	495.10	110.34	4.49 ± 0.92	2.12	0	–	
0055–328	2FGL J0057.9–3236	60.15	4.47	13.47 ± 1.41	2.40	0	–	
0208–512	2FGL J0210.7–5102	341.07	6.31	54.03 ± 2.52	2.64	8	0.79	X
0227–369	2FGL J0229.3–3644	137.63	13.63	10.09 ± 1.33	2.85	1	13.63	X
0244–470	2FGL J0245.9–4652	234.19	4.90	47.82 ± 2.38	2.80	2	2.45	
0302–623	2FGL J0303.5–6209	62.66	6.54	9.59 ± 1.23	2.47	0	–	
0308–611	2FGL J0310.0–6058	115.44	9.39	12.29 ± 1.36	2.50	1	9.39	X
0332–376	2FGL J0334.3–3728	155.13	4.85	31.96 ± 2.00	2.18	1	4.85	
0332–403	2FGL J0334.2–4008	259.07	5.53	46.87 ± 2.34	2.34	5	1.11	X
0402–362	2FGL J0403.9–3604	883.17	13.95	63.30 ± 2.72	2.59	5	2.79	X
0405–385	2FGL J0407.3–3826	126.30	7.08	17.83 ± 1.61	2.53	1	7.08	X
0412–536	2FGL J0413.5–5332	110.21	12.32	8.95 ± 1.19	2.11	1	12.32	X
0426–380	2FGL J0428.6–3756	769.40	3.71	207.58 ± 4.67	1.60	17	0.22	
0447–439	2FGL J0449.4–4350	266.96	2.33	114.48 ± 3.41	1.88	1	2.33	
0454–463	2FGL J0456.1–4613	108.36	7.03	15.41 ± 1.56	2.69	1	7.03	X
0516–621	2FGL J0516.8–6207	96.22	3.12	30.81 ± 1.77	2.27	0	–	
0521–365	2FGL J0523.0–3628	369.86	7.48	49.42 ± 2.53	2.65	2	3.74	X
0524–485	2FGL J0526.1–4829	138.22	10.73	12.88 ± 1.56	2.22	1	10.73	
0537–441	2FGL J0538.8–4405	1167.79	3.29	355.31 ± 5.87	1.84	19	0.17	
0625–354	2FGL J0627.1–3528	61.81	4.18	14.80 ± 1.60	1.90	0	–	
0637–752	2FGL J0635.5–7516	105.35	8.02	13.14 ± 1.53	3.12	1	8.02	X
0700–661	2FGL J0700.3–6611	108.06	2.94	36.73 ± 2.14	2.15	0	–	
0717–432	2FGL J0718.7–4320	75.69	2.86	26.47 ± 2.00	1.91	0	–	
0736–770	2FGL J0734.2–7706	77.32	4.69	16.50 ± 1.84	2.42	0	–	
0745–330	2FGL J0747.5–3305	201.42	5.50	36.62 ± 3.58	2.63	1	5.50	X
0812–736	2FGL J0811.1–7527	72.96	2.52	28.94 ± 2.03	1.93	0	–	
1057–797	2FGL J1057.0–8004	185.60	5.03	36.90 ± 2.35	2.23	2	2.51	X
1101–536	2FGL J1103.9–5356	216.48	4.71	46.01 ± 2.72	2.32	1	4.71	
1104–445	2FGL J1107.2–4448	125.62	13.06	9.62 ± 1.59	2.98	0	–	
1144–379	2FGL J1146.8–3812	76.69	4.44	17.27 ± 1.70	2.31	0	–	
1313–333	2FGL J1315.9–3339	323.61	11.74	27.57 ± 2.18	2.39	2	5.87	X
1322–428	2FGL J1325.6–4300	137.21	4.33	31.70 ± 2.66	2.42	0	–	
1323–526	2FGL J1326.7–5254	206.92	6	34.50 ± 2.66	2.57	2	3.00	X
1325–558	2FGL J1329.2–5608	308.35	4.05	76.20 ± 3.63	2.38	3	1.35	
1344–376	2FGL J1347.7–3752	110.42	9.88	11.17 ± 1.57	2.46	1	9.88	X
1424–418	2FGL J1428.0–4206	1456.38	8.14	178.90 ± 4.61	1.92	12	0.68	X
1440–389	2FGL J1443.9–3908	106.46	2.61	40.77 ± 2.46	1.86	0	–	
1454–354	2FGL J1457.4–3540	468.96	6.24	75.20 ± 3.17	2.03	8	0.78	X
1501–343	2FGL J1504.9–3433	54.46	5.52	9.86 ± 1.60	2.65	0	–	
1505–496*	2FGL J1508.5–4957	–	–	13.78 ± 2.21	2.74	–	–	
1600–445	2FGL J1604.5–4442	243.09	3.78	64.27 ± 3.79	2.69	1	3.78	
1600–489	2FGL J1603.8–4904	246.84	1.84	133.90 ± 5.23	2.18	0	–	
1606–667	2FGL J1610.8–6650	94.78	3.64	26.07 ± 1.97	1.84	0	–	
1610–771	2FGL J1618.2–7718	82.23	4.40	18.67 ± 1.85	2.94	0	–	
1646–506	2FGL J1650.1–5044	197.25	2.66	74.18 ± 2.48	2.45	0	–	
1714–336	2FGL J1717.7–3342	576.70	5.98	96.46 ± 5.40	1.93	1	5.98	X
1716–771	2FGL J1725.1–7714	84.38	5.21	16.18 ± 1.84	2.91	0	–	
1759–396	2FGL J1802.6–3940	507.60	4.68	108.48 ± 3.97	1.66	13	0.36	
1933–400	2FGL J1937.2–3955	83.23	8.08	10.31 ± 1.65	2.35	0	–	
1954–388	2FGL J1958.2–3848	170.39	5.13	33.20 ± 2.32	2.69	3	1.71	X
2005–489	2FGL J2009.5–4850	141.42	3.55	39.83 ± 2.28	1.81	0	–	
2052–474	2FGL J2056.2–4715	333.20	4.84	68.78 ± 4.22	2.65	6	0.81	
2136–428	2FGL J2139.3–4236	187.56	3.69	50.85 ± 2.55	2.28	1	3.69	
2149–306	2FGL J2151.5–3021	36.34	5.31	6.85 ± 1.37	4.00	0	–	
2155–304	2FGL J2158.8–3013	507.45	2.23	227.30 ± 4.81	1.91	4	0.56	
2204–540	2FGL J2208.1–5345	167.88	15.10	11.12 ± 1.36	2.59	1	15.10	X
2326–477	2FGL J2329.7–4744	69.39	16.07	4.32 ± 1.15	2.43	0	–	

Notes. Columns give the TANAMI source name, 2FGL catalog name, minimum/maximum γ-ray flux (1-100 GeV), the ratio to the 4 yrs averaged flux, the 4 yrs flux, the photon index, the number of bins N which fulfill the criterion $S \geq S_{4\,\mathrm{yrs}} + 3\sigma$, and weighting factor (see text for details). *For the source PKS 1505–496 the light curve analysis for the 1-100 GeV range with 2-weeks binning resulted in no detection.

4.3. Outlook

As outlined above, this selection analysis is part of a joint project of the TANAMI, *Fermi* and ANTARES Collaborations. Applying the same short-flare selection method, but using data of a larger energy range (100 MeV to 300 GeV) and the averaged flux from the 2FGL catalog for this energy range, a subsample of TANAMI sources was selected to perform the ANTARES search (see Fehn, 2014, for more information). It can be shown that the criterion to select for short flares significantly increases the sensitivity compared to selecting only for variability.

The analysis described in this work is more self-contained, since the selection is based on the averaged flux of four instead of two years. Moreover, by neglecting the soft photons below 1 GeV, hard spectrum sources are preferentially selected. Further discussion is required and ongoing, whether the spectral information and the source class should be taken into account.

As a next step, this analysis will be expanded to include further time information. As soon as the TANAMI monitoring provides sufficient observing epochs to determine jet ejection times for all sources, these dates will provide further constraints in time and, hence, an increase in sensitivity.

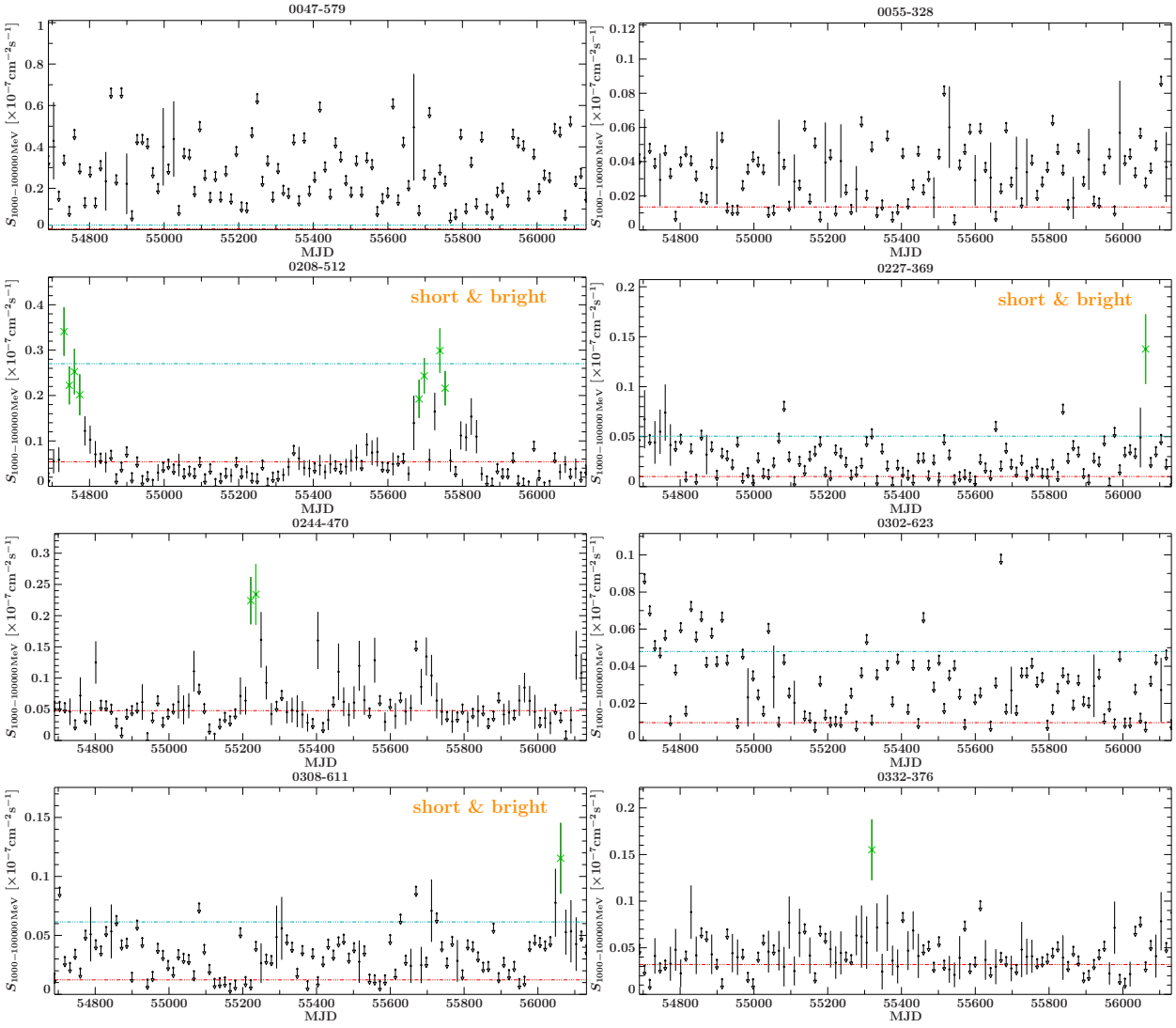

Figure 4.3.: γ-ray light curves of TANAMI associated *Fermi*/LAT sources for the energy range of (1–100) GeV and the time range MJD 54689.65 to MJD 56131.65 (first four years of *Fermi*/LAT observations). The source name is given as title of each plot. Note that the x-axis is scaled to show all detections, therefore, some upper limits may lie outside the plotted range. Table 4.1 lists the details. The red dashed line indicates the averaged flux level $S_{4\,\mathrm{years}}$ (for 1–100 GeV) for the analyzed time range of 4 years, used for the selection of short flares (see Sect. 4.2). If the source fulfills the criterion $S_{\mathrm{max}}/S_{4,\mathrm{yrs}} > 5$ (i.e., source with relatively large flux density changes with respect to the 4-years average), a blue-dashed line indicates the $5 \times S_{4,\mathrm{yrs}}$-level. All 2-weeks bins with $S \geq S_{4\,\mathrm{yrs}} + 3\sigma$ are marked in green. The sources meeting the combination of both criteria are selected as the short-flaring, bright candidates and marked in particular with "short & bright"-tag in orange (see also Table 4.1).

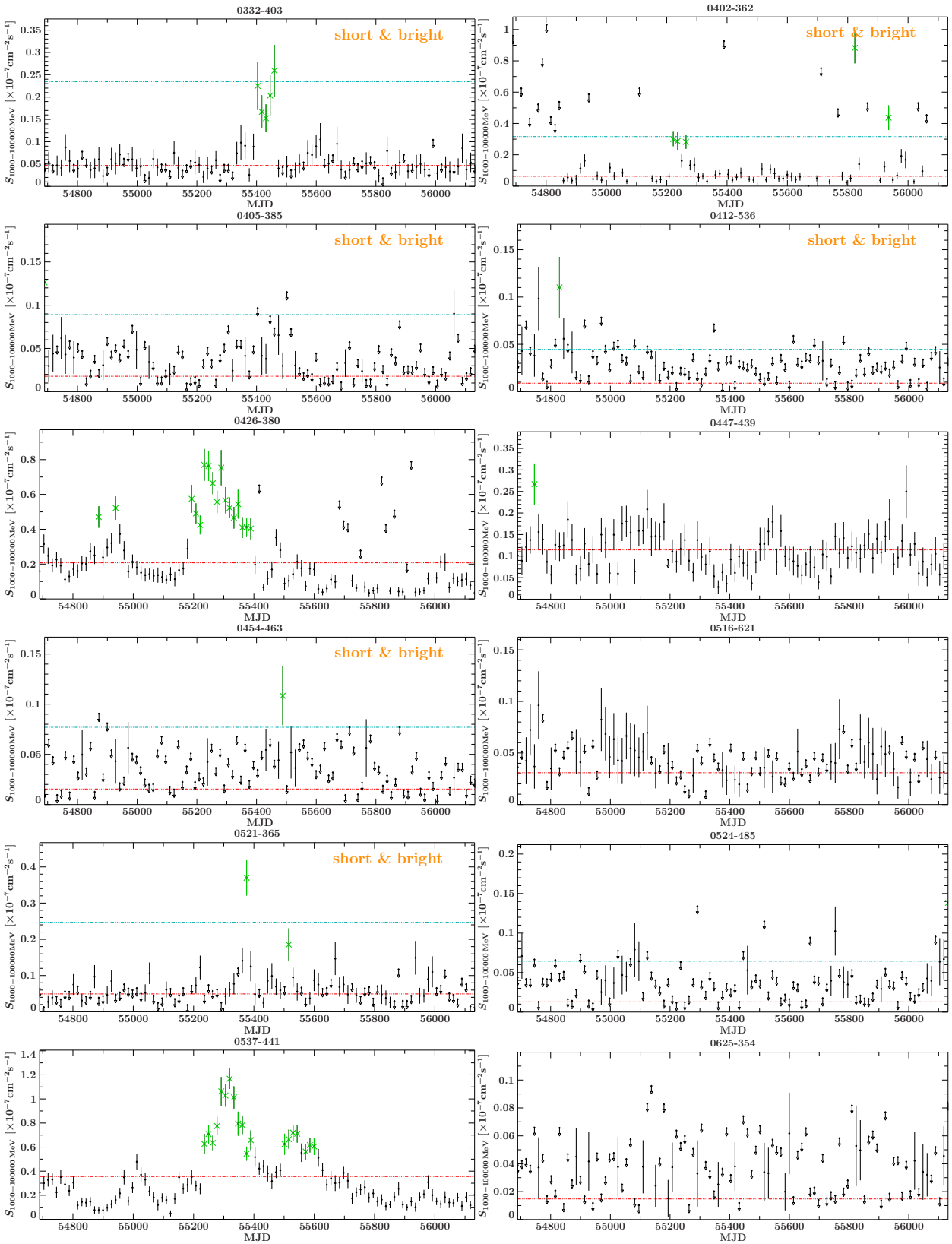

Figure 4.4.: Same as Fig. 4.3.

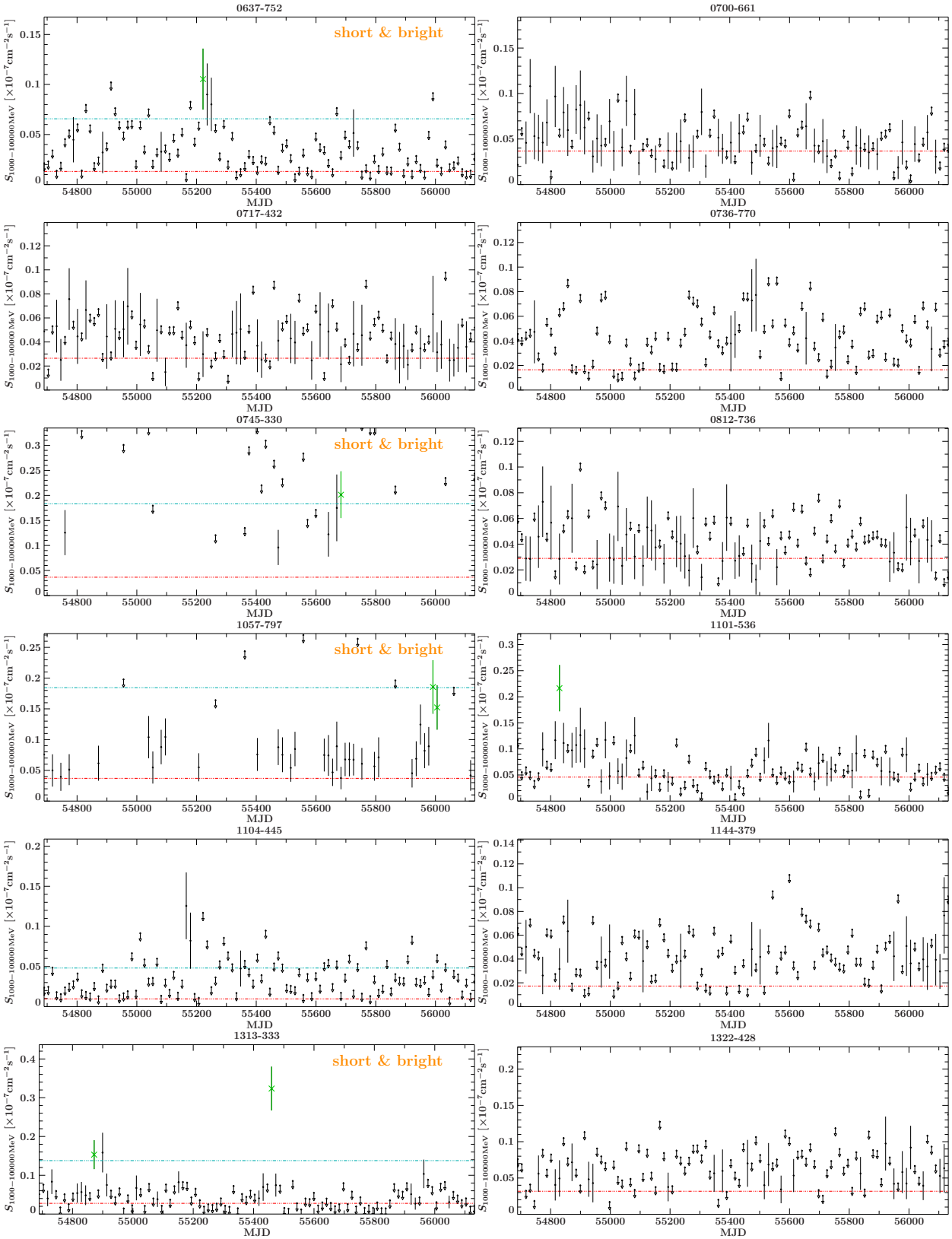

Figure 4.5.: Same as Fig. 4.3.

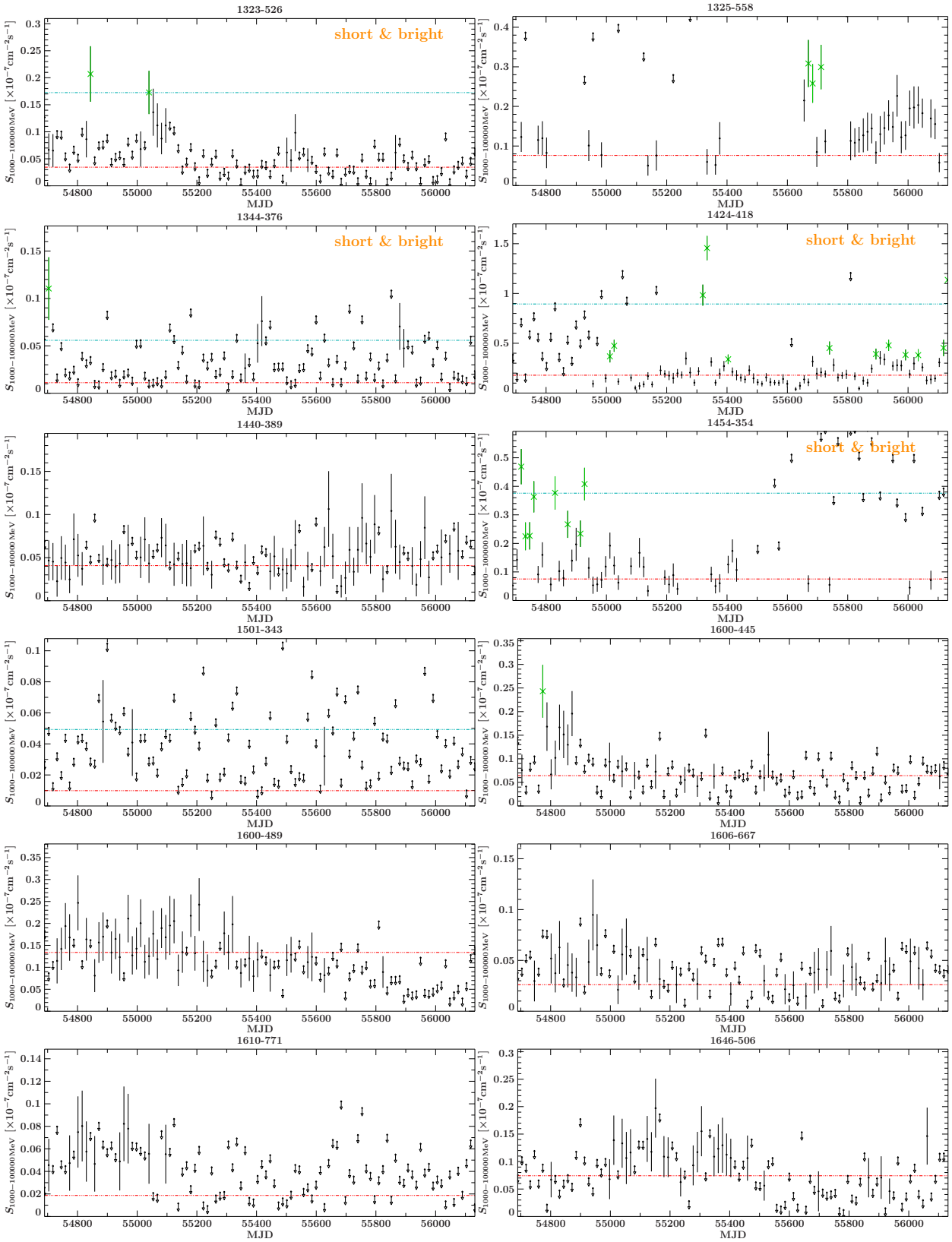

Figure 4.6.: Same as Fig. 4.3.

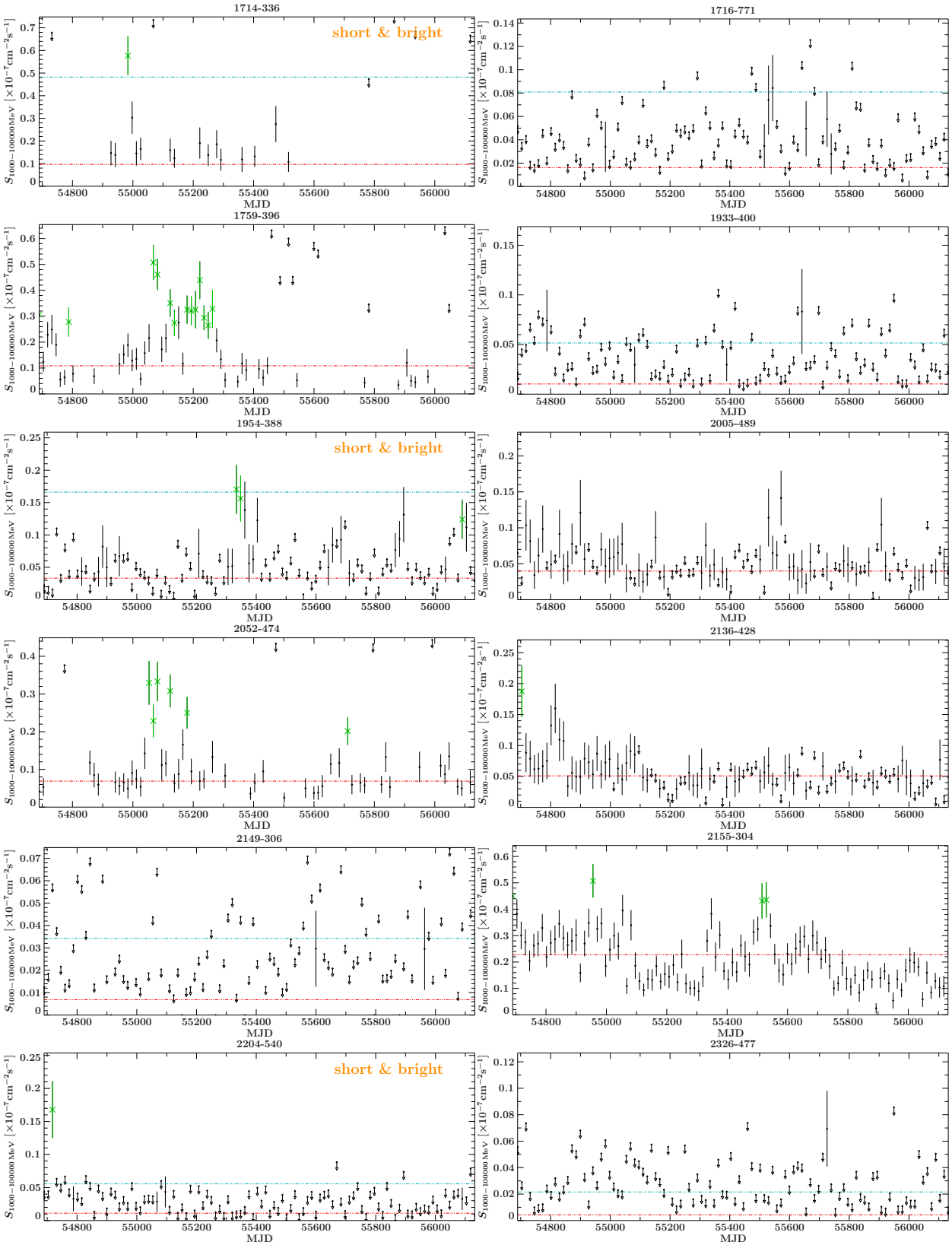

Figure 4.7.: Same as Fig. 4.3.

We find them smaller and fainter, in constantly increasing numbers, and we know that we are reaching into space, farther and farther, until, with the faintest nebulae that can be detected with the greatest telescopes, we arrive at the frontier of the known universe.

(Edwin Hubble)

5. Gamma-ray loudness and milliarcsecond-scale properties of TANAMI sources

The initial TANAMI sample consisted of 43 sources (see Ch. 3 and Ojha et al., 2010). Further bright extragalactic jets on the Southern Hemisphere which are associated counterparts of newly detected *Fermi* γ-ray sources have been added, resulting in a total number of 75 objects after the first year of *Fermi*/LAT operations (see Table 5.1). As summarized in Sect. 3.2, the study of the γ-ray properties with respect to the radio fluxes densities of the TANAMI sample indicates a correlation of the γ-ray and radio luminosities. However, a part of the TANAMI sample – including some of the radio-brightest objects in the southern sky – remain undetected in γ-rays, raising the question, whether there may be an intrinsic difference or dichotomy of γ-ray loud and faint AGN jets. These results require a detailed, corresponding analysis of the mas-scale properties to check whether the γ-ray loud and fainter subsamples are intrinsically different.

In order to ensure (quasi-) simultaneity, the study of the γ-ray properties and correlations with radio (VLBI core) brightness temperatures of the 75 TANAMI sources discussed by Böck (2012) and Böck et al. (2014), is based on γ-ray data of the 1FGL time range (Abdo et al., 2010) and contemporaneous TANAMI observations[1]. This approach further enables the study of the whole sample during a specific, short time period without averaging over different possible source activity phases.

In the following, the analysis of the parsec-scale properties at 8.4 GHz of the whole 75 sources sample on which the values (contained in Böck et al., 2014) are based on, is shown. In particular, the first-epoch images of the additional sources, which are not included in the initial TANAMI sample, are presented and discussed for the first time (following and completing the discussion of the first images of the initial sample by Ojha et al., 2010).

The TANAMI sample is not a static sample. It was defined (see Sect. 3.1) such that it can be extended by adding newly detected γ-ray jets. The initial sample was comprised of 43 radio-loud AGN south of $-30°$ declination meeting the defined radio flux and flat-spectrum criteria and/or have been EGRET detected or candidate sources (Ojha et al., 2010). After three months of *Fermi*/LAT monitoring $\sim$28% of the initial sample had been detected (Abdo et al., 2009). Based on this 3-months and the subsequent (*Fermi* internal) 6-months list of γ-ray sources associated with known

[1]The first VLBI observation epoch coinciding with the 1FGL time range was used, if possible. Note that, for the sake of completeness and to discuss in this work the VLBI properties of all 75 sources analyzed in Böck et al. (2014), the first radio data of 6 sources are not simultaneous to the 1FGL time range, but are taken from the first subsequent TANAMI observation (see Table 5.1).

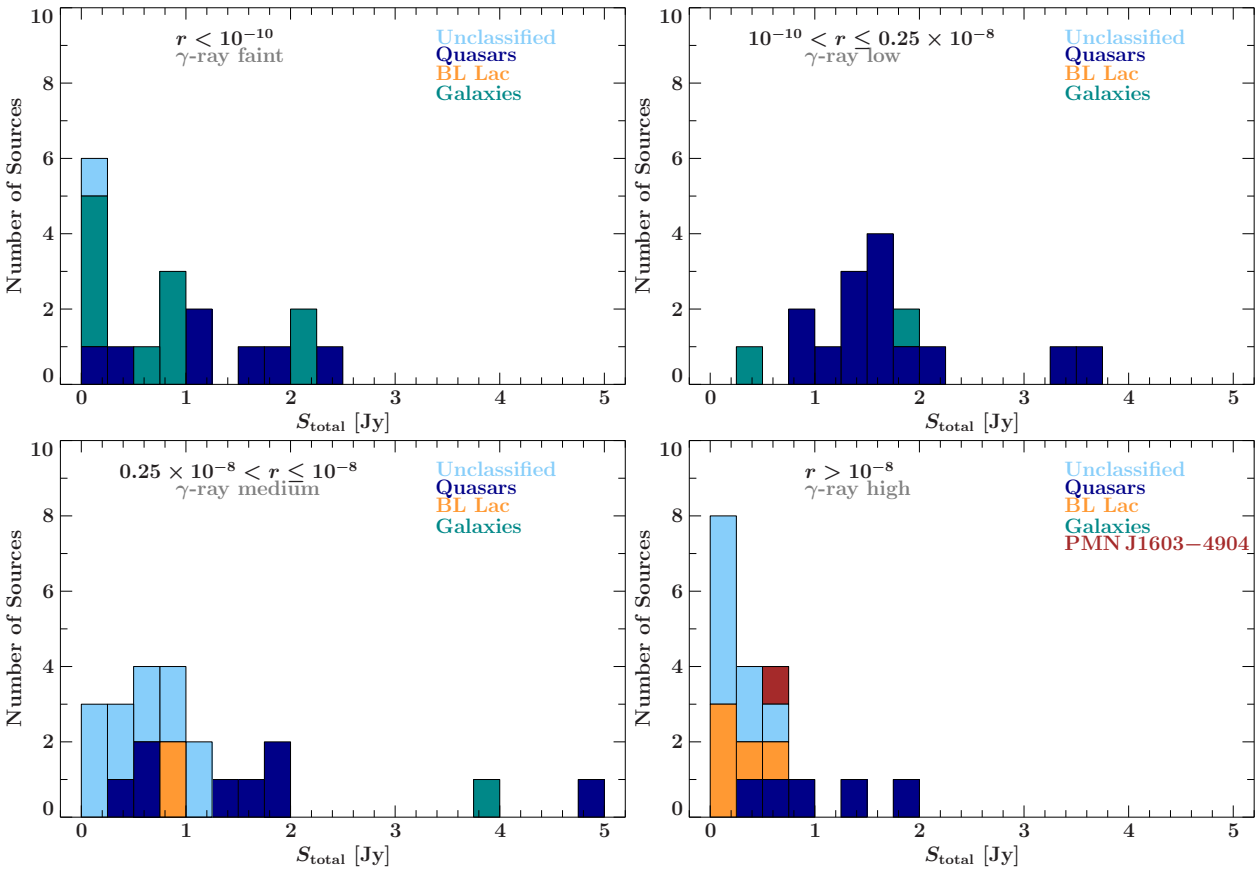

Figure 5.1.: Distribution of the total 8.4 GHz flux density for the subsamples defined by the ratio r [in units of $\mathrm{cm^{-2}\,s^{-1}\,Jy^{-1}}$] of the flux density at (1-100) GeV (Abdo et al., 2010) and the 8.4 GHz core flux density. The source PMN J1603−4904 is particularly marked because of its unusual multiwavelength properties discussed in Chapter 6.

bright extragalactic jets and later based on the 1FGL catalog (Abdo et al., 2010), new sources have been continuously added to the sample throughout 2009. The requirements are a significant γ-ray brightness during the first year of *Fermi*/LAT measurements and a radio flux density of $S_{8.4\,\mathrm{GHz}} \geq 100\,\mathrm{mJy}$ in order to ensure sufficient dynamic ranges in the VLBI images. In addition, flaring and Atel *Fermi*/LAT sources were included. After one year of *Fermi* operations, the sample consisted of 75 sources (Table 5.1). Note however, that it is not complete, but the majority of the γ-ray loud AGN south of -30° are included. In Sect. 5.2 the statistics of their mas-scale properties are discussed with the objective to make out critical differences between γ-ray loud and faint subsamples.

The extended TANAMI sample is composed of a small fraction (24%) of sources, which remain undetected in γ-rays after one year of *Fermi*/LAT monitoring[2]. The combined radio and γ-ray selection criteria give the following distinction, based on which the statistics of the VLBI-properties are discussed below: The ratio $r = S_{1-100\,\mathrm{GeV}}/S_{8.4\,\mathrm{GHz,core}}\ \mathrm{cm^{-2}\,s^{-1}\,Jy^{-1}}$ of the flux density at (1-100) GeV (Abdo et al., 2010) to the 8.4 GHz core flux density is used to define four subsamples reflecting the γ-ray loudness. Figure 5.1 shows the total flux density distribution for $r < 10^{-10}\,\mathrm{cm^{-2}\,s^{-1}\,Jy^{-1}}$ (corresponding to all non-detected sources, i.e., γ-ray faint), $10^{-10}\,\mathrm{cm^{-2}\,s^{-1}\,Jy^{-1}} < r \leq 0.25 \times 10^{-8}\,\mathrm{cm^{-2}\,s^{-1}\,Jy^{-1}}$ (low γ-ray brightness), $0.25 \times 10^{-8}\,\mathrm{cm^{-2}\,s^{-1}\,Jy^{-1}} < r \leq 10^{-8}\,\mathrm{cm^{-2}\,s^{-1}\,Jy^{-1}}$

[2]Even after two years, 25% of the TANAMI sources have still not been detected (see Ch. 4 and Nolan et al., 2012).

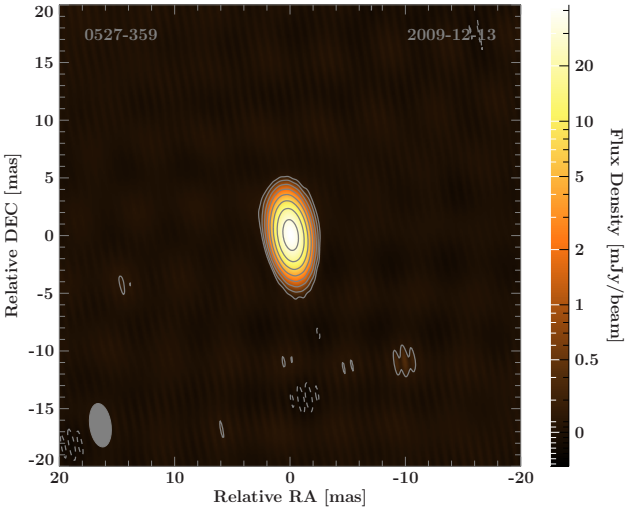

Figure 5.2: First epoch image of 0527−359 (PMN J0529−355). The contours (and the color scale) indicate the flux density level, scaled logarithmically and separated by a factor of 2, with the lowest level set to the 3σ-noise level (for more details see Table 5.1). The size of the synthesized beam is shown as a gray ellipse in the lower left corner of the image.

(medium) and $r > 10^{-8}\,\mathrm{cm}^{-2}\,\mathrm{s}^{-1}\,\mathrm{Jy}^{-1}$ (high). This classification into four subsamples displays clearly the TANAMI sample definition, with the brightest γ-ray sources being fainter radio sources.

5.1. Total intensity images of additional sources

In this section, the first epoch images at 8.4 GHz are presented (Figs. 5.3 to 5.7), completing the list of Ojha et al. (2010). Most of the sources were included in the sample due to their γ-ray detection during the first year of *Fermi*/LAT monitoring. In addition, the first-epoch image of 0527−359, an EGRET candidate blazar (Sowards-Emmerd et al., 2004) and hence a source of the initial sample (Ojha et al., 2010), is shown in Fig. 5.2. This source was not observed by TANAMI until 2009 December. The source shows only weak, compact radio emission at mas-scales and was not detected by the *Fermi*/LAT. Hence, a follow-up by TANAMI should be reconsidered.

The observational parameters, information and derived image properties on these additional sources are given in Table 5.1. Figure 5.3 shows the corresponding first-epoch contour images. The VLBI radio analysis of the TANAMI sources follows Ojha et al. (2010) and Sect. 2.1.2.

Table 5.1.: Observational parameters at 8.4 GHz

Name[a]	Common Name[a]	initial[a]	Class[b]	z[c]	Morphology[d]	obs. date[e] [year]	b_{maj}[f] [mas]	b_{min}[f] [mas]	P.A.[f] [°]	S_{total}[g] [Jy]	RMS[g] [mJy]	S_{core}[g] [Jy]	T_B[h] [$\times 10^{10}$K]	$T_B(1+z)$[h] [$\times 10^{10}$K]	Name1FGL[i]	$S_{1-100\,GeV}$[i] [$\times 10^{10}$cm^{-2} s^{-1}]
0047−579	[HB89] 0047−579	y	Q	1.80	SS	2008.60	3.51	1.32	0.04	1.55	0.35	1.35	17.11	47.90	1FGL J0049.8−5738	6.28 ± 2.29
0055−328	PKS 0055−328	–	X	–	SS	2009.16	2.61	1.75	32.02	0.10	0.14	0.08	0.86	–	1FGL J0058.4−3235	7.76 ± 2.32
0208−512	[HB89] 0208−512	y	Q	1.00	SS	2008.90	0.81	0.71	58.10	1.63	0.54	1.39	11.55	23.09	1FGL J0210.6−5101	70.89 ± 5.81
0227−369	PKS 0227−369	–	Q	2.12	SS	2009.16	2.48	1.17	36.95	0.57	0.22	0.56	21.61	67.30	1FGL J0229.3−3644	20.04 ± 3.29
0244−470	PKS 0244−470	–	X	–	SS	2009.16	2.42	1.12	43.54	0.26	0.15	0.23	7.26	–	1FGL J0245.9−4652	28.12 ± 3.87
0302−623	PKS 0302−623	–	Q	1.35	IRR	2009.16	1.20	0.59	41.56	1.52	0.39	1.07	7.59	17.83	1FGL J0303.4−6209	12.68 ± 2.89
0308−611	PKS 0308−611	–	Q	1.48	SS	2009.68	1.93	1.31	53.80	0.83	0.33	0.81	8.94	22.18	1FGL J0310.1−6058	14.30 ± 3.08
0332−376	PMN J0334−3725	–	X	–	SS	2009.16	3.11	1.33	35.11	0.29	0.14	0.28	15.55	–	1FGL J0334.4−3727	26.22 ± 3.74
0332−403	[HB89] 0332−403	y	B	1.45	SS	2008.60	5.53	3.43	−71.76	0.95	0.28	0.95	7.54	18.48	1FGL J0334.2−4010	37.64 ± 4.34
0402−362	PKS 0402−362	–	Q	1.42	SS	2009.68	3.64	0.91	14.32	0.56	0.23	0.53	5.41	13.09	1FGL J0403.9−3603	27.27 ± 3.78
0405−385	[HB89] 0405−385	y	Q	1.29	SS	2008.60	3.16	1.09	5.87	1.40	0.41	1.38	6.30	14.43	1FGL J0407.4−3827	24.79 ± 3.79
0412−536[j]	PMN J0413−5332	–	X	–	C	2009.95	3.66	1.31	24.95	0.03	0.35	0.03	>4.66	–	1FGL J0413.4−5334	24.48 ± 3.76
0426−380	PKS 0426−380	–	Q	1.11	SS	2009.16	2.53	0.63	29.43	1.81	0.43	1.78	74.66	157.54	1FGL J0428.6−3756	257.15 ± 10.19
0438−436	[HB89] 0438−436	y	Q	2.86	SS	2008.90	1.08	0.82	32.54	1.16	0.32	0.59	3.68	14.20		
0447−439	PKS 0447−439	–	B	0.11	SS	2009.16	3.10	1.43	36.01	0.10	0.11	0.09	4.72	5.22	1FGL J0449.5−4350	110.81 ± 6.85
0454−463	[HB89] 0454−463	y	Q	0.85	SS	2008.90	3.00	0.68	43.47	3.41	0.91	3.24	22.47	41.56	1FGL J0455.6−4618	15.58 ± 3.25
0506−612	[HB89] 0506−612	y	Q	1.09	SS	2008.60	3.46	1.40	11.53	1.13	0.32	1.12	15.86	33.14	1FGL J0507.3−6103	19.10 ± 3.43
0516−621	PKS 0516−621	–	X	–	C	2009.15	2.46	0.62	78.60	0.88	0.38	0.88	31.13	–	1FGL J0516.7−6207	32.31 ± 4.19
0518−458	PICTOR A	y	G	0.04	SS	2008.90	1.43	0.76	12.44	0.82	0.19	0.55	2.59	2.69		
0521−365	ESO 362− G 021	y	G	0.06	SS	2008.60	3.26	1.47	−3.78	1.85	0.41	1.52	27.46	29.10	1FGL J0522.8−3632	28.54 ± 4.06
0524−485	PKS 0524−485	–	X	–	SS	2009.16	2.48	0.92	30.05	0.55	0.19	0.54	13.44	–	1FGL J0526.3−4829	14.96 ± 3.14
0527−359[j,l]	PMN J0529−3555	–	U	–	C	2009.95	3.79	1.85	7.91	0.04	0.27	0.04	>7.52	–		
0537−441	[HB89] 0537−441	y	Q	0.89	SS	2008.60	3.21	1.05	−2.47	4.84	0.93	4.71	295.78	559.03	1FGL J0538.8−4404	212.88 ± 9.48
0625−354	PKS 0625−35	y	G	0.05	SS	2008.90	2.04	1.35	34.30	0.41	0.18	0.35	11.64	12.23	1FGL J0627.3−3530	8.43 ± 3.03
0637−752	[HB89] 0637−752	y	Q	0.65	SS	2008.60	3.37	1.04	−9.05	3.53	0.83	3.02	12.00	19.81	1FGL J0636.1−7521	17.53 ± 3.76
0700−661	PKS 0700−661	–	X	–	SS	2009.16	1.78	1.31	53.11	0.14	0.12	0.13	2.16	–	1FGL J0700.4−6611	47.30 ± 5.04
0717−432[k]	PMN J0718−4319	–	X	–	SS	2009.16	1.87	0.91	26.46	0.03	0.14	0.03	>25.58	–	1FGL J0718.7−4320	30.08 ± 4.13
0736−770[j]	PKS 0736−770	–	Q	–	SS	2009.95	1.48	1.12	0.86	0.31	0.28	0.31	8.36	–	1FGL J0734.1−7715	14.30 ± 3.96
0745−330[j]	PKS 0745−330	–	U	–	SS	2009.95	3.26	1.28	16.23	0.66	0.38	0.59	7.27	–	1FGL J0747.4−3303	43.62 ± 6.69
0812−736[k]	PMN J0810−7530	–	X	–	SS	2009.16	1.45	1.11	22.21	0.04	0.14	0.03	>42.70	–	1FGL J0811.1−7527	25.28 ± 4.22
1057−797	PKS 1057−79	–	Q	0.58	C	2009.16	1.05	0.55	-31.48	2.02	0.54	1.93	30.03	47.47	1FGL J1058.1−8006	21.62 ± 3.99
1101−536	PKS 1101−536	–	Q	–	SS	2009.68	4.07	1.00	21.71	0.41	0.19	0.39	5.43	–	1FGL J1103.9−5355	60.66 ± 6.31
1104−445	[HB89] 1104−445	y	Q	1.60	SS	2008.90	1.54	0.88	30.88	1.76	0.33	1.41	10.39	27.02		
1144−379	[HB89] 1144−379	y	Q	1.05	SS	2008.60	4.72	3.01	−67.71	1.98	0.60	1.91	28.89	59.23	1FGL J1146.9−3812	24.34 ± 3.82
1257−326	PKS 1257−326	y	Q	1.26	SS	2008.90	2.43	0.88	29.48	0.15	0.15	0.13	1.75	3.95		
1258−321[j]	ESO 443− G 024	–	G	0.02	SS	2009.95	4.08	1.77	26.71	0.12	0.28	0.11	1.89	1.93		
1313−333	[HB89] 1313−333	y	Q	1.21	SS	2008.60	3.49	1.47	−3.54	1.41	0.36	1.33	166.71	368.42	1FGL J1316.1−3341	39.35 ± 4.96
1322−428	Cen A	y	G	0.00	DS	2008.90	0.97	0.59	31.39	3.91	0.64	0.72	8.63	8.63	1FGL J1325.6−4300	35.00 ± 5.01

Notes. [a] IAU B1950 name and common name. "y" indicates that source included in initial TANAMI sample. [b] Optical classification after Véron-Cetty & Véron (2006) with Q: quasar, B: BL Lac, G: galaxy, X/U: unidentified object. [c] Redshift from NED. [d] Morphology scheme according to Ojha et al. (2010); Kellermann et al. (1998). [e] Date of first TANAMI 8.4 GHz observation. [f] Major, minor axis and position angle of synthesized beam. [g] Total and core flux density and RMS in the 8.4 GHz image. [h] Uncorrected and corrected (factor $1+z$) core brightness temperature. [i] Source name in 1FGL (Abdo et al., 2010) and corresponding γ-ray flux density between (1-100) GeV. [j] Note that radio fluxes of sources first observed by TANAMI after 2009 September are not included in Böck et al. (2014). [k] Source dropped from VLBI monitoring list in 2011 due to low radio flux densities. [l] Source 0527−359 was an EGRET candidate blazar (Sowards-Emmerd et al., 2004) and therefore included in the initial TANAMI sample (Ojha et al., 2010) but no first-epoch image has been published before. [m] A detailed analysis on PMN J1603−4904 can be found in Ch. 6. The source classification, redshift and morphology are discussed in detail.

Name[a]	Common Name[a]	initial[a]	Class[b]	z[c]	Morphology[d]	obs. date[e] [year]	b_{maj}[f] [mas]	b_{min}[f] [mas]	P.A.[f] [°]	S_{total}[g] [Jy]	RMS[g] [mJy]	S_{core}[g] [Jy]	T_B[h] [$\times 10^{10}$K]	$T_B(1+z)$[h] [$\times 10^{10}$K]	Name1FGL[i]	$S_{1-100\,GeV}$[i] [$\times 10^{10}$cm^{-2}s^{-1}]
1323−526	PMN J1326−5256	y	U	–	SS	2008.60	5.26	3.58	−71.64	1.24	0.34	1.19	21.55	–	1FGL J1327.0−5257	51.73 ± 6.03
1325−558	PMN J1329−5608	–	U	–	SS	2009.15	2.02	1.39	83.53	0.41	0.27	0.40	4.06	–	1FGL J1329.2−5605	40.73 ± 6.06
1333−337	IC 4296	y	G	0.01	DS	2008.90	4.19	2.12	−62.49	0.22	0.17	0.22	0.61	0.62		
1344−376	PMN J1347−3750	–	X	–	SS	2009.16	3.53	1.27	14.27	0.21	0.14	0.20	5.40	–	1FGL J1347.8−3751	10.88 ± 3.35
1424−418	[HB89] 1424−418	y	Q	1.52	SS	2008.60	3.20	1.48	−0.91	1.61	0.38	1.47	45.39	114.38	1FGL J1428.2−4204	33.60 ± 4.88
1440−389	PKS 1440−389	–	B	0.07	SS	2009.16	3.22	1.30	24.13	0.09	0.11	0.08	1.14	1.22	1FGL J1444.0−3906	34.52 ± 4.50
1454−354	PKS 1454−354	y	Q	1.42	SS	2008.90	1.24	0.63	25.88	0.75	0.38	0.70	6.89	16.67	1FGL J1457.5−3540	168.70 ± 8.80
1501−343	PMN J1505−3432	y	U	–	C	2008.60	3.64	2.26	1.24	0.14	0.13	0.14	5.13	–	1FGL J1505.1−3435	7.61 ± 3.10
1505−496	PMN J1508−4953	–	X	–	C	2009.16	4.94	3.38	−67.37	0.51	0.25	0.50	124.99	–	1FGL J1514.1−4945	77.75 ± 7.17
1549−790	PKS 1549−79	y	G	0.15	DS	2008.90	1.03	0.59	87.32	0.99	0.39	0.36	1.41	1.62		
1600−445	PMN J1604−4441	–	U	–	SS	2009.68	2.36	0.63	17.82	1.04	0.38	0.95	7.17	–	1FGL J1604.7−4443	77.21 ± 7.83
1600−489[m]	PMN J1603−4904	–	(B/G)[m]	0.18	DS	2009.16	2.51	0.98	30.10	0.59	0.21	0.22	0.89	1.05	1FGL J1603.8−4903	134.07 ± 10.67
1606−667[k]	PMN J1610−6649	–	X	–	C	2009.16	3.04	1.11	−52.79	0.04	0.17	0.04	>21.29	–	1FGL J1610.6−6649	29.47 ± 4.30
1610−771	[HB89] 1610−771	y	Q	1.71	SS	2008.60	4.90	3.87	70.43	1.84	0.40	1.38	3.54	9.58	1FGL J1617.9−7716	36.80 ± 4.93
1613−586	PMN J1617−5848	–	Q	–	SS	2009.68	1.02	0.59	21.59	2.34	0.55	1.59	7.48	–		
1646−506[j]	PMN J1650−5044	–	U	–	SS	2010.35	3.07	1.53	19.76	0.96	0.15	0.91	14.18	–	1FGL J1650.4−5042	48.81 ± 7.09
1714−336	PMN J1717−3342	y	B	–	SS	2008.90	4.20	3.29	60.00	0.56	0.42	0.54	0.12	–	1FGL J1717.9−3343	76.35 ± 9.68
1716−771	PKS 1716−771	y	U	–	SS	2008.60	4.37	1.97	4.00	0.45	0.15	0.43	9.00	–	1FGL J1743.8−7620	40.16 ± 5.11
1718−649	NGC 6328	y	G	0.01	IRR	2008.90	0.95	0.50	−52.10	2.21	0.64	–	–	–		
1733−565	PKS 1733−56	y	G	0.10	SS	2008.60	5.01	3.57	84.00	0.19	0.19	0.18	4.46	4.91	1FGL J1702.4−5653	39.64 ± 5.81
1759−396	PMN J1802−3940	y	Q	0.30	SS	2008.90	1.11	1.06	31.82	1.00	0.29	0.89	16.03	20.83	1FGL J1802.5−3939	103.99 ± 7.76
1804−502	PMN J1808−5011	y	Q	1.61	SS	2008.60	3.63	1.60	−2.14	0.45	0.15	0.45	227.49	593.76		
1814−637	PKS 1814−63	y	G	0.06	DS	2008.90	2.57	1.20	−41.30	0.84	0.37	0.32	6.13	6.50		
1933−400	PKS 1933−400	y	Q	0.97	SS	2008.60	3.81	1.27	0.29	1.45	0.30	1.40	1254.59	2471.54	1FGL J1938.2−3957	17.95 ± 4.05
1934−638	PKS 1934−63	y	G	0.18	DS	2008.60	3.28	1.73	6.13	2.08	0.14	–	–	–		
1954−388	[HB89] 1954−388	y	Q	0.63	SS	2008.90	0.82	0.66	49.59	1.61	0.74	1.57	13.38	21.81	1FGL J1958.4−3847	27.10 ± 4.23
2005−489	[HB89] 2005−489	y	B	0.07	SS	2008.60	3.61	0.95	−4.47	0.78	0.15	0.76	2.37	2.53	1FGL J2009.5−4849	49.89 ± 5.14
2027−308	ESO 462− G 027	y	G	0.02	SS	2008.90	3.66	1.70	42.35	0.10	0.25	0.08	3.36	3.42		
2052−474	[HB89] 2052−474	y	Q	1.49	SS	2008.60	3.87	1.15	0.72	1.79	0.39	1.74	61.26	152.53	1FGL J2056.3−4714	45.98 ± 5.03
2106−413	[HB89] 2106−413	y	Q	1.06	SS	2008.90	2.35	1.22	62.14	1.18	0.23	1.04	7.86	16.18		
2136−428	PMN J2139−4235	–	B	–	SS	2009.95	4.13	2.23	33.78	0.10	0.19	0.09	>38.46	–	1FGL J2139.3−4235	82.86 ± 6.20
2149−306	PKS 2149−306	y	Q	2.35	SS	2008.60	4.34	1.33	1.48	1.40	0.32	1.27	41.39	138.64	1FGL J2158.8−3013	271.26 ± 10.34
2152−699	ESO 075− G 041	y	G	0.03	SS	2008.90	2.10	0.88	−15.20	0.54	0.35	0.43	4.02	4.14		
2155−304	[HB89] 2155−304	y	B	0.12	SS	2008.60	4.59	1.69	2.98	0.42	0.13	0.38	6.90	7.73	1FGL J2158.8−3013	271.26 ± 10.34
2204−540	[HB89] 2204−540	y	Q	1.21	SS	2008.90	0.59	0.50	53.69	0.91	1.14	0.71	9.85	21.77	1FGL J2207.8−5344	16.47 ± 3.32
2326−477	[HB89] 2326−477	y	Q	1.30	SS	2008.60	3.92	2.61	−10.93	1.33	0.14	0.81	4.23	9.74	1FGL J2330.3−4745	9.48 ± 2.75
2355−534	[HB89] 2355−534	y	Q	1.01	SS	2008.90	1.33	0.56	−16.46	1.73	0.57	1.53	25.14	50.53		

Notes. [(a−m)] see Table 5.1.

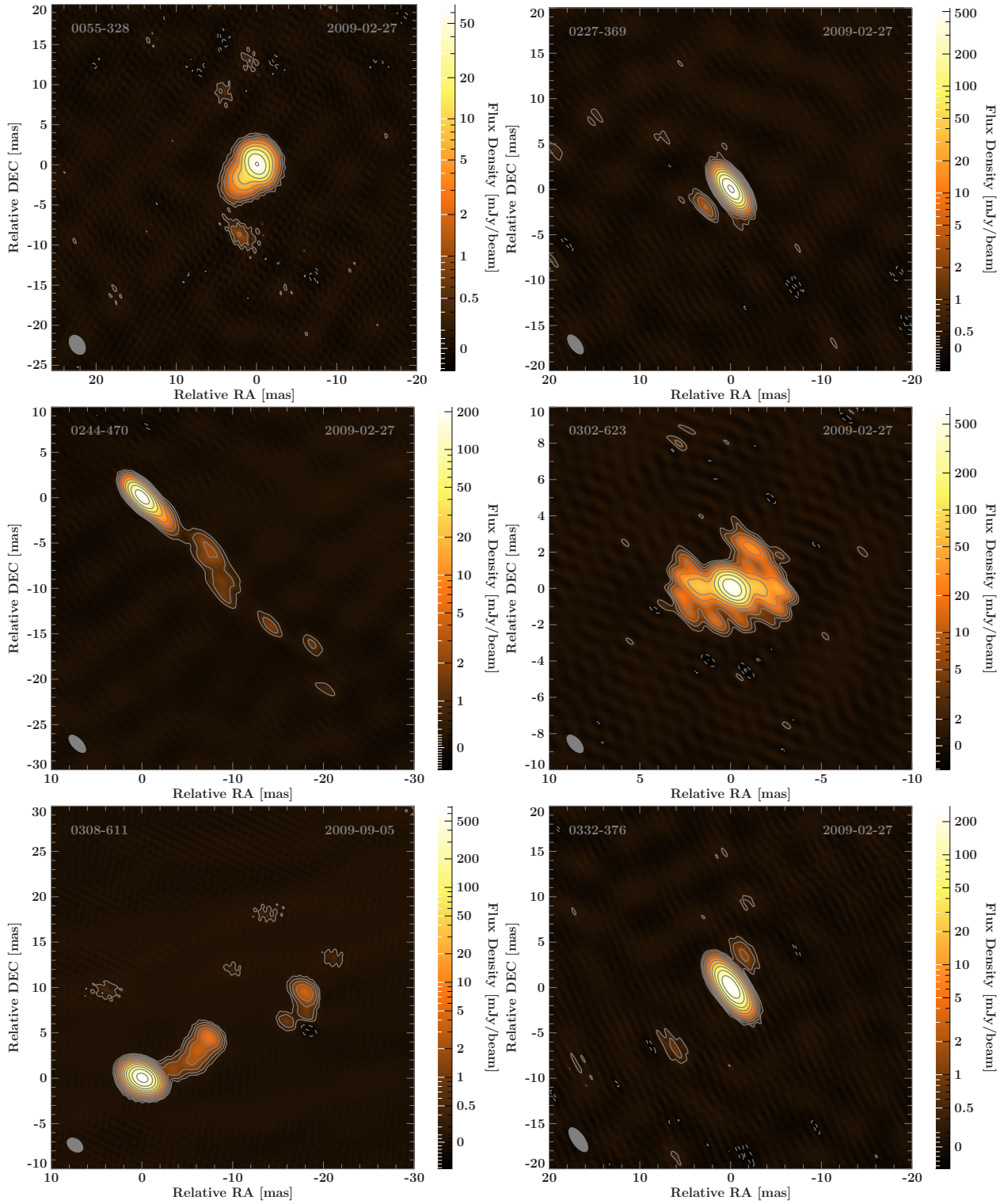

Figure 5.3.: First epoch `clean` images of additional TANAMI sources. The contours indicate the flux density level, scaled logarithmically and separated by a factor of 2, with the lowest level set to the 3σ-noise level (for more details see Table 5.1). The size of the synthesized beam for each observation is shown as gray ellipse in the lower left corner of each image. The color scale is scaled logarithmically indicating the flux density level in mJy.

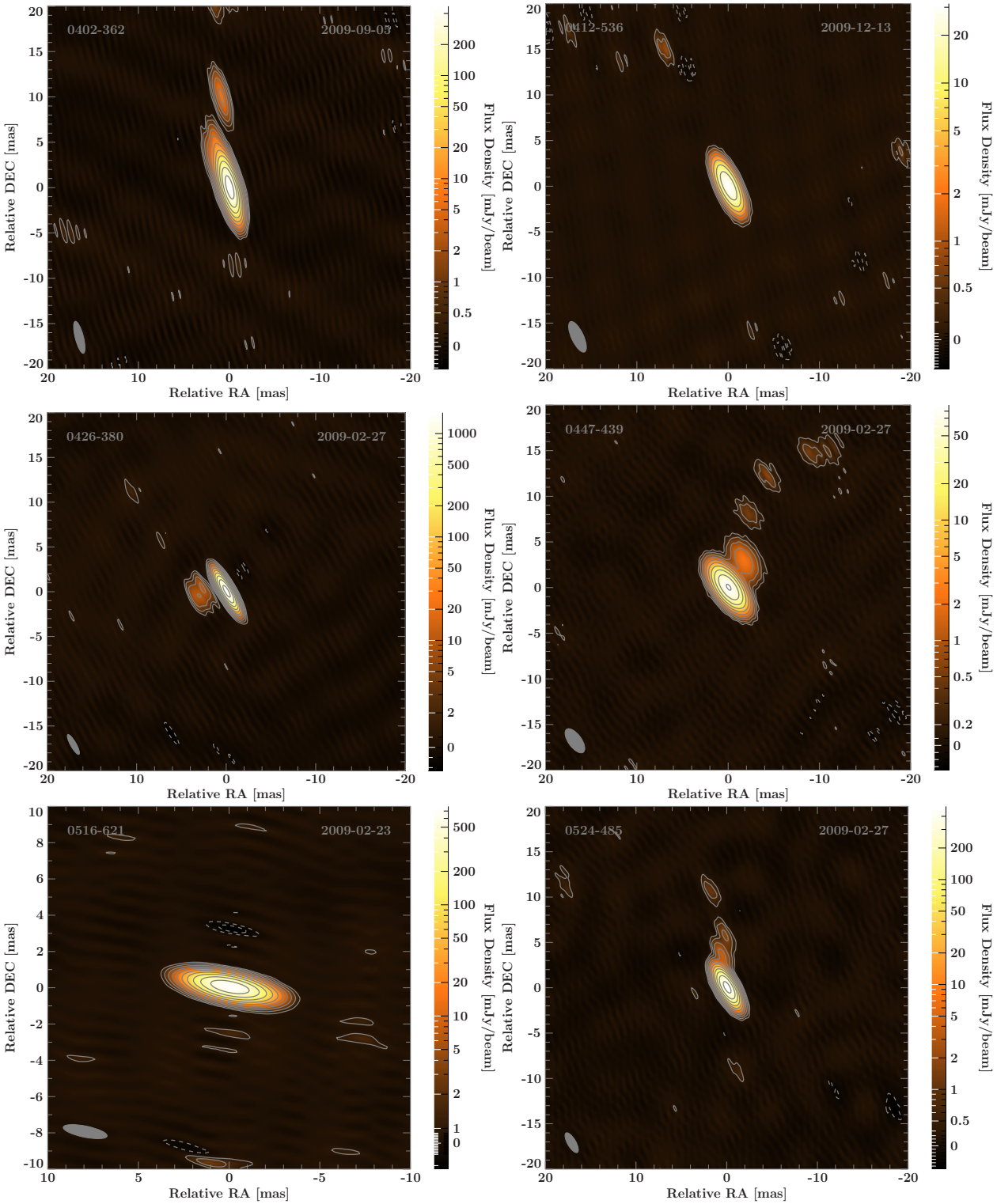

Figure 5.4.: First epoch `clean` images of additional TANAMI sources – Fig 5.3 continued.

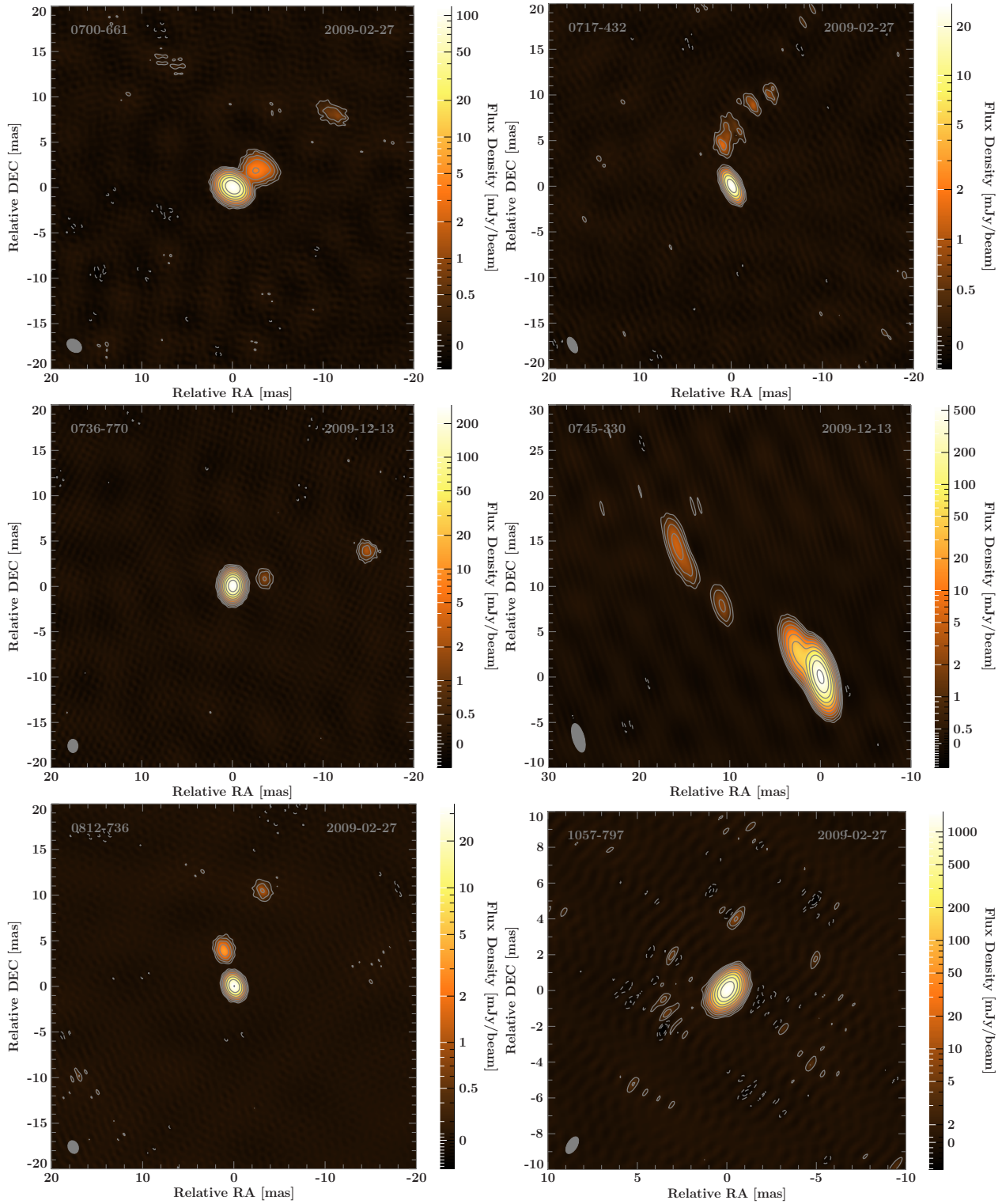

Figure 5.5.: First epoch `clean` images of additional TANAMI sources – Fig. 5.3 continued.

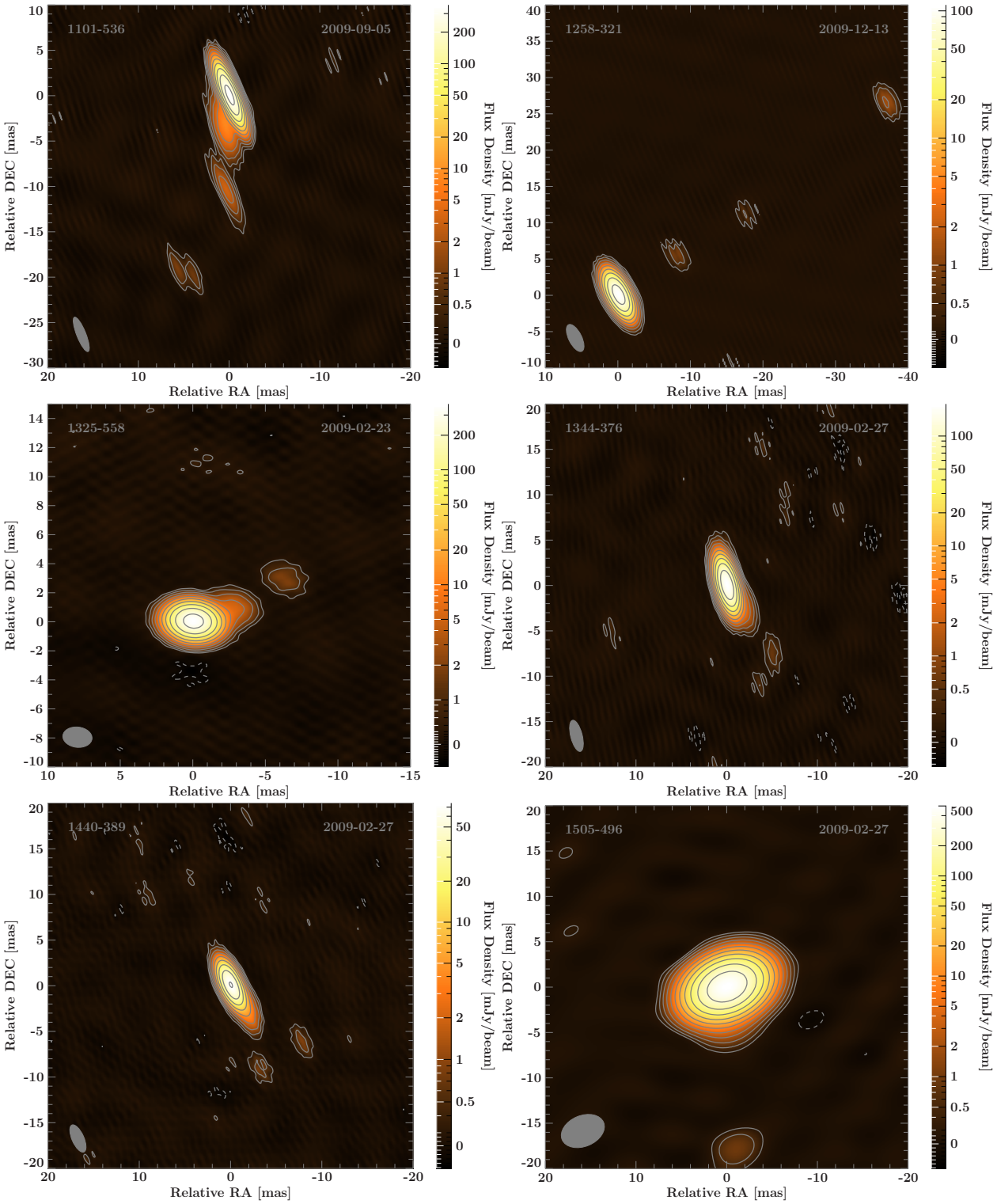

Figure 5.6.: First epoch `clean` images of additional TANAMI sources – Fig. 5.3 continued.

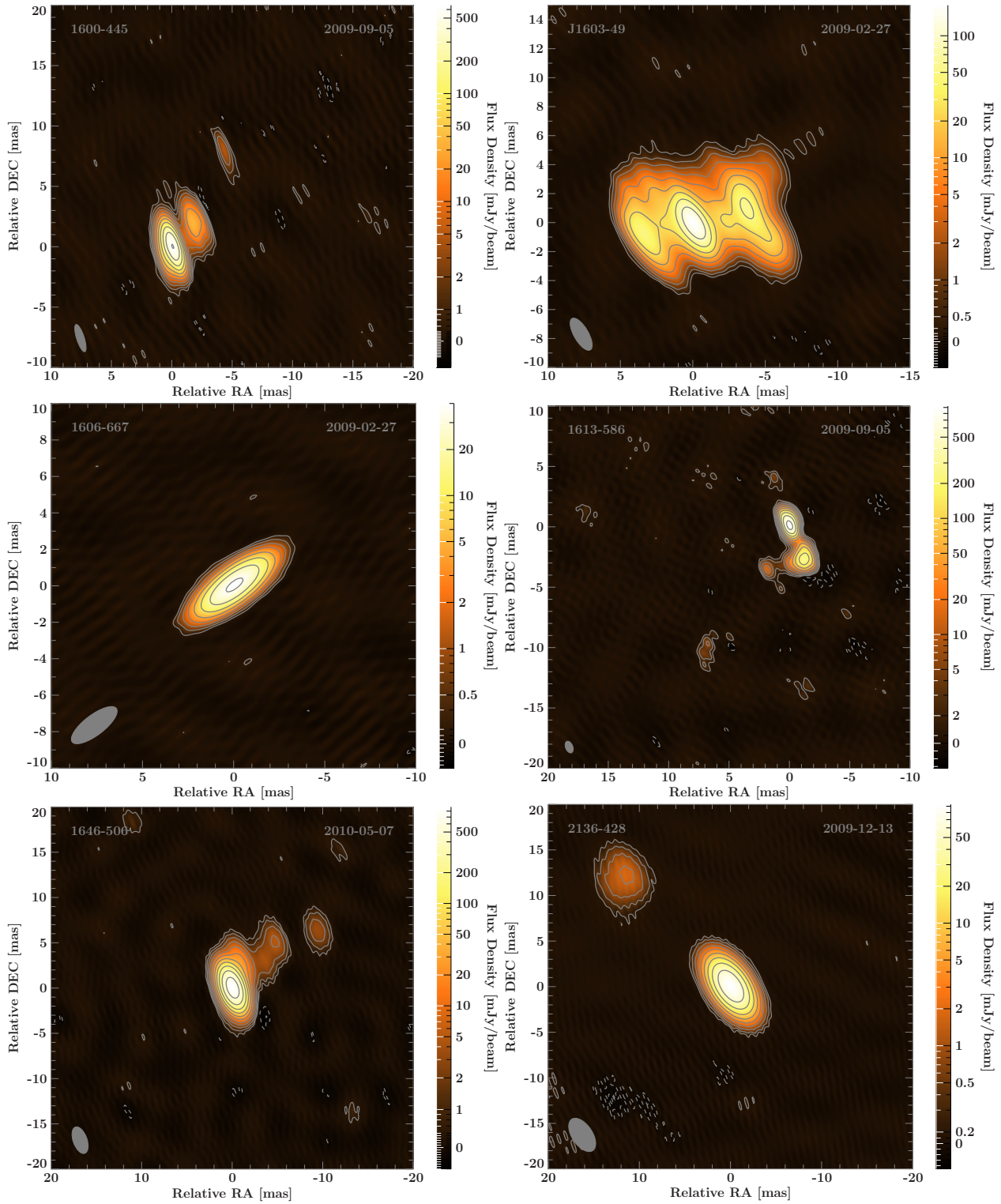

Figure 5.7.: First epoch `clean` images of additional TANAMI sources – Fig. 5.3 continued.

5.2. Milliarcsecond-scale properties

In this section, I examine the mas-scale properties of the TANAMI sample (of the 75-sources, Table 5.1) with respect to their γ-ray loudness (Böck et al., 2014). This study follows the discussion of the initial sample (Ojha et al., 2010), trying to extract distinguishing features in the mas-scale properties which could shed light on the possible dichotomy of γ-ray faint and loud jets. As described above, the following investigations are based on the TANAMI observations (quasi-)simultaneous to the first year of *Fermi* monitoring. The corresponding ratios of the γ-ray to radio core flux density at 8.4 GHz ($r = S_{1-100\,\mathrm{GeV}}/S_{8.4\,\mathrm{GHz,core}}$) are used as a key differentiator as it clearly displays the setup of the hybrid sample (see Fig. 5.1).

5.2.1. Redshift distribution

The redshift distribution of the initial TANAMI sample (Ojha et al., 2010) showed no significant difference for the radio-selected and the γ-ray-selected subsamples comparable to the z-distribution of LAT Bright AGN sample (LBAS; Abdo et al., 2009) further indicating a strong connection between bright radio and gamma-ray emission. However, the comparison of the *Fermi*/LAT-detected AGN in the TANAMI sample with that of all *Fermi*/LAT-detected AGN given in 2LAC (Ackermann et al., 2011) indicates slight differences caused by the radio flux-limited sample selection for the TANAMI sample: the fraction of quasars is larger in the TANAMI sample. There is no obvious difference between the z-distribution of quasars in TANAMI and 2LAC, while the flux-limited selection criteria of TANAMI seems to select less distant BL Lac objects (see Fig. 5.8 and Böck et al., 2014).

Figure 5.8 shows the redshift distribution of all 75 TANAMI sources. The quasars span a wide range up to $z \sim 2.86$ (γ-ray faint source 0438−436), while both, the BL Lac objects and the radio galaxies are found at low redshifts. Comparing the distributions of the γ-ray faintest with the ones of the brightest sources, a Kolmogorov-Smirnov-Test (KS-test) gives a probability of 23% that they are taken from the same parent population. It is clear that the large fraction of less beamed sources (i.e., radio galaxies) make up this difference. Note that for the unclassified objects no redshift is known, missing in this figure. The radio galaxies are all found at low redshift and only in the γ-ray faint and low subsamples. In contrast, the BL Lacs are also found at small z-values, but belong only to the γ-ray brighter subsamples. Quasars, in particular γ-ray faint ones, are spread over the whole redshift range.

5.2.2. Flux and brightness temperature distribution

The total flux density is derived from the `clean` images (Fig. 5.3 to 5.7). The core flux densities are obtained by fitting an elliptical Gaussian model components to the core components following the approach described in Ojha et al. (2010).

The total flux density distribution (Fig. 5.1) shows lower radio flux densities for the γ-ray loud sources than for the ones of the radio subsample. A KS-Test of the γ-ray faintest (undetected, $r < 10^{-10}\,\mathrm{cm^{-2}\,s^{-1}\,Jy^{-1}}$) and the brightest ($r > 10^{-8}\,\mathrm{cm^{-2}\,s^{-1}\,Jy^{-1}}$) gives a probability of 9% that both distributions are drawn from the same parent distribution. However, note that this test is biased by the sample definition criteria. The core flux density distribution of the γ-ray loud sources (Fig. 5.9) does not differ much from the S_{total}-distribution, indicating that most ($\geq$ 80%) of the emission is not coming from the extended structure but from the unresolved sub-mas scales, though most of the sources show clearly a resolved (not compact) mas-scale structure. A KS-test for the

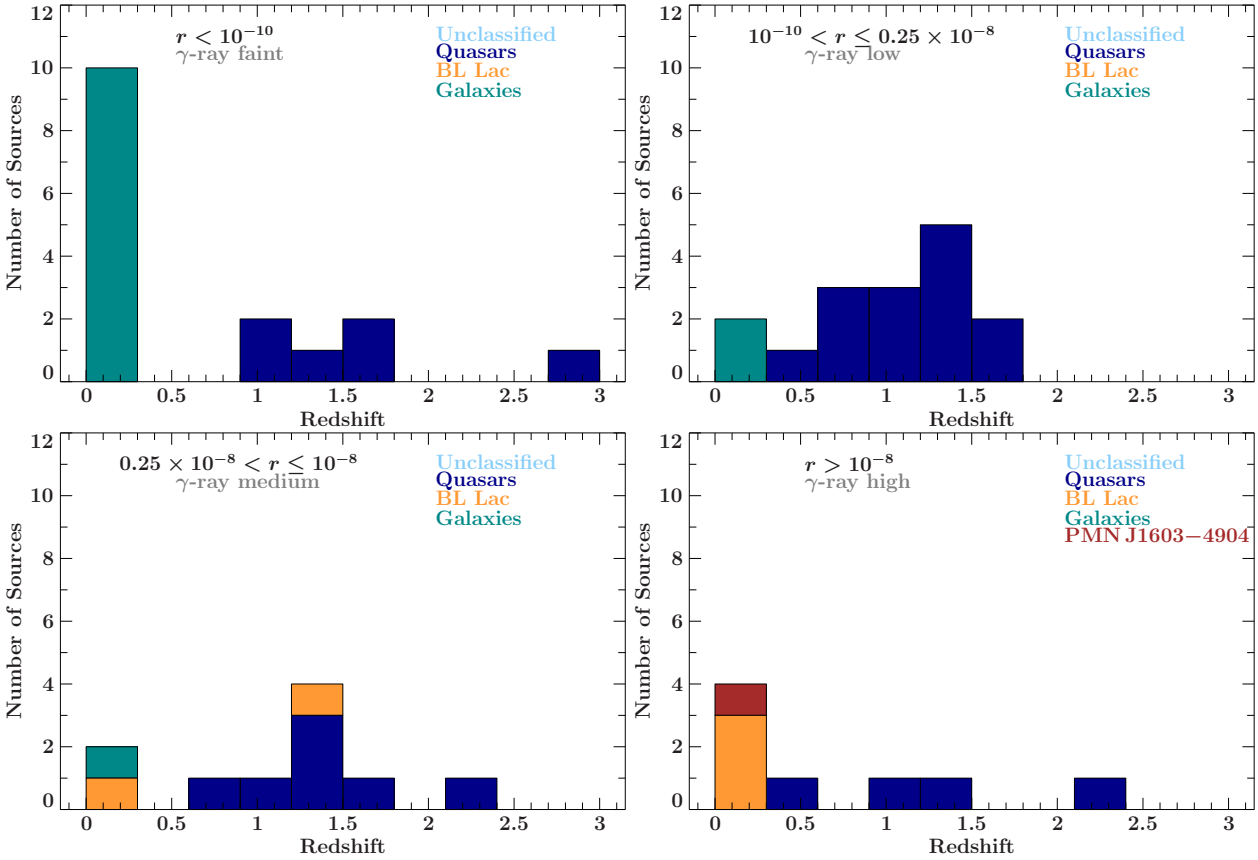

Figure 5.8.: Redshift distribution of all TANAMI sources divided in γ-ray faint to loud subsamples . *From upper left to bottom right:* z-distribution of γ-ray faint sources, with low, medium and high γ-ray to 8.4 GHz flux density ratios (r in units of $\mathrm{cm^{-2}\,s^{-1}\,Jy^{-1}}$). Note that for most of the newly added (γ-ray loud) sources no redshift is known (see Table 5.1).

flux-ratio distributions (see Fig. 5.10) of the γ-ray brightest to faintest[3] (as well as of all γ-ray loud sources to the faint ones) indicates that both samples belong to the same distribution. This result, supported by the result of the evaluation of the morphology distribution (see below), shows that the γ-ray loud sources tend to be more compact and are more core dominated.

The difference in total radio flux, i.e., the lower 8.4 GHz flux for the brightest γ-ray sources in comparison with the fainter ones, is consistent with a shift in synchrotron peak frequency in the SED (assuming a similar luminosity): for high peaked sources the radio flux tends to be lower while being bright in γ-rays and vice versa (compare also corresponding γ-ray properties in Böck et al., 2014).

The brightness temperature for the radio core at 8.4 GHz of each source was determined using

$$T_\mathrm{B} = \frac{2\ln 2}{\pi k_\mathrm{B}} \frac{S_\mathrm{core}\lambda^2(1+z)}{\theta_\mathrm{maj}\theta_\mathrm{min}} \quad , \tag{5.1}$$

where S_core,θ_maj and θ_min are the flux, the semi-major, and semi-minor axis of a two dimensional Gaussian model component for the core in the radio image, k_B is the Boltzmann constant, z the redshift of the source, and λ the observing frequency. If the size of the fitted model component for the core emission falls below the resolution limit, we calculated lower limits for T_B following

[3]Note that these both subsamples are of similar size.

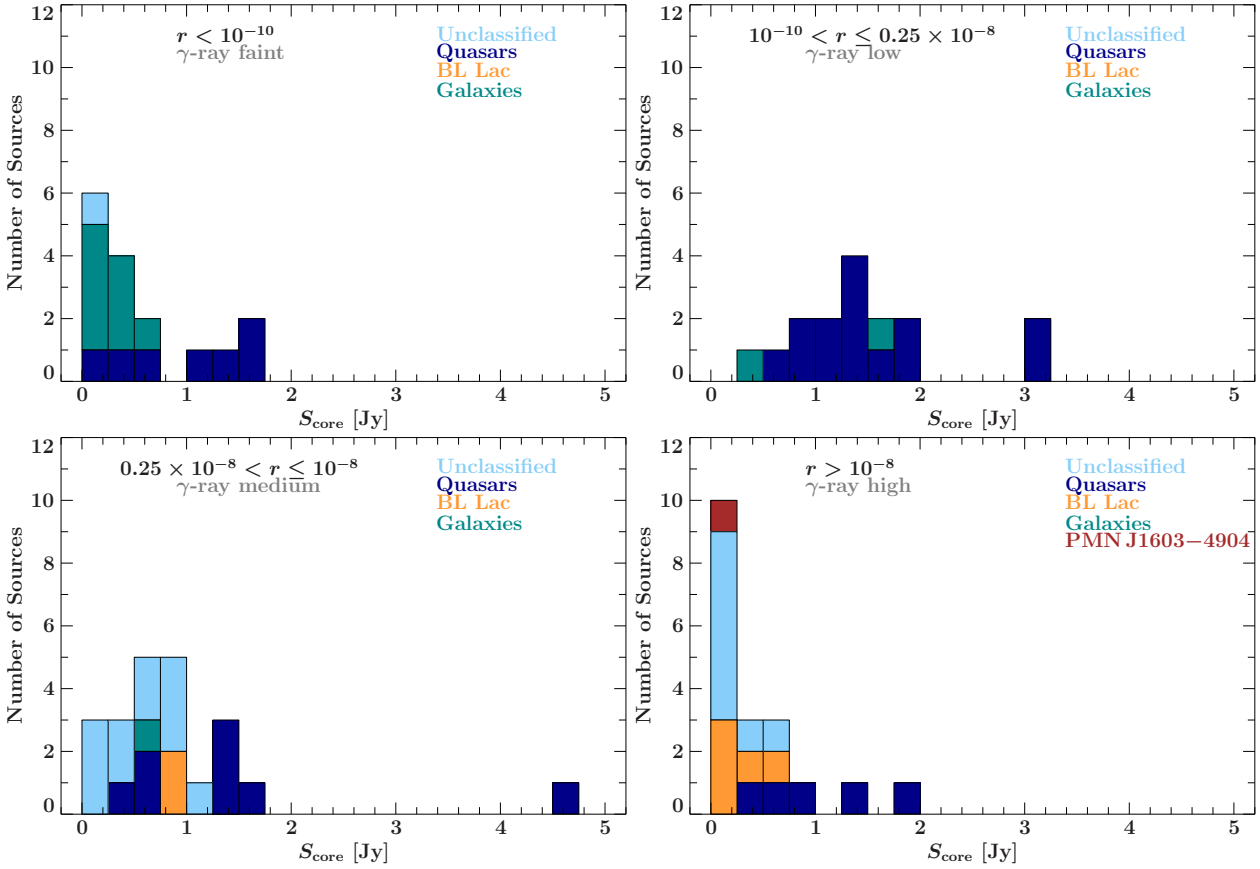

Figure 5.9.: Core flux density distribution (r in units of $\mathrm{cm^{-2}\,s^{-1}\,Jy^{-1}}$).

Kovalev et al. (2005). The sources for which only a lower limit on $T_{\rm B}$ can be given are 0412−536, 0527−359, 0717−432, 0812−736, 1606−667, and PKS 2136−428. Furthermore, for the two compact symmetric objects in the sample (1718−649 and 1934−638) no significant core emission could be detected. The $T_{\rm B}$-distribution is shown in Fig. 3.5. Since for 36% of all sources no redshift measurement is available, the uncorrected values are discussed. Taking the $(1+z)$ factor into account, the distribution would be shifted towards higher values, peaking at $\sim 0.5 \times 10^{12}$ K, which is consistent with the overall brightness temperatures found for the total TANAMI sample (see Fig.5.11, Ojha et al., 2010; Böck et al., 2014). The segmented $T_{\rm B}$-distributions indicate that γ-ray brighter sources have higher brightness temperatures (see also Böck et al., 2014).

5.2.3. Morphologies at mas-scale

The morphology classification scheme is adopted from Kellermann et al. (1998) as used by Ojha et al. (2010): barely resolved sources are classified as compact (C), those with a core-jet like structure, i.e., with the most compact feature at either end of the source structure as single-sided (SS), those with the most compact component in the middle as double-sided (DS)[4], and an irregular two-dimensional structure is defined as IRR.

[4]Note that this morphology scheme takes no spectral information into account. As an example, the extensively discussed source PMN J1603−4904 (see Ch. 6) shows a symmetric brightness distribution on mas scales with the most compact component in the center. According to Kellermann et al. (1998) this source can here be classified as double-sided, but this morphology classification does not compare to a jet-counterjet system (see Kellermann et al., 1998, for more details).

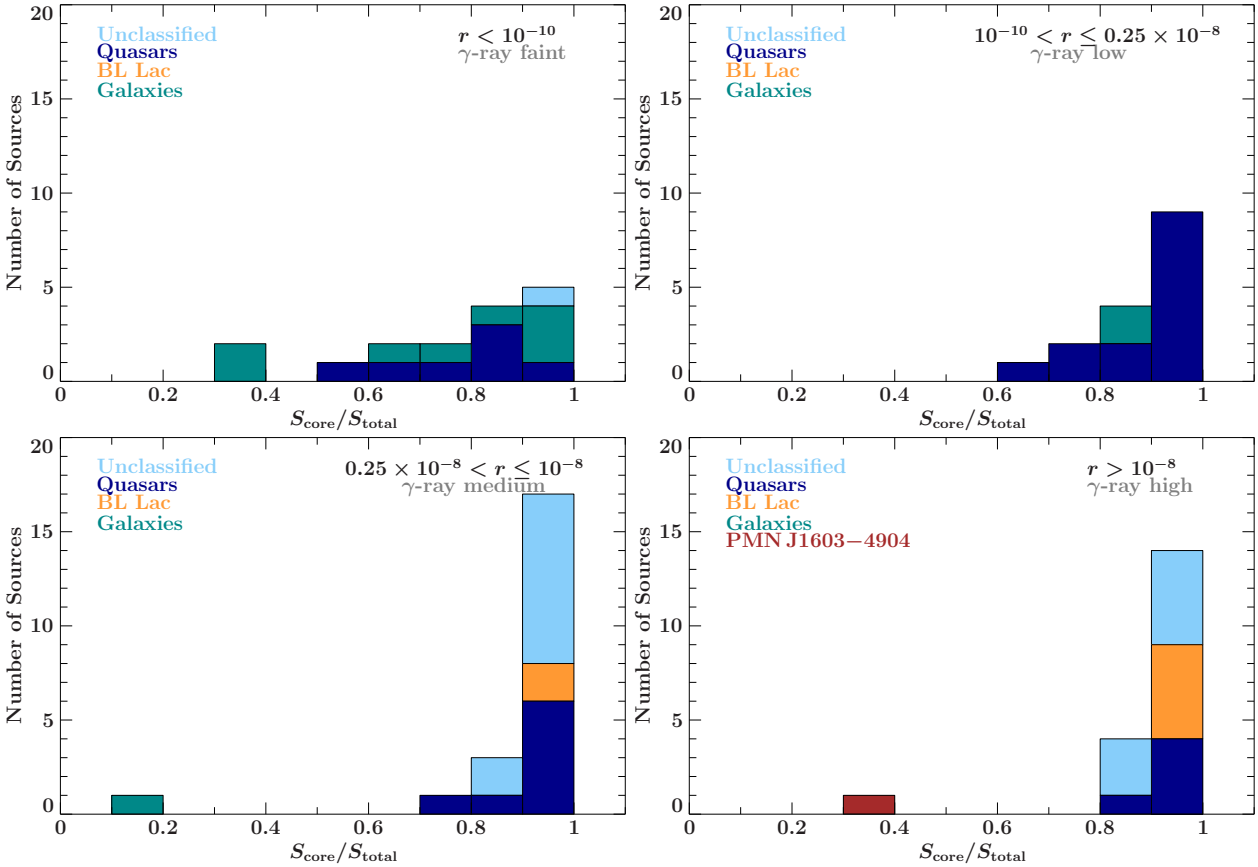

Figure 5.10.: Distribution of the flux density ratio or core dominance $\kappa = S_{\mathrm{core}}/S_{\mathrm{total}}$ (r in units of $\mathrm{cm}^{-2}\,\mathrm{s}^{-1}\,\mathrm{Jy}^{-1}$).

67 out of 75 objects are found to be resolved, while only 8 are classified as compact. Only two of the γ-ray bright sources are classified as double-sided: Centaurus A and PKS 1600−489 (PMN J1603−4904). The γ-ray detection of Centaurus A has been extensively discussed (Abdo et al., 2010e,d), resulting in general acceptance that its brightness at high energies is mostly due to its proximity. For PMN J1603−4904, however, the situation is not yet that clear (see Sect. 6.4), bringing up the question whether the underlying physical processes are the same as in blazars. Both sources are discussed in detail in Chapters 6 and 7, respectively.

The core dominance, defined as the ratio of the core to the total flux density $\kappa = S_{\mathrm{core}}/S_{\mathrm{total}}$ (see Fig. 5.10) gives generally a measure of the compactness of the source. The comparison of total flux densities of jet sources measured by single-dish observations and with VLBA (Kovalev et al., 2005) shows that compactness on arcsecond scales is $\geq 90\%$, i.e., most of the flux density is contained within (sub-)mas scales. This compactness-measure can be taken as an indicator for Doppler boosting and hence the inclination angle of the jet. Kovalev et al. (2005) further showed that the VLBI core dominance (i.e., the ratio of the core to the total flux density on VLBI scales) of galaxies is the least, while the quasars and BL Lacs are far more compact on (sub-)mas-scales, consistent with the unified model that the blazars are seen at smaller inclination angles.

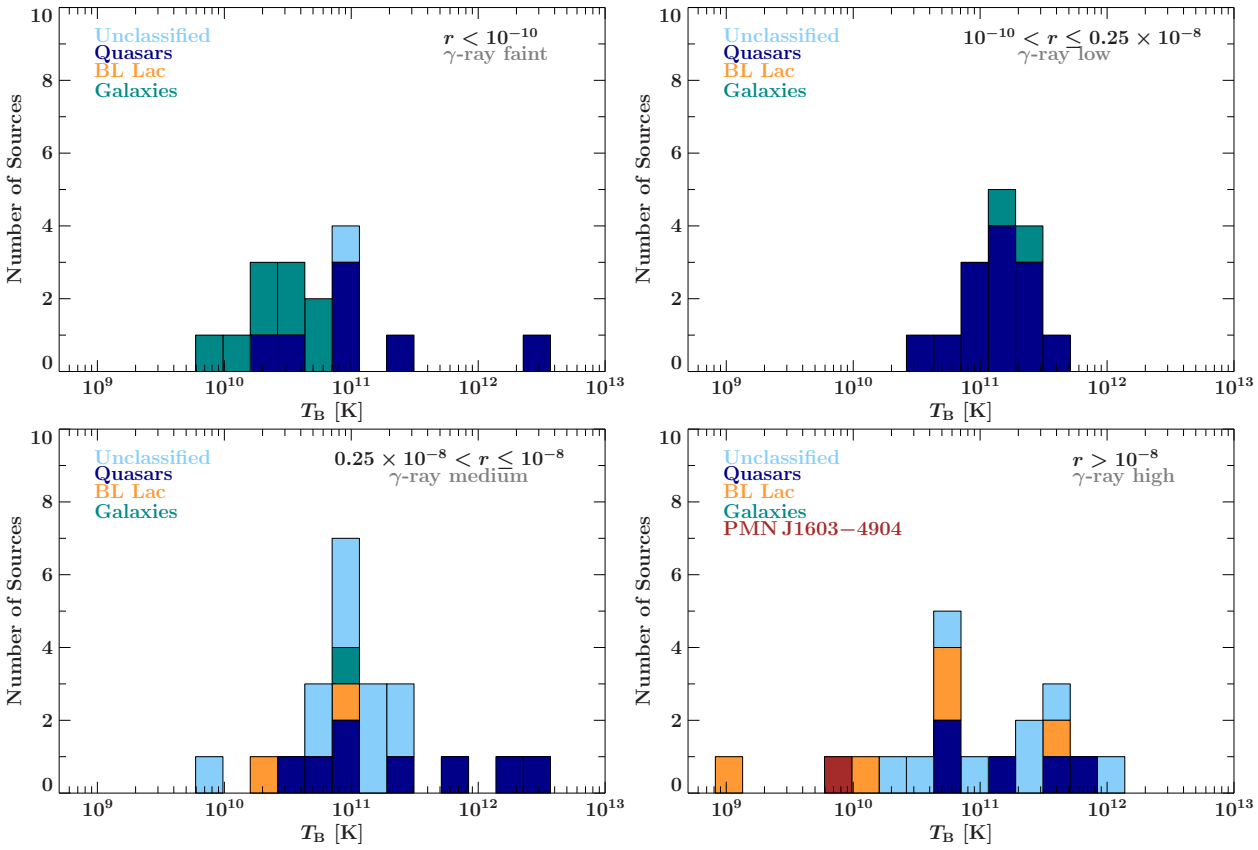

Figure 5.11.: Brightness temperature distribution, including lower limits (r in units of $\mathrm{cm^{-2}\,s^{-1}\,Jy^{-1}}$). Note that due to the lack of redshift information for 36% of all sources (see Fig. 5.8), the T_B values in both plots are not corrected for z (see Eq. 5.1).

For the following morphology study of TANAMI sources, S_{total} gives the total flux density contained in the VLBI image. Using the respective κ-value of every source, the morphology scheme for the single-sided sources can be expanded. Three sub-categories are defined as follows: $\kappa \leq 0.8$ for the single-sided sources with the most significant jet contribution, $0.8 \leq \kappa < 0.9$ for the intermediate, and $\kappa > 0.9$ for the most compact sources (see Fig. 5.12).

It can be clearly seen that the γ-ray loud objects are generally more core dominated than the faint objects. This result is consistent with the picture that γ-ray loud blazars are pointing closer to the line of sight (Ojha et al., 2010). Furthermore, all unclassified objects of the sample are potential blazars, most probably BL Lac-type objects, since all of them show a high core dominance. The high κ of BL Lacs is most likely correlated with the γ-ray loudness. The distribution of the quasars, however, is obviously much broader, also ranging to κ-values comparable to radio galaxies. There potentially exists a dichotomy of γ-ray faint and loud quasars, with a trend that more compact objects tend to be brighter in γ-ray, though the broad distribution suspects further distinctive parameters.

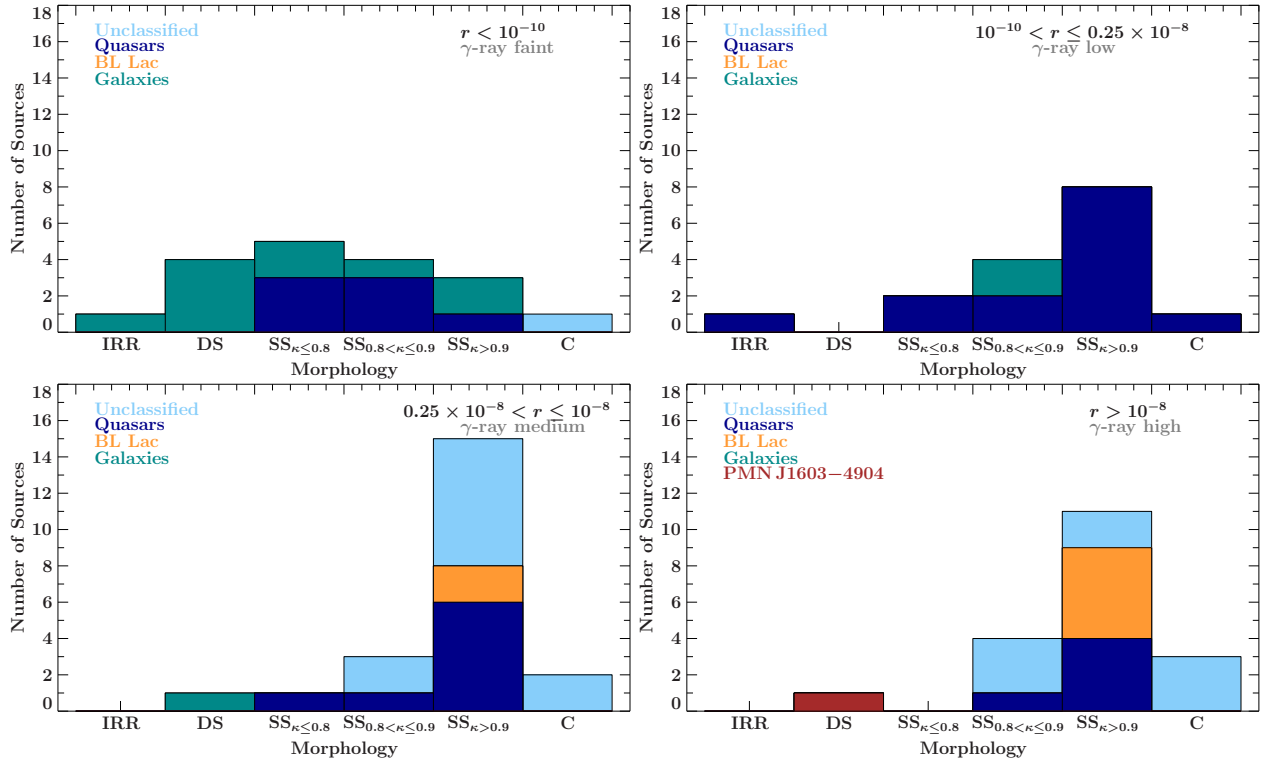

Figure 5.12.: Distribution of the 8.4 GHz morphologies, subdividing the single-sided sources depending on the core dominance $\kappa = S_{\text{core}}/S_{\text{total}}$ at 8.4 GHz to divide the single-sided sources into sub-categories. Flux density ratio r given in units of $\text{cm}^{-2}\,\text{s}^{-1}\,\text{Jy}^{-1}$.

5.3. Discussion

Confirming the findings by other authors for similar source samples (e.g., Kovalev et al., 2009; Böck et al., 2014), the γ-ray bright TANAMI sources have higher brightness temperatures and are more compact than the γ-ray faint ones, indicating higher Doppler beaming factors.

The fraction of unclassified sources in the sample shows strikingly similar mas-scale properties as the BL Lac type objects, suggesting that they also belong to this class. BL Lacs show a correlation of low radio flux densities with higher γ-ray fluxes. The correlation of higher brightness temperatures and compact morphologies with γ-ray loudness, can be well explained by a shift in synchrotron and self-Compton peak frequencies in the SED as known as the blazar sequence (Fossati et al., 1998; Lister et al., 2011; Böck et al., 2014).

Interestingly, the quasars in our sample show no such simple trend. The brightness temperatures are broadly distributed. Similar, the core dominance of the single-sided objects indicate a broad distribution in morphology. The TANAMI sample includes also less core dominanted ($\kappa < 0.8$) radio-bright quasars which seem to be γ-ray fainter. In contrast to the BL Lac objects, whose broadband spectra can generally be modeled with single-zone SSC models (e.g., Tavecchio et al., 1998; Cerruti et al., 2013), FSRQs require models involving external radiation fields to explain their broadband SEDs (e.g., Dermer et al., 2009). Hence, the complexity and diversity of their SEDs and morphologies can be taken as indications for the existence of different sub-types, including intrinsically γ-ray faint, but radio-loud quasars.

In summary, the full set of mas-scale data of the TANAMI sources, (quasi-)simultaneous to the 1FGL data allow to study the possible dichotomy of γ-ray bright and faint jets. It has been

well established that the γ-ray brightness is related to higher beaming factors and is confirmed by this work. The high-angular resolution observations are a unique tool to look for morphological differences between these source types. Further investigations and correlation studies are required, in order to check for further indications which might explain the γ-ray faintness of some sources. This work is in preparation and will be published elsewhere.

5.4. Notes on individual sources

For most of the newly detected extragalactic γ-ray sources in the Southern Hemisphere not much was known of the mas-scale properties before including them in the TANAMI monitoring list. In the following, brief information on individual, striking sources is given.

PKS 0227–369: This highly flaring γ-ray quasar (Abdo et al., 2010; Nolan et al., 2012) has an redshift of $z = 2.1150$ and was therefore included in a study by Ghisellini et al. (2011) on high-redshift *Fermi* blazars. The TANAMI image shows a well collimated jet to the south-west. The variability analysis (see Ch. 4) selects it as one of the short-flare candidates.

PKS 0302–623: This quasar at $z = 1.351$ was imaged with space VLBI in the VSOP 5 GHz AGN survey by Dodson et al. (2008). TANAMI images (see also Krauß et al., 2014) reveal a very irregular, extended structure. Its position is coincident with one of the two PeV neutrino events (Halzen & Klein, 2010).

PKS 0402–362: The source is included in the *Fermi* Monitored Source List, being one of the brightest quasars ($z = 1.417$) with a high activity in the sky.

PKS 0447–439: This blazar was discovered at TeV energies by H.E.S.S. (H.E.S.S. Collaboration et al., 2013b). It is a highly variable and bright γ-ray source (see Ch. 4). The TANAMI monitoring detects a faint jet structure to the north-west.

PKS 1258-321, ESO 443–G 024: This galaxy has a very extended emission to the north-west in the TANAMI images. It shows a clear FR I morphology in VLA images and may have extended halo emission in the X-rays (Marshall et al., 2005). It was included in the LBAS 3-months catalog (Abdo et al., 2009), but further *Fermi* monitoring did not yield significant detection (Abdo et al., 2010; Nolan et al., 2012; Böck et al., 2014).

PKS 1600−489, PMN 1603−4904: TANAMI observations provide the first VLBI image of this source, revealing a symmetric morphology with the most compact component in the center. It is one of the brightest γ-ray sources detected by *Fermi*/LAT (Abdo et al., 2010; Nolan et al., 2012). Its broadband properties point to a very unusual object, questioning its blazar classification (Shaw et al., 2013). In the following Chapter 6, this peculiar source is discussed in detail.

It is difficult to say what is impossible, for the dream of yesterday is the hope of today and the reality of tomorrow.

(Robert H. Goddard)

6. The unusual multiwavelength properties of PMN J1603−4904

Not much was known about the radio-loud object PMN J1603−4904 close to the Galactic plane before its detection in γ-rays attracted attention (Abdo et al., 2009; Kovalev, 2009). It had been "just" one of the bright radio sources in the southern sky, also known as PKS 1600−48, an ATCA calibrator source, for which no redshift information was available and no exiting variability was observed. However, it is one of the brightest γ-ray sources detected in the first two years of operation of *Fermi*/LAT (Abdo et al., 2010; Nolan et al., 2012). Böck (2012) already pointed out that as a γ-ray source PMN J1603−4904 is striking due to its high brightness, a very hard γ-ray spectrum and the low variability. The high-confidence association of the known radio source PMN J1603−4904 with γ-ray detection 1FGL J1603.8−4903 (see Fig. 6.1, Abdo et al., 2010) made it to an ideal candidate for the extended TANAMI sample of "additional sources" (see Ch. 5). It has previously been classified as a low-peaked BL Lac object based on its broadband emission and the absence of optical emission lines, but optical measurements suffer strongly from extinction (Shaw et al., 2013). A large majority of *Fermi*/LAT detected sources turned out to be of the blazar class (flat spectrum quasars or BL Lacs, Abdo et al., 2010b; Ackermann et al., 2011), so there were reasons to not suspect this original classification until the high resolution observations with TANAMI revealed a very atypical (for a blazar) mas-scale structure and lead to the (serendipitous) discovery of further unusual multiwavelength properties (Müller et al., 2014a). These broadband data require to reconsider the current classification and open room for a possible, alternative classification as a young, γ-ray bright radio galaxy. The TANAMI 8.4 GHz images

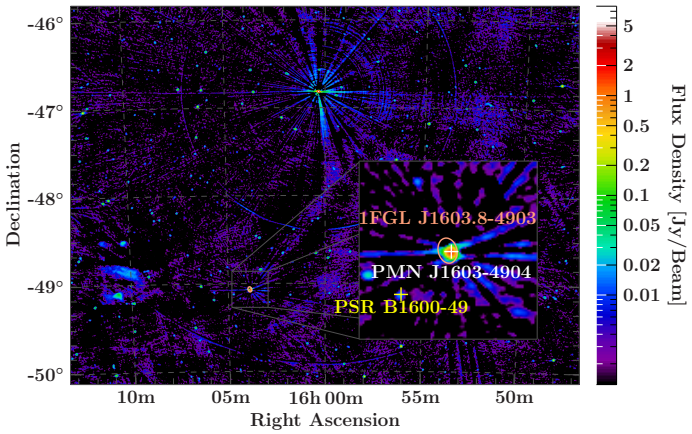

Figure 6.1: The radio image at 843 MHz from the Sydney University Molonglo Sky Survey (Mauch et al., 2003, SUMSS) shows clearly that no other (known) bright radio source is close enough to challenge the association (by positional coincidence) of PMN J1603−4904 with the γ-ray source 1FGL J1603.8−4903 (the only γ-ray source in this field). Shown is the 95% *Fermi*/LAT confidence ellipse (with a semi major axis of 0.°0296, Abdo et al., 2010), the position of the radio source PMN J1603−4904, and the close pulsar PSR B1600−49 with a distance of 0.°13. (Image adapted from Böck, 2012)

show that PMN J1603−4904 has a symmetric brightness distribution on milliarcsecond scales. The brightest, and most compact, component lies in the center of the emission region, so that its morphology is reminiscent of a Compact Symmetric Object (CSO) – objects thought to be the younger versions of evolved radio galaxies (see Sect. 6.4.3). Furthermore, infrared data show a clear excess in the spectral energy distribution (SED), which is usually not present in blazar SEDs and can be interpreted as enhanced starburst activity.

In this Chapter, I will present new and archival multiwavelength data of PMN J1603−4904 and will discuss in detail different plausible classification scenarios in order to explain the nature of this unusual γ-ray source. This Chapter is based on the related refereed publication in 'Astronomy and Astrophysics' (Müller et al., 2014a), such that some of the following sections are strongly based on this paper and large parts (including figures) are taken verbatim from there[1]. I also present more recent high sensitivity X-ray observations, which have been proposed by myself within the framework of the reported multiwavelength analysis to further constrain the SED of PMN J1603−4904 (Müller et al., in prep.). They reveal a narrow iron line which allows a first redshift measurement of this source (see Sect. 6.2.4).

6.1. Context

The TANAMI monitoring of newly detected γ-ray loud extragalactic jets (see Ch. 5) yielded the first observation at milliarcsecond scale resolution of the radio morphology of PMN J1603−4904. The resulting images are combined with multiwavelength data in the radio, IR, optical/UV, X-ray, and γ-ray regimes (see Sect. 6.2). These multiwavelength investigations revealed properties which are very atypical for a BL Lac object – as such this source was originally classified. To further constrain its broadband emission, *XMM-Newton* and *Suzaku* observations were performed in 2013 September (see Sect. 6.2.4).

Among the *Fermi*/LAT extragalactic γ-ray sources (Nolan et al., 2012), blazars are the largest class of detected objects. Misaligned objects (jets seen side-on where the relativistic beaming effects are small, see Sect. 1.3.3 and Abdo et al., 2010g), are rarely detected in γ-rays. In the radio regime, one sub-class of these misaligned objects consists of young radio galaxies, also referred to as Compact Symmetric Objects (CSO; O'Dea, 1998; Readhead et al., 1996). Theoretical models have predicted γ-ray emission from CSOs (Stawarz et al., 2008; Kino et al., 2007, 2009; Kino & Asano, 2011), but until now they are not confirmed as γ-ray loud yet. These models expect γ-ray variability time scales substantially longer than that typically observed from blazars (Abdo et al., 2010a).

Due to low signal-to-noise measurements in the optical, no significant detection of line emission was possible, hence, the radio source PMN J1603−4904 (Griffith et al., 1994) has been classified as a low synchrotron peaked (LSP) BL Lac object (Nolan et al., 2012; Shaw et al., 2013). Furthermore, as it is located close to the Galactic plane ($l = 332.^\circ15$, $b = 2.^\circ57$), no redshift measurement has been reported prior to this work (see Sect. 6.2.4).

It is associated with a bright, hard-spectrum γ-ray source detected by *Fermi*/LAT and called 0FGL J1604.0−4904, 1FGL J1603.8−4903, 2FGL J1603.8−4904, and 1FHL J1603.7−4903 in the respective γ-ray catalogs (Abdo et al., 2009, 2010; Nolan et al., 2012; Ackermann et al., 2011; Ackermann et al., 2013). The radio source lies well within the *Fermi*/LAT 95 %-error radius of only $0.^\circ023$ (see Fig. 6.1, Nolan et al., 2012). Since no known radio is found in the vicinity of the γ-ray region, this is a very high confidence association (Böck, 2012). It is among the 30 brightest objects in

[1] Note that 'Astronomy and Astrophysics' holds the copyright for the content.

the 2LAC-catalog (Ackermann et al., 2011); one out of only two sources classified as non-variable[2] with a flux of $F_{1-100\,\mathrm{GeV}} = 1.29\times10^{-8}\,\mathrm{ph\,cm^{-2}\,s^{-1}}$ over the first two years of *Fermi*/LAT observations. At higher γ-ray energies, PMN J1603−4904 shows a hard spectral index of $\Gamma_{10-500\,\mathrm{GeV}} = 1.96\pm0.14$ and a high flux above 50 GeV of $S_{>50\,\mathrm{GeV}} = (19\pm5)\times10^{-11}\,\mathrm{ph\,cm^{-2}\,s^{-1}}$ (Ackermann et al., 2013). The Bayesian block analysis (Scargle et al., 2013) in this catalog of the 10 GeV to 500 GeV emission over three years of *Fermi*/LAT monitoring shows evidence for mild variability on longer timescales but no flaring on timescales of days to weeks (Ackermann et al., 2013; Nolan et al., 2012).

The radio source PMN J1603−4904 was observed in several large surveys (Griffith & Wright, 1993; Gregory et al., 1994; Massardi et al., 2011), but no high resolution VLBI observations have been reported before it was included in the TANAMI sample.

6.2. Multiwavelength observations

In this section, the TANAMI VLBI observations (Sect. 6.2.1) of PMN J1603−4904, the analysis of additional radio to X-ray monitoring (Sect. 6.2.2 to 6.2.3) and more recent *XMM*-Newton and *Suzaku* observations (Sect. 6.2.4) are presented. Note that the analysis of the latter is a follow-up study and therefore, unlike the other analyses, not included in Müller et al. (2014a).

6.2.1. TANAMI VLBI observations

PMN J1603−4904 has been observed by TANAMI for five times between 2009 February and 2011 August at 8.4 GHz, including one simultaneous dual-frequency observation at 8.4 GHz and 22.3 GHz in 2010 May. The first three observations between 2009 February and 2010 May have been presented in Müller et al. (2014a). The details of the observations are given in Table 6.1. For further information on TANAMI observations and data analysis, see Chapter 3.

Because of the different number of telescopes in these TANAMI experiments, the (u,v)-coverage, array sensitivity, and angular resolution vary between the observing epochs (see also Sect. 3.1). The largest number of antennas for all observations was involved in the 8.4 GHz observation in 2009 February. Figure 6.2 shows the corresponding (u,v)-coverage.

[2] It was reported as non-variable based on a $\mathrm{TS_{var}} = 39.254$, where $\mathrm{TS_{var}} > 41.64$ indicates a $> 99\%$-chance of variability. The second non-variable source is 4C +55.17. This source has γ-ray properties similar to PMN J1603−4904. See McConville et al. (2011) for a discussion of the emission properties of 4C +55.17 in the context of a CSO model.

Table 6.1.: 8.4 and 22.3 GHz TANAMI VLBI observations of PMN J1603−4904 and image parameters

Date yyyy-mm-dd	Freq. [GHz]	Array Configuration[a]	S_{peak} [Jy beam^{-1}]	RMS [mJy beam^{-1}]	S_{total} [Jy]	b_{maj}[c] [mas]	b_{min}[c] [mas]	P.A.[c] [°]
2009-02-23/27[b]	8.4	PKS-CD-HO-MP-AT-DSS43-DSS34-TC-OH	0.18	0.13	0.59	2.51	0.98	30.1
2009-09-06	8.4	PKS-CD-HO-MP-DSS43-TC	0.17	0.23	0.57	3.36	1.15	19.2
2010-05-07	8.4	PKS-CD-HO-MP-AT-TC	0.17	0.16	0.57	2.91	1.12	14.9
2010-12-14	8.4	MP-HO-DSS43-DSS34-CD-AT	0.19	0.16	0.54	2.06	0.80	0.04
2011-08-14	8.4	YG-DSS43-TC-PKS-MP-KE-HO-CD-AT	0.21	0.17	0.63	2.54	1.55	22.6
2010-05-05	22.3	PKS-HO-MP-AT	0.14	0.35	0.29	2.09	1.16	83.9

Notes. [(a)] AT: Australia Telescope Compact Array (ATCA), CD: Ceduna, HO: Hobart, MP: Mopra, OH: GARS/O'Higgins, PKS: Parkes, TC: TIGO, DSS34 & 43: Tidbinbilla (34 m & 70 m), YG: Yarragadee, KE: Katherine [(b)] The two consecutive 2009 February experiments were combined, due to poorer (u,v)-sampling compared to the subsequent experiments at 8 GHz. [(c)] Major, minor axis and position angle of the restoring beam.

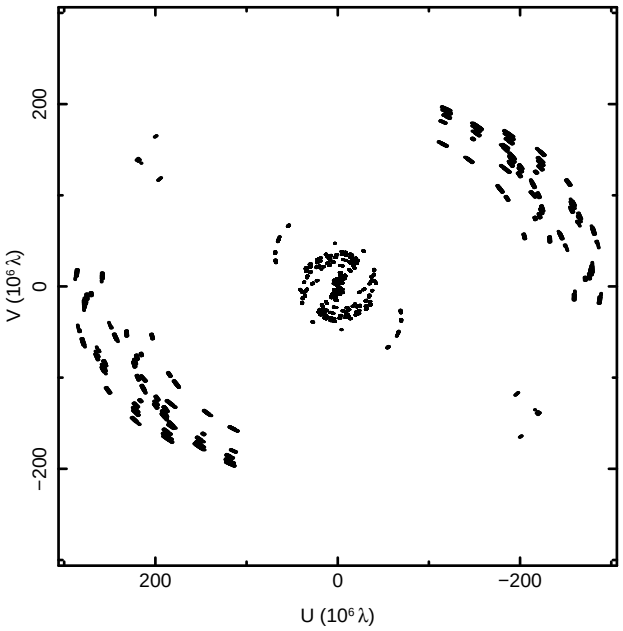

Figure 6.2: (u, v)-coverage at 8.4 GHz of the combined 2009 February TANAMI observations (see Table 6.1 for details). Figure from Müller et al. (2014a).

6.2.2. ATCA radio observations

The TANAMI sample (see also Ch. 5) is regularly monitored with the Australia Telescope Compact Array (ATCA). "Snapshot" observations as part of the C1730 monitoring project (Stevens et al., 2012) are made at 5.5, 9, 17, 19, 38 and 40 GHz. Each frequency is the center of a 2 GHz wide band. The flux densities are calibrated against the ATCA primary flux calibrator PKS 1934−638 and/or Uranus at 7 mm. The primary beam widths of the ATCA at the observed frequencies range from $10'$ at 5.5 GHz to $1'$ at 40 GHz. PMN J1603−4904 is not resolved in these measurements, independent of the exact array configuration of ATCA.

6.2.3. Optical and *Swift* observations

As mentioned above, the multiwavelength coverage (besides information in the radio band, though no VLBI) of PMN J1603−4904 has been not very extensive. Including the source in the TANAMI sample and the high confidence association with a γ-ray source, triggered first observations at higher frequencies.

In the optical, PMN J1603−4904 was observed with the Gemini South telescope using the Gemini Multi-Object Spectrograph (GMOS) on 2013 March 10. The observation was made in snapshot mode in the r' band (centered at $\lambda \sim 6250$Å). The main goal of this observations was to identify the optical counterpart of the radio source and to facilitate spectroscopic follow-up. The source was observed for 120 seconds, under $0\farcs6$ seeing and a limiting magnitude of about 25 mag was achieved. These observations confirmed the previous results by Shaw et al. (2013): a very faint optical counterpart with no significant line emission in the optical spectrum, hence, neither an optical classification nor a redshift measurement were possible.

With *Swift* (Gehrels et al., 2004) the source has been observed three times between 2009 May and 2010 July for a total exposure of 6.15 ks. At optical/ultraviolet wavelengths, observations with the *Swift* UV/Optical Telescope were made (UVOT, Roming et al., 2005, UVM2 and U filter), however, the source could not be detected at the 3σ level. Hence, only upper limits on the flux, estimated from the background, can be reported. Simultaneous to the UVOT observations, *Swift*

Table 6.2.: Summary of deep X-ray observations

ObsID	Obs. Date	Camera	Exposure [ksec]
0724700101 (PI: C. Müller)	2013-09-17	PN	39.0
		MOS 1	33.4
708035010 (PI: R. Ojha)	2013-09-13	XIS 0/1/3	48.5

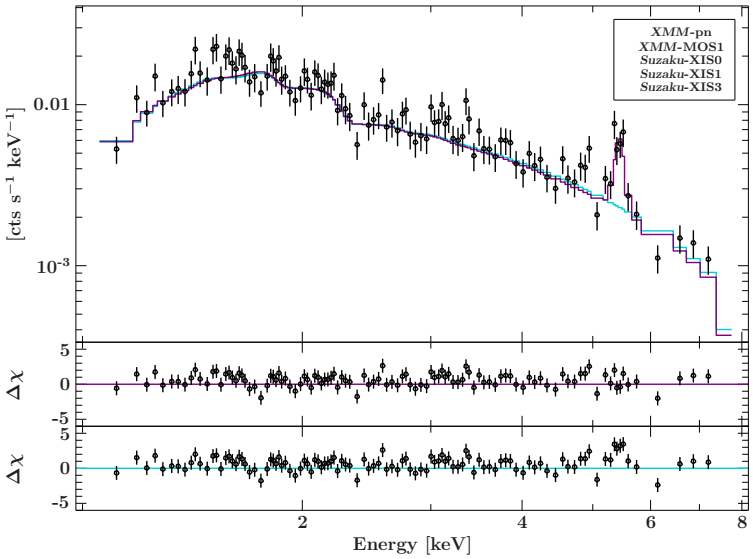

Figure 6.3: Combined fit to the (quasi-)simultaneous high resolution X-ray spectra obtained by *XMM-Newton* and *Suzaku* (see Table 6.2). The data were fitted by an absorbed power law component with an emission line. Shown is the best fit (purple, χ^2/d.o.f. = 488.7/540, see Table 6.3) resulting in a redshift measurement for the source of $z \sim 0.174$ based on the detection of a narrow Fe Kα line at $\sim$ 5.45 keV (see Sect. 6.2.4 for details). For comparison, a simple fit of an absorbed power law without an emission line is shown in cyan with respective residuals in the bottom panel.

X-ray Telescope (XRT, Burrows et al., 2005) revealed an X-ray source which is positionally consistent with the radio source. At the time of the first multiwavelength analysis of PMN J1603−4904, no other (archival) X-ray observations are available (see Sect. 6.2.4). The accumulated data of three *Swift*/XRT observations were used, since a separate X-ray data analysis of each single observation was not possible, yielding a total of only 77 source photons. The details on the *Swift*/XRT data processing and analysis are given in Müller et al. (2014a). The observed X-ray counts yield a roughly estimated flux of $\sim 5 \times 10^{-13}$ erg cm^{-2} s^{-1} in the 0.5–10 keV band. Better constraints can be obtained with high sensitivity X-ray observations, which are presented in the next section.

6.2.4. High sensitive X-ray observations with *XMM-Newton* and *Suzaku*

As part of this work, high sensitivity X-ray spectroscopy of PMN J1603−4904 with *XMM-Newton* and *Suzaku* have been proposed and were performed quasi-simultaneously in 2013 September (PI: C. Müller & R. Ojha, see Table 6.2 for details), with the main objective to better constrain the X-ray spectrum than previous observations with *Swift*/XRT (see above).

The *XMM* processing, data analysis, and the extraction of the spectrum was performed using the *XMM System Analysis Software* (SAS 13.5.0). Only data from *XMM*/PN and MOS 1 detector were usable. The extraction of the PN data was performed by selecting a 35″ extraction radius centered on the source coordinates. For the background extraction a region with a radius of 50″ was chosen. Similarly, for the MOS 1 data extraction, regions with radii of 100″ were used.

For the *Suzaku* data the HEASOFT v6.15 package was applied. Extraction and background regions of 94″, respectively, were used for all XIS detectors. The spectral analysis was then performed using the *Interactive Spectral Interpretation System* (ISIS, Version 1.6.2-27, Houck & Denicola, 2000).

Table 6.3.: Best Fit Parameters

Parameter	Value
$N_{\rm H}$ (galactic)	$0.63 \times 10^{22}\,{\rm cm}^{-2}$
$N_{\rm H}$ (intrinsic)	$2.1 \pm 0.4 \times 10^{22}\,{\rm cm}^{-2}$
Redshift z	0.174
$A_{\rm powerlaw}$	$1.78^{+0.37}_{-0.30} \times 10^{-04}$
$\Gamma_{\rm pow}$	$2.06^{+0.14}_{-0.13}$
$F_{6.4\,{\rm keV}}$	$(2.0 \pm 0.6) \times 10^{-6}{\rm erg\,s}^{-1}$
$E_{\rm gauss}$	$5.450^{+0.020}_{-0.066}\,{\rm keV}$
E_σ	$(1.0 \times 10^{-6})^{+0.9}_{-1.1\times10^{-6}}\,{\rm keV}$
χ^2/d.o.f.	488.7/540

In order to improve the statistics, all (quasi-)simultaneous *XMM-Newton* and *Suzaku* datasets were simultaneously fitted. The spectral model consists of an absorbed power law component and an Gaussian emission line. The complete model can be written as follows:

$$\texttt{C} \times \texttt{tbnew}_{\texttt{gal}} \times \texttt{tbnew\_z} \times (\texttt{Powerlaw} + \texttt{egauss}) \tag{6.1}$$

C is a cross-calibration constant to compensate the different flux calibrations of the different instruments (relative to XIS 0). The `tbnew` model (Wilms et al., 2000; Wilms et al., 2012) accounts for neutral Galactic absorption and was fixed to the Galactic HI value of $N_{\rm H} = 6.32 \times 10^{21}\,{\rm cm}^{-2}$ (in this direction, Kalberla et al., 2005), using the cross sections and abundances of Verner et al. (1996) and Wilms et al. (2000). The source intrinsic photoelectric absorption is modeled by `tbnew_z`.

The (quasi-)simultaneous data of *XMM*/EPIC-pn and MOS 1 and *Suzaku*/XIS0,1,3 were jointly rebinned to a minimal signal-to-noise ratio of 5 to ensure the validity of χ^2-statistics (see Fig. 6.3). The best fit model parameters can be found in Table 6.3. The best fit model gives a χ^2/d.o.f. $= 488.7/540$ and shows a photon index of $\Gamma_{\rm X} = 2.06^{+0.14}_{-0.13}$ with an intrinsic absorption of $N_{\rm H} = 2.1 \pm 0.4 \times 10^{22}\,{\rm cm}^{-2}$.

From the center energy of the Gaussian emission line, the redshift of PMN J1603−4904 can be measured for the first time. The most prominent emission line in X-ray spectra of AGN is the Kα line of neutral iron at 6.4 keV (e.g., Yaqoob & Padmanabhan, 2004; Nandra, 2006; Shu et al., 2010). The line is usually explained by photoabsorption and fluorescence (in "cold" iron) of power law photons in the innermost part of the AGN, possibly in the broad line region or the torus. Such emission lines are very common in Seyfert galaxies (Bianchi et al., 2004), i.e., radio-quiet systems, suggesting the presence of a torus in such sources, and also observed in few radio-loud AGN spectra (Gambill et al., 2003). Hence, if the prominent emission line in PMN J1603−4904 at ~ 5.43 keV is associated with an Fe Kα line, a limit on the redshift of the source of $z = 0.174 \pm 0.007$ can be obtained (Müller et al, in prep.). There are few other sources for which such a measurement of the redshift was performed. Tengstrand et al. (2009), for example, recalculated the redshift of the GPS source PKS 1607+26 due to a detection of a weak, narrow iron line.

6.3. Results of multiwavelength observations

6.3.1. Brightness distribution on milliarcsecond-scales and kinematics

Table 6.1 summarizes the results of hybrid imaging of the 8.4 GHz data using the `clean` algorithm (Högbom, 1974). The five 8.4 GHz VLBI observations of PMN J1603−4904 show an almost con-

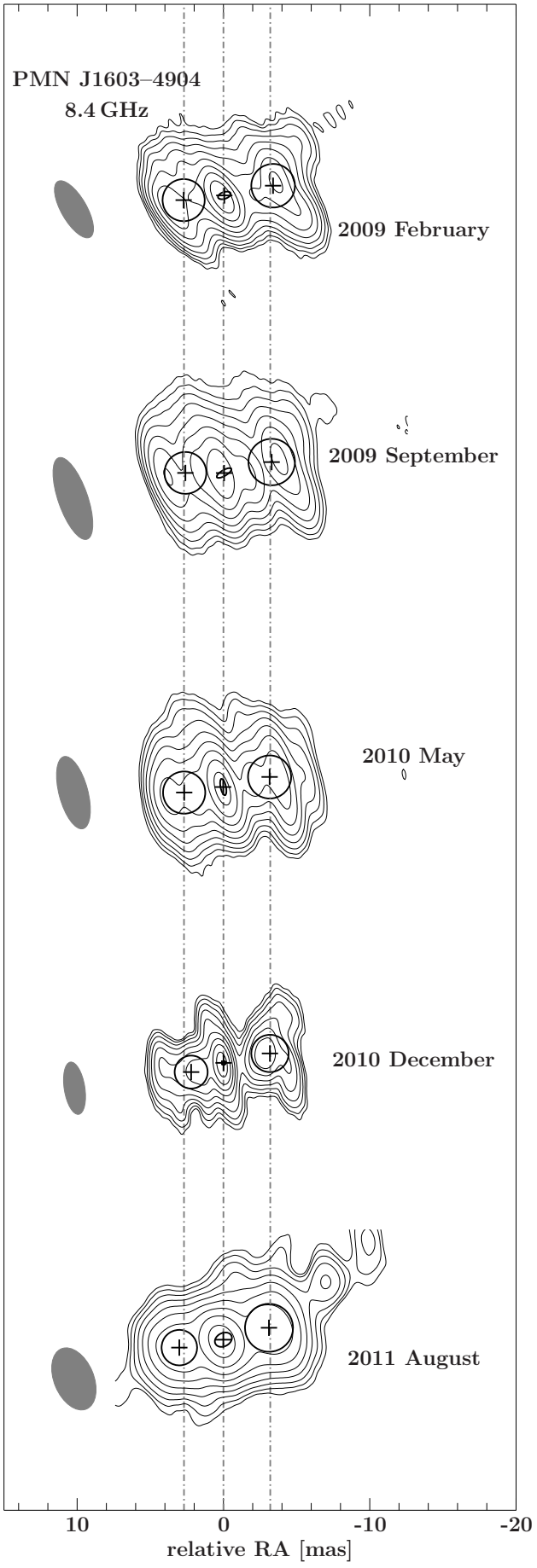

Figure 6.4: Time evolution of PMN J1603−4904. `clean` images of the first 8 GHz TANAMI observations are shown. The contours indicate the flux density level, scaled logarithmically and separated by a factor of 2, with the lowest level set to the 3σ-noise-level (for more details see Table 6.1). The positions and FWHMs of the Gaussian emission components are overlaid as black ellipses (for model parameters see Table 6.4). From top to bottom: 2009 February (combined image of 23$^{\text{th}}$ and 27$^{\text{th}}$), 2009 September, 2010 May, and 2011 August. The size of the restoring beams for each individual observation is shown as gray ellipse in the lower left corners. Vertical dashed lines to indicate the relative positions of the eastern and western features with respect to the central component are drawn at of 2.7 mas and −3.2 mas, respectively. (Compare to Fig. 2 in Müller et al., 2014a, showing the time evolution of the first three TANAMI observations.)

stant total correlated flux density of 570 mJy to 630 mJy. Changes in the measured values are well below the (conservative) estimate of absolute calibration uncertainties of ∼15-20% (Ojha et al., 2010) and are also due to the change in the (u, v)-coverage. The images have a dynamic range (ratio of peak brightness to five times the root-mean-squared noise level) of ∼80 to ∼280 (Müller et al., 2014a).

TANAMI observations resolve the source in all directions. It shows an east-west orientation at a position angle of PA$\sim -80°$ with three resolved distinct regions within $\lesssim$15 mas. The brightest, most compact feature is located in the center (see Fig. 6.4).

In order to study the flux density and structural variability of the individual prominent jet features, the self-calibrated visibility data were fitted with a simple model of three elliptical Gaussian emission components (using `difmap`, Shepherd, 1997). The parameters of the model components are reported in Table 6.4. The smallest and most compact feature is the central component, though it is resolved (see Kovalev et al., 2005, for details on the resolution limit). The brightness temperature (see Eq. 5.1 and Kovalev et al., 2005) of this brightest component is $T_{\mathrm{B,central}} \gtrsim 1\times10^{10}$ K. Note that a higher brightness temperature for the highest resolved epoch in 2010 December is obtained, where small-scale structures were better sampled and the component size is reduced (compare also Fig. 6.4).

In Müller et al. (2014a) the first three TANAMI observations (over a time range of 15 months) were presented, showing no significant flux density or brightness temperature variability for all components. Figure 6.5 shows that the additional epochs show a similar trend, considering the array-dependent resolution effects (see discussion above). However, in 2010 December, the highest resolution observation shows an increase in brightness temperature. Since the central component is resolved in all observations, this increase in T_{B} indicates the most compact region of the source. The symmetry of the mas-scale structure is also well represented in the T_{B}-distribution of both outer components.

The eastern and western regions can each be modeled with circular Gaussian flux distributions. The eastern component is about (0.2 ± 0.1) Jy weaker and about 0.6 mas closer (see Fig. 6.6) to the central component than the western one. The brightness temperatures of both outer components are constant at $\sim$ (4–6) $\times\, 10^8$ K.

To test for structural variability, component positions relative to the eastern and central component are measured (see Fig. 6.6). Within the uncertainties, no significant component motions could be found over the covered period. Therefore we can set a limit for the relative motions of $|v_{\mathrm{app}}| < 0.2\,\mathrm{mas\,yr^{-1}}$. In summary, after $\sim$ 2.5 years of VLBI observations PMN J1603−4904 shows no significant proper motion in neither direction.

6.3.2. Spectral properties on milliarcsecond-scale

In 2010 May, contemporaneous 8.4 GHz and 22.3 GHz TANAMI VLBI observations were performed (see Table 6.1). Since the TIGO antenna is not equipped with a 22.3 GHz receiver, the (u, v)-coverage at 22.3 GHz is poorer than that at 8.4 GHz. Furthermore, the Ceduna data were not usable due to problems with the maser. Hence, effectively only 22.3 GHz data from four Australian antennas were available, i.e. only of four stations. Hybrid imaging using the `clean` algorithm (Högbom, 1974) was not possible, because the algorithm fails to unambiguously model these sparse data. Therefore, in order to model and self-calibrate the 22.3 GHz (u, v)-data, the simple structural model found for the simultaneous 8.4 GHz observation was used (see Fig. 6.4 and Table 6.4).

In VLBI images, it is unlikely that 22.3 GHz data show more extended emission beyond the 8.4 GHz emission, since the larger scale emission of extragalactic jets has steep spectra. Hence,

Table 6.4.: Modelfit parameters for TANAMI VLBI images

8.4 GHz

S^a [Jy]	d^b [mas]	θ^b [°]	$a_{\mathrm{maj}}{}^c$ [mas]	$a_{\mathrm{min}}{}^c$ [mas]	P.A.^{c} [°]	$T_B{}^d$ [10^9 K]	$(1+z)T_B{}^e$ [10^9 K]
Combined 2009-02-23 & 2009-02-27:							
0.17	2.8	97.0	2.9	2.9	138.0	0.35	0.41
0.22	0.0	—	0.9	0.5	33.0	9.1	10.7
0.20	3.4	−79.0	3.0	3.0	−114.0	0.39	0.46
2009-09-05:							
0.16	2.6	90.0	2.9	2.9	−155.0	0.34	0.47
0.22	0.0	—	1.1	0.4	17.0	8.6	10.10
0.19	3.3	−77.0	3.2	3.2	−153.0	0.32	0.38
2010-05-07:							
0.17	2.7	98.0	3.0	3.0	177.0	0.35	0.41
0.21	0.0	—	1.1	0.4	12.0	8.6	10.10
0.19	3.2	−78.0	2.9	2.9	20.0	0.38	0.45
2010-12-14:							
0.16	2.3	105.8	2.3	2.3	61.7	0.54	0.63
0.22	0.0	—	0.3	0.3	45.64	56.1	65.9
0.17	3.2	−78.5	2.6	2.6	-39.1	0.45	0.53
2011-08-14:							
0.15	3.1	100.2	2.4	2.4	−8.9	0.44	0.52
0.27	0.0	—	1.2	0.9	−33.1	4.19	4.92
0.21	3.2	−75.4	3.3	3.3	−58.2	0.34	0.40

22.3 GHz

S^a [Jy]	d^b [mas]	θ^b [°]	$a_{\mathrm{maj}}{}^c$ [mas]	$a_{\mathrm{min}}{}^c$ [mas]	P.A.^{c} [°]	$T_B{}^d$ [10^9 K]	$(1+z)T_B{}^e$ [10^9 K]
2010-05-05:							
0.04	2.7	98.0	3.0	3.0	177.0	0.01	0.01
0.19	0.0	—	1.1	0.4	12.0	1.1	1.3
0.07	3.2	−78.0	2.9	2.9	20.0	0.02	0.02

Notes. $^{(a)}$ Integrated flux density of model component. $^{(b)}$ Distance and position angle of the model component from the designated phase center $^{(c)}$ Major, minor axis extent (FWHM) of the model component and position angle of the major axis. $^{(d)}$ Brightness temperature of model component (without redshift correction). $^{(e)}$ Corrected brightness temperature of model component using $z = 0.174$ obtained from X-ray spectral fitting (see Sect. 6.2.4).

this approach is an acceptable starting model. The relative positions of the three components from the high-quality 8.4 GHz data were fixed, but their flux densities were allowed to vary. With this model, an amplitude self-calibration on long time scales was performed. In order to further model the 22.3 GHz data, the component flux densities were again fitted and iterative self-calibration steps on shorter time scales were performed, while overall self-calibration corrections were small. The final model consisting of three Gaussian components is in good agreement with the original data (see Fig. 6.7). This model represents hence the most extended structure of the source at mas scales. It is still consistent with both the (u, v)-data at 22.3 GHz itself and with the brightness distribution found at 8.4 GHz and will be called 'extended model' in the following.

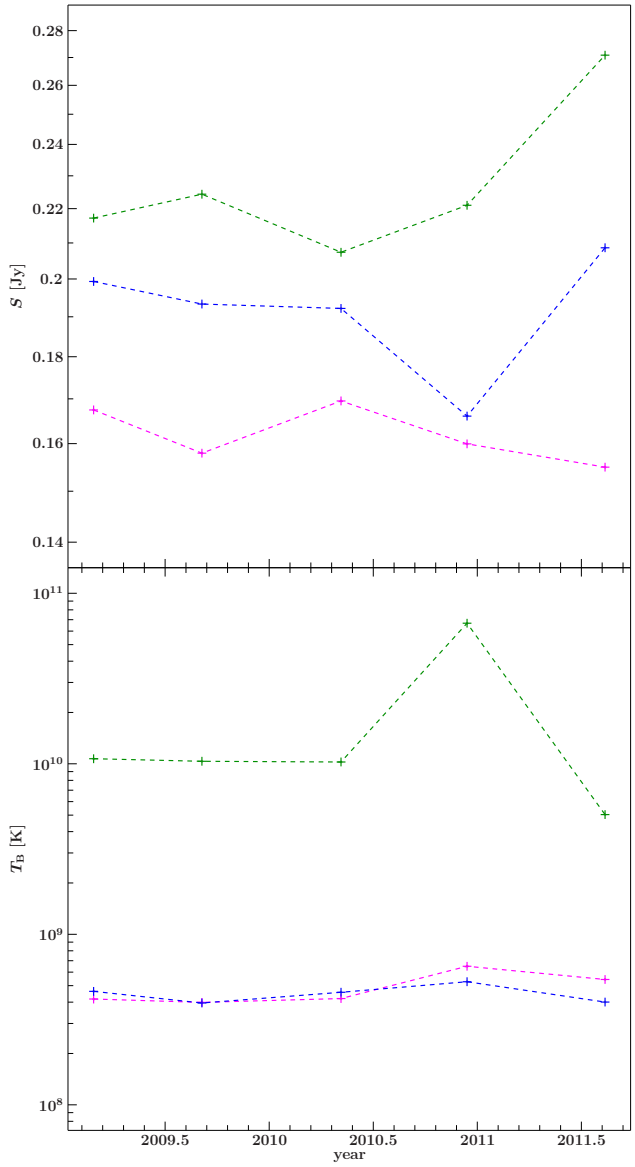

Figure 6.5: Flux density and brightness temperature evolution. Shown are the model component parameters (see Table 6.4) for each single epoch. The evolution of the eastern/central/western component is marked in pink/green/blue, respectively (compare to Fig. 6.6). Note that due to resolution effects an apparent change is measured and within the conservative errors of $\sim 20\%$ in flux, the source shows a stable behavior, since it cannot be excluded that the variability in the data is due to observational effects.

Formally, uncertainties to the 8.4 GHz and 22.3 GHz profile can be assigned according to the absolute calibration uncertainties in both frequency bands, i.e., for TANAMI observations, conservative $15-20\%$ are normally applied (Ojha et al., 2010). Due to the sparse (u,v)-coverage at 22.3 GHz, the structural uncertainties are much larger than at 8.4 GHz. Hence, in order to study the spatial spectral index distribution, i.e., combining these dual-frequency images, positional uncertainties need to be assigned. To constrain these uncertainties, a so called 'compact model' for the 22.3 GHz data was derived: the (u,v)-data can be modeled by only one elliptical Gaussian component. As described above, using this 'compact model' the same model fitting/self-calibration cycle was applied. In Figure 6.7 both 22.3 GHz models are compared to the original (uncalibrated) data. Especially the lack of long baselines prevents a clear modeling, hence, those two models are the respective extreme representation of this VLBI data set. The spatial spectral index distribution can then be calculated combining the 8.4 GHz image of 2010 May with the quasi-simultaneous 22.3 GHz image. Both data sets were convolved with a common circular beam with a major axis of 3 mas. Cuts through the two brightness distributions along the position angle P.A. $= -80^\circ$ give the resulting formal spectral index profiles for both models (see Fig. 6.8).

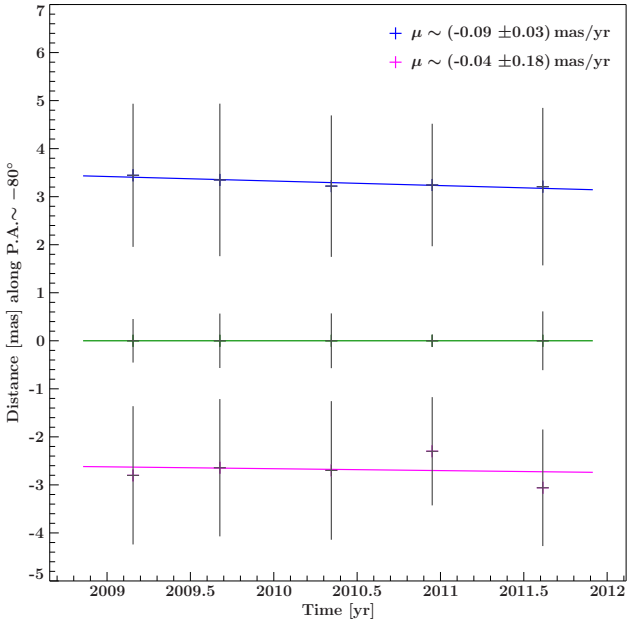

Figure 6.6: Kinematics of PMN J1603−4904. Shown is the evolution of the position of the outer two model components (eastern in pink, western in blue) with respect to the central feature (green, see Table 6.4). The size of the semi-major axis of the Gaussian component is shown as a measure of the positional uncertainty. The central component (yellow) is set to zero as a reference in order to fit the motion of the eastern and western regions with a simple ballistic track. Linear regression fits result in a proper motion of $\mu \sim -0.09 \pm 0.03\,\mathrm{mas\,yr^{-1}}$ for the western and $\mu \sim -0.04 \pm 0.18\,\mathrm{mas\,yr^{-1}}$ for the eastern component. All components are stationary within the errors.

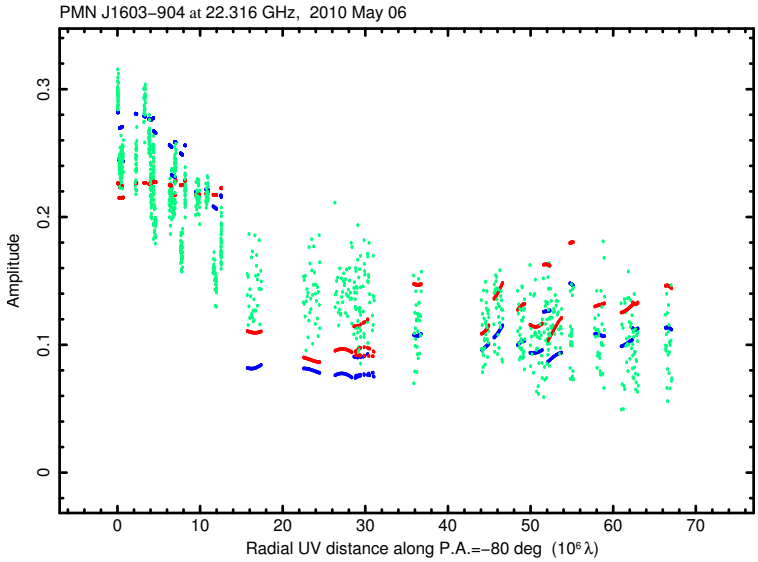

Figure 6.7: Projected (P.A.= −80°) visibilities at 22.3 GHz (green) (uncalibrated). The 'compact model' with one Gaussian component is shown in red, the 'extended model' with three Gaussian components based on the 8.4 GHz model is shown in blue.

The Figures 6.7 and 6.8 clearly show that the sparse (u, v)-sampling at 22.3 GHz mainly affects the eastern and western wings of the spectral index profile with steep spectra in the 'extended model' of $-2.0 \lesssim \alpha \lesssim -1.0$. For the 'compact model', however, the spectral index distribution reaches unrealistically steep values of $\alpha \ll -2.0$. For the central feature both models give a consistent spectral index of $-0.75 \lesssim \alpha \lesssim -0.25$. Though formally the 'compact model' represents the 22.3 GHz data sufficiently well, the spectral index analysis shows that this model does not lead to a physical, self-consistent dual-frequency model.

The absolute position information is lost due to the self-calibration steps in the imaging process. Therefore, the 'compact model' would in principle allow different alignments with respect to the 8.4 GHz image. Following and testing the original classification of PMN J1603−4904 as a blazar (see Sect. 6.4), in such scenario one might associate the peak of the 22.3 GHz emission in the 'compact model' with the eastern source component at 8.4 GHz. This alignment would require a shift of ∼2.7 mas, since the tapered 8.4 GHz image shows a potential, faint extension to the west.

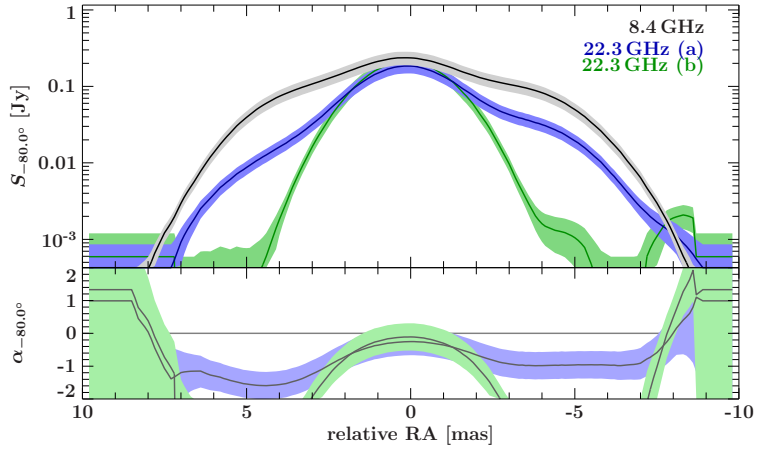

Figure 6.8: *Top:* Flux density profiles along P.A.= −80° at 8.4 GHz (gray) and the 22.3 GHz 'extended model' (blue, (a)) and 'compact model' (green, (b)). *Bottom:* Spectral index distribution along P.A.= −80°, with the 'extended model' in light blue, the 'compact model' is shown in light green. Displayed uncertainties correspond to a conservative estimate of absolute calibration uncertainties and on-source errors of ∼20%. Figure from Müller et al. (2014a).

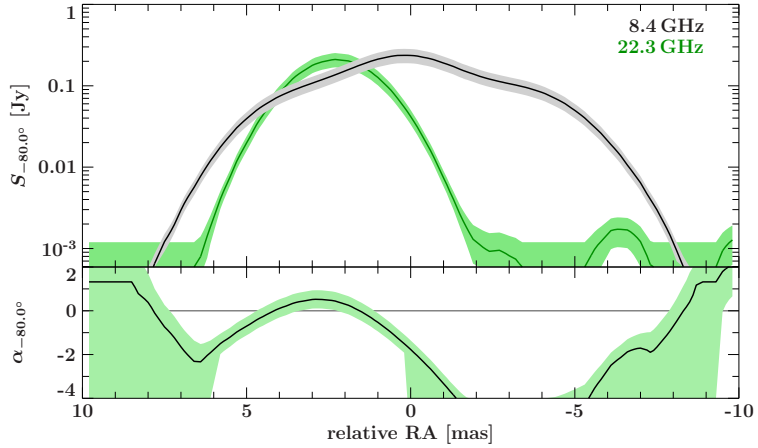

Figure 6.9: Flux density (*top*) and spectral index (*bottom*) distribution for the "blazar scenario" (see Sect. 6.4): a respective shift of ∼ 2.7 mas was applied to both images in order to align the eastern component at 8.4 GHz with the brightest feature at 22.3 GHz and to get a one-sided structure with a declining spectral index distribution from "the core" downstream the jet - as expected for a blazar. This alignment leads to unphysically steep spectral indices and is therefore rejected.

With this alternate alignment, the putative blazar core in the east would have a slightly inverted spectrum, but the bright 8.4 GHz emission westward would reach again unphysical, extremely steep spectral-index values ($\alpha \ll -4$, see Fig. 6.9).

These considerations reveal the central feature as the most plausible 'core' of PMN J1603−4904, as the region with the flattest spectral index and the highest brightness temperature.

6.3.3. Integrated ATCA radio spectral monitoring

In Fig. 6.10 and 6.11 the ATCA radio spectra and light curves are shown (Stevens et al., 2012) as well as of archival ATCA observations. Simultaneous to the TANAMI observations (between 2009 and 2012), no significant variability is measured. The source spectrum has a spectral index of $\alpha \sim -0.4$. This value is consistent with the one determined from the integrated VLBI images ($-1.0 \lesssim \alpha \lesssim 0.0$, assuming the 'extended model' at 22.3 GHz). The ATCA flux densities at 8.4 GHz and 22.3 GHz are ∼200 mJy brighter, indicating a diffuse extended emission component which is resolved out by the TANAMI VLBI array. As discussed above, due to the varying array configurations of the VLBI observations, the small and large scale structure is differently addressed. The latest 8.4 GHz observation in 2011 April lacked long baseline information but reveals more extended structures of PMN J1603−4904, further indicating this "missing" flux component.

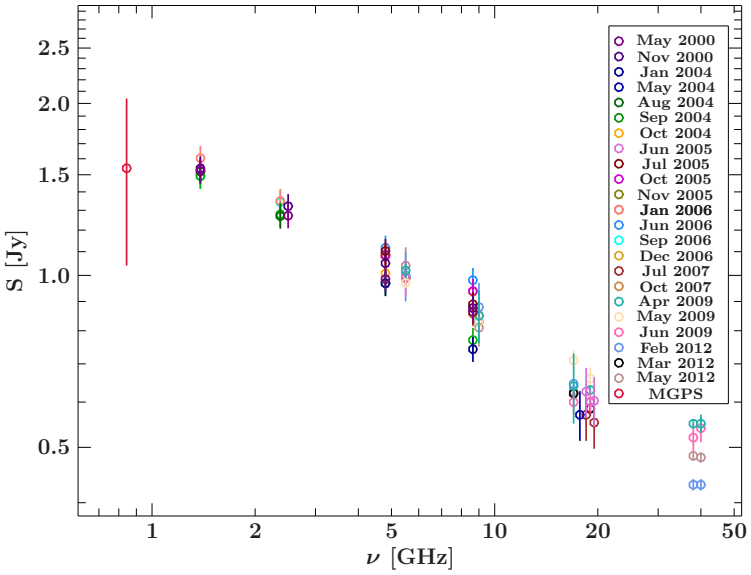

Figure 6.10: Radio spectrum of PMN J1603−4904 at 6 frequencies based on the ATCA monitoring. The error bars are calculated as a frequency-dependent fraction of the flux density at each frequency. The archival data of the MGPS catalog might indicate a turnover of the spectrum below 0.8 GHz. Figure from Müller et al. (2014a).

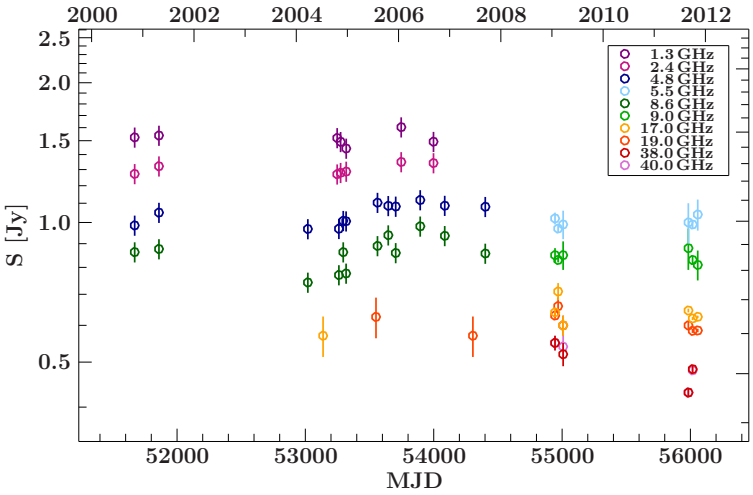

Figure 6.11: Radio light curve of PMN J1603−4904 from the ATCA monitoring at 6 frequencies. Error bars as in Fig. 6.10. Note the lack of variability between 2009 and 2012. On longer timescales some evidence for low-level variability is seen. Figure from Müller et al. (2014a).

6.3.4. Multiwavelength source association

The association of the γ-ray source 2FGL J1603.8−4904 with the radio object PMN J1603−4904 is well established (Abdo et al., 2009, 2010; Nolan et al., 2012). The Molonglo Galactic Plane Survey catalog lists the source with $S_{843\,\mathrm{MHz}} = (1.54 \pm 0.5)$ Jy (MGPS, source ID: J160350−490403, Murphy et al., 2007). *Swift*/XRT (and subsequent *XMM* and *Suzaku*) observations reveal a single X-ray source, positionally consistent with the radio source. Due to this positional coincidence combined with the favorable extrapolation of the non-thermal X-ray emission into the γ-ray regime (see Sect. 6.3.5 below for more details), PMN J1603−4904 is the most likely association of the X-ray source.

To identify the optical/IR counterpart of PMN J1603−4904, data from various sky surveys were used. In 2010, NASA's Wide-field Infrared Survey Explorer (*WISE*; Wright et al., 2010) mapped the sky at 3.4, 4.6, 12, and 22 μm (bands W1, W2, W3, and W4) with 6″–12″ resolution. The *WISE* catalogs flags the associated source WISE J160350.68−490405.6 as "extended", i.e., not being consistent with a point source. Since the closest detected *WISE* source has a distance of $\approx 12''$ from PMN J1603−4904, the extension must be caused by a closer object that is not resolved with *WISE*. Higher resolved infrared and optical images give some indication of the close neighborhood

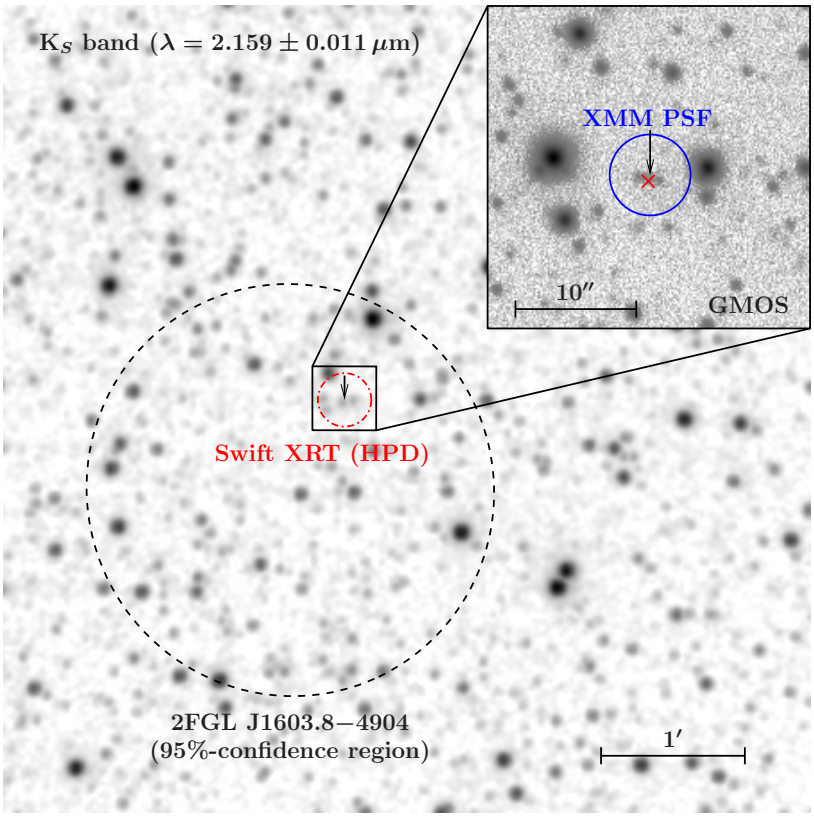

Figure 6.12: Grayscale 2MASS image (K_S band) of the region around the radio position of PMN J1603−4904, indicated by the black arrow. The black-dotted circle indicates the 95 %-confidence ellipse of *Fermi*/LAT, the red-dotted circle the *Swift*/XRT HPD and the blue circle the *XMM*-Newton PSF. The close-up in the north western corner shows the higher resolved GMOS (r' band) image revealing a faint elliptically-shaped source. The red cross marks the position of the associated *WISE*/2MASS source. No other known radio source is found in this region, indicating a high-confidence association with the high-energy counterpart. Figure adapted from Müller et al. (2014a).

of PMN J1603−4904. Figure 6.12 shows the higher resolved 2MASS image (Skrutskie et al., 2006, angular resolution of $\sim 2''$). In this K_S band (2.159 μm) image a very faint IR source is seen which is positionally consistent and associated with PMN J1603−4904 (2MASS 16035069−4904054, ID: 655163671). This counterpart is also flagged as "photometric confused", likely due to a $4\farcs8$ distant neighboring star of comparable IR magnitude. Relatively to the counterpart to PMN J1603−4904, this object becomes fainter towards longer wavelengths. This indicates that the emission seen in *WISE* (i.e. at lower energies) is probably dominated by PMN J1603−4904, however, in the following the infrared fluxes from WISE and 2MASS are considered to be contaminated, as a contribution of this neighboring star in these surveys cannot be fully excluded (see also Sect. 6.3.5).

Going to even higher angular resolution, the r'-band GMOS observation is able to separate the neighboring star and PMN J1603−4904 (see Fig. 6.12). The GMOS image reveals a faint, extended emission with an East-West extension of $2\farcs5$ and $1\farcs3$ in North-South direction at the position of PMN J1603−4904. The apparent magnitude of the Eastern part of the emission is about 24 mag, which is taken to be the upper limit of the point source flux density of the optical counterpart (Fig. 6.12).

The original classification of PMN J1603−4904 is based on optical observations by Shaw et al. (2013) who performed optical spectroscopy of all 2LAC BL Lac objects. PMN J1603−4904 was observed (on 2009 August 22) with the New Technology Telescope (NTT) at La Silla Observatory. Based on low signal-to-noise spectra these authors labeled the source as a BL Lac using their standard criteria and determined a limit for the redshift of $z_{\rm max} = 4.24$. Due to its location in the Galactic plane, these optical observations suffered from strong extinction along the line of sight. Hence, more sensitive optical observations are required to better constrain this limit and to obtain more information on the optical counterpart. Absorption is also responsible for the absence of a matching *Swift*/UVOT counterpart (see Sect. 6.2.3). With additional positional constraints from in-

frared information by 2MASS (Skrutskie et al., 2006) and *WISE* the two nearby UV-sources visible in the UVOT image can be excluded as possible optical counterparts of PMN J1603−4904.

In the following, it is assumed that the reported multiwavelength counterparts are all positionally consistent with PMN J1603−4904 and discuss on this basis the broadband properties of this source.

6.3.5. The broadband SED

Figure 6.13 shows the constructed non-simultaneous broadband spectral energy distribution (SED) from radio[3], optical/UV, and *Swift* X-ray data, *XMM-Newton*, *Suzaku*, as well as published IR, optical[4], and *Fermi*/LAT γ-ray data (Nolan et al., 2012). Since the broadband spectral shape of PMN J1603−4904 resembles the typical double-humped SEDs of blazars, the data were parametrized with two logarithmic parabolas (Giommi et al., 2012; Chang, 2010; Massaro et al., 2004), as well as the photoelectric absorption component at X-ray energies[5] with $N_{\rm H} = 2.1 \times 10^{22}\,{\rm cm}^{-2}$ (see Table 6.3) using the `tbnew` model of Wilms et al. (2012) with abundances from Wilms et al. (2000) and cross-sections from Verner et al. (1996), and an extinction model for the optical (Predehl & Schmitt, 1995; Fitzpatrick, 1999; Nowak et al., 2012). This results in a synchrotron peak frequency of $\nu_{\rm sync} \simeq 2.2 \times 10^{12}$ Hz.

As discussed in Sect. 6.3.4, the IR fluxes are likely to be contaminated due to source confusion, however, the contribution of the neighboring star is expected not to exceed 50% (see Fig. 6.12). Therefore, the remaining excess is attributed to PMN J1603−4904. The most striking feature in this SED is the strong excess of a factor of ten in flux in the IR band. This IR excess can be fitted with a black body spectrum with a temperature of $T = 1662^{+120.0}_{-150.0}\,{\rm K}$ to the 2MASS and GMOS data[6] giving an estimate on the blackbody temperature of PMN J1603−4904 and accounting for the contribution of the neighboring star. This can most likely be associated with a dusty torus, the host galaxy (Malmrose et al., 2011), or starburst activity (see Sect. 6.4.2).

Given the optical source morphology, it is very unlikely that the IR excess is a foreground star: A red giant ($L = 115 L_\odot$) with this surface temperature would need to be at a distance of 35.7 kpc, well outside the disk of the Galaxy, while an M-dwarf with $L = 2.21 \times 10^{-5} L_\odot$ would have to be very close at 15.7 pc. The latter is unlikely, since the absorption along the line of sight is constrained by the Galactic Hi value of $N_{\rm H} = 6.32 \times 10^{21}\,{\rm cm}^{-2}$ in this direction (Kalberla et al., 2005). A nearby M-dwarf would exhibit a significantly smaller extinction.

6.3.6. *Fermi*/LAT 4-years analysis

The *Fermi* analysis of four years of γ-ray monitoring reveals a constant but low decrease in the γ-ray flux and confirms the non-flaring behaviour of the source over long time scales (see Fig. 6.14).

[3] For the SED parametrization, the ATCA rather than the VLBI data were used because of better frequency coverage. Additional measurements in the mm/sub-mm band (e.g. with ALMA) will allow us to constrain the shape of the synchrotron peak, since the synchrotron photons can either be dominated by the more extended structure or the compact radio source, addressed by ATCA or TANAMI, respectively.

[4] Catalog values corrected for extinction using standard values (see Shaw et al., 2013, for more information).

[5] Note that the more sensitive X-ray observations with *Suzaku* and *XMM* allow to better constrain the absorption and the X-ray spectrum than with only *Swift*/XRT data as presented in Müller et al. (2014a).

[6] As the NTT data were already corrected for extinction using a different correction factor, only the GMOS data were used for the parametrization in this work. The *WISE* data were excluded in the parametrization, due to poorer angular resolution compared to 2MASS, declining towards longer wavelengths of the *WISE* bands (6.″1, 6.″4, 6.″5, 12.″0 at 3.4, 4.6, 12, and 22 μm, respectively, Wright et al., 2010). Nevertheless, the *WISE* data match this parametrization of the SED, further indicating that PMN J1603−4904 is dominating the emission in this band.

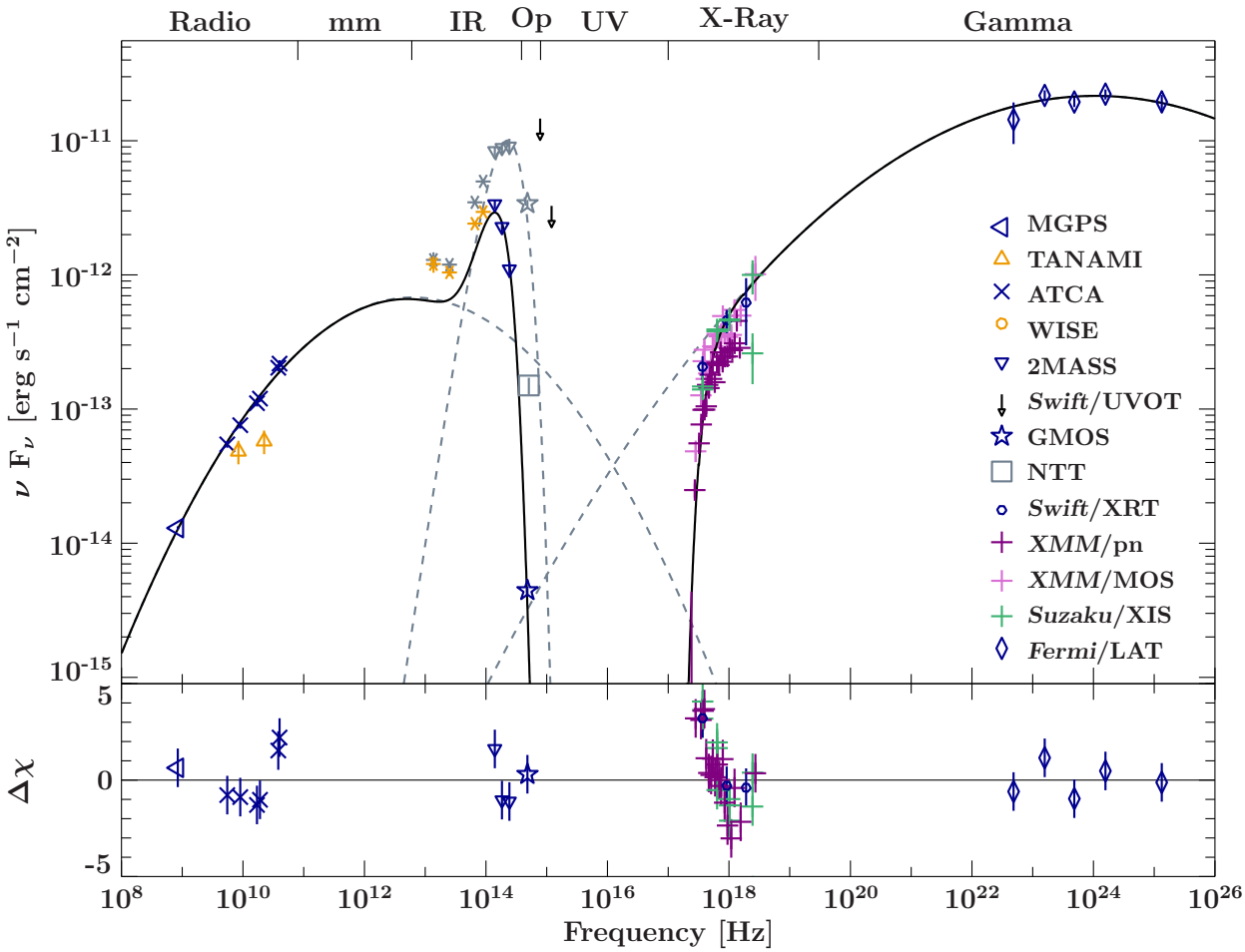

Figure 6.13.: Broadband νF_ν SED including total fluxes of simultaneous TANAMI observations (of 2010 May), non-simultaneous measurements in the radio by the Molonglo Galactic Plane Survey (MGPS, Murphy et al., 2007), by ATCA (Stevens et al., 2012), by *WISE* (Wright et al., 2010) and 2MASS (Skrutskie et al., 2006), by GMOS and NTT (Shaw et al., 2013), by *Swift*/XRT, UVOT, *XMM-Newton*, *Suzaku* and *Fermi*/LAT (2FGL, Nolan et al., 2012). The data are parametrized with two logarithmic parabolas absorbed by photoelectric absorption at X-ray energies with $N_\mathrm{H} \sim 2.1 \times 10^{22}\,\mathrm{cm}^{-2}$ (see Table 6.3) and an additional blackbody component (see Sect. 6.3.5 for details; $\chi^2 = 23$ for 12 degrees of freedom). Blue/Orange symbols mark the data used/ignored for the SED parametrization (black solid line) as described in Sect. 6.3.5. The IR and optical data are corrected for extinction (Fitzpatrick, 1999; Nowak et al., 2012), and the X-ray data for absorption (Wilms et al., 2000; Verner et al., 1996; Wilms et al., 2012), shown as corresponding gray symbols. The gray-dashed lines represent the unabsorbed logarithmic parabolas as well as the extinction corrected blackbody component. The bottom panel shows the residuals of the fit in units of the standard deviation of the individual data points. Figure adapted from Müller et al. (2014a).

The 4-years averaged γ-ray spectrum (Fig. 6.15) is still remarkably flat with $\Gamma_{1-100\,\mathrm{GeV}} = 2.18 \pm 0.03$ and a photon flux of $S_{1-100\,\mathrm{GeV}} = (134 \pm 5) \times 10^{-10}\,\mathrm{ph\,cm^{-2}\,s^{-1}}$. Though the activity is decreasing in the second half of this monitoring period, PMN J1603−4904 is still one of the brightest, hard spectrum γ-ray sources in the sky and therefore a promising candidate for a detection in the TeV range by the ground based Cherenkov telescope H.E.S.S. (Ackermann et al., 2013).

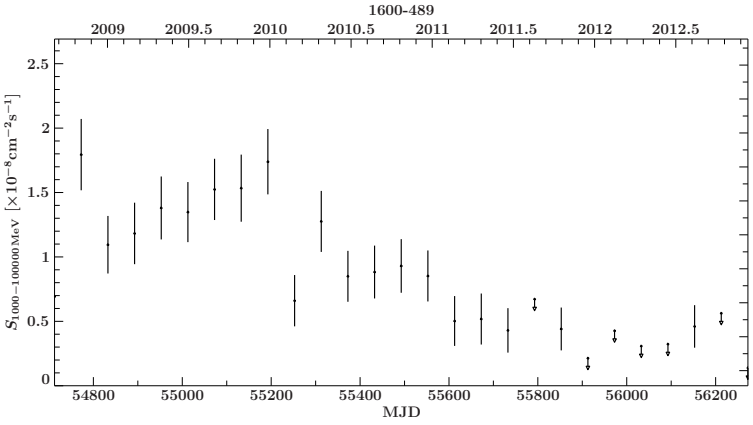

Figure 6.14: *Fermi*/LAT monitoring of PMN J1603−4904 over four years. Shown is the γ-ray light curve for the energy range $1-100$ GeV with a binning of 60 days. Over the first two years of monitoring the source flux density showed no variability, but afterwards it constantly declined (upper limits for TS≤ 9).

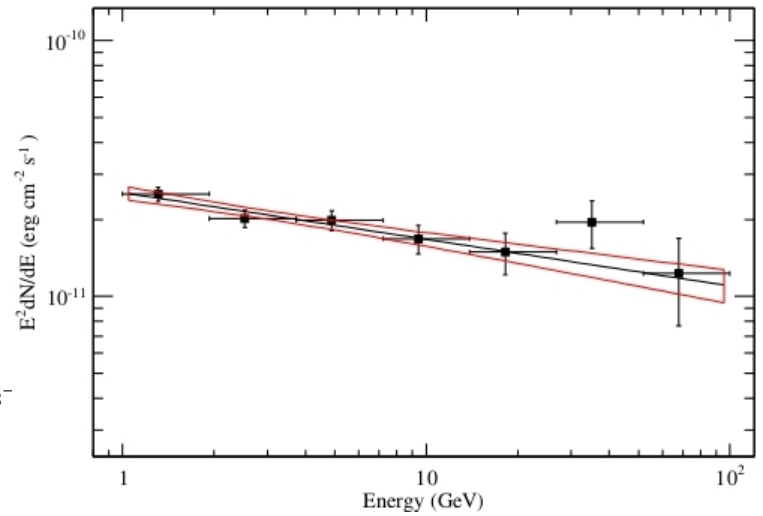

Figure 6.15: 4-years *Fermi*/LAT spectrum of PMN J1603−4904. The γ-ray spectral index ($\Gamma_{1-100\,\mathrm{GeV}} = 2.18 \pm 0.03$) and total γ-ray flux ($S_{1-100\,\mathrm{GeV}} = (134 \pm 5) \times 10^{-10}$ ph cm^{-2} s^{-} are comparable to the values in the 2FGL catalog (Nolan et al., 2012) indicating no major source activity.

6.4. Discussion of source classification

PMN J1603−4904 has traditionally been classified as a low-peaked BL Lac object based on its γ-ray to low-energy properties (Nolan et al., 2012) and the lack of emission lines (Shaw et al., 2013). However, the source location close to the Galactic plane makes high resolution optical spectroscopy difficult. In the following, the blazar scenario is first reviewed before possible alternative source classifications are discussed (based on Müller et al., 2014a).

6.4.1. PMN J1603−4904 as a BL Lac type object

Within the unification scheme of radio-loud AGN (see Sect. 1.2.1 and Antonucci, 1993; Urry & Padovani, 1995), BL Lac objects are considered to be the beamed version of FR I type galaxies (Fanaroff & Riley, 1974), with jets pointing close to the line of sight. The broadband SED can locally be well-described by a power law component. Thermal emission features in the optical and infrared are usually outshined by the non-thermal jet emission (e.g., Abdo et al., 2010a; Chen & Shan, 2011; Plotkin et al., 2012). It is only in very few blazars that an IR excess over the underlying power law component can be related to a hot torus (Malmrose et al., 2011).

BL Lacs are in general strongly variable across the whole electromagnetic spectrum and show a clear double-humped SED shape (see Sect. 1.3.1). Based on the position of the synchrotron hump, sub-classifications are made into low- (LSP), intermediate- (ISP) and high-synchrotron-

peaked (HSP) BL Lacs with $\nu^S_{\rm peak} < 10^{14}$ Hz, $10^{14} < \nu^S_{\rm peak} < 10^{15}$ Hz and $\nu^S_{\rm peak} > 10^{15}$ Hz, respectively (e.g., Donato et al., 2001). High angular resolution VLBI measurements of BL Lacs in general reveal highly polarized (∼10%) jet emission (Lister & Homan, 2005; Hovatta et al., 2010; Linford et al., 2011) and apparent superluminal motion of individual jet components (Kellermann et al., 2004; Lister et al., 2009b). Multifrequency VLBI observations (e.g., Taylor et al., 2005) of mas-scale blazar jets show that the radio spectral index distribution of the core is flat to inverted, i.e., self-absorbed while outer jet emission becomes optically thin.

Within the blazar-classification scenario, multiple observational facts of PMN J1603−4904 point to a highly peculiar object:

Variability:

Multiwavelength monitoring of PMN J1603−4904 reveals no short-term or rapid flaring variability (Fig. 6.14 and 6.11). After two years of *Fermi*/LAT monitoring, PMN J1603−4904 was listed as a non-variable blazar-like object (2FGL catalog Nolan et al., 2012). However, recently, a low, long-time variability at ≥10 GeV was reported (Ackermann et al., 2013) and confirmed by the 4-years analysis (Fig. 6.14). No major outburst at γ-rays was seen in PMN J1603−4904 (see Fig. 6.15), in contrast to most other blazars (Abdo et al., 2010a). This lack of short-term variability over years and across the electromagnetic spectrum is generally unusual, although *Fermi*/LAT monitoring shows that blazars can stay in non-flaring states over long periods (Abdo et al., 2010a). A similar stable behavior of PMN J1603−4904 is seen at radio wavelengths. The multifrequency ATCA light curve shows no significant variability over ∼ 4 years (see Fig. 6.11). Note, however, that long term radio monitoring at mm-wavelengths (Hovatta et al., 2007) determined variability time scales of AGN of about ∼ 4 years. Archival ATCA data of PMN J1603−4904 going back about a dozen years, however, show some evidence for low-level, long timescale flux density variation similar to that seen in some Gigahertz-peaked (GPS) and compact steep spectrum (CSS) sources (Tingay et al., 2003). At milliarcsecond resolution, the TANAMI VLBI observations show no structural or flux density variability for more than 2 years (see Sect. 6.3). No fast motion of jet components was detected (see Fig. 6.4), which is uncommon for γ-ray bright, highly beamed jets (Lister et al., 2011). However, Piner et al. (2010) found that TeV blazars can exhibit undetectable parsec-scale motions despite being very strong in γ-rays. Note that the TeV blazars are generally HSPs while PMN J1603−4904 has a synchrotron peak frequency below 10^{14} Hz, though the detection of PMN J1603−4904 at TeV energies is considered.

Polarization:

For PMN J1603−4904, observations by Murphy et al. (2010) put a limit on the overall polarization of <1.2% at 20 GHz and <1% at 5 and 8.4 GHz. A higher degree of polarization on smaller angular scales cannot be excluded and might be detected by polarization measurements at higher angular resolution, as the VLBI observations presented here do not include polarimetry.

Broadband spectral properties:

The γ-ray spectral slope of PMN J1603−4904 (see Sect. 6.1) matches the ones of the luminous, hard-spectrum *Fermi*/LAT AGN: with $\Gamma_{100\,\mathrm{MeV}-100\,\mathrm{GeV}} = 2.04 \pm 0.04$ the source is among the 30 brightest 2LAC objects which have a mean γ-ray spectral index of $\Gamma_{100\,\mathrm{MeV}-100\,\mathrm{GeV}} \approx 2.0$ (Ackermann et al., 2011) . With the exception of the radio galaxy NGC 1275 all of these 30 brightest sources are either classified as FSRQs or BL Lacs.

Based on its infrared colors, WISE J160350.68−490405.6 (the counterpart associated with PMN J1603−4904) would be consistent with the definition of the *WISE* Gamma-ray Strip for BL Lacs (Massaro et al., 2011, 2012). However, the "*WISE* blazar strip" is defined based on sources at high galactic latitudes and all projections in the *WISE* color space were treated separately, while D'Abrusco et al. (2013) modeled and selected the "*WISE* locus" based on the Principal Component space generated by the whole three-dimensional *WISE* color distribution corrected for galactic extinction of confirmed γ-ray blazars. Using the extinction corrected colors[7] instead and applying the method described in D'Abrusco et al. (2013), the source is not a candidate blazar within the definition the 3D-*WISE* locus (R. D'Abrusco, priv. comm.).

In a typical BL Lac, the non-thermal jet emission would outshine all other broadband emission components and the infrared component is expected to be primarily due to synchrotron processes. Contrary to this, the broadband SED of PMN J1603−4904 (Fig. 6.13) shows a strong excess in the infrared and the broadband parametrization requires an additional blackbody component with an approximate[8] temperature of ≈ 1600 K. Such infrared emission features are not expected to show up in BL Lac SEDs (Abdo et al., 2010a).

The high sensitivity X-ray spectra from the follow-up observations with *XMM* and *Suzaku* of this multiwavelength study reveal a narrow Fe Kα line (see Fig. 6.3). Similar to the excess in the infrared, no such emission line is typically expected to show up in blazar X-ray spectra[9], as the power law component would fully dominate the emission (Sambruna et al., 1994; Grandi et al., 2006; Rivers et al., 2013). Since this emission line shows no broadening, it can be attributed to emission further away from the black hole, i.e., the broad line region or the torus. The X-ray absorption ($N_{\rm H} > 2 \times 10^{22}\,{\rm cm}^2$) is atypically high compared to other blazars (Urry et al., 1996), but could be explained with Galactic absorption due to ionizes gas. The detection of a narrow iron line and the high intrinsic absorption are strongly questioning the classification as a "pure" blazar.

Overall, the broadband SED parametrization (Fig. 6.13) shows a striking Compton dominance. The high energy emission hump is about two orders of magnitude above the synchrotron peak, which further challenges the BL Lac classification scenario[10]. The double-humped broadband emission of BL Lacs is generally well described by synchrotron-self Compton models (see Sect. 1.3.1 and, e.g., Ghisellini et al., 2010), and such a dominance at high energies would then lead to the "Compton catastrophe". As long as no external radiation fields are considered, this particular broadband feature of PMN J1603−4904 is difficult to reconcile with the BL Lac classification. Broadband emission models including external photons from the accretion disk, the broad line region or the cosmic microwave background (e.g., Dermer et al., 2009; Finke, 2013; Potter & Cotter, 2013) could explain the SED, but are more commonly used for flat spectrum radio quasars, and would hence be disfavored for this source due to the lack of optical emission lines or thermal disk emission.

Milliarcsecond structure:

The TANAMI dual-frequency VLBI observations reveal a resolved and symmetric brightness distribution on milliarcsecond scales. The brightest component in the center shows a flat spectrum and

[7] Extinction corrected colors are derived from our broadband SED parametrization (see Sect. 6.3.5).

[8] As discussed Sect. 6.3.4, we cannot exclude that the reported *WISE* fluxes of PMN J1603−4904 are contaminated by the emission of a neighboring source.

[9] As an exception, Grandi & Palumbo (2004) discuss the detection of a narrow Fe Kα line in the flat-spectrum radio quasar 3C 273, so that the thermal (unbeamed) and the beamed jet emission can be disentangled suggesting the presence of an underlying Seyfert-like component.

[10] However, note that the peak flux of the simple, analytical parametrization with two logarithmic parabolas is not well constrained in the low energy regime and strongly depends on modelling either the extended or compact radio emission (see discussion above).

the highest brightness temperature. This result is in contrast to the typical BL Lac structure of an optically thick core component as the bright end of an one-sided (beamed) jet, where the spectral index changes from flat or inverted to steep further downstream (e.g., Taylor et al., 2005). The brightness temperature of the three components of $T_B \leq 10^{10}$ K is much lower than comparable values of blazars, i.e., of beamed emission (Ojha et al., 2010).

Due to the limited (u, v)-coverage at 22.3 GHz, no unique well-defined model of the brightness distribution at this frequency could be derived. As described above, different extreme models and image alignments were tested within the ranges allowed by the visibility data. No other alignment resulted in a physical representation of the spectral index distribution along the jet (see Sect. 6.3.2).

The comparison of our TANAMI results with flux density measurements of ATCA reveals that the VLBI observations miss ∼20 % of the total flux density at 8.4 GHz. If PMN J1603−4904 is indeed a BL Lac object, this difference could be explained by halo emission equivalent to the top-view of FR I lobes (e.g., Giroletti et al., 2004; Kharb et al., 2010) which might be detected with deeper ATCA observations.

In conclusion, the variability, polarization, and its broadband SED, as well as the VLBI structure and spatial spectral distribution of PMN J1603−4904 appears very atypical compared to blazar properties.

6.4.2. Alternative classification scenarios

The peculiarity of PMN J1603−4904 regarding its classification as a BL Lac type object leaves room for alternative interpretations of the multiwavelength data. In the following we discuss several possible scenarios in an attempt to get a better description of the observed broadband properties. First the more unlikely scenarios are presented, while in Sect. 6.4.3 the more suitable classifications besides the (original) blazar scenario are discussed.

PMN J1603−4904 as a Galactic source:

The source location close to the Galactic plane, the lack of a redshift measurement, and its non-thermal broadband emission might suggest a possible Galactic origin. The very low variability at high energies, however, combined with the lack of periodicity, and the non-detection of an optical galactic companion excludes the possibility that PMN J1603−4904 is a black hole binary system. The unlikely classification as a pulsar wind nebula (PWN), even though no matching pulsar is known, was also considered. Based on its VLBI properties this scenario can easily be excluded: the radio luminosity of PMN J1603−4904 is much higher than usually measured for PWNe (e.g., Frail & Scharringhausen, 1997). Moreover, assuming that the VLBI structure of ∼15 mas corresponds to an extension of a few parsec, which is the mean PWN extension (Gaensler & Slane, 2006), would place PMN J1603−4904 well outside the Galaxy at a distance of a few Mpc. With recent X-ray measurements the location of the (X-ray) source can be confirmed to be well outside the Galaxy (Sect. 6.2.4), further rejecting this scenario.

Symmetric mas-scale morphology caused by gravitational lensing:

As PMN J1603−4904 shows a striking symmetry on mas scales, both in structure and flux density distribution, the possibility of seeing a gravitationally lensed object should be considered. Assuming that this symmetric VLBI structure is influenced by lensing causing fainter doubles of the lensed source within a region of ∼15 mas, the corresponding Einstein radius would be on the order of

several milliarcseconds. It could also be larger, assuming that the lens is located north/south of the source, i.e., not the full ring is seen but only a part of it (yielding the observed elongation). Due to the constant and stable multiwavelength behavior over months to years, a lens of a few solar masses in the parsec regime can be excluded. Moreover, Wilkinson et al. (2001) found that lensing by intergalactic massive objects in the mas-regime is highly unlikely. The lensed system with the smallest separation known to date is S3 0218+35 with 335 mas (Biggs et al., 1999), while other gravitationally lensed systems are beyond VLBI scales. While it is not possible to fully exclude a more massive object ($M_{\rm lens} \gtrsim 10^6\,M_\odot$) located at a distance of a few Mpc causing lensing on mas-scales based on our data, it can be considered to be very unlikely due to the non-detection of a bright optical source within the line of sight. More exotic lenses with masses around $10^{2-5} M_\odot$ at shorter distances (such as intermediate-mass black holes in the Galactic halo or beyond) are unlikely.

6.4.3. More likely alternative classification scenarios

As shown in the previous section, the unusual multiwavelength properties of PMN J1603−4904 cannot be explained by a Galactic black hole or a gravitationally lensed system. Hence, in the following more likely classification scenarios are presented, referring to some of its multiwavelength particularities.

PMN J1603−4904 as an edge-on jet system:

The 8.4 GHz VLBI structure of PMN J1603−4904 suggests a double-sided source like in FR I radio galaxies, but on smaller scales, i.e., a jet-counterjet system seen side-on. The intrinsic symmetry and especially the compactness with a small angular separation could indicate a young, not yet evolved, radio galaxy. In the following we discuss in particular how the multiwavelength data of PMN J1603−4904 are in agreement with general properties of Compact Symmetric Objects (CSOs).

The similarity to the double-sided morphologies of present-day radio galaxies has thus led to the hypotheses that these objects are either the young versions of their larger FR I/FR II counterparts (Fanaroff & Riley, 1974; Readhead et al., 1996; Fanti et al., 1995) or "frustrated" jets, i.e., confined due to interaction with a dense, surrounding medium (e.g., Bicknell et al., 1997; Carvalho, 1998). However, the "evolution" or "youth" scenario is more commonly accepted and further supported by kinematic measurements of the hot spots revealing characteristic ages less than 10^3 years (e.g., Owsianik & Conway, 1998; An et al., 2012). Contrary to flat blazar spectra, the radio spectra of these compact objects show a peak at ∼1 GHz or even a steep spectrum, leading to classification as a GPS or CSS, respectively. CSOs are characterized by a distinct double structure with an intensity ratio of less than 10:1 and similar steep spectra and a central, flat-spectrum component (Peck & Taylor, 2000; Sokolovsky et al., 2011b). They can be distinguished from other radio-loud AGN based on their low radio variability (typically <10% over timescales of years; Fassnacht & Taylor, 2001) and their low radio polarization (≤1%; Peck & Taylor, 2000). Due to the high jet inclination angle little to no motion of individual jet components is observed (with very few exceptions; Owsianik & Conway, 1998; Taylor et al., 2009). Since short-time variability is linked to relativistic beaming, we expect that young radio galaxies show at most only mild broadband variability.

The possibility of γ-ray emission from CSO objects has been considered due to inverse-Compton up-scattering of surrounding photon fields by the lobe electrons (Stawarz et al., 2008; Orienti et al., 2011) and based on that, the first set of *Fermi*/LAT sources has been investigated (McConville et al., 2011), but no unambiguous detection of a γ-ray loud CSO has been confirmed, yet. As a class, CSOs are important sources to probe the origin of high-energy emission in active galaxies and to study

the interaction of jets with the ambient medium in the nuclear region.

The high-resolution TANAMI images of PMN J1603−4904 at 8.4 GHz show a mas-scale structure in agreement with a CSO morphology. This structure, the low $T_{\rm B}$ values, and the steep spectral index distribution of the outer components may indicate a very high jet inclination angle. In such a case, at most moderate relativistic beaming is expected. This possible classification is further supported by only mild long-time multiwavelength variability (Fig. 6.11), the lack of apparent superluminal motion (Fig. 6.6) and high-energy flares (Fig. 6.14), and the stability in flux density and size of the individual jet components. The morphologies of most CSOs show a relatively faint core with respect to the lobe emission (Taylor et al., 1996). If we see PMN J1603−4904 at a large inclination angle, the prominent and putative most active feature would be the central component, which could explain the observed mild variability. Usually CSOs are dominated by their steep spectrum lobes but the greater contribution from the core with its flatter spectrum here could be flattening the overall radio spectrum, resulting in the observed spectral index of $\alpha = -0.4$. In particular, the detected brightness temperatures and the overall radio spectral index of PMN J1603−4904 is consistent with mean values for CSOs of $T_{\rm B,mean} \sim 10^9$ K and $\alpha_{\rm mean} = -0.52$ (between 2.3 GHz and 8.4 GHz) reported by Sokolovsky et al. (2011b), lower than values for bright beamed core-jet sources (Kovalev et al., 2005; Ojha et al., 2010). Due to very sparse frequency coverage below 1 GHz, the available ATCA observations are not sufficient to probe a possible spectral turnover as seen in CSO/GPS sources, though the archival MGPS data could indicate a GHz-peak. The archival measurements by Murphy et al. (2010) give upper limits to the overall polarization of ≤1.2% further supporting the CSO classification.

Our kinematic analysis of three VLBI observation epochs only results in an upper limit on the apparent jet speed (Müller et al., 2014a). Further monitoring showed no significant motion neither in one or in two opposite directions with respect to the central feature. Fig. 6.6 clearly shows that within the errors no relative motion can be measured. Hence, it is not possible (yet) to directly prove a two-sided motion and to determine the age of the radio source.

However, assuming axial symmetry and a jet orientation close to the plane of the sky and using the modelfit parameters (see Table 6.4), the flux ratio of the two extended features gives $R \approx 1.2$, i.e., a corresponding jet-to-counterjet surface brightness ratio. Hence, jet and counterjet exhibit a similar Doppler factor. For other sources in the plane of the sky, e.g., NGC 1052 (Vermeulen et al., 2003), a pattern speed of $\beta \approx 0.25$ is measured. Together with the assumption of optically thin emission with $\alpha = -0.5$, comparing the brightness ratio of the eastern and western component ($R \approx 1.2$) and using Eq. 1.8 (with index $i = 3$) results in an inclination angle of $\theta \sim 84°$. Since both, β and α are rather conservative assumptions, it is unlikely that the inclination angle is smaller.

The intriguing double-sided, symmetric 8.4 GHz emission is confined to an extension of less than ∼ 15 mas (see Fig. 6.4). At a redshift of $z \sim 0.174$ this angular extension of the VLBI structure would translate to a projected size of ∼ 44 pc. There is evidence for a western extension of the mas-scale jet seen in the 8.4 GHz VLBI data and we find a discrepancy between TANAMI and ATCA flux density measurements at 8.4 GHz of ∼20%. This could indicate radio emission at larger scales. Although unexpected for young radio sources, such extended emission in association with a young double source has been reported in the literature (Baum et al., 1990; Tingay et al., 2003) and proposed to be due to recurrent activity in these objects with the extended emission attributed to past epochs of activity. Edwards & Tingay (2004, their Fig. 9) suggest that such 'missing' flux between ATCA and VLBI baselines is more common for a CSS than for a GPS source. ATCA observations at 5.5 GHz and 9 GHz show no extended emission, confirming the compact overall structure of this source down to ∼ 1′, corresponding to ∼ 3 kpc at $z \sim 0.174$.

Adopting this redshift, the radio luminosity at 8.4 GHz is $L_{\rm R} \sim 5 \times 10^{25}$ W Hz$^{-1} = 4 \times 10^{42}$ erg s^{-1} (for a total flux of $S_{8.4\,\rm GHz} \sim 0.6$ Jy), and the X-ray luminosity is $L_X \sim 5 \times 10^{43}$ erg s^{-1} (for $S_{1-10\,\rm keV} \sim$

$5.8 \times 10^{-13}\,\mathrm{erg\,cm^{-2}\,s^{-1}}$). The radio luminosity of PMN J1603−4904 is comparable to the BL Lacs and radio galaxies of the TANAMI sample (Ojha et al., 2010), while the X-ray luminosity is similar to Seyfert galaxies (Type 2 objects) rather than to blazars (Rivers et al., 2013).

Interestingly, the X-ray properties of PMN J1603−4904 resemble those observed for GPS sources (Siemiginowska et al., 2008; Tengstrand et al., 2009) and for CSOs (Vink et al., 2006): compared to quasars the X-ray emission (2-10 keV) of these sources is weak and the absorption columns are higher ($> 10^{22}\,\mathrm{cm^2}$), their median photon index is steeper than for normal radio-loud quasars ($\Gamma = 1.84 \pm 0.24$, Siemiginowska et al., 2008), and the X-ray luminosities are within $10^{42} - 10^{46}\mathrm{erg\,s^{-1}}$. The radio and X-ray luminosities of PMN J1603−4904 are also comparable to corresponding values of strong GPS/CSS sources (Kunert-Bajraszewska et al., 2014). Further, the values derived for PMN J1603−4904 fit into the N_H versus linear size distribution of this study, though its radio to X-ray luminosity ratio is higher for objects with comparable sizes. These additional spectral results make it difficult to reconcile with a common blazar emission model and could further point to a different source classification.

Starburst-like broadband emission:

In general the spectral energy distribution resembles the broadband emission of starburst galaxies (Lenain et al., 2010), where the enhanced IR emission is due to star formation activity. One expects temperatures on the order of a few tens of Kelvin for dust emission (Elbaz et al., 2011) while higher temperatures are explained by enhanced star emission. Nuclear temperatures around $(1\text{–}2)\times10^3$ K are found in Type II Seyferts (Lira et al., 2013).

Four starburst galaxies are also detected in γ-rays by *Fermi*/LAT (Abdo et al., 2010c; Ackermann et al., 2011), M 82 and NGC 253 even up into the TeV range (VERITAS Collaboration et al., 2009; Acero et al., 2009). For this source type, the origin of the γ-ray emission is explained by interactions of cosmic rays with interstellar gas rather than due to AGN activity. At these high energies, starburst galaxies show no significant variability with spectral indices in the range of $\Gamma_\gamma = 2.1\text{–}2.4$ (Ackermann et al., 2012a). In contrast, PMN J1603−4904 shows a mild variability on longer timescales in the γ-rays (see Fig. 6.14 and Ackermann et al., 2013).

Moreover, the γ-ray fluxes of these starburst galaxies are in the range of $(5\text{–}11) \times 10^{-10}\,\mathrm{ph\,cm^{-2}\,s^{-1}}$ (Ackermann et al., 2011). These fluxes are about ten times fainter than the reported γ-ray flux of PMN J1603−4904, which is the most important caveat for this interpretation. Assuming a similar γ-ray luminosity for all sources of this class and assuming the γ-ray emission of PMN J1603−4904 is only due to starburst activity, this would make PMN J1603−4904 the by far most luminous γ-ray loud starburst galaxy. This constraint is a strong argument against the starburst interpretation of the SED, but only if no γ-rays are emitted by an additional AGN or jet. These constraints require further statistics on the γ-ray properties of starbursts.

Lenain et al. (2010) report on the γ-ray emission of radio-loud starburst galaxies and conclude that the parsec-scale jet of NGC 1068 shows a significant contribution to the high-energy emission. These findings could explain the long-term γ-ray variability and the higher flux compared to other γ-ray bright starbursts by a significant influence of the AGN. This is further supported by the high core dominance, suggesting that the center is the putative most active region if we really see the source at a large inclination angle, as discussed in the previous paragraph.

Though better multiwavelength coverage is required to precisely interpret the SED, it is striking that the IR emission, the γ-ray spectral index and its low (long-term) variability are in good agreement with starburst broadband properties. Further optical, IR and mm/sub-mm observations are required to confirm this result.

Observations of radio-loud starbursts show evidence for a CSO-starburst connection. Tadhunter et al. (2011) find that radio-loud starburst galaxies tend to show morphologies unlike typical FR I/II-class objects. Compact radio sources ($d < 15$ kpc) are found to have a significantly higher star formation rate than more evolved sources, however, a possible selection effect must be considered (Dicken et al., 2012). Hence, no simple interpretation of merger-induced star formation triggering jet activity can generally be applied.

According to the available multiwavelength data and keeping in mind the most limiting factor, the lack of well constrained optical spectra, this classification scenario gives an intriguing picture of the possible nature of PMN J1603−4904. The γ-ray emission could be explained by a contribution of the starburst activity but definitely requires an additional (dominating) spectral component to model the contribution of the AGN emission to compensate for the disagreement in brightness and long-term variability not seen in γ-ray bright starburst galaxies. This alternative interpretation of the broadband emission would be more plausible, but contributions of the young radio jet as proposed by Stawarz et al. (2008) should still be considered.

6.5. Summary and conclusions

The first VLBI observations and additional multiwavelength data for PMN J1603−4904 were presented. It exhibits multiwavelength properties atypical for well-established γ-ray emitting object classes. Therefore, several classification scenarios are discussed and it is found that the source is most likely either a very peculiar BL Lac object or a CSO. The γ-ray brightness is well explained if PMN J1603−4904 is indeed a blazar, though the broadband emission and the mas-scale structure are very unusual. These spectral and structural features, atypical for a blazar, are accounted for by the alternative classification as a misaligned young radio source, possibly in a host galaxy with starburst activity.

If it is confirmed that this source is indeed not a BL Lac, it will add to the class of misaligned γ-ray bright sources. Only a few such sources are known and PMN J1603−4904 would be the first CSO in this class (Abdo et al., 2010g). The confirmed detection of a γ-ray bright CSO would challenge current jet emission models attempting to explain the high-energy spectral component with high beaming factors and would help to determine the region from where γ-rays are emitted. Hence, PMN J1603−4904 would be an important object to study the emission of high-energy photons in these misaligned sources and to address the open question of whether their γ-ray brightness is due to a beamed jet, lobe emission, or a combination of both.

6.6. Outlook

TANAMI observations are ongoing, and with additional VLBI epochs, the kinematic analysis will be better constrained. Low resolution radio observations will be made at lower frequencies to better constrain the radio spectrum.

The TANAMI team will be attempting deeper photometric observations in the NIR (where the effects of Galactic extinction would be less severe) in order to establish the point source counterpart and obtain a spectrum further constraining the redshift. With additional sub-mm/mm and optical observations the broadband SED will be much better constrained. The presented preliminary results of the recent X-ray observations with *Suzaku* and *XMM* will be studied in more detail and are in preparation for publication (Müller et al., in prep). Further data of the ongoing *Fermi*/LAT monitoring will be analyzed, to investigate the high energy properties of this source.

A very singular double nebula, about 2.5′ long, and 1′ broad, a little unequal...

(James Dunlop, 1826, "A Catalogue of Nebulae and Clusters of Stars in the Southern Hemisphere")

7. Centaurus A at sub-parsec scales

At a distance of only about 3.8 Mpc (Harris et al., 2010), the giant elliptical galaxy Centaurus A (Cen A, PKS 1322−428, NGC 5128) hosts the nearest active galactic nucleus. The radio source Cen A is usually classified as a Fanaroff-Riley Type I radio galaxy (Fanaroff & Riley, 1974), showing double-sided jets which end in giant radio lobes at kiloparsec scales (see Fig. 7.1 and Clarke et al., 1992). Due to its proximity, an angular resolution of one milliarcsecond (mas) corresponds to a linear size of just ∼0.018 pc (see Fig. 1.2), this source is an exceptionally good laboratory for studying the innermost regions of AGN, testing different jet formation, collimation and emission models. In this Chapter, the spectral and kinematical properties of the jet-counterjet system of Cen A at sub-parsec scales are presented. The observations were performed in the framework of the TANAMI program and are complemented by additional multiwavelength data to establish an overall image of the innermost region of this radio galaxy.

Figure 7.1.: Multiwavelength view of Cen A: *Left:* Extreme deep field optical image of the elliptical host galaxy taken by the amateur astronomer R. Olsen (120 hours of total exposure, `www.rolfolsenastrophotography.com`). *Middle:* Multiwavelength composite of the inner lobes reaching beyond the extension of the elliptical galaxy. *Chandra* X-ray data in blue, microwave APEX in orange and optical (Credit: ESO/WFI; MPIfR/ESO/APEX/Weiss et al.; NASA/CXC/CfA/Kraft et al.). *Right:* 1.4 GHz image of the giant radio lobes with an extension 20 times larger than the projected size of the full moon, by ATCA and Parkes (Credit: CSIRO/ATNF). The innermost part (less than 1 pc) of these jets (see also Fig. 1.2) is addressed in this Chapter.

7.1. Introduction: multiwavelength view of Cen A

Centaurus A is by far the closest active galaxy and detected throughout the electromagnetic spectrum and is considered to be a likely source candidate to produce ultra-high energy cosmic rays (UHECRs; Clay et al., 2010) and extragalactic neutrinos (Cuoco & Hannestad, 2008; IceCube Collaboration et al., 2009). Hence, it is hardly surprising that it is considered to be an ideal candidate to study extragalactic jets (and more), and that it is one of the most studied sources in the sky. It would be beyond the scope of this thesis to cover all studies and results on this prominent object. Detailed reviews are given by Israel (1998) and Steinle (2006, 2010). In the following, its multiwavelength characteristics (from pc to kpc scales) will be introduced focussing on the properties, which are further investigated as part of this work.

All the individual features of this FR I radio source with its elliptical host galaxy can only be studied with extensive multiwavelength observations to get "the big picture" of Cen A. These observations reaveal star forming regions, compact galactic objects, neutral, molecular and ionised gas, X-ray radiation due to the diffuse, hot gas, and broadband emission of the powerful radio jets. The proximity of Cen A allows us to study this source in incomparable detail in the context of AGN and merger physics trying to disentangle the complex source properties, like emission processes or interactions between individual components.

Parsec- to kiloparsec-scale structure

Centaurus A is thought to be a recent merger which was likely to be responsible for the complex appearance and properties observed today, for example the dust lane bisecting the galaxy (see Fig. 7.1) and the higher star formation rate than expected for elliptical galaxies (e.g., Beasley et al., 2008). The central engine of the AGN activity is the supermassive black hole with a mass of $M = 5.5 \pm 3.0 \times 10^7 \mathrm{M}_\odot$ (Neumayer, 2010). Beyond the elliptical galaxy, the powerful jets are ejected under a large angle to the line of sight[1] and extend up to kilo-parsec scales ending in the giant (outer) radio lobes. They comprise the inner lobes, detected in the radio as well as in the X-rays (see Fig. 7.1 and Kraft et al., 2002; Hardcastle et al., 2003). The innermost of the jet-counterjet system has been well studied at parsec-scales prior to the observations presented in this Chapter. Studies by Tingay et al. (1998, 2001) and Horiuchi et al. (2006) revealed a bright jet and a faint counterjet at a viewing angle of $50^\circ - 80^\circ$ to the line of sight. Kinematic studies resulted in a sub-luminal apparent motion of $v_{\mathrm{app}} = 0.1c$ to $0.45c$ (Tingay et al., 2001; Hardcastle et al., 2003).

The appearance of Cen A heavily changes when switching the observing frequency. In the optical, Dunlop (1828, and later J. Herschel) already noticed the peculiar shape with apparently two emission zones of the *"very singular double nebula"* in the constellation Centaurus, which is now resolved and explained by an edge-on dust lane across the elliptical galaxy. This dusty and gaseous band lies almost perpendicular to the radio jets and is obscuring the (optical) view to the inner parts of the galaxy. In the infrared, *Spitzer* observations revealed a dusty wrapped disk with a parallelogram shape within this gas and dust lane (Quillen et al., 2006), recently further investigated in the (sub-)mm band by ALMA (ESO Publication Office, 2012). Going to higher angular resolution, mid-IR VLTI observations by Meisenheimer et al. (2007) and Burtscher (2011) indicate an unresolved point source at pc-scales with an additional extended emission component, possibly identified with a torus-like structure. Interestingly, at higher energies, X-ray monitoring with the *Rossi X-ray Timing Explorer (RXTE)* detected variability of the absorption column, which

[1] The angle to the line of sight is not constant over the extension of the radio source but thought to be more tilted towards the observer than at parsec scales (Hardcastle et al., 2003). In general, the northern part is thought to be beamed towards the observer. See Sect. 7.6.1 for more details.

can be well explained in the context of a clumpy torus model (Rothschild et al., 2011; Rivers et al., 2011). Further supporting the picture of large amount of gas and dust close to the SMBH with a non-isotropic distribution are the observations by Ott et al. (2013). They report on the detection of H_2O maser emission line from the inner 3 pc, possibly due to jet maser emission, i.e., a molecular cloud is shocked by the jet.

The kiloparsec scale jets of Cen A are detected and resolved in the X-rays by *Chandra* observations (see Fig. 7.1 and Kraft et al., 2002). Individual jet "knots" are moving with an apparent speed of $\beta_{\rm app} \sim 0.5$ and can be associated with bright radio features seen in the VLA images (Hardcastle et al., 2003). This "knotiness" of the jet at kpc-scales can be explained by collisions with stars in the host galaxy (Goodger et al., 2010; Tingay & Lenc, 2009; Hardcastle et al., 2003) and give evidence for a spine-sheath structure due to the distribution of the spectral indices of individual knots (Worrall et al., 2008). This is further discussed in Sect. 7.6.

Due to its proximity, also two different γ-ray emission components in Cen A can be resolved by *Fermi*/LAT: besides the powerful active nucleus (for which the explicit emission region(s) are still under debate, see Sect. 7.3), the giant lobes are detected by the *Fermi*/LAT (Abdo et al., 2010e,d). It is hence one of the rare extended objects at these high energies.

In order to study the high energy emission properties of extragalactic jets, observations of Cen A allow us to better (spatially) disentangle the individual emission components of the central region, which make up the broadband SED, than for (most) other extragalactic jets (see below).

Broadband spectral energy distribution of the AGN

Cen A is detected throughout the electromagnetic spectrum. Its proximity allows us to study individual emission features in detail. Even at X-rays and γ-rays, it appears not as a point source, in contrast to many other extragalactic jets. The broadband spectral energy distribution of its core/nucleus[2] resembles blazar SEDs clearly showing a double-humped shape (see Fig. 7.2, Sect. 1.3.1, and Abdo et al., 2010e).

Cen A is a bright radio source with a strong jet and lobe emission at different scales (see above). In the IR to optical regime the dust emission is dominating the spectrum. At higher energies, the emission associated with the AGN makes up the spectrum. In the X-rays, the overall spectral shape can be described by an absorbed power law (with $\Gamma \sim 1.8$) with fluorescence lines (Markowitz et al., 2007; Evans et al., 2004), though the spectrum shows various complex features, like the soft diffuse component. Fukazawa et al. (2011) reported on spectral hardening in the X-rays during an active phase (onset end of 2007), suggesting a jet origin of the X-ray brightening, as Cen A shows a "harder when brighter" behaviour (see Sect. 7.7 for further discussion).

After the detection in the γ-rays by *CGRO*/EGRET (Hartman et al., 1999), *Fermi*/LAT confirmed that Cen A is a bright and steady (i.e., no major flaring events are detected) source (Nolan et al., 2012; Sahakyan et al., 2013). At TeV energies, it was detected by HESS (Aharonian et al., 2009).

Why are high-resolution observations of Cen A indispensable?

In our cosmic neighbourhood, Cen A is the closest radio galaxy with a broadband spectrum very similar to blazar SEDs. Observations at high angular resolution give insight at unprecedented linear scales down to some tens of light days. It is a perfect laboratory to study AGN activity and the interaction with the ambient medium. The multiwavelength monitoring allows us to test

[2]Note that the spectrum of "the core or nucleus" includes all unresolved (i.e., from the central point source) emission components.

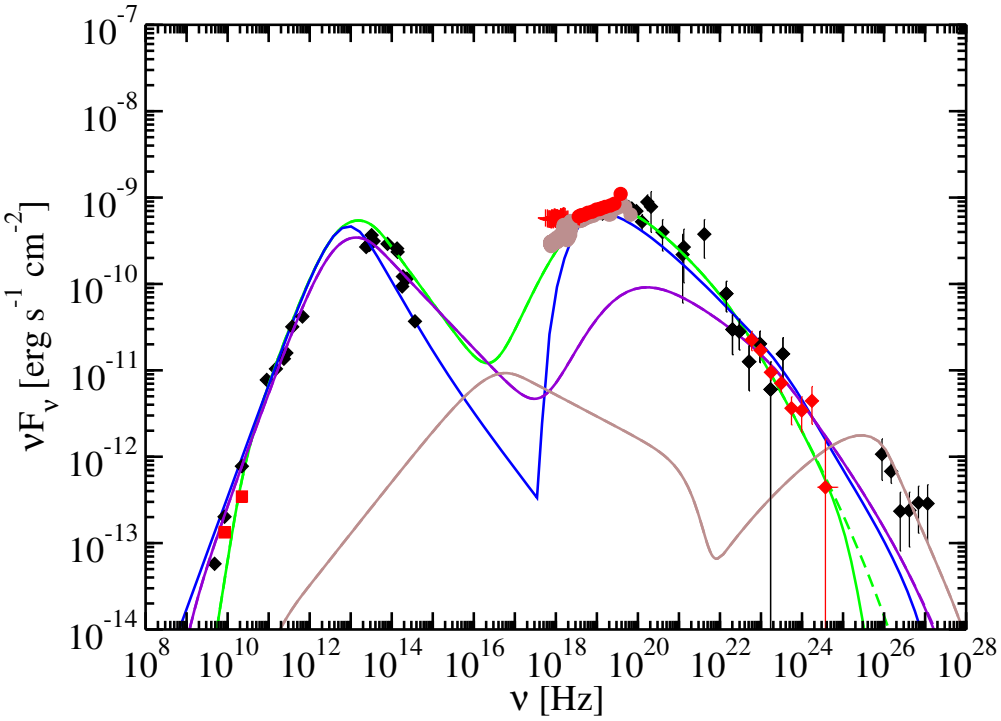

Figure 7.2.: Broadband SED of the core of Cen A from Abdo et al. (2010e) including TANAMI dual-frequency measurements of 2008 November (see Sect. 7.3 and Müller et al., 2011). Simultaneous observations are shown in red (radio: TANAMI, X-ray: *Swift*/XRT & BAT *Suzaku*, γ-ray: *Fermi*/LAT), archival in black (including H.E.S.S.). Different SED models are shown: synchrotron/SSC fit to the entire data set (green), under-fitting the X-ray data (violet), and fitting H.E.S.S. data included (brown). The blue curve gives a decelerating jet model fit (details in Georganopoulos & Kazanas, 2003b). Note that the proximity of Cen A allows us to associate parts of the emission with extended features, but for most instruments it remains a point source. Therefore, this SED is composed of the unresolved emission components, assuming that the main part originates from the central component (see Sect. 7.3 for detailed discussion). Figure from Abdo et al. (2010e).

jet emission and formation models. Such detail investigations aim for information about AGN in general and allow the transfer to findings of more distant objects.

In this work, I present detailed the analyses of the highest resolution observations of an AGN jet ever. This study gives information on the jet structure and propagation close to the SMBH at sub-parsec scales. The spectral index distribution helps to constrain the production sites of high energy photons (Müller et al., 2011). The combination of multiwavelength and the high resolution monitoring of the jet evolution allows me to investigate possible intraband correlations, an important indication on the underlying emission mechanism.

The following sections on the spectral index imaging are strongly based on the conference proceedings Müller et al. (2010), and the related publication in 'Astronomy and Astrophysics' (Müller et al., 2011) and taken partly almost verbatim from there. First results on the kinematics have been discussed in my Diploma thesis (Müller, 2010), the conference proceedings Müller et al. (2012) and Müller et al. (2013), and will be published in 'Astronomy and Astrophysics' (Müller et al., 2014b), such that large parts of the following sections are there adopted.

7.2. VLBI observations with TANAMI

In the framework of the VLBI monitoring program TANAMI (see Sect. 3 and Ojha et al., 2010), Cen A has been monitored at 8.4 GHz since 2007 approximately twice a year, including one simultaneous observation at 22.3 GHz in 2008 November. The data processing was performed as described in Sect. 3.1. A log of observations and the corresponding image parameters can be found in Table 7.1. This includes the specific array configuration of each experiment which, in general, varies from epoch to epoch. Due to the contribution of different non-LBA telescopes at different epochs, the (u, v)-coverage, array sensitivity, and angular resolution varies between the different observations.

The highest angular resolution was achieved in 2008 November (Müller et al., 2011), resulting in the best-ever image of an AGN jet. In addition, this experiment was designed as a dual-frequency observation to obtain the highest resolution spectral index image of Cen A. For that reason, first, the results of this particular observation are summarized in Sect. 7.3. Note that first results of the corresponding dual-frequency analysis were already presented in Müller (2010). This study was continued within the scope of this thesis (see also Müller et al., 2014b). The series of 8.4 GHz observations from 2007 November to 2011 April are presented in Sect. 7.4, leading over to the discussion of the jet dynamics (Sect. 7.5).

Table 7.1.: Details on TANAMI observations of Centaurus A (natural weighting)

Observation Date (yyyy-mm-dd)	Array Configuration[a]	S_{peak} (Jy beam^{-1})	RMS (mJy beam^{-1})	S_{total} (Jy)	b_{maj} (mas)	b_{min} (mas)	P.A. (°)
8.4 GHz							
2007-11-10	PKS-HART-CD-HO-MP-AT	0.60 ± 0.09	0.40 ± 0.06	2.61 ± 0.39	1.64	0.41	7.9
2008-06-09	PKS-HART-CD-HO-MP-AT	1.06 ± 0.16	0.63 ± 0.09	3.11 ± 0.47	2.86	1.18	−12.7
2008-11-27[b]	PKS-CD-HO-MP-AT-DSS43-TC-OH	0.74 ± 0.11	0.37 ± 0.06	3.91 ± 0.59	0.98	0.59	31.4
2009-09-05	PKS-CD-HO-MP-AT-DSS43-TC-OH	0.76 ± 0.11	0.45 ± 0.07	3.97 ± 0.60	2.29	0.58	15.6
2009-12-13	PKS-CD-HO-MP-AT-TC	1.03 ± 0.15	0.18 ± 0.03	3.82 ± 0.57	3.33	0.78	26.3
2010-07-24	PKS-CD-HO-MP-AT-TC	1.21 ± 0.18	0.38 ± 0.06	4.20 ± 0.63	2.60	0.87	21.4
2011-04-01	HART-CD-HO-MP-AT-DSS43-WW	0.63 ± 0.09	0.31 ± 0.05	5.10 ± 0.77	2.31	0.514	−0.7
22.3 GHz							
2008-11-29[b]	PKS-CD-HO-MP-DSS43-AT	1.77 ± 0.27	0.47 ± 0.03	3.41 ± 0.5	2.01	1.27	−87.9

[a] AT: Australia Telescope Compact Array, CD: Ceduna, HART: Hartebeesthoek, HO: Hobart, MP: Mopra, OH: GARS/O'Higgins, PKS: Parkes, TC: TIGO, TI: DSS43 - NASA's Deep Space Network Tidbinbilla (70 m), WW: Warkworth

[b] The dual-frequency and especially the 8.4 GHz observations are presented in detail in Sect. 7.3 and are published in Müller et al. (2011).

7.3. Spectral analysis on sub-parsec scales

The combination of the excellent (u,v)-coverage of the TANAMI array at 8.4 GHz and 22.3 GHz (see Fig. 7.3) and the proximity of Cen A results in the highest resolution observation of an AGN jet (see Fig. 1.2) and, in addition, the construction of the best resolved spectral index map of Cen A. Here, I summarize the results of this dual-frequency observation of 2008 November. The following section is strongly based on the corresponding results published in Müller et al. (2011), such that parts are quoted verbatim from there[3], and analyses presented in Müller (2010).

7.3.1. Dual-frequency observations

In 2008 November 27/29, Cen A was observed by TANAMI at 8.4 GHz and 22.3 GHz at mas resolution. Table 7.1 summarizes the array configuration and the corresponding image parameters using natural weighting. In addition, to make the best of these highest resolution observations, uniformly weighted images were produced. Table 7.2 gives the corresponding image parameters. Figure 7.4 shows the imaging results at 8.4 GHz and 22.3 GHz with both weightings, respectively. Using uniform weighting at 8.4 GHz, an angular resolution of (0.7×0.4) mas at a position angle of $\sim 33^\circ$ is achieved corresponding to linear scales of less than 0.013 pc (≤ 3500 AU).

The lack of intermediate baselines at 8.4 GHz is the major constraint on the image fidelity (see Fig. 7.3). Such uneven sampling of the (u,v)-coverage can cause spurious artefacts (see, e.g., Lister et al., 2000). The reliability of the imaging with the `clean` algorithm is tested in several ways. First, it was checked whether the model consistently describes the uncalibrated visibility data. Secondly, the effect of self-calibration was tested by iteratively modeling the data with and without including particular features. Finally, the total calibration uncertainties and on-source errors due to the uneven (u,v)-coverage were estimated to be on the order of 15 % at both frequencies along the inner $\sim$15 mas of the jet. In Sect. 7.3.2 the error estimation is described in detail. The comparison with the series of 8.4 GHz TANAMI images of Cen A, though at lower resolution, lead to the identification of the same bright features, hence, a certain self-consistency (see Sect. 7.4).

At both frequencies, the TANAMI images show a well collimated jet[4] with an opening angle $\theta \lesssim 12^\circ$ at a mean position angle of PA$\sim 50^\circ$ and a fainter counterjet at PA$\sim -130^\circ$. The highly resolved 8.4 GHz image shows a small displacement of the counterjet from the axis with an emis-

[3] Note that 'Astronomy and Astrophysics' holds the copyright for the content.

[4] In contrast to M 87 (Junor et al., 1999), no rapid broadening of the jet opening angle is seen, although the linear resolutions are comparable. The jet of Cen A is therefore already well collimated on scales of 0.1 pc $= 10^{15}$ m. However, the mass of the central black hole of M 87 is two orders of magnitude higher than that of Cen A so TANAMI observations are accessing very different parts of the jet as measured in Schwarzschild radii.

Table 7.2.: Image parameters (uniform weighting)

Frequency [GHz]	RMS [mJy beam^{-1}]	S_{peak} [Jy beam^{-1}]	$T_{\mathrm{B,peak}}$ [10^{10}K]	S_{total} [Jy]	b_{maj} [mas]	b_{min} [mas]	P.A. [°]
8.4	0.45 ± 0.02	0.48	2.84	3.2 ± 0.1	0.68	0.43	33
22.3	1.20 ± 0.10	1.46	0.19	3.3 ± 0.1	1.55	1.21	-75

Columns show: (1) weighting scheme; (2) observing frequency; (3) observation epoch; (4) RMS noise in the clean images; (5) peak flux density; (6) brightness temperature; (7) total integrated flux density; (8,9,10) major axis, minor axis, and position angle of the restoring beam

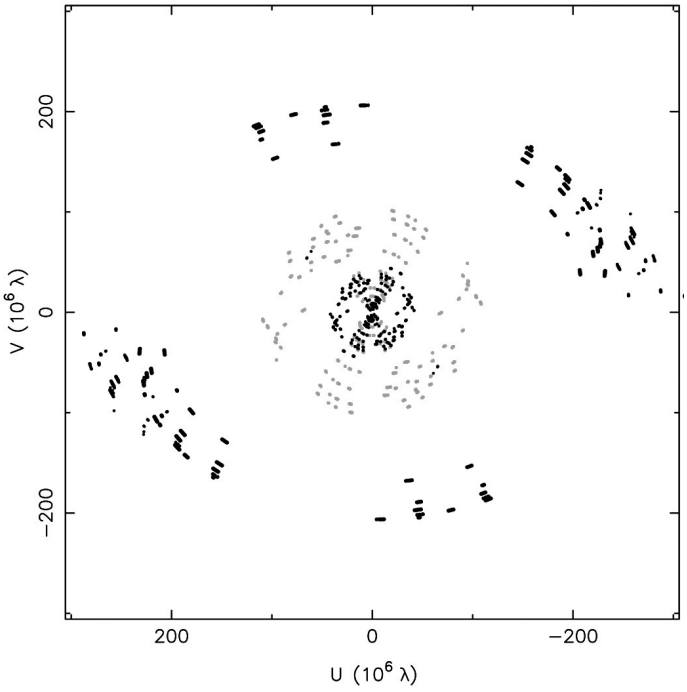

Figure 7.3: TANAMI (u, v)-coverage at 8.4 GHz (black) and 22.3 GHz for Cen A (2008 November, Figure from Müller et al., 2011).

sion gap in between the approaching and receding jet. At 22.3 GHz, the counterjet is considerably weaker. At 8.4 GHz, the counterjet feature around position R.A. $= -18$, Dec $= -14$, a limit of the spectral index of $\alpha < -2.5$ can be derived. The overall structure, like the position and opening angle at both frequencies are remarkably similar to the corresponding values of the kiloparsec scale jet seen on scales of $\lesssim 4'$ (Clarke et al., 1992). Several significant emission features are distinctly detected at both frequencies. In Sect. 7.6, I discuss the findings in detail. At this high resolution, a jet widening and subsequent narrowing at ∼25 mas (≈ 0.45 pc), is clearly detected (see Sect. 7.6.3).

7.3.2. Estimation of VLBI calibration-error of TANAMI observations

VLBI observations always suffer from incomplete sampling in the spatial frequency regime which can result in image artefacts. In the case of the TANAMI array, the lack of intermediate baselines between the LBA and the two transoceanic antennas (see Fig. 3.2 and 7.3) is the major constraint. The total calibration uncertainty is conservatively set to ∼20%. In order to determine the on-source errors occurring due to the incomplete (u, v)-coverage the following test was performed using the example of the dual-frequency observation of Cen A.

"Fake" data sets at both frequencies were produced. For the simulated data, we used the (u, v)-coverage of Cen A in the experiments of November 2008 (see Fig. 7.3 and Müller et al., 2011). The brightness distributions from the naturally weighted `clean` images (see Fig. 7.4) were used as the input models. At both frequencies, five data sets were simulated, each with slightly different (randomized) noise parameters. These were imaged and convolved with the same beam and compared to the "real" map from the input models.

Focussing on the inner ∼15 mas of the jet and sampling the cut along the jet (PA∼ 50°) at every 0.1 mas, the distribution of the deviations between "real" and "fake" data can be fitted with a Gaussian to determine the standard deviation (see Fig. 7.5). Even though the individual data points are not fully independent and the number of data sets is too small for a true Monte Carlo analysis,

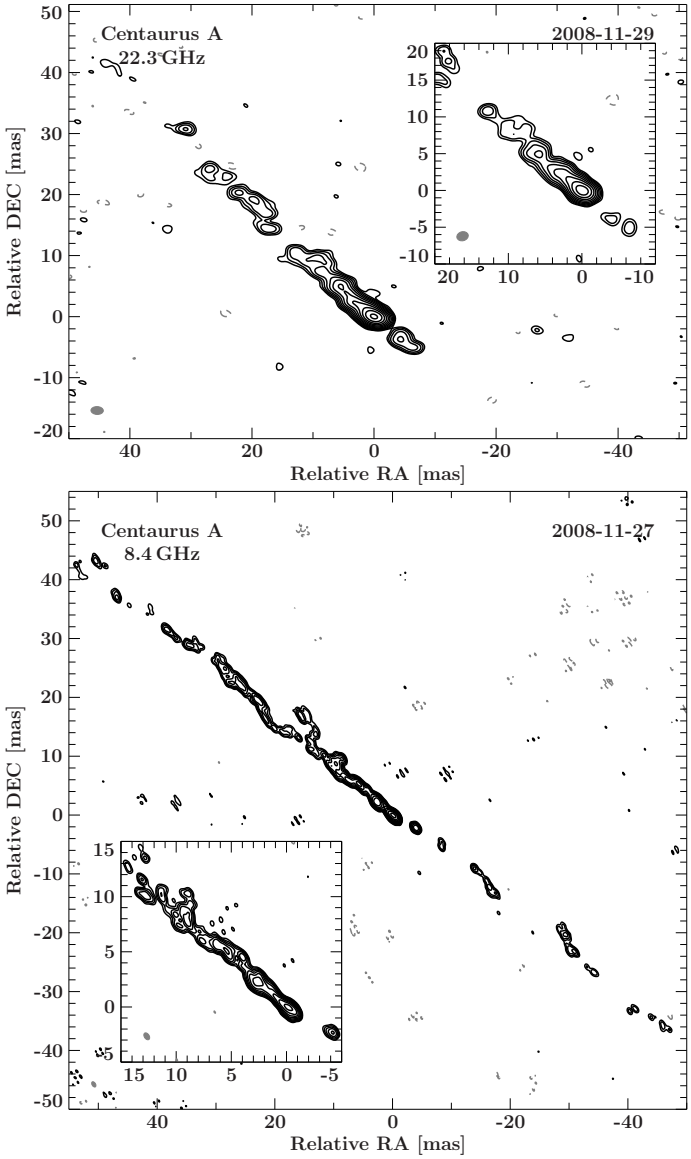

Figure 7.4.: 22.3 GHz (*top*) and 8.4 GHz (*bottom*) `clean` contour image of Cen A from the dual-frequency observation in 2008 November using natural weighting (see Table 7.1). The inset shows the innermost region using uniform weighting (see Table 7.2). The black contours indicate the flux density level, scaled logarithmically and separated by a factor 2, with the lowest level set to the 3σ-noise-level. Gray contours are negative. All axes are in units of mas relative to the phase center. The ellipse in the lower left corner of each panel indicates the restoring beam. Images based on Müller et al. (2011).

this distribution shows the typical scale of on-source fluctuations along the jet of Cen A. The on-source errors are typically smaller than 15% for the bright part of the jet. For the outer regions in the image, the on-source errors gradually grow and can exceed 100 % towards the counterjet at 8.4 GHz.

7.3.3. Spectral index image

The simultaneity of this TANAMI dual-frequency observation allows the construction of a spectral index image to study the spectral distribution along Cen A's jet constraining the physical properties of the radio emission (see Müller et al., 2011, for more details).

The self-calibration procedure of the synthesis imaging results in a loss of absolute source position information. In order to determine the spatial spectral index distribution, the frequency-dependent "core" shift of self-absorbed, optically thick emission features (see Sect. 1.3.1 and, e.g., Lobanov, 1998) has to be taken into account. Modeling the visibility data with Gaussian components and aligning the optically thin jet components results in an offset between both images

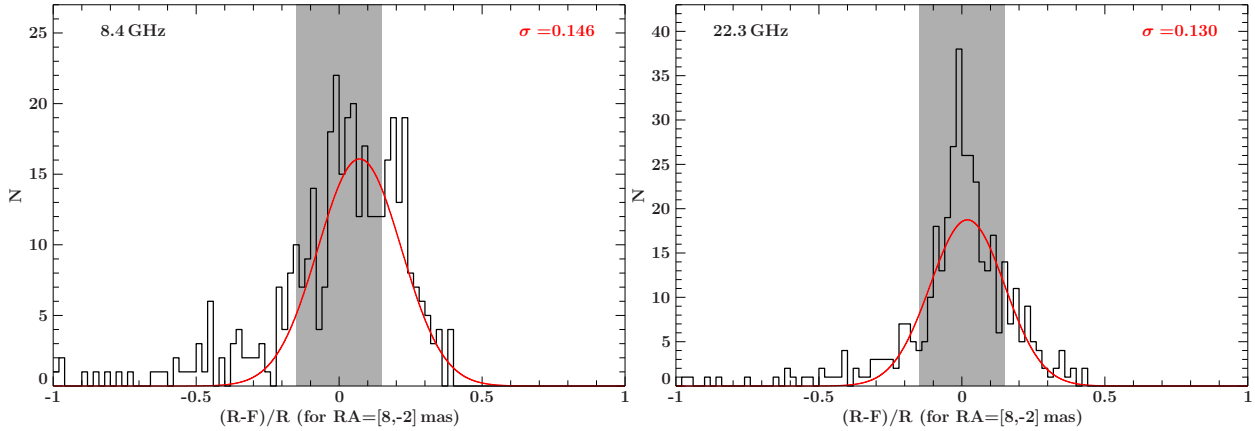

Figure 7.5.: Estimation of VLBI on-source errors due to incomplete (u, v)-coverage of the TANAMI array. Shown are the distributions of (normalized) deviations of the "fake" (F) to the "real" (R) data for both frequencies (left: 8.4 GHz, right 22.3 GHz) for the inner jet of Cen A (defined by RA= $[8, -2]$ mas, see Fig. 7.4). The distribution are fitted with a Gaussian to determine the standard deviation σ. In both cases the uncertainty is less than 15% (given by the gray shaded area).

of $\Delta\mathrm{RA}_{\mathrm{rel}} = -0.25$ mas and $\Delta\mathrm{DEC}_{\mathrm{rel}} = -0.2$ mas. Applying the shift to the images and restoring both images with a common beam of (1.61×1.02) mas (PA= 88°), a spectral index image can be constructed (see Fig. 7.6). For further details on the analysis see Müller (2010) and Müller et al. (2011).

The innermost jet emission feature with the highest flux density has an inverted spectrum and shares other characteristics of the compact feature at the upstream-end of most blazar jets, therefore, it will here also called "the core" of the jet.

It is worth mentioning that the linear resolution in these VLBI images is orders of magnitude better than in most images of blazar jets. As a consequence most of the structure seen here within the central parsec would be contained in "the core" if Cen A was observed at a smaller angle to the line of sight or at a larger distance.

7.3.4. Discussion of the spectral index distribution

The first sub-parsec scale spectral index image of Cen A is presented in Fig. 7.6 (Müller et al., 2011). The overall spectral index (bottom panel) of the inner $\sim$ 18 mas of the jet changes from inverted/flat $(0 < \alpha < 2)$ to steep further downstream. The core region shows an optically thick spectrum, remaining remarkably flat over the inner few milliarcseconds. Numerical simulations by Mimica et al. (2009) showed a similar trend of the evolution of the spectral index and flux distribution along the jet for overpressured jets. In contrast to the theoretical expectations (Marscher, 1980; Königl, 1981) of an inhomogeneous[5] jet, the expansion does not result in a spectral steeping but shows a pattern of with steep to flat spectral indices. The formation of such a spectral index distribution along the jet axis strongly depends on the magnetic field strength and the pressure conditions (see Mimica et al., 2009, for details).

The core is the innermost visible part of the jet at these frequencies, while further upstream the central part is self-absorbed. The second brightest emission component at ~3.5 mas downstream at both frequencies is found to be stationary (see Sect. 7.6.2) with a steep spectrum. Co-spatial with

[5]The jet is inhomogeneous due to the decrease of magnetic field strength, electron population density and electron density with increasing radius.

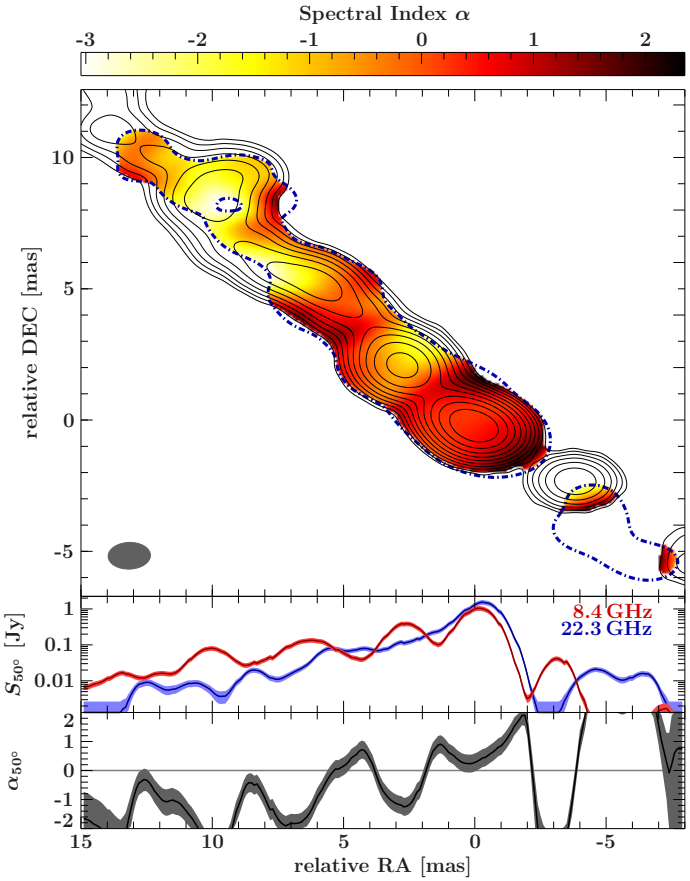

Figure 7.6: *Top:* Spectral index image derived from the flux densities at 8.4 GHz and 22.3 GHz. The flux density distribution at 8.4 GHz is shown in solid black contours. The dashed blue contour shows the 3σ-noise level at 22.3 GHz. Both maps have been restored with a common beam of (1.61 × 1.02) mas (at 88°) represented by the gray ellipse in the lower left corner. *Middle:* Flux density distribution at 8.4 GHz (red) and 22.3 GHz (blue) for a narrow strip (width of 0.1 mas) along the jet at a PA=50° corrected for the shift of $\Delta\text{RA} = -0.25$ mas and $\Delta\text{DEC} = -0.2$ mas. *Bottom:* Spectral index given by the flux densities at PA=50°. Uncertainties correspond to the absolute calibration uncertainties and on-source errors of ∼15 % and consider the image noise at both frequencies, shown as shaded regions around the best-fit distributions (solid lines). Figure adapted from Müller et al. (2011).

the jet-widening region at ∼25 mas at 8.4 GHz, the 22.3 GHz image suggests a possible emission component, which might be interpreted as an obstacle hit by the jet (see Sect. 7.6.3). However, the limited (u, v)-coverage complicates spatially resolved spectroscopic analysis and requires further high-resolution observation at 22.3 GHz.

The central part of the jet indicates a sign of free-free absorption as already observed by Tingay et al. (2001). The peak of the innermost 22.3 GHz counterjet component has an offset of about 1 mas to the south-west with respect to the 8.4 GHz counterjet. This appearance can be interpreted by free-free absorption in an obscuring torus as observed in other two-sided extragalactic jets (e.g., Kadler et al., 2004). Further 22.3 GHz observations of Cen A at this high resolution are required to confirm this result, as it is puzzling that the well-defined 8.4 GHz component at $\Delta\text{RA} = -4$ mas, $\Delta\text{DEC} = -2$ mas seems to have no obvious counterpart at 22.3 GHz. Free-free absorption might also affect the innermost part of the approaching jet and could be a possible explanation for the observed flat spectral index distribution.

It is still an open question, where the high energetic photons detected from extragalactic jets are produced. *Fermi*/LAT detected γ-ray emission from the core of Cen A (Abdo et al., 2010e), though the angular resolution of the LAT prevents to locate the emission region(s) better than ∼ 1° (see Sect. 2.2.1). The TANAMI VLBI observations allow us to study the spectral index distribution at mas scales. The production sites of high energetic photons are expected to be compact, and to have high brightness temperatures and inverted to flat spectral indices. Therefore, resolving the jet at sub-parsec scales, such emission features can be identified.

The spectral index distribution of the inner jet of Cen A indicates multiple optically thick emission regions in the core region although a gradual steepening behavior can be seen. These optically

thick regions can hence be identified as multiple possible production sites of high energy photons. The (quasi-)simultaneous broadband SED of the core of Cen A by Abdo et al. (2010e, see Fig. 7.2) includes these TANAMI spectral data from the inner 0.9 mas × 0.29 mas[6]. The authors model the broadband emission with single-zone models. However, the results of the detailed TANAMI analysis strongly suggest to consider also multi-zone emission models to describe the full radio to TeV range of the SED. Furthermore, in order to distinguish between the different emission models, the broadband coverage needs to be improved, especially in the (soft) X-ray regime. Within the scope of this work *XMM-Newton* and *Suzaku* observations have been performed[7] to study the evolution of the X-ray spectrum. The main goal is to construct simultaneous broadband SEDs to better constrain emission models. For that purpose it is crucial to disentangle the emission components, and hence determine the physical emission sites, contributing to the X-ray spectrum (see also Sect. 7.7).

7.4. Total intensity 8.4 GHz images

Figures 7.7 and 7.8 show the series of naturally weighted images of the first seven TANAMI observations at 8.4 GHz with mas-resolution (Müller et al., 2014b). The image parameters and observation characteristics are listed in Table 7.1. The comparison of the images with different angular resolutions and dynamic ranges (defined as ratio of peak brightness to three times the RMS noise level) from ∼500 to ∼1900, give a better constraint on the position and motion of individual bright jet features.

These images display the jet of Centaurus A in unprecedented detail, clearly resolving particular jet features. The jet-counterjet system is detected in all images and is already well collimated on sub-parsec scales. The jet emission is significantly detected up to a maximum extent of ∼ 70 mas from the image phase center. Hence, TANAMI observations probe the inner ∼ 1.3 pc of the jet. The overall appearance is of a confined, straight jet, showing particular bright emission features which are partly resolved. No major kinks or bends are detected. The detection of the counterjet is significant with a much lower signal-to-noise ratio. It is as strongly collimated as the jet.

The stacked flux density profile along the jet axis with a mean position angle of P.A. ∼ 50° (Fig. 7.9) reveals a declining surface brightness distribution, with resolved individual emission humps.

Assuming an overall calibration uncertainty of 15% (see Sect. 7.3.2 and Müller et al., 2011), the flux density of the inner jet (defined as $-2\,\mathrm{mas} \leq \mathrm{RA}_{\mathrm{relative}} \leq 15\,\mathrm{mas}$) shows an increasing trend over the period of observations reported here (∼3.5 years). In particular, a flux density increase between 2007 and 2009 is measured (see discussion in Sect. 7.7).

The VLBI core of the jet at 8.4 GHz is identified as the brightest feature in the map. This result is based on the spectral index imaging in Müller et al. (2011) as well as on the comparison of every single epoch with each other, i.e., the remarkably similar overall jet structure and a stable peak flux density. The brightest jet knot appears as a pronounced, isolated feature in the stacked profile (see Fig. 7.9). It is assumed to be stationary and can be considered to be the 8.4 GHz core.

The second brightest jet feature, an isolated component downstream next to the core at a distance of ∼3.5 mas (see Fig. 7.9), is found to be stationary with respect to the core (see Sect. 7.5.2 and 7.6.2). It most probably corresponds to the stationary component C3 next to the core at ∼4 mas, with a stable flux density of $\sim 0.5 \pm 0.3$ Jy, detected by Tingay et al. (2001). Preceding this bright stationary feature (labeled as $\mathrm{J}_{\mathrm{stat}}$), i.e., between this component and the core

[6] Note the slightly different model component values as compared to the values reported in Abdo et al. (2010e), which reflect self-calibration and model-fitting uncertainties.

[7] Four 12 ksec observations with *XMM-Newton* (PI: C.Müller) and two 10 ksec *Suzaku* observations (PI: R. Ojha).

component, a clear decrease in brightness is measured. Figure 7.9 shows that this dip is also not moving over our monitoring period. However, in epoch 2008.9, an additional component, later associated with J10, is found in this region.

In Müller et al. (2011) we reported on a possible widening and subsequent narrowing of the jet appearing downstream at a distance of ~ 25 mas from the core. Based on these seven highly resolved 8.4 GHz observations, the significant detection of this feature, which appears in all images, can now be confirmed (Müller et al., 2014b). The best resolved 8.4 GHz image of 2008 November shows an bifurcation-like emission structure[8] around 25.5 ± 2.0 mas, which will be called – as reminiscent of a – "tuning fork" in the following, where the surface brightness along the jet axis drops below $\lesssim 5\sigma$ in the center and the radio emission is separated into two different initially symmetric regions. The flux density profile of the stacked image (Fig. 7.9) shows that the flux decrease and the respective widening of the collimated jet is observed to be positionally stable between 2007 and 2011. Note that the overall jet flux density distribution is declining with distance and drops significantly when the jet widens. In Sect. 7.6.3 the nature of this particular jet structure is further discussed.

[8]Previously described as a jet widening (see Sect. 7.3.1 and 7.3.4).

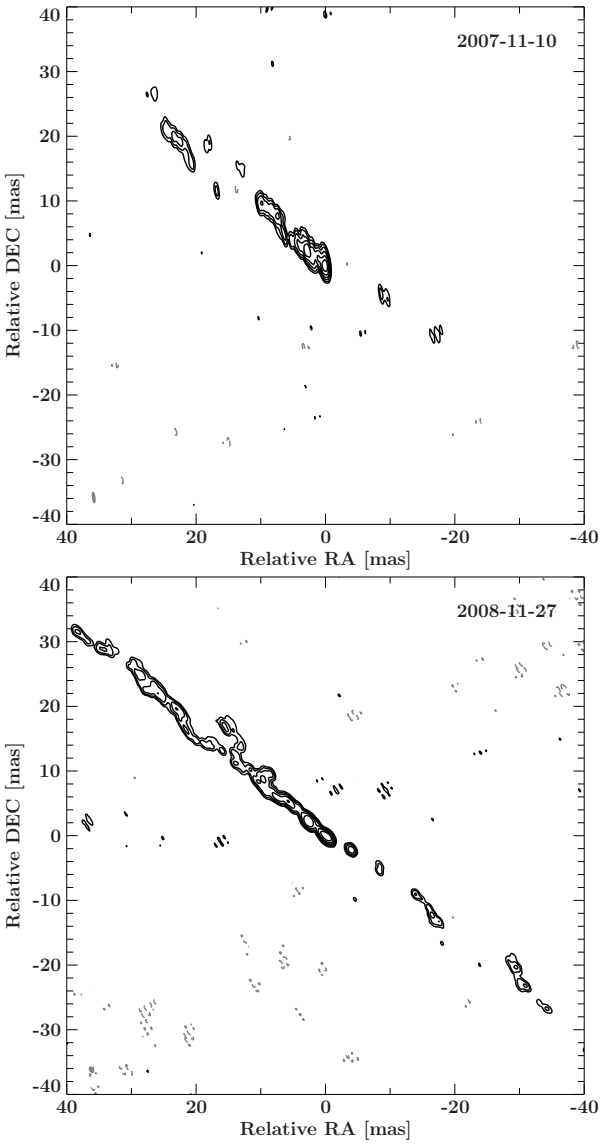

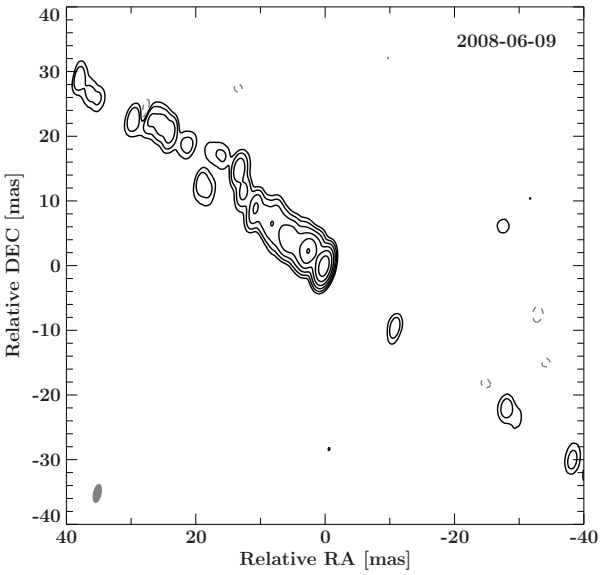

Figure 7.7.: Contour `clean` images of the first three 8.4 GHz TANAMI observations with natural weighting. The (black) contours indicate the flux density level, scaled logarithmically and increased by a factor of 3, with the lowest level set to the 3σ-noise-level (for more details see Table 7.1). Negative contours are shown in gray. *From top left to bottom right:* 2007 November (Ojha et al., 2010), 2008 June, 2008 November (Müller et al., 2011). The FWHM of the restoring beams for each observation is shown as a gray ellipse in the lower left corner. 1 mas in the image corresponds to 0.018 pc. Figures from Müller et al. (2014b).

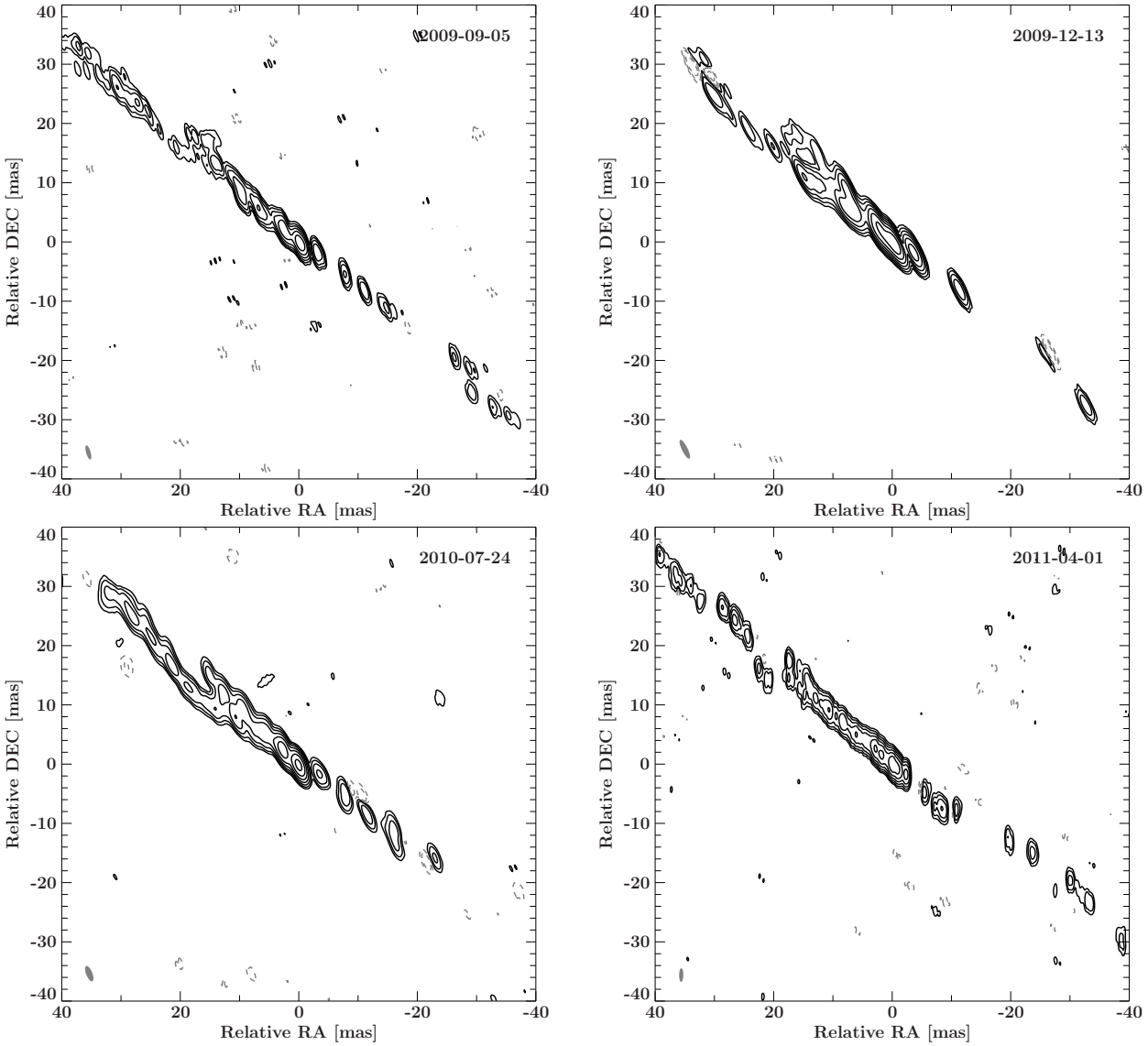

Figure 7.8.: Same as Fig. 7.7 for the 4th to 7th TANAMI observation. *From top left to bottom right:* 2009 September, 2009 December, 2010 July, and 2011 April. Figures from Müller et al. (2014b).

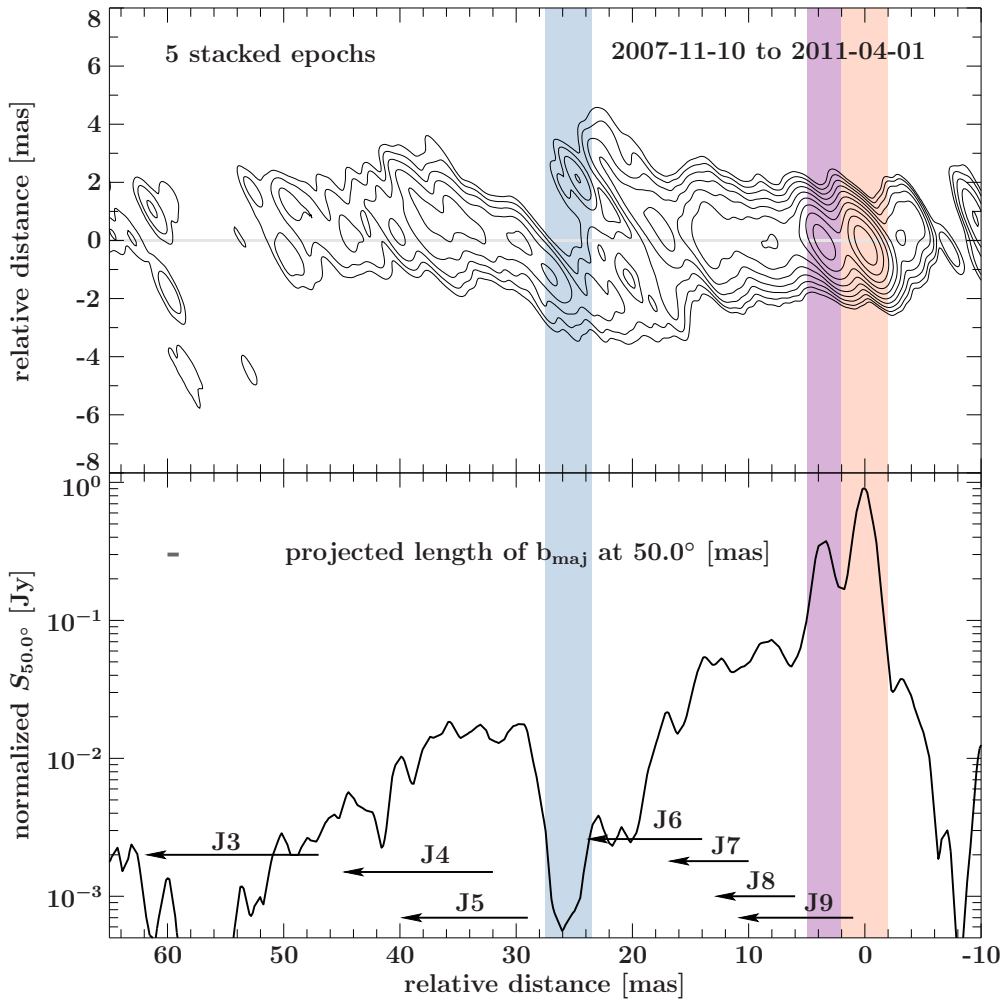

Figure 7.9.: *Top:* Stacked `clean` image. The five highest resolution TANAMI images (epoch 2007.86, 2008.9, 2009.68, 2010.56, 2011.25) were restored with a common beam of size (2.29×0.58) mas at P.A. $= 15.6°$ and rotated by 40°. *Bottom:* Flux density profile along the jet axis (at P.A. $= 50°$) of stacked 8.4 GHz `clean` images. All images were normalized to the peak flux before stacking. The orange/purple shaded area marks the core region and the stationary component, respectively. The blue shaded area at 25.5 ± 2.0 mas away from the phase center indicates the region of the jet where the widening and decrease in surface brightness at 8 GHz occurs. The projection of the restoring beam onto the jet axis is shown as a gray line. The black arrows indicate the traveled distances of the identified components causing a smoothing of the profile due to the jet flow with $\mu_{\mathrm{mean}} \sim (2-3)\,\mathrm{mas\,yr^{-1}}$ (see Sect. 7.5.2 and compare to Tingay et al., 2001). The flux density distribution along the jet is clearly resolved and shows emission humps which are not easily explained with convolution effects. Figure from Müller et al. (2014b).

7.5. Jet kinematics of the inner parsec

Long term monitoring of AGN jets allows the study of the jet kinematics revealing an overall jet flow, which often shows significant acceleration downstream. The formation and propagation of extragalactic jets is still not completely understood. As summarized in Sect. 1.3.4, particular characteristics are observed, requiring further investigations with high-resolution observations to test and compare the results with theoretical models and simulations. The jet of Cen A presents an ideal target to substantiate proposed explanations.

The time evolution of its mas-scale jet has been well studied over 12 years (1988 to 2000) with VLBI techniques by Tingay et al. (1998) and Tingay et al. (2001). An apparent jet speed has been measured tracking two prominent components with proper motion $\mu \sim 2\,\mathrm{mas\,yr^{-1}}$, corresponding to an apparent velocity $\beta_{\mathrm{app}} \sim 0.12$ (where $\beta = v/c$) for the inner mas-scale jet (up to ~ 30 mas distance from the core). Horiuchi et al. (2006) reported on a single-epoch space-VLBI observation of Cen A at 5 GHz showing a well collimated jet, with intriguingly similar structure to the TANAMI results (Müller et al., 2011), suggesting a very stable overall formation and propagation of the jet. On larger scales, up to 100 pc from the core, Hardcastle et al. (2003) measured a bulk velocity of $\beta_{\mathrm{app}} \sim 0.5$ using Very Large Array (VLA) and *Chandra* observations.

In this Section, I will discuss the jet kinematics of Cen A at sub-mas-scales, i.e., the investigation of the jet evolution within the central parsec (see also Müller et al., 2014b).

7.5.1. Tapered data analysis

The high-resolution TANAMI observations of Cen A are clearly resolving the innermost parsec of the jet along and perpendicular to its axis. The overall appearance suggests that sub-structure in the underlying jet flow is detected.

In order to test this assumption and to connect the TANAMI results to previous VLBI studies of the Cen A jet (Tingay et al., 1998, 2001), a (u, v)-taper was applied to each dataset, such that the angular resolution compares to previous measurements. As an example, Fig. 7.10 shows the naturally weighted image at (sub-)mas resolution as well as the tapered and restored image with comparable resolution to the earlier observations of Tingay et al. (2001). It is obvious that the TANAMI array is resolving small jet sub-structures, while the main emission zones, which appear as single jet knots in these previous (lower-resolution) images, look remarkable similar. This result shows that the observed high resolution structures are consistent with earlier measurements. This comparison is further discussed in Sect. 7.6.

7.5.2. Time evolution of the (sub-)parsec scale jet

The high spatial resolution and the good sampling of the TANAMI monitoring of Cen A at 8.4 GHz allow us to study the time evolution of the closest extragalactic jet in unprecedented detail. In order to parametrize individual jet features and to track their evolution with time, Gaussian emission model components were fitted to the self-calibrated visibility data (see Sect. 7.4) using the `modelfit` task in `difmap` (Shepherd, 1997). The best-fit parameters for each TANAMI 8.4 GHz observation of Cen A are listed in Table A.1 to A.7. The identified jet components, which can be tracked over several epochs, are explicitly labeled.

The models for every single epoch were constructed following the same procedure: The self-calibrated visibility data were fitted with sufficient model components to describe the prominent bright jet features. Iteratively, Gaussian components were fitted and phase self-calibration steps

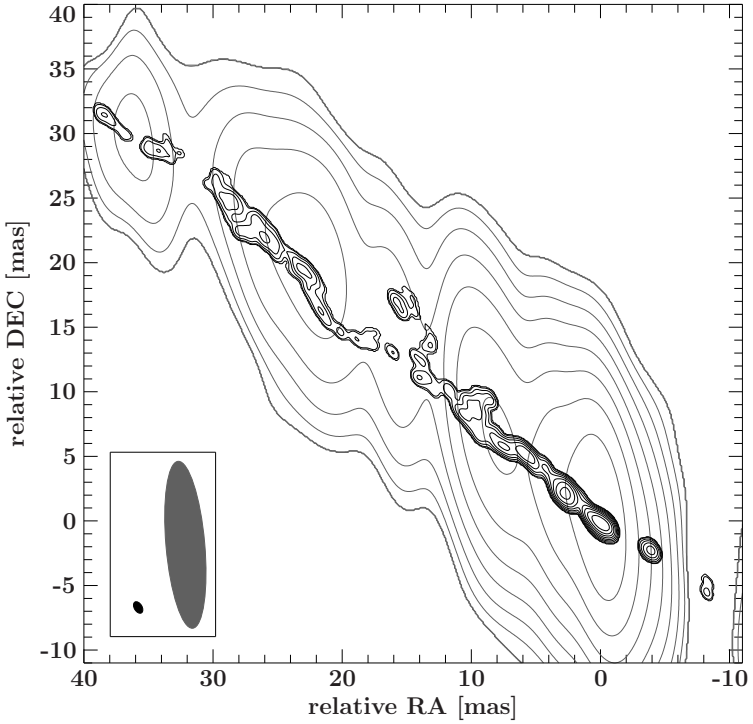

Figure 7.10: Tapered (dark gray) and original 2008 November TANAMI image (black). A taper of 0.1 at $25\,M\lambda$ was chosen and the image was restored with the common beam of (3×13) mas at 5° as applied in Tingay et al. (2001), in order to compare the TANAMI observations with these previous VLBI measurements. In the lower left the size of the respective restoring beam is shown as a gray/black ellipse. The tapered TANAMI image is remarkably similar to the images by Tingay et al. (1998, 2001).

were performed, leading to final models with $\chi^2 \sim 1909$ (d.o.f= 3828) to ~ 24152 (d.o.f= 6846, see Tables A.1 to A.7). The inclusion of phase self-calibration during model fitting leads to a final multi-epoch model, which is in good agreement with the closure phases measured at all triangles of telescopes in all seven experiments. This model does not necessarily represent the best fit to the `clean`-image data sets (because additional phase self-calibration steps have been introduced in the model-fitting procedure). This approach was chosen because limitations in the (u, v)-coverage may lead to ambiguities in the `clean` process of individual images (see also discussion of (u, v)-coverage limitations in Müller et al., 2011). In effect, some of the fainter model components may not coincide perfectly with peaks in the brightness distribution of the `clean` images. Figure 7.11 summarizes the result of the kinematic study showing the contour images overlaid by the corresponding Gaussian model components[9]. The brightest upstream feature, identified as the core (see Sect. 7.4), was taken as a reference position and all positions are measured with respect to it.

Within `difmap` no uncertainties for the model fit parameters can be derived. In order to determine the statistical errors of the Gaussian components we interfaced `difmap` with the data reduction package `ISIS` (Houck & Denicola, 2000). This approach allows us to use the functionality contained in this general purpose system to efficiently determine the parameter values and their uncertainties based on the χ^2 statistics. The error calculation was performed for each parameter. Tables A.1 to A.7 give the best fit values. Note that the (statistical) positional uncertainties derived this way are in general agreement with the values obtained, e.g., by the MOJAVE project (Lister et al., 2009b, 2013, Grossberger et al., in prep.,). We found that the positional accuracy depends on the size and flux of the component. Therefore the semi-major axis of each component is adopted as the systematic uncertainty (see Fig. 7.12). However, the systematic errors clearly dominate the measurements. In particular, all flux-density measurements are dominated by such systematic errors, which can be estimated to be smaller than 15% (see Sect. 7.3.2). Therefore, the derived statistical 1σ-uncertainties are not shown in Tables A.1 to A.7.

[9]Note that due to the lower SNR of the counterjet, no kinematic measurements could be obtained.

Table 7.3.: Apparent speeds of individual jet components

ID	μ[mas/yr]	$\beta_{\rm app}$	$d_{\rm mean}$[mas]^a	$t_{\rm ejection}$
J3	4.98 ± 0.35	0.29 ± 0.02	53.58	$\sim$1983^b
J4	3.55 ± 0.26	0.21 ± 0.01	38.81	$\sim$1989^b
J5	3.05 ± 0.13	0.18 ± 0.01	34.46	$\sim$1989^b
J6	2.92 ± 0.09	0.17 ± 0.01	18.47	2002.0±1.0
J7	1.73 ± 0.22	0.10 ± 0.01	13.63	2002.0±2.0
J8	1.85 ± 0.15	0.11 ± 0.01	9.72	2005.0±1.0
J9	2.67 ± 0.13	0.16 ± 0.01	6.13	2007.5±0.5
J10	2.68 ± 0.14	0.16 ± 0.01	4.30	2008.5±0.5

Notes. $^{(a)}$ Mean component distance from the core. Note that the time range over which single components have been tracked is shorter for the two newly emerged components J9 and J10. $^{(b)}$ Results from Tingay et al. (2001), see main text for details.

The kinematics of eleven individual components besides the core can be studied (Fig. 7.12). These components are explicitly labeled in Tables A.1 to A.7. Eight (J3 to J10) components show significant motion along the jet axis with position angle of P.A. $\sim 50°$. One component is found to be stationary ($J_{\rm stat}$). It shows a remarkably stable flux density and brightness temperature behavior. For the analysis of the time evolution of the components we excluded the whole region of the jet widening (Sect. 7.4), since cross-identification of related edge-components suffers larger positional uncertainties and larger offsets to the jet axis. The position of the "tuning fork" like emission and the "hole" with lower surface brightness remains stationary as clearly seen in the stacked flux density profile (Fig. 7.9).

Of the moving components, seven are detected in more than four consecutive epochs. Two newly emerged components (J10 and J9) are ejected into the jet during the TANAMI monitoring period. Component J10 could only be detected in three epochs so far and further VLBI observations are required to better constrain its trajectory (see below). The two outermost components J2 and J1 only appear in two data sets because of limited short-baseline (u, v)-coverage in some epochs. The components $J_{\rm stat}$ and J3 to J10 are considered robust and our study of the jet kinematics of Cen A will be discussed based on the time evolution of these components.

Assuming ballistic motion for each component, individual apparent speeds for the components J3 to J10 are determined, using linear regression fits to the centroid position of associated Gaussians. This is the most solid approach as testing for possible acceleration of single components is not reliable until robust detection of components in more than ten consecutive epochs as discussed in (Lister et al., 2013). We detect a clear velocity dispersion (see Table 7.3). The individual component proper motions range from $\mu = 1.73 \pm 0.22\,{\rm mas\,yr^{-1}}$ for J7 to $\mu = 4.98 \pm 0.35\,{\rm mas\,yr^{-1}}$ for J3.

The mean apparent speed of these eight components is $\mu_{\rm mean} = 2.93\,{\rm mas\,yr^{-1}}$ and the median is $\mu_{\rm median} = 2.68\,{\rm mas\,yr^{-1}}$. This shows a broader range of speeds for the different resolved components than the values determined by Tingay et al. (2001). The tapered analysis explains this discrepancy. Performing a kinematic study with the tapered images (Sect. 7.5.1) yields a mean component motion of $\sim 2\,{\rm mas\,yr^{-1}}$, comparable to the results by Tingay et al. (2001). Extrapolating the previous VLBI results to the time of the TANAMI observations (Fig. 7.13) then allows us to identify the component complex J5 to J3 with the components C2 and C1 of Tingay et al. (2001), respectively (see Sect. 7.6 for further details).

This comparison shows that limited angular resolution can mimic an continuous, smooth jet flow. Higher-resolution TANAMI observations allow us to detect small-scale structures which seem to follow a preexisting channel defined by the flow, but show distinct apparent speeds.

Assuming constant component velocities and no intrinsic acceleration, the back-extrapolation of the component tracks constrains the ejection times for the innermost components (see Table 7.3). The ejection times of J5 to J3 are obtained using the tapered analysis and the cross-identification with C2 ($1989.2^{+0.9}_{-0.7}$) and C1 ($1983.5^{+2.2}_{-3.2}$) from Tingay et al. (2001).

Figure 7.14 shows the $\beta_{\rm app}$-distribution for each component as a function of mean distance from the core. The pc-scale jet of Cen A shows a trend of increasing component velocity further downstream which can be parameterized by a linear fit of $\beta_{\rm app} = 0.16\,d + 0.12$, where d is the mean component distance in pc over the observed time range. Components J4 and J3 show significantly higher speeds than components closer to the core, suggesting that the jet undergoes acceleration further out as seen in a large sample of AGN jets by Lister et al. (2013).

The best-fit apparent velocities of the two newly emerged components J9 and J10 agree within their errors, but deviate from the mean jet speed. Both components pass the stationary feature during the time of TANAMI monitoring, a very complex region where misidentification is possible. They are faster than the more robust components J7 and J8. Further VLBI observations will be able to test the higher speeds of J9 and J10.

7.5.3. Simultaneous ballistic fit

The characterization of the jet flow with ballistic tracks is a good approach to determine the motion of the individual components. However, the motion tracks could in principle be more complex. In order to test whether the components trajectories are consistent with ballistic tracks we fit all datasets simultaneously[10], i.e., instead of treating the observations individually, we couple the positions of all components in the different observations using a single linear model and then solve for all component velocities by performing a simultaneous fit to all VLBI observations.

As a starting model, in order to identify the components, the models obtained for each single (u, v)-dataset (see Sect. 7.5.2 and Tables A.1 to A.7) were used. Assuming ballistic motion, the time evolution of each identified component i (with $i = 1 \ldots 10$) can then be described by

$$\begin{aligned} x &= x_{0,i} + \cos(\phi_i) v_i (t - t_{0,i}) \\ y &= y_{0,i} + \sin(\phi_i) v_i (t - t_{0,i}) \end{aligned} \tag{7.1}$$

where (x_0, y_0) is the the starting position, ϕ_i is the ejection angle, $t_{0,i}$ is ejection date $t_{0,i}$, and v_i is the velocity. Based on this input model we performed a simultaneous fit to all datasets by fitting ballistic motion to all identified components resulting in a combined χ^2. As a consequence of this approach, if the motion is non-ballistic the fit will result in a high χ^2-value, so that we can reject the hypothesis of simple ballistic motion.

This approach results in a $\chi^2 = 74149$ with 39044 degrees of freedom ($\chi^2_{\rm red} = 1.9$) for the combined, simultaneous fit. The resulting component velocities are in agreement with the values obtained by the single fits using the "classical" approach (see Sect. 7.5.2). We conclude that the motion of the identified components are well described by ballistic motion on the basis of seven consecutive observations, though the best-fit has only a moderate $\chi^2_{\rm red}$-value. The downstream acceleration is confirmed by this analysis, with $\sim$ 1-2 mas yr^{-1} faster speeds for J5 to J3 than for the inner components. We expect that with further monitoring epochs this analysis will yield a good test of the continuous acceleration model along the jet.

[10]These calculations were performed in close collaboration with C. Großberger.

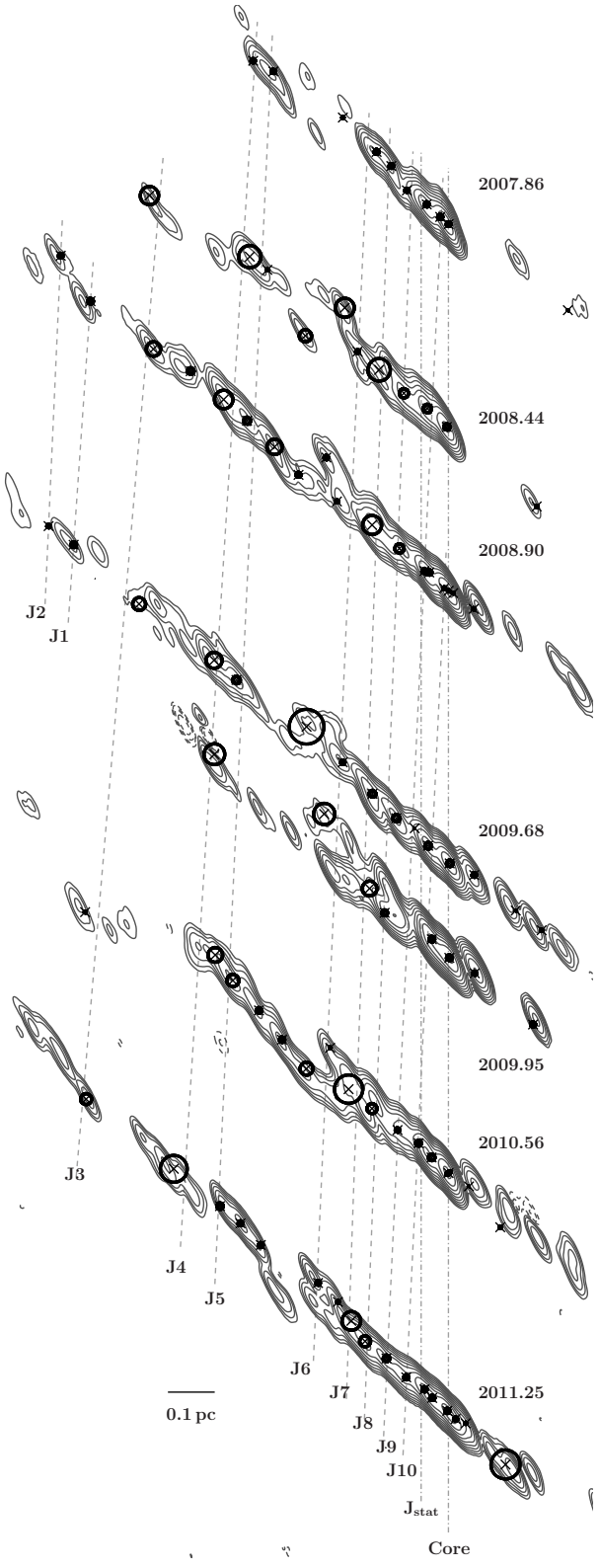

Figure 7.11: Time evolution of Cen A at 8.4 GHz. Contour clean images, restored with a common beam of (3.33×0.78) mas at P.A.$=26.3°$. The contours indicate the flux density level, scaled logarithmically and increased by a factor of 2, with the lowest level set to the 5σ-noise-level. The positions and FWHMs of the Gaussian `modelfit` components are overlaid as black circles (for model parameters see Table 7.1).

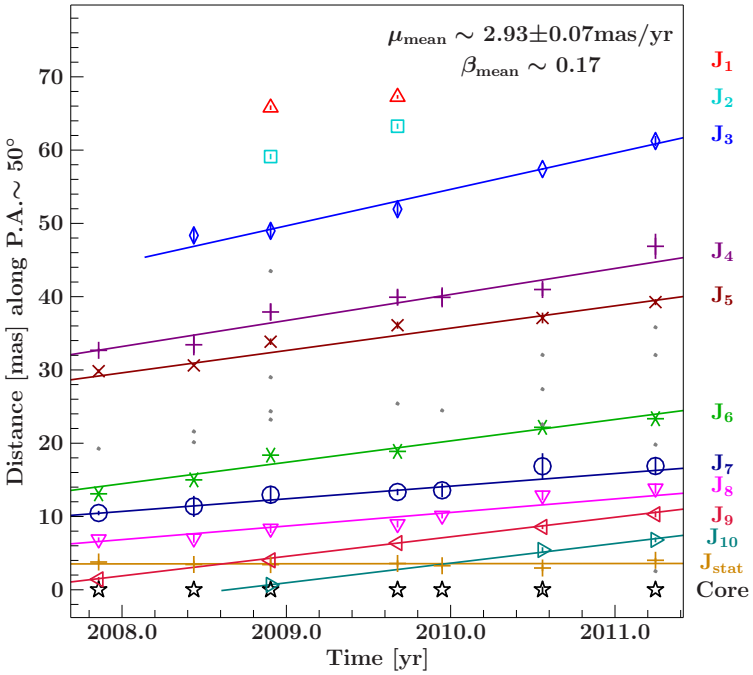

Figure 7.12: Component distance from the core component (set to zero) as a function of time. For the identified components (colored symbols), the error bars show the combination of the statistical errors and systematic errors (defined as $0.5 \times b_{\mathrm{maj}}$) or are smaller than symbol sizes. A linear regression fit to associated components with all values weighted equally is shown. Components not included in the fit are marked in gray. Note, in particular, the components in the region of the "tuning fork" are excluded since the region is too complex. The mean apparent speed is determined for all components tracked in five or more epochs.

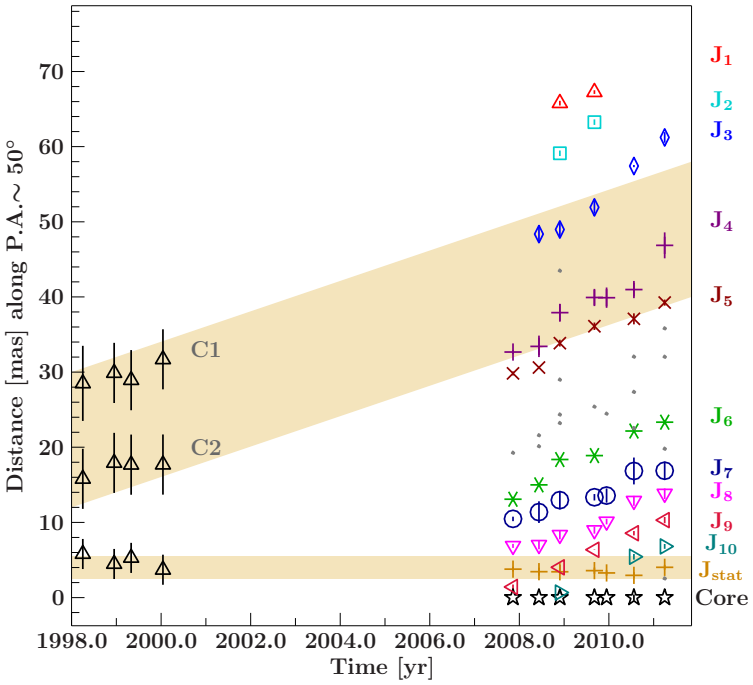

Figure 7.13: 8.4 GHz kinematic results of Cen A by Tingay et al. (2001) (open triangles) and the 2007–2011 TANAMI data. The shaded region marks the expected velocity evolution using $\mu = 2\,\mathrm{mas\,yr^{-1}}$, which is comparable to the mean apparent speed given by the tapered TANAMI images (see text for details).

7.6. Discussion of the complex dynamics

In the following sections the Cen A jet kinematics are discussed. On top of the overall jet flow, the series of highly resolved images of Cen A reveal particular bright and interestingly shaped structures which are discussed in detail (Müller et al., 2014b).

7.6.1. Overall jet structure and flow

The TANAMI observations of Cen A reveal a complex jet flow with a wide range of individual component velocities (Sect. 7.5.2). Although a significant component motion is measured, the observed features in the VSOP image of 2000 (Horiuchi et al., 2006) show that the basic jet structure is stable over years, forming a well confined channel. The median apparent speed then may be associated with the underlying flow which follows this preformed jet structure. At the same time, due to the interaction between the jet and the ambient medium, individual jet features are developed which can be slower or even stationary.

As shown by the tapered analysis (see Sect. 7.5.1), the TANAMI observations resolve the sub-structure of prominent regions into components of a few light days in size. Tingay et al. (2001) reported on some dramatic internal variability of components without major changes in apparent speed. This already hinted at a finer sub-structure.

A position-dependent acceleration (see Fig. 7.14) of the outer components (beyond ~ 0.3 pc) is measured, very similar to the velocity distribution seen in the sub-parsec region of NGC 1052 (see Fig. 13 in Lister et al., 2013). If one assumes that the acceleration continues downstream, it could be the explanation for the apparent mismatch in jet velocity at a distance of ~ 100 pc ($\sim 0.5c$; Hardcastle et al., 2003), and the parsec-scale velocities measured by VLBI (Tingay et al., 2001, and this work). Assuming the measured acceleration continues downstream, the jet flow would already reach a speed of $\beta_{\rm app} \sim 0.5$ at a distance of ~ 2.5 pc. Alternatively, jet bending within the inner few parsecs could also explain the observed apparent acceleration. Tingay et al. (1998) constrained the inclination angle at parsec scales to 50°–80°, while the analysis at ~ 100 pc by Hardcastle et al. (2003) resulted in $\sim 15°$.

TANAMI observations yield surface brightness jet-to-counterjet ratios of $R = 4$ and $R = 7$, using the two observations with the best-sampled (u, v)-coverage of 2008 November and 2011 April, respectively, and excluding core emission between $-2\,\text{mas} < \text{RA}_{\rm relative} < 2\,\text{mas}$ to account for possible absorption effects (Paper I; Tingay & Murphy, 2001). Figure 7.15 shows the resulting constraints on the inclination angle θ and the intrinsic speed β. For an optically thin ($\alpha = -1$), smooth jet we

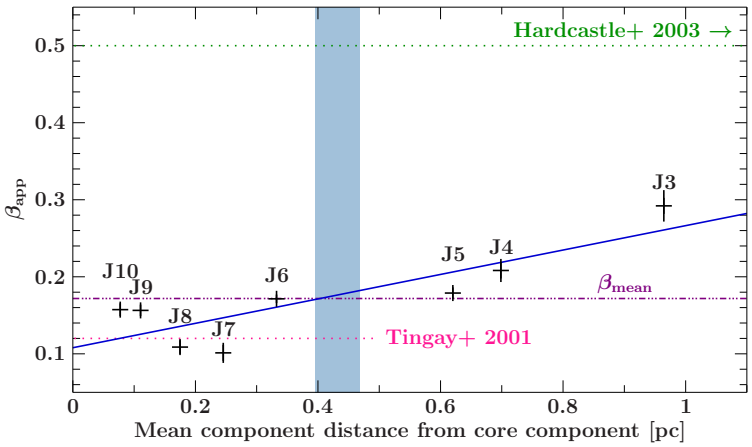

Figure 7.14: Evolution of individual component velocities as a function of mean component distance from the core component, which can be parameterized by a linear fit of $\beta_{\rm app} = 0.16\,d + 0.12$ (blue line). The blue shaded area marks the position and extent of the jet widening (Sect. 7.6). The mean component speed and archival measurements by Tingay et al. (2001) and Hardcastle et al. (2003) are indicated by straight lines.

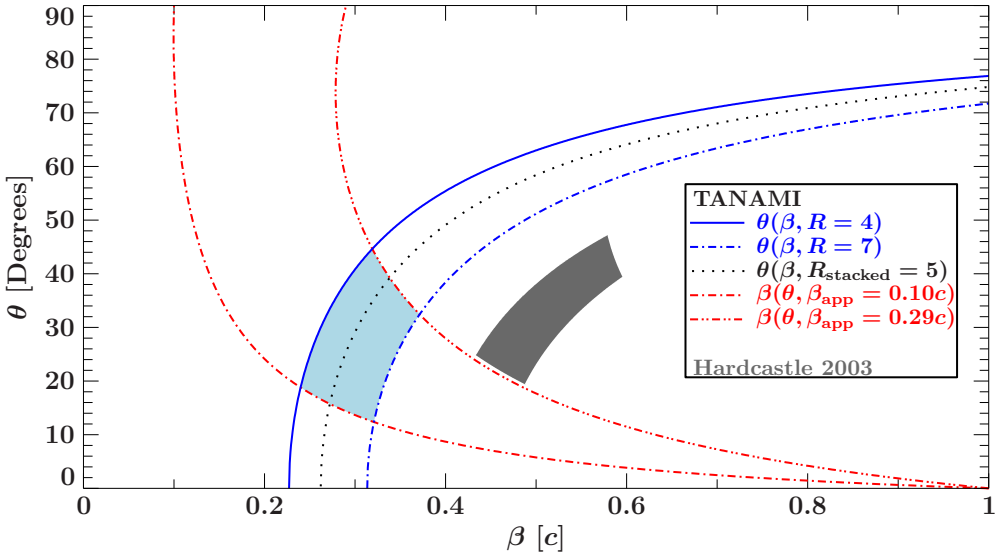

Figure 7.15.: Constraints on the values of the intrinsic jet speed β and the inclination angle θ consistent with our measurements. Blue lines show the constraints on θ-range for the measured jet-to-counterjet ratio. The black-dotted curve gives the corresponding values for the stacked image. The red lines give the constraints on intrinsic jet speeds based on the measured apparent speeds of the slowest and fastest component (see Table 7.3). The blue-shaded intersection area marks the region of permitted parameter space for both values. The gray-shaded region indicates the constraints according to measurements by Hardcastle et al. (2003). Figure from Müller et al. (2014b).

use Eq. 1.8 to constrain these parameters. The measured brightness ratio in combination with the minimum and maximum measured proper motion limits the jet inclination angle to $\theta \sim 12° - 45°$. Additionally, we can constrain the intrinsic speed $\beta \sim 0.24 - 0.37$, comparable to measurements for NGC 1052 ($\beta = 0.25$, Vermeulen et al., 2003).

Within the uncertainties, the upper limit of our derived angles is consistent with the lower limits obtained by Jones et al. (1996) and (Tingay et al., 1998), while our lower limit overlaps with the values by Hardcastle et al. (2003). These authors explained the discrepancy in measured apparent speed between the parsec and the kilo-parsec scale jet via a resolution effect and point out that Tingay et al. (1998) found hints of faster moving sub-components. With these higher resolved observations component speeds with $\beta_{\rm app} > 0.3$ can be excluded, but indications of downstream acceleration are found. A larger inclination angle cannot solely explain the faster apparent speed measured by Hardcastle2003, but requires in addition an increase in β from $\lesssim 0.3$ to $\gtrsim 0.45$, since the angle is well below the critical angle. The higher apparent speeds at kilo-parsec scales could hence consistently be explained with intrinsic acceleration assuming a constant angle to the line of sight.

The spectral index distribution of the inner few light days of the jet shows an optically thick core region with a steepening of the spectrum downstream (see Sect. 7.3). It is striking that the region of the faster moving components (J5 to J3) coincides with the optically thin region of the jet. A spine-sheath like jet-structure, as proposed by Ghisellini et al. (2005) and Tavecchio & Ghisellini (2008), can explain this whole appearance, since a faster spine at small optical depth could be revealed. For optically thick regions, only the outer – slower – layer can be probed. Further high-resolution spectral index imaging is required, however, to confirm that coincidence.

A layered jet structure can also explain the different results on the inclination angle of Cen A at parsec and kilo-parsec scales. Observations of optically thin jet regions would address the faster and

brighter spine, resulting in larger brightness ratios and hence, smaller estimated angles to the line of sight. Hence, the different inclination angle measurements can be better reconciled assuming a spine-sheath structure, with possible intrinsic acceleration, rather than a large jet bending within 100 pc.

In principle, the observed downstream acceleration could also be explained via an expansion of a hot jet in pressure equilibrium with the ambient medium. If the ambient pressure has a steep density gradient, the jet expands adiabatically and accelerates (Perucho & Martí, 2007). In this scenario, standing, conical (recollimation) shocks are expected to develop, though TANAMI observations do not conclusively show such features (see Sect. 7.6.2 and 7.6.3).

7.6.2. The stationary component

At a distance of ~ 3.5 mas, the second brightest jet component J_{stat} is found to be stationary, stable in flux and brightness temperature, and is clearly resolved from the core (Table A.1–A.7). The spectral index of J_{stat} is $\alpha \approx -1$, i.e., optically thin (see Sect. 7.3). Tingay et al. (2001) discussed the appearance of a stationary component (C3) approximately at 4 mas in mid-1993 with a stable flux density of about 1 Jy (for a beam size of about (3×13) mas). This result suggests that J_{stat} is a long-term stable feature. Stationary components in extragalactic jets are often observed and can be explained by locally beamed emission or standing shocks (Lister et al., 2009b; Piner et al., 2007). The alternative interpretation, a large jet bending at this position (Fujisawa et al., 2000), had already been rejected by Tingay et al. (2001), as the position angles of the modelfit-components are all found to be similar. We confirm this rejection based on our even higher resolution images.

It should also be noted that while J9 and J10 pass through J_{stat}, neither of them shows significant evidence of interactions, e.g., a flux change[11]. A possible interpretation of J_{stat} is that it represents a cross-shock in the jet flow as seen in simulations of over-pressured jets (Mimica et al., 2009). In these features a spectral inversion is expected, which is associated with recollimation shocks, in which passing components are accelerated in the following expansion. To confirm J_{stat} as such a recollimation shock will require further dual-frequency monitoring. Given the measured steep spectrum, it is more likely that this feature is the result of an internal, local pressure enhancement increasing the density and emission, similar to a jet nozzle.

7.6.3. The jet widening - the "tuning fork"

The "tuning fork"-like structure at $\sim 25.5 \pm 2.0$ mas (projected distance ~ 0.4 pc) downstream is significantly detected in multiple 8.4 GHz TANAMI observations and is most prominently seen in the highest dynamic range images. The dip in the surface brightness remains stationary, and the local jet morphology indicates a circumfluent behavior (Fig. 7.11). According to this result, we can conclude that we do not observe a moving disturbance of the jet, caused by a temporal disruption with subsequent restructuring of the jet, but that this feature is likely a standing discontinuity.

Tingay et al. (1998) measured a strong increase in flux density of component C1 when it reached the location of the "tuning fork". The positional uncertainties of these previous VLBI measurements are not comparable to our results but their Gaussian modelfits indicated an increase of the diameter of C1 from $\sim$4 mas to $\sim$ 14mas within $\sim$3.5 months. Tingay et al. (2001) reported on no strong variations of the subsequent component C2, however, it did not reach this location during their monitoring. Therefore, the jet widening might be a long-term stable feature such as J_{stat}.

[11] However, note that due to the TANAMI observation cadence, a short-time flux change might have been missed by our observations.

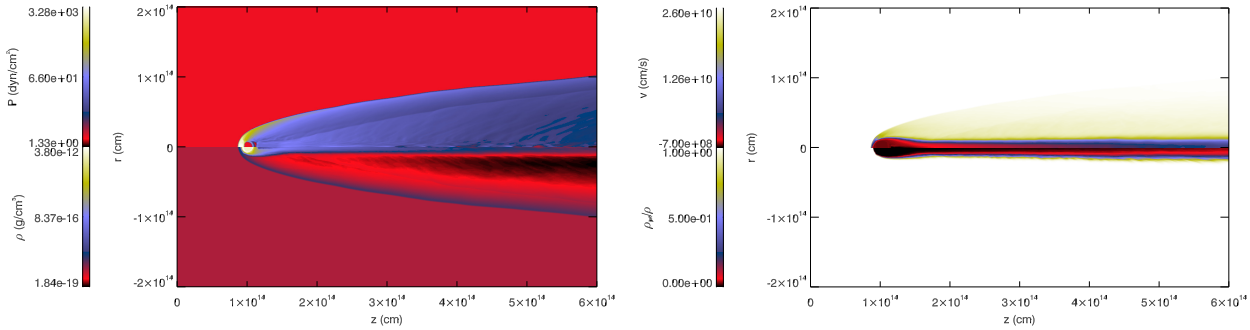

Figure 7.16.: Simulation results of an interaction between a spherical, homogeneous obstacle and the jet. Shown are combined maps of the logarithm of pressure (*top left panel*), density (*bottom left*), axial velocity (*top right*), and jet mass fraction (*bottom right*). Figure from Bosch-Ramon et al. (2012).

At first glance, the appearance of the "tuning fork" resembles a recollimation shock creating a Mach disk which decelerates the jet flow and separates it into two faster streams surrounding the central Mach disk as seen in simulations by Perucho & Martí (2007). In between this "tuning fork"-like emission zone, i.e., behind the shock, one expects optically thick emission and subsequent acceleration of the jet flow. While such a recollimation shock scenario could well describe the position-dependent acceleration in the succeeding components J5 to J3, the overall appearance of the structure is difficult to reconcile with the theoretical expectations: When a Mach disk is formed, one expects a strong jet expansion prior to the shock. Additionally, after the Mach disk the jet should undergo further strong reconfinement shocks and be strongly decelerated. Observations show, however, that it is still well collimated and not slowing down up to a hundred parsecs (Hardcastle et al., 2003; Goodger et al., 2010). Finally, a recollimation shock would also create a bright standing feature downstream of the Mach disk, which is not observed. Thus, it can be concluded that the "tuning fork" is probably not caused by a recollimation shock.

A different explanation of the feature is a standing, local disturbance that does not disrupt the entire jet, such as an interaction with a massive object. Figure 7.9 shows that the jet surface brightness sharply increases behind the gap and starts to decline again downstream. This already suggests that the jet flow is probably intermitted but not totally stopped. In particular, we consider the penetration of a cloud or a star, which is highly likely in the inner parsec of the galaxy with estimated stellar number densities of thousands per pc^3 close to the galactic center (Lauer et al., 1992; Araudo et al., 2013). For comparison, observations of Sgr A* show stars orbiting the SMBH at a distance of $\sim$ 15 light days (Schödel et al., 2002). Since Cen A hosts a SMBH at its center about ten times more massive SMBH than the Galaxy, we can expect stars or dust-clumps orbiting the central engine down to distances of at least a few hundred light days. The distance of the "tuning fork" matches this expected range, with $\sim$ 25 mas corresponding to $\sim$ 600 light days.

Simulations by Bosch-Ramon et al. (2012, see Fig. 7.16) describe the interaction of a jet and a cloud/star orbiting the center of the AGN in context of the formation of high-energy flaring events (Bednarek & Protheroe, 1997; Khangulyan et al., 2013).

Such an interaction scenario between Cen A's jet and stars of the galaxy was already discussed by Hardcastle et al. (2003), Tingay & Lenc (2009) and Goodger et al. (2010) to explain the radio and X-ray knots in the hundred-parsec scale jet. The presence of a dusty torus-like structure in the vicinity of the central black hole in Cen A is confirmed by measurements in the infrared and X-rays. Rivers et al. (2011) reported on an occultation event observed during twelve years of X-ray monitoring with *RXTE* at a distance commensurate with the molecular torus whose properties have been adopted from IR measurements by Meisenheimer et al. (2007). These measurements

confine the dust torus to a maximum extension of $\sim 0.6\,\mathrm{pc}$ ($\sim 700\,\mathrm{light\ days}$) with an orientation axis aligned with the jet axis, also matching the distance of the jet widening from the jet core.

Interpreting the "tuning fork" as a bow-shock structure due to jet-star/cloud interaction[12], the VLBI observations constrain its size to about $D_{\mathrm{bowshock}} \simeq 0.5\,\mathrm{mas} \simeq 0.01\,\mathrm{pc}$, with a jet diameter of $R_{\mathrm{jet}} \simeq 5\,\mathrm{mas} \simeq 0.1\,\mathrm{pc}$. The jet crossing time for such an object orbiting the center of Cen A with $v \simeq 10^4\,\mathrm{km\,s^{-1}}$ (a typical galactic rotation velocity, see Araudo et al., 2010), is given by

$$t_j \simeq 6.2 \times 10^8 \left(\frac{R_j}{3.1 \times 10^{17}\,\mathrm{cm}}\right)\left(\frac{v_c}{10^9\,\mathrm{cm\,s^{-1}}}\right)^{-1}\,\mathrm{s}, \tag{7.2}$$

which is approximately 20 years. Assuming that the very middle of the interaction process is in 2009/2010, where our VLBI images show that the obstacle is clearly surrounded by the jet, we can thus set 1995-2005 as the decade in which the obstacle started entering into the jet. This point in time is consistent with the end of monitoring by Tingay et al. (2001), whose low resolution images do not show clear evidence of such a feature. 3D simulations of a star/stellar wind region entering a relativistic jet (Perucho & Bosch Ramon, in prep.) show that even when the obstacle starts to enter the jet, part of the jet flow will already surround it on the outer side of the obstacle, resulting in the circumfluent behavior as observed in the VLBI images.

Taking into account that the size of the shocked region ($D_{\mathrm{bowshock}} \simeq 0.5\,\mathrm{mas} \simeq 0.01\,\mathrm{pc}$) can be of the order of several times the size of the obstacle (Bosch-Ramon et al., 2012), the size of the obstacle can be estimated to be about $0.1 D_{\mathrm{bowshock}}$, i.e., $D_{\mathrm{obstacle}} \simeq 10^{-3}\,\mathrm{pc} \sim 200\,\mathrm{AU}$.

With additional assumptions following the analysis by Rivers et al. (2011) and Araudo et al. (2010) and adopting that the obstacle has been in the jet for at least $\sim$3.5 years, we can conclude that the obstacle is more likely to be a red giant than a cloud (for more detailed calculations see Appendix A.2): A cloud would be disrupted and the bow-shock like structure would have disappeared if the penetration time of a shock is smaller than the jet crossing time. With calculations by Araudo et al. (2010) (Eq. 4), we can determine a lower limit on the cloud density[13] of $n_{\mathrm{cloud}} \geq 1.5 \times 10^{10}\,\mathrm{cm^{-3}}$ which is three magnitudes higher than the values obtained by Rivers et al. (2011). Moreover, the determined cloud velocity of the occultation event is about one magnitude smaller than the one we assumed. An hypothetical cloud with similar parameters would be disrupted within one year. Hence, such an event cannot convincingly explain the stable "tuning fork"-like structure. However, a more dense object, like a red giant would meet the requirements, as this scenario provides expected values and is thus favored by our calculations.

The equilibrium point between the stellar wind and a relativistic jet is determined by the wind and jet ram pressure. Following Komissarov (1994, Eq. 2)

$$R_{\mathrm{s}} \;=\; 2.3 \times 10^{13} \left(\frac{\gamma_j}{5}\right)^{-1} \left(\frac{\dot{M}}{10^{-12}\,\mathrm{M_\odot\,yr^{-1}}}\right)^{1/2} \left(\frac{v_{\mathrm{w}}}{10\,\mathrm{km\,s^{-1}}}\right)^{1/2} \left(\frac{P_{\mathrm{e}}}{10^{-10}\,\mathrm{dyn\,cm^{-2}}}\right)^{-1/2}\,\mathrm{cm}, \tag{7.3}$$

where γ_{j} is the jet flow Lorentz factor, $\dot{M}$ is the typical mass loss rate of the stellar wind of an old late type star (expected in elliptical galaxies), v_{w} is the velocity of the wind and P_{e} is the external pressure, considering that the jet is close to pressure equilibrium with the ambient medium, which is a reasonable assumption in the absence of strong recollimation shocks. However, it is very difficult to give an accurate number for this parameter, so it represents a source of error in the determination of the properties of the wind.

[12] These theoretical calculations were performed in close collaboration with M. Perucho.

[13] Estimations for a jet power of $L_{\mathrm{jet}} \simeq 10^{44}\,\mathrm{ergs^{-1}}$ (Abdo et al., 2010e), a location of the cloud of 0.4 pc, a cloud shocking time of 10 years and a cloud radius $\simeq 10^{-3}$ pc.

With $R_s = 0.01\,\mathrm{pc}$ (bow shock diameter D_{bs}) and a jet flow velocity of $0.5\,c$ (Hardcastle et al., 2003), a typical stellar wind velocity of $v_w = 100\,\mathrm{km\,s^{-1}}$ and an ambient pressure[14] of $P_e = 10^{-10}\,\mathrm{dyn\,cm^{-2}}$, we obtain an estimate for the mass loss rate of the star, $\dot{M}$:

$$\dot{M} \simeq 10^{-8} \left(\frac{R_s}{3.1\times10^{16}\,\mathrm{cm}}\right)^2 \left(\frac{\gamma_j}{1.15}\right)^2 \left(\frac{v_w}{100\,\mathrm{km\,s^{-1}}}\right)^{-1} \left(\frac{P_e}{10^{-10}\,\mathrm{dyn\,cm^{-2}}}\right) \mathrm{M_\odot\,yr^{-1}}. \quad (7.4)$$

A red giant with a stellar wind of $v_{wind} \simeq 100\,\mathrm{km\,s^{-1}}$ and a mass loss of $\dot{M} \simeq 10^{-8}\mathrm{M_\odot yr^{-1}}$ could create such an equilibrium point at $R_s = 0.01$ pc if the jet flow has a velocity $v_j = 0.5\,c$, preventing the approach of the jet flow to the star during the whole crossing time of the star through the jet, provided that the conditions in the wind and the jet do not change dramatically.

Regarding the possibility of an obstacle, an increase in the radio-emission of the region is expected when the interaction started. From our estimations we conclude that the onset of the interaction must have been started between 1995 and 2005. High-energy emission is expected to increase when the star enters the jet[15] (Bosch-Ramon et al., 2012; Barkov et al., 2010, 2012). In Sect. 7.7 the flux density variability of Cen A in various frequency bands is discussed. In 2000/2001, an enhancement of emission in the radio and X-ray is observed, but a mere coincidence cannot be excluded. The high-energy emission could be produced simultaneously by different processes and therefore, it is difficult to disentangle them with our current data. Interestingly, Sahakyan et al. (2013), analyzing four years of *Fermi*/LAT data, report on a possible second γ-ray spectral component in the core emission of Cen A. The average high energy spectrum shows a broken-powerlaw shape with a harder spectral index above $\sim 4\,\mathrm{GeV}$. Since the broadband SED of Cen A can be well described by a Synchrotron Self-Compton model (Abdo et al., 2010e), this hardening suggest another high-energy emission component, supporting the results by Araudo et al. (2010, 2013) explicitly discussing the consequences of an interaction event in Cen A and predicting significant γ-ray emission.

Alternative explanations of the "tuning fork" involving for example recollimation shocks or changes in the spine-sheath structure, are not completely ruled out on the basis of the reported observations. However, we conclude that the jet-star interaction scenario can sufficiently well explain the observations and is particularly interesting from the perspective of testability. If the "tuning fork" is caused by an obstacle moving with typical rotation velocities, it should be gone in 10 to 20 years through the edge of the jet. If it is a cloud, on the one hand, it could be completely shocked and advected with the jet flow before that moment, depending on its properties (Araudo et al., 2010; Bosch-Ramon et al., 2012). If, on the other hand, it is a star, we should expect it to cross the jet. In either case, the situation is dynamic and, as such, temporary. If the structure is generated by a stable recollimation shock or anything else, it should last longer. With ongoing VLBI monitoring we will be able to discriminate between these scenarios.

7.6.4. The outer jet flow – components J5 to J3.

The time evolution of the outer components J5 to J3 reveals an increase in apparent speed with distance from the core (Fig. 7.14). This coincides with the region where the jet becomes optically thin (Müller et al., 2011). As discussed in Sect. 7.6.1, the better (u,v)-coverage of the TANAMI array allows us to resolve out bright emission regions of the jet, picking up substructure of the underlying jet flow. Assuming a spine-sheath structure of the jet, the correlation of higher speeds

[14] We adopt here the values estimated at the core of the radio galaxy 3C 31 from X-ray observations (Hardcastle et al., 2002).

[15] Note that the *CGRO*/OSSE and COMPTEL monitoring of Cen A was between 1991 and 1995 (Steinle et al., 1998). At higher energies, a 3σ-detection by EGRET was reported (Hartman et al., 1999).

measured in optically thin regions could consistently be explained without claiming an internal acceleration. Furthermore, the tapered analysis of the seven TANAMI observations of Cen A allows the association of the prominent emission region composed of J3 and J4/J5 with the previously defined and tracked components C1 and C2 by Tingay et al. (2001). This connection is the most natural overall description of the long term evolution of the jet.

However, as there is evidence for ae position-dependent acceleration and a clear substructure in this outer region of the jet can be modeled, other interpretation scenarios are plausible.

Regardless of the nature of the jet widening – though there is most likely an inter-relation – the motion of the outer components can be explained in the context of a forward shock triggering trailing components. Tingay et al. (2001) discussed C2 and C3 as trailing components of a forward shock (C1). Following this interpretation, we can directly compare the behavior of C1/C2 to J3/J4/J5. Due to a local perturbation in the jet, a major forward shock component can be formed followed by trailing components (Agudo et al., 2001). The simulations show an increase in velocity of the trailing components, i.e., an acceleration as function of distance up to the jet speed – as a consequence of fluid expansion. The fact that $v_{J3} \leq v_{J4} \leq v_{J5}$ fits this picture. A back-extrapolation of the motion tracks of J5 and J4 gives an intersection point at ~ 25 mas from the core in early 2006. Trailing components of a forward shock can be easily distinguished from "normal" jet ejections, since they are not ejected from the core but created in the wake of the main perturbation (Agudo et al., 2001; Mimica et al., 2009). If J3 is a forward shock, we can constrain the jet proper motion to $v_{J5} \leq v_{\rm jet} \lesssim 3.05 \pm 0.13\,{\rm mas\,yr^{-1}}$ (see Table 7.3), as the flow cannot be slower than the trailing components.

Hence, J3 to J5 give a consistent picture of a forward shock and trailing components. Note, in such a case the direct association of J3 with C1 is difficult to reconcile, since the component speeds differ significantly and internal acceleration would need to be invoked. Furthermore, the extrapolation of the tracks of C1 and C2 assuming a constant velocity of $\mu \sim 2$ mas/yr (Tingay et al., 2001) implies that the TANAMI observations should capture at least the remnants of these components at the end of the observable jet. These constraints support the more reasonable picture of the detection and association of the emerging components, but rejecting this proposed shock-scenario. The only way to resolve this contradiction is the formation of a faster shock front (J3) on top of, passing and exceeding in flux density, the underlying jet flow observed by Tingay et al. (i.e., C1 and C2, 2001). This can be easily tested by future VLBI observations looking for further trailing components.

7.7. Multiwavelength variability

Cen A is a well-known high-energy emitter detected up to TeV energies (Aharonian et al., 2009) with a blazar-like broadband SED of the core emission (Abdo et al., 2010e). Although intensely studied, the origin and mechanism behind the hard X-ray emission is still under debate. The soft X-ray observations by Kraft et al. (2002) and Hardcastle et al. (2003) clearly show a contribution from the jet at kilo-parsec scales. Evans et al. (2004) suggested non-thermal X-ray emission from the parsec-scale jet. In the hard X-ray band the situation is still ambiguous. Hard X-ray observations reveal strong absorption below $2-3$ keV, above which the spectrum in the hard X-rays can be modeled with a power law ($\Gamma \sim 1.8$) and narrow fluorescence lines (Evans et al., 2004; Markowitz et al., 2007). The observed emission is similar to those in Seyfert galaxies, but it is not clear if the hard X-ray origin is also the disk or corona like in these systems. Several results point to a jet-related spectral component, linking (jet) activity to hardening of the X-ray spectrum (Tingay et al., 1998; Fukazawa et al., 2011; Beckmann et al., 2011). Hard X-ray observations with *Suzaku* by Fukazawa

et al. (2011) indicated jet-emission in this energy band. Tingay et al. (1998) discussed a possible correlation of X-ray enhancements with jet component ejection. From these observations, however, a possible coincidence could not be excluded. Furthermore, a single-zone synchrotron/synchrotron self-Compton model can sufficiently describe the broadband spectral energy distribution of Cen A (Abdo et al., 2010e) without including an additional jet related emission component. Note, however, recent analysis by Sahakyan et al. (2013) indicate a second spectral component in the γ-ray core emission.

The TANAMI jet kinematics of Cen A can help to further constrain the emission origin of the hard X-rays (Müller et al., 2014b). In principle, the correlation of a jet ejection event with a high X-ray flux phase would indicate a similar emission origin. Tingay et al. (1998) discussed the coincidence of the ejection times of C1 and C2 with X-ray high states of Cen A, but this correlation study lacks a comparable, continuous monitoring at these higher energies.

Figure 7.17 compares archival X-ray light curves of continuous monitoring by *Swift*/BAT, *RXTE*/ASM and *RXTE*/PCA, *CGRO*/BATSE with radio monitoring with SEST at (90 GHz to 350 GHz) by Israel et al. (2008) and the TANAMI monitoring results. In the γ-rays, *Fermi*/LAT monitoring reveals Cen A as a persistent source without any flaring over more than 2 years (Nolan et al., 2012; Ackermann et al., 2013).

The periods of long, persistently-high X-ray states are highlighted in Fig. 7.17. The approximate ejection times of individual radio knots are also indicated. A partial overlap of the higher X-ray activity and jet-component ejection is found, although, it is not significant enough to claim a common emission origin. The observation of more such correlated events are required to confirm this result. Furthermore, as discussed in Sect. 7.6.3, there is an indication of higher X-ray activity in 1999/2000 with the possible onset of the jet/obstacle interaction, though it is difficult to distinguish between the contributions of different emission mechanisms causing high energy activity. It is, however, striking that the continuous increase in the radio flux density of the inner jet (observed with TANAMI) follows the onset of activity in hard X-rays from end of 2007 onwards, supporting the results by Fukazawa et al. (2011). The authors report on an additional power law component required to model the hard X-ray spectrum at this high activity phase, possibly due to enhanced jet emission. This is in contrast to spectral models describing the hard X-ray spectrum during low X-ray activity (Markowitz et al., 2007). Furthermore, note that the higher 8.4 GHz flux density in the inner jet follows the ejection of the latest components J9 and J10. The radio flux is rising simultaneously to the detection of those components. Hence, where the jet is becoming optically thin and when the components are detected the total flux density is increasing, following the X-ray flux increase. A similar correlation might be seen between the years 2001 and 2003 where the detection of J6 to J8 follows a X-ray high flux state. The radio light curve from the Swedish–ESO Submillimetre Telescope (SEST) from Israel et al. (2008) and Tornikoski et al. (1996) does not allow to identify a correlated radio flare due to the sparse sampling and the large uncertainties.

It can be concluded that there is a possible evidence for a connection between hard X-ray and jet activity in Cen A. Due to the large uncertainties in the ejection times, the possibility that Cen A shows a similar behavior to 3C 120 and 3C 111 where jet ejections follow a dip in the X-ray light curves, cannot be fully excluded (Marscher et al., 2002; Marscher, 2006; Tombesi et al., 2012). Such event can be taken as a proof of the accretion disk-jet interaction. Note that the reported X-ray dips are shorter than the phases of lower X-ray emission in Cen A. Our observations point rather to jet-related hard X-ray activity than to such a direct proof of disk-jet connection. More ejection events and higher resolved X-ray spectra are required to confirm this result.

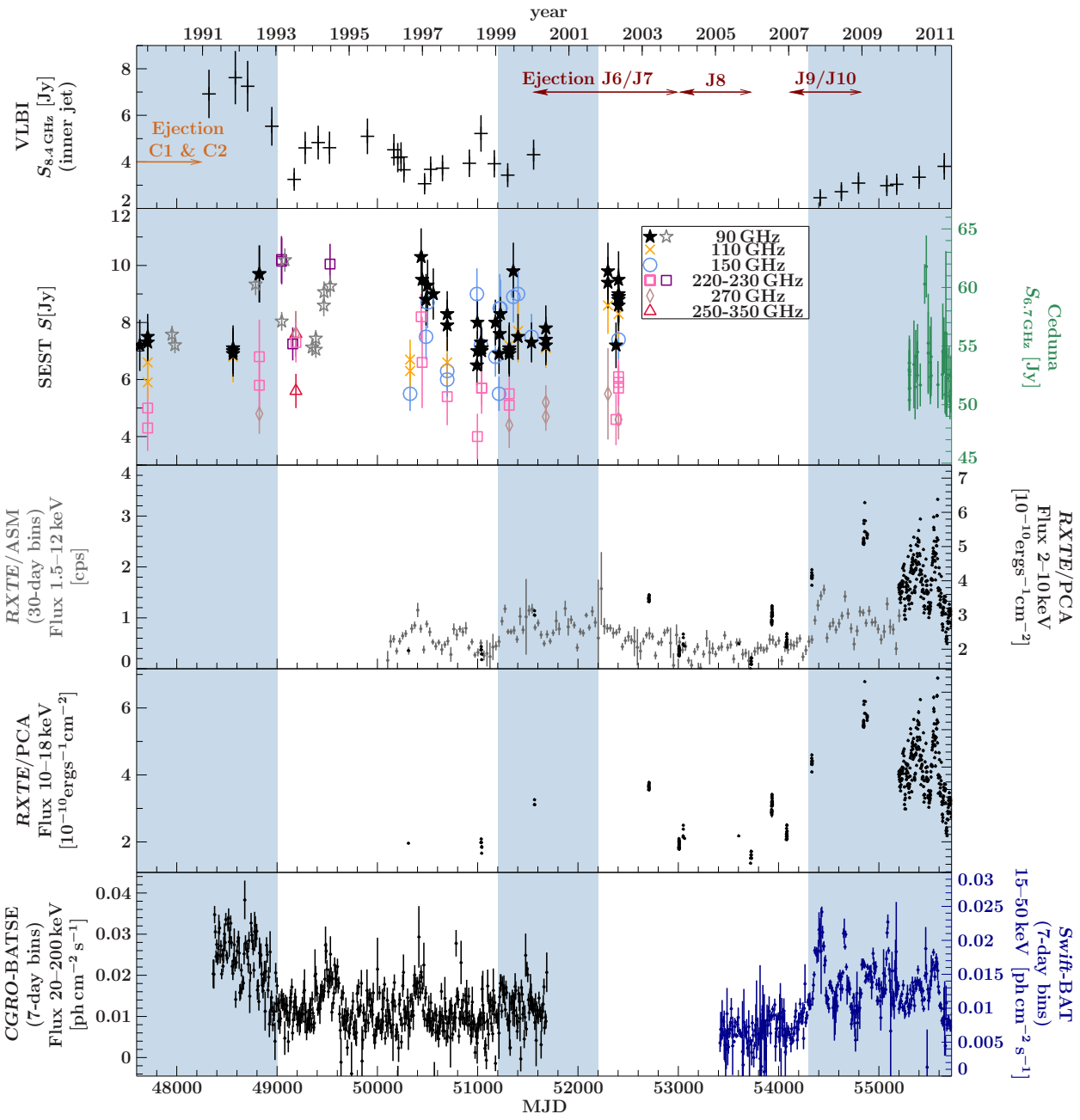

Figure 7.17.: Radio and X-ray light curves of the Cen A core. *From top to bottom*: Archival (Tingay et al., 1998, 2001,) and TANAMI 8.4 GHz flux density of inner jet (-2 mas $\leq$ $\mathrm{RA}_{\mathrm{relative}}$ $\leq$ 15 mas) adopting an uncertainty of 15%, ejection times including uncertainties indicated by arrows (see Table 7.3), SEST data (90 GHz – 350 GHz) from Israel et al. (2008) and Tornikoski et al. (1996), Ceduna monitoring at 6.7 GHz, *RXTE*/ASM (Data taken after MJD 55200 are affected by an instrumental decline and were therefore excluded, see e.g., Grinberg et al., 2013) and *RXTE*/PCA, *CGRO*/BATSE and *Swift*/BAT data after background subtraction. The blue shaded areas mark the time ranges of higher X-ray activity, defined by a flux increase of 3σ above the mean. Figure based on Müller et al. (2014b).

7.8. Zooming into the closest AGN - the big picture

The analysis of $\sim$ 3.5 years TANAMI monitoring of Cen A's jet have been presented. At 8.4 GHz and 22.3 GHz, these observations, at the highest angular resolution ever obtained for this source, resolve features of the inner parsec of less than 0.02 pc in size.

Up to 10 individual bright jet features can be tracked revealing complex dynamicals. Connecting these results with previous VLBI studies, a consistent picture of the central pc-scale jet is established. The jet kinematics are best explained by a spine-sheath structure. The similar appearance as a decade before (Horiuchi et al., 2006) in combination with a mean apparent speed as previously observed for larger structure (Tingay et al., 2001) indicates an underlying jet flow which is confined within a persistent channel. TANAMI observations clearly resolve this flow into individual jet knots. Their apparent speeds suggest a downstream acceleration, coinciding with the optically thin jet.

The TANAMI monitoring allows us to capture the evolution of both, the continuous flow in the stable jet sheath, with a faster spine resolved into discrete components. This result connects to the findings of a faster jet at 100 pc with a spectral steepening in the outer jet regions, explainable by layers with different particle acceleration conditions (Hardcastle et al., 2003; Worrall et al., 2008). Furthermore the discrepancy in inclination angle measurements for the parsec and 100 pc-scale jet is solved assuming a layered jet, for which the faster spine is dominating further downstream. The jet-to-counterjet ratio allows us to further constrain the inclination angle to $\theta \sim 12^\circ - 45^\circ$, indicating a possible intrinsic acceleration further connecting to the faster motion detected at kilo-parsec scales.

The nature of stationary jet features, which persist within the flow, were discussed. The second brightest, stationary feature at a distance of $\sim$ 3.5 mas from the core, is a long term stable component which has lasted in the jet for more than 15 years. It is most possibly due to a locally pressure maximum, similar to a jet nozzle. Further downstream (at $\sim$ 25.5 mas) a significant decrease of the surface brightness accompanied with a widening of the jet is detected. This "tuning fork"-like structure can well be explained by the jet hitting a star. This interaction causes a local increase of the optical depth and forces the jet into a circumfluent behaviour, without an entire disruption. On the basis of the reported observations, the different explanation of this jet feature as a recollimation shock cannot be excluded. However, such interaction events are expected for the denser populated central galactic region and have already been proposed to explain jet knots at several 100 pc (Hardcastle et al., 2003). Due to the expected short time range of such an event, further VLBI monitoring will be able to test this scenario.

TANAMI observations show a very dynamic innermost parsec of the jet with structural changes on timescales of months to years. The long time monitoring in the X-rays reveals several relatively high-flux states, prompting us to test for a correlation with phases of stronger jet activity. The onset of the higher X-ray emission end of 2007 is followed by an increase in the radio flux density of the inner jet contemporaneous with the detection of two new components. A similar coincidence is indicated during active phases between 1999 and 2001 and was discussed for the activity before 1992 by Tingay et al. (1998). If such a correlation of higher (hard) X-ray flux with higher jet activity is confirmed by further VLBI monitoring, it will be a clear indication for the emission origin of hard X-rays in Cen A. As discussed by Fukazawa et al. (2011), the high hard X-ray flux phase of Cen A is correlated with spectral hardening in the X-rays, possibly due to increased jet emission. The time evolution of the innermost part of Cen A in radio to X-rays could then be explained by higher jet activity causing an increase in high energy emission. This is followed by a rise in radio brightness when these newly emerged components move downstream and become optically thin.

It is crucial to disentangle the emission components in the X-rays and γ-rays in order to better constrain the broadband spectral energy distribution of Cen A. The best-resolved spectral index image of Cen A reveals a remarkably flat spectrum over the inner few mas, indicating multiple optically thick emission zones. These regions can be identified as production sites of highly energetic photons, thus, already challenging current one-zone broadband emission models. Recent findings of an additional hard spectral component in the γ-rays (Sahakyan et al., 2013) support the idea of multiple emission zones. Star-jet interactions could explain the observed high energy emission and should be taken into account when modeling the broadband SED.

In summary, these VLBI observations of the closest extragalactic jet provide an unprecedented view on the complex dynamics, spectral properties and interaction events with the environment in the inner parsec of an AGN. Supporting multiwavelength monitoring gives important information to link changes and particular features in the sub-parsec scale jet with activity at higher energies, helping to identify the emission origin and mechanism.

The most beautiful thing we can experience is the mysterious. It is the source of all true art and science.

(Albert Einstein)

8. Conclusion and outlook

The study of emission mechanisms and formation of extragalactic jets requires the combination of multiwavelength observations – monitoring their activity and spectral changes – and high angular resolution observations – probing the innermost parts of these powerful objects. In this thesis, AGN jets in the Southern Hemisphere have been studied using VLBI techniques and (quasi-)simultaneous multiwavelength observations throughout the spectrum. I have concentrated on the TANAMI sample, providing detailed, mostly best-ever, information on the mas-scale properties of these sources. Simultaneous *Fermi*/LAT monitoring gives valuable information on their high-energy emission behavior. Two TANAMI sources have been analyzed in great detail, namely PMN J1603−4904 and Centaurus A. Both stand out in their own particular way – be it the atypical multiwavelength characteristics or the proximity. Sharing many properties with the TANAMI sample, these two sources are ideal candidates to address certain open questions of jet physics, which are outlined in Sect. 1.4.

The composition of jets is still matter of debate. Multimessenger astronomy can help to distinguish whether jets purely consist of leptons or also of hadrons by testing AGN jets as potential neutrino emitters. Assuming that γ-ray emission is correlated with enhanced neutrino flux, I analyzed the *Fermi*/LAT light curves of all γ-ray loud TANAMI sources to select the ones showing significant short and bright flares (see Ch. 4). We found that the ANTARES sensitivity can be considerably enhanced, using this time information. This selection study prepares the ground for further neutrino point-source searches. A clear neutrino signal from an extragalactic jet would give evidence for hadronic emission and would identify jets as cosmic-ray accelerators.

Of all TANAMI sources, 25% remain undetected in γ-rays while for all others a relation between the radio and γ-ray luminosities was found (Böck, 2012). The high-energy properties raise the question, whether there are differences in the mas-scale structure of the γ-ray bright to the faint sources. I have presented the mas-scale properties of all 75 TANAMI sources in Ch. 5 with respect to their γ-ray loudness. This analysis confirms the well established relation of higher γ-ray brightness with higher beaming factors. Moreover, the radio flux density and morphological properties of the unidentified sources further suggest that these are potential BL Lac objects. The quasars in the TANAMI sample, however, do not show a simple "core-dominated and γ-bright"-behavior. The flux density distribution as well as their various mas-scale morphologies indicate possible sub-types, possibly including intrinsically γ-ray faint, but radio-loud quasars. The vast number of emission components required to model FSRQ SEDs already hint at a large variety of quasars and support this result.

This leads me to the investigation of the underlying emission mechanism and production sites of high energy photons. Kinematic studies have shown that jets are highly relativistic, producing shocks, in which high energy photons can be accelerated (see Sect. 1.3.1 and, e.g., Marscher,

2009). However, this is just one of many explanations, where and how the high-energy hump in blazar SEDs is formed. Taking advantage of Cen A's proximity, dual-frequency VLBI observations provide insight into the spectral index distribution along the inner parsec of the jet, revealing multiple possible emission sites for γ-rays (Müller et al., 2011). The comparison of multiwavelength monitoring and VLBI observations (Müller et al., 2014b) show a possible correlation of jet and hard X-ray activity (see Sect. 7.7). If confirmed, this result will effectively constrain emission models for the broadband SED of Cen A. In a future work, I will investigate high sensitivity *XMM-Newton* and *Suzaku* observations of Cen A with the aim to disentangle different emission components of the X-ray spectrum, i.e., I will address this issue with two different approaches.

PMN J1603−4904 was one of the brightest AGN in the γ-ray sky, but showed no major flaring activity (Nolan et al., 2012). It remains an open question, what causes this high flux density. The multiwavelength properties point towards either a very atypical blazar or a possible young radio source with starburst contribution (see Ch. 6 and Müller et al., 2014a). Recent high sensitivity X-ray observations reveal a narrow iron line, which allows the first redshift measurement of the system ($z \sim 0.174$, see Sect. 6.2.4, Müller et al. in prep.). Furthermore this spectral component is another feature very unusual for a blazar and is compatible with a jet-system seen under a higher inclination angle. This object plays an important role in investigating the broadband emission of extragalactic jets because it exhibits these ambiguous properties. The analysis is ongoing and observations with ALMA, the *Hubble Space Telescope* and *Chandra* are proposed to further shed light on this peculiar source.

VLBI observations of extragalactic jets allows us to address their parsec-scale structure. In the case of Cen A, (sub-)mas resolution probes the innermost parsec, resolving features of ~ 0.02 pc in size. With TANAMI observations we gain the most detailed view on this jet, revealing complex dynamics. At these scales, the jet is already well collimated and indicates downstream acceleration. The jet kinematic and overall appearance can be well explained by a spine-sheath structure (Müller et al., 2014b). Future studies, including the evolution of the brightness temperature distribution along the jet will provide further information on the jet formation and structure of Cen A. These high-resolution information are crucial to compare with theoretical models and simulations, since such cannot be obtained for any other source.

Furthermore, the TANAMI observations of Cen A's jet have been full of surprises: the γ-ray emission of a blazar can be explained by interactions of stars or clouds with the jet (e.g., Barkov et al., 2010; Bosch-Ramon et al., 2012; Araudo et al., 2013). There exist several theoretical considerations and some indications for such events in other sources or in Cen A at larger scales (see Sect. 7.6.3), but a direct observation within the central parsec of an AGN has not been observed. The TANAMI observations of Cen A show a standing disturbance causing a "tuning-fork" like emission feature. This appearance is best explained by the scenario, in which the jet hits a red giant (Müller et al., 2014b), and can be easily tested with ongoing TANAMI monitoring. Interactions of this kind open room for alternative interpretations of high energy emission components in broadband SEDs, which are difficult to reconcile with a single-zone SSC model.

With the results presented in this thesis, I have contributed some valuable information on AGN jet physics. I have shown that only the combination of detailed studies of complex sources with sample analyses obtains a deeper understanding. Future observations throughout the spectrum will substantiate these findings and provide better insights into these (still) enigmatic objects.

A. Appendix

A.1. Modelfit parameters of Cen A's jet kinematics

Tables A.1 to A.7 give the modelfit parameters for individual jet components of the corresponding kinematic study of Cen A (see Sect. 7.5) without statistical uncertainties, since they are dominated by systematics. The columns successively give the label of the model component, if identified in several consecutive epochs, the integrated flux density S at 8.4 GHz, the distance d and position angle θ from the designated phase center, the major axis extent b_{maj} (FWHM), and the logarithm of the brightness temperature of the Gaussian model component.

Table A.1.: Modelfit parameters: **2007-11-10** ($\chi^2 = 4904.3$, d.o.f= 1954)

Label	$S_{8.4\,\mathrm{GHz}}$ [Jy]	d [mas]	θ [°]	b_{maj}	$\log T_{\mathrm{B}}$
	0.01	18.88	−125.81	0.11	10.31
Core	0.99	0.00	–	0.59	10.70
J9	0.47	1.41	49.48	0.64	10.30
$\mathrm{J_{stat}}$	0.62	3.78	48.02	0.65	10.41
J8	0.13	6.88	51.07	0.53	9.91
J7	0.11	10.47	44.62	0.60	9.75
J6	0.13	13.08	44.91	0.63	9.76
	0.02	19.26	44.77	0.25	9.72
J5	0.07	29.82	48.96	0.54	9.65
J4	0.06	32.68	50.13	0.54	9.51

Table A.2.: Modelfit parameters: **2008-06-09** ($\chi^2 = 1909.4$, d.o.f= 3828)

Label	$S_{8.4\,\mathrm{GHz}}$ [Jy]	d [mas]	θ [°]	b_{maj}	$\log T_{\mathrm{B}}$
	0.06	50.42	−128.60	2.61	8.18
	0.04	35.69	−127.68	0.42	9.58
	0.04	15.40	−131.46	0.28	9.97
Core	1.33	0.00	–	0.78	10.59
J_{stat}	0.81	3.45	46.72	1.07	10.10
J8	0.34	7.01	51.88	1.17	9.64
J7	0.29	11.37	49.88	2.89	8.79
J6	0.07	14.99	49.86	0.47	9.73
	0.08	20.14	40.58	2.44	8.38
	0.03	21.59	57.21	1.57	8.38
J5	0.05	30.61	48.83	0.24	10.21
J4	0.17	33.43	49.19	2.86	8.55
J3	0.05	48.36	52.14	2.34	8.22

Table A.3.: Modelfit parameters **2008-11-27** ($\chi^2 = 5389.6$, d.o.f= 7526)

Label	$S_{8.4\,\mathrm{GHz}}$ [Jy]	d [mas]	θ [°]	b_{maj}	$\log T_{\mathrm{B}}$
	0.03	86.44	−128.07	0.77	8.90
	0.02	80.77	−126.69	0.76	8.87
	0.04	52.38	−129.23	0.93	8.87
	0.02	35.51	−124.87	0.50	9.06
	0.03	21.76	−126.69	0.47	9.37
	0.05	3.97	−125.86	0.28	10.07
	0.38	0.65	−117.53	0.22	11.15
Core	0.74	0.00	–	0.29	11.19
J10	0.48	0.67	60.90	0.33	10.88
J_{stat}	0.45	3.43	46.85	0.68	10.23
J9	0.26	4.02	50.92	0.64	10.04
J8	0.32	8.34	49.39	1.17	9.61
J7	0.33	12.96	49.37	2.43	8.99
J6	0.05	18.36	51.39	0.39	9.76
	0.04	23.22	42.60	0.57	9.33
	0.07	24.35	52.36	0.63	9.51
	0.13	29.00	50.45	1.97	8.76
J5	0.15	33.85	49.87	0.89	9.52
J4	0.18	37.91	49.66	2.36	8.75
	0.06	43.49	49.62	0.85	9.16
J3	0.05	48.98	50.71	1.84	8.38
J2	0.03	59.12	51.06	0.72	9.05
J1	0.02	65.79	49.20	0.61	9.02

Table A.4.: Modelfit parameters: **2009-09-05** ($\chi^2 = 5076.96$, d.o.f= 7824)

Label	$S_{8.4\,\mathrm{GHz}}$ [Jy]	d [mas]	θ [°]	b_{maj}	$\log T_{\mathrm{B}}$
	0.06	45.06	−129.90	3.68	7.87
	0.06	33.30	−124.66	3.38	7.94
	0.03	20.40	−124.02	0.42	9.40
	0.04	14.58	−126.01	0.25	10.07
	0.07	10.41	−125.56	0.11	11.01
	0.15	3.48	−115.44	0.58	9.88
Core	1.61	0.00	–	0.82	10.62
$\mathrm{J}_{\mathrm{stat}}$	0.71	3.58	50.82	0.85	10.23
J9	0.03	6.37	44.95	0.00	33.88
J8	0.37	8.97	49.76	0.93	9.88
J7	0.26	13.34	48.03	0.86	9.79
J6	0.07	18.89	46.66	0.54	9.62
	0.12	25.40	46.35	4.45	8.01
J5	0.11	36.10	49.32	0.98	9.32
J4	0.16	39.92	49.27	2.05	8.81
J3	0.04	51.93	50.16	1.66	8.40
J2	0.05	63.26	49.75	0.71	9.24
J1	0.01	67.26	49.96	0.44	9.11
	0.04	93.49	51.11	2.04	8.20

Table A.5.: Modelfit parameters: **2009-12-13** ($\chi^2 = 2235.6$, d.o.f= 2350)

Label	$S_{8.4\,\mathrm{GHz}}$ [Jy]	d [mas]	θ [°]	b_{maj}	$\log T_{\mathrm{B}}$
	0.05	44.78	−128.36	3.23	7.93
	0.08	13.73	−128.49	0.64	9.56
	0.35	3.81	−121.27	0.52	10.36
Core	1.76	0.00	–	0.72	10.78
$\mathrm{J}_{\mathrm{stat}}$	0.83	3.28	43.32	0.72	10.45
J8	0.31	10.12	55.21	0.75	9.98
J7	0.33	13.57	49.04	1.89	9.21
	0.12	24.47	41.05	2.73	8.45
J4	0.07	39.91	49.12	2.67	8.21

Table A.6.: Modelfit parameters: **2010-07-24** ($\chi^2 = 5076.4$, d.o.f= 8644)

Label	$S_{8.4\,\mathrm{GHz}}$ [Jy]	d [mas]	θ [°]	b_{maj}	$\log T_{\mathrm{B}}$
	0.02	67.55	−123.51	2.93	7.52
	0.08	19.84	−121.78	4.17	7.92
	0.03	9.61	−136.30	0.30	9.79
	0.02	3.15	−123.14	< 0.05	> 11.14
Core*	1.58	0.00	−145.70	0.82	10.93
$\mathrm{J_{stat}}$	0.77	2.96	47.26	0.83	10.29
J10	0.38	5.43	45.07	0.73	10.11
J9	0.15	8.56	49.87	0.56	9.94
J8	0.23	12.87	49.94	1.31	9.39
J7	0.35	16.85	50.09	3.57	8.67
J6	0.02	22.16	45.63	0.35	9.72
	0.07	22.56	53.91	0.89	8.74
	0.12	27.37	51.33	0.68	9.65
	0.08	32.05	49.39	0.71	9.42
J5	0.13	37.09	48.22	1.45	8.99
J4	0.09	40.98	46.92	1.79	8.65
J3	0.01	57.42	54.34	0.22	9.62

*Elliptical component with $b_{\mathrm{maj}} = 0.82$ mas, axis ratio of 0.47 and PA= −232°.

Table A.7.: Modelfit parameters: **2011-04-01** ($\chi^2 = 24151.7$, d.o.f= 6846)

Label	$S_{8.4\,\mathrm{GHz}}$ [Jy]	d [mas]	θ [°]	b_{maj}	$\log T_{\mathrm{B}}$
	0.06	113.32	−126.83	1.95	8.41
	0.03	51.59	−127.97	0.43	9.44
	0.03	41.46	−125.16	0.44	9.43
	0.13	36.89	−123.15	3.85	8.19
	0.05	24.83	−125.86	0.37	9.80
	0.38	10.16	−132.63	3.72	8.68
	0.20	2.85	−124.05	0.25	10.75
	0.68	1.50	−134.03	0.52	10.64
Core	1.21	0.00	–	0.65	10.70
	0.74	2.54	49.21	0.65	10.49
$\mathrm{J_{stat}}$	0.38	4.02	46.51	0.64	10.21
J10	0.32	6.80	50.72	0.64	10.13
J9	0.22	10.31	49.18	0.83	9.76
J8	0.36	13.82	49.74	1.40	9.50
J7	0.29	16.88	46.85	2.39	8.95
	0.05	19.80	45.11	0.35	9.82
J6	0.11	23.33	45.31	0.57	9.78
	0.10	32.03	48.36	0.58	9.71
	0.13	35.82	47.80	0.62	9.78
J5	0.15	39.25	48.00	0.82	9.59
J4	0.22	46.87	48.51	3.45	8.51
J3	0.12	61.23	49.21	1.41	9.03
	0.04	105.52	47.34	2.15	8.15

A.2. The "tuning fork" and a possible obstacle

In Sect. 7.6.3 possible explanations of the jet widening are discussed together with a decrease in surface brightness which appears to be stationary over the TANAMI monitoring period. The jet flow is likely to be disturbed by an obstacle. In the main text, the scenario including a red-giant with a significant stellar wind is favored by the calculations and observations. In the following, the corresponding calculations, assuming the obstacle is a cloud, are summarized.

The interaction with the jet should produce a shock in the cloud. The cloud would be disrupted by the shock, if the jet crossing time of the cloud is larger than the propagation time of the shock. In this case, the bow-shock structure would have disappeared (Araudo et al., 2010; Bosch-Ramon et al., 2012). Hence, assuming that the obstacle has been within the jet for at least ten years, gives a cloud shocking time of $t_{\rm cs} > 3.1 \times 10^8\,$s. Then, Eq. 4 in Araudo et al. (2010) can be used to determine a lower limit of the density of the cloud

$$t_{\rm cs} = \frac{2R_{\rm c}}{v_{\rm cs}} \simeq 6.2 \times 10^8 \left(\frac{R_{\rm c}}{3.1\times10^{15}\,{\rm cm}}\right)\left(\frac{n_{\rm c}}{10^{10}\,{\rm cm^{-3}}}\right)^{1/2}\left(\frac{z}{3.1\times10^{18}\,{\rm cm}}\right)\left(\frac{L_{\rm j}}{10^{44}\,{\rm erg\,s^{-1}}}\right)^{-1/2}{\rm s}, \tag{A.1}$$

where $z = 1\,{\rm pc} = 3.1 \times 10^{18}\,$cm was taken as a reference. Taking into account the aforementioned lower limit on time, and taking as input data the obstacle radius $R_{\rm c} = 10^{-3}\,$pc, the jet power from the literature ($L_{\rm j} \simeq 10^{44}\,{\rm erg\,s^{-1}}$, Abdo et al., 2010e), and the location of the "tuning fork" along the jet $z \simeq 0.4\,$pc, a limit on the cloud density is given by

$$n_{\rm c} \;>\; 1.5 \times 10^{10}\left(\frac{t_{\rm cs}}{3.1\times10^{8}\,{\rm s}}\right)^{2}\left(\frac{R_{\rm c}}{3.1\times10^{15}\,{\rm cm}}\right)^{-2}\left(\frac{z}{1.2\times10^{18}\,{\rm cm}}\right)^{-2}\left(\frac{L_{\rm j}}{10^{44}\,{\rm erg\,s^{-1}}}\right){\rm cm^{-3}}. \tag{A.2}$$

Rivers et al. (2011) have reported on an occultation of the central core for 170 days due to the passage of a discrete clump of material through the line of sight in the context of a clumpy torus model. The eclipse is short because the angular size of the eclipsed region must be small. Interestingly, for the hypothetical clump, which is located at a similar distance to the core to that reported for the location of the "tuning fork" ($0.1 \ldots 0.3\,$pc, adopting measurements by Meisenheimer et al., 2007), the authors obtain a central density of $n_{\rm clump} = (1.8 - 3.0) \times 10^7\,{\rm cm^{-3}}$ and a size of $R_{\rm clump} = (1.4 - 2.4) \times 10^{15}\,$cm. The size of the clump would be in agreement with our result, but the density, required for the cloud to survive the interaction for ten years, is three orders of magnitude larger. In addition, the cloud velocity estimated by Rivers et al. (2011) is one order of magnitude smaller than the one used for the here presented calculations ($v_{\rm clump} \simeq 1000\,{\rm km\,s^{-1}}$, Eq. 7.2). Such a decrease in velocity would have two effects: first, the crossing time would be increased in a factor of 10 in Eq. 7.2, i.e., $t_{\rm j} \simeq 6.2 \times 10^9\,$s ($\sim 200\,$years), and secondly, due to this increase in the crossing time, the lower limit in the cloud density obtained in Eq. A.2 would be increased in a factor of 100 ($n_{\rm c} > 1.5 \times 10^{12}\,{\rm cm^{-3}}$). Following the result by Rivers et al. (2011), we could thus conclude that the cloud scenario should be ruled out for the "tuning fork". First, clumps with larger densities at larger distances from the nucleus are unexpected. Secondly, the shock crossing time of the cloud, given by Eq. A.1 would be reduced by a factor of 20 for the cloud density given in Rivers et al. (2011), giving thus $t_{\rm cs} \simeq 3.4 \times 10^7\,$s ($\sim 1\,$year).

Clumps of the size and density as those obtained by Rivers et al. (2011) for the case of a clumpy torus would survive a jet interaction for about one year before being disrupted. They would be destroyed close to the jet boundary, provided that their jet crossing time is $\sim$200 years. Therefore, this scenario cannot explain the steady situation that is observed at the "tuning fork".

Bibliography

Abdo A.A., Ackermann M., Agudo I., et al., 2010a, ApJ 716, 30
Abdo A.A., Ackermann M., Ajello M., et al., 2010b, ApJ 715, 429
Abdo A.A., Ackermann M., Ajello M., et al., 2010, ApJS 188, 405
Abdo A.A., Ackermann M., Ajello M., et al., 2010a, ApJ 722, 520
Abdo A.A., Ackermann M., Ajello M., et al., 2009, ApJ 700, 597
Abdo A.A., Ackermann M., Ajello M., et al., 2010b, ApJ 708, 1310
Abdo A.A., Ackermann M., Ajello M., et al., 2010c, ApJ 709, L152
Abdo A.A., Ackermann M., Ajello M., et al., 2010d, Science 328, 725
Abdo A.A., Ackermann M., Ajello M., et al., 2010e, ApJ 719, 1433
Abdo A.A., Ackermann M., Ajello M., et al., 2010f, Nat 463, 919
Abdo A.A., Ackermann M., Ajello M., et al., 2010g, ApJ 720, 912
Abdo A.A., Ackermann M., Arimoto M., et al., 2009, Science 323, 1688
Acero F., Aharonian F., Akhperjanian A.G., et al., 2009, Science 326, 1080
Ackermann M., Ajello M., Allafort A., et al., 2011, ApJ 743, 171
Ackermann M., Ajello M., Allafort A., et al., 2013, ApJS 209, 34
Ackermann M., Ajello M., Allafort A., et al., 2012a, ApJ 755, 164
Ackermann M., Ajello M., Allafort A., et al., 2012b, Science 338, 1190
Ageron M., Aguilar J.A., Al Samarai I., et al., 2011, Nuclear Instruments and Methods in Physics Research A 656, 11
Agudo I., Gómez J.L., Martí J.M., et al., 2001, ApJ 549, L183
Aharonian F., Akhperjanian A.G., Anton G., et al., 2009, ApJ 695, L40
Alfvén H., Herlofson N., 1950, Physical Review 78, 616
An T., Wu F., Yang J., et al., 2012, ApJS 198, 5
Antonucci R., 1993, ARA&A 31, 473
Araudo A.T., Bosch-Ramon V., Romero G.E., 2010, A&A 522, A97
Araudo A.T., Bosch-Ramon V., Romero G.E., 2013, MNRAS 436, 3626
Atoyan A., Dermer C.D., 2001, Physical Review Letters 87, 221102
Atwood W.B., Abdo A.A., Ackermann M., et al., 2009, ApJ 697, 1071
Baade W., Minkowski R., 1954, ApJ 119, 215
Barkov M.V., Aharonian F.A., Bosch-Ramon V., 2010, ApJ 724, 1517
Barkov M.V., Bosch-Ramon V., Aharonian F.A., 2012, ApJ 755, 170
Baum S.A., O'Dea C.P., Murphy D.W., de Bruyn A.G., 1990, A&A 232, 19
Baumgartner W.H., Tueller J., Markwardt C., Skinner G., 2010, In: AAS/High Energy Astrophysics Division #11, Vol. 42. Bulletin of the American Astronomical Society, p. 675
Beasley M.A., Bridges T., Peng E., et al., 2008, MNRAS 386, 1443
Beckmann V., Jean P., Lubiński P., et al., 2011, A&A 531, A70+
Beckmann V., Shrader C.R., 2012, Active Galactic Nuclei, Wiley-VCH Verlag GmbH
Bednarek W., Protheroe R.J., 1997, MNRAS 287, L9

Benson A.J., 2010, Physics Reports 495, 33
Bethe H., Heitler W., 1934, Royal Society of London Proceedings Series A 146, 83
Bevington P.R., Robinson D.K., 2003, Data reduction and error analysis for the physical sciences, Boston: McGraw-Hill
Bianchi S., Maiolino R., Risaliti G., 2012, Advances in Astronomy 2012
Bianchi S., Matt G., Balestra I., et al., 2004, A&A 422, 65
Bicknell G.V., Dopita M.A., O'Dea C.P.O., 1997, ApJ 485, 112
Biggs A.D., Browne I.W.A., Helbig P., et al., 1999, MNRAS 304, 349
Blanchard J.M., Lovell J.E.J., Ojha R., et al., 2012, A&A 538, A150
Blandford R.D., Königl A., 1979, ApJ 232, 34
Blandford R.D., Payne D.G., 1982, MNRAS 199, 883
Blandford R.D., Rees M.J., 1978, Physica Scripta 17, 265
Blandford R.D., Znajek R.L., 1977, MNRAS 179, 433
Böck M., 2012, Ph.D. thesis, Friedrich-Alexander-Universität, Erlangen-Nürnberg, Germany
Böck M., Kadler M., Müller C., et al., 2014, A&A submitted
Boettcher M., 2010, In: Savolainen, T., Ros, E., Porcas, R.W. & Zensus, J.A. (ed.) Proceedings of the Workshop "Fermi meets Jansky - AGN in Radio and Gamma-Rays", Bonn: MPIfR.
Boettcher M., Harris D.E., Krawczynski H., 2012, Relativistic Jets from Active Galactic Nuclei, Berlin: Wiley
Bosch-Ramon V., Perucho M., Barkov M.V., 2012, A&A 539, A69
Böttcher M., Dermer C.D., 2010, ApJ 711, 445
Brand T., 2013, *Master's thesis*, Friedrich-Alexander Universität Erlangen/Nürnberg, Germany
Britzen S., Vermeulen R.C., Campbell R.M., et al., 2008, A&A 484, 119
Britzen S., Vermeulen R.C., Taylor G.B., et al., 2007, A&A 472, 763
Burke & Graham-Smith (ed.) 2002, An Introduction to Radio Astronomy: Second Edition, Cambridge, Cambridge University Press
Burrows D.N., Hill J.E., Nousek J.A., et al., 2005, Space Sci. Rev. 120, 165
Burtscher L., 2011, Ph.D. thesis, Max-Planck-Institut für Astronomie, Königstuhl 17, 69117 Heidelberg, Germany
Carvalho J.C., 1998, A&A 329, 845
Cash W., 1979, ApJ 228, 939
Cerruti M., Boisson C., Zech A., 2013, A&A 558, A47
Chang C.S., 2010, Ph.D. thesis, Max-Planck-Institut für Radioastronomie
Chen P.S., Shan H.G., 2011, ApJ 732, 22
Ciaramella A., Bongardo C., Aller H.D., et al., 2004, A&A 419, 485
Ciprini S., Thompson D.J., on behalf of the Fermi LAT collaboration 2013, In: 2012 Fermi Symposium proceedings - eConf C121028.
Clarke D.A., Burns J.O., Norman M.L., 1992, ApJ 395, 444
Clay R.W., Whelan B.J., Edwards P.G., 2010, PASA in press
Cohen M.H., Linfield R.P., Moffet A.T., et al., 1977, Nat 268, 405
Compton A.H., 1923, Physical Review 21, 483
Condon J.J., Cotton W.D., Greisen E.W., et al., 1998, AJ 115, 1693
Cotton W.D., 1995, In: Zensus J.A., Diamond P.J., Napier P.J. (eds.) Very Long Baseline Interferometry and the VLBA, Vol. 82. Astronomical Society of the Pacific Conference Series, p. 189
Cuoco A., Hannestad S., 2008, Phys. Rev. D 78
D'Abrusco R., Massaro F., Paggi A., et al., 2013, ApJS 206, 12
Deller A.T., Tingay S.J., Bailes M., West C., 2007, PASP 119, 318
Dermer C., Lott B., 2012, Journal of Physics Conference Series 355, 012010
Dermer C.D., Finke J.D., Krug H., Böttcher M., 2009, ApJ 692, 32
Dermer C.D., Schlickeiser R., 1993, ApJ 416, 458
Dermer C.D., Schlickeiser R., 2002, ApJ 575, 667
Dermer C.D., Schlickeiser R., Mastichiadis A., 1992, A&A 256, L27

Dermer C.D., Sturner S.J., Schlickeiser R., 1997, ApJS 109, 103
Di Matteo T., Springel V., Hernquist L., 2005, Nat 433, 604
Diamond P.J., 1995, In: J. A. Zensus, P. J. Diamond, & P. J. Napier (ed.) Very Long Baseline Interferometry and the VLBA. ASP Conf. Proc., 82, p.227
Dicken D., Tadhunter C., Axon D., et al., 2012, ApJ 745, 172
Dodson R., Fomalont E.B., Wiik K., et al., 2008, ApJS 175, 314
Donato D., Ghisellini G., Tagliaferri G., Fossati G., 2001, A&A 375, 739
Dunlop J., 1828, Royal Society of London Philosophical Transactions Series I 118, 113
Dutka M.S., Ojha R., Pottschmidt K., et al., 2013, ApJ 779, 174
Edwards P.G., Tingay S.J., 2004, A&A 424, 91
Elbaz D., Dickinson M., Hwang H.S., et al., 2011, A&A 533, A119
Ellingson S.W., Clarke T.E., Cohen A., et al., 2009, IEEE Proceedings 97, 1421
ESO Publication Office 2012, Astronomy and Geophysics 53, 040000
Evans D.A., Kraft R.P., Worrall D.M., et al., 2004, ApJ 612, 786
Fabian A.C., 2012, ARA&A 50, 455
Fanaroff B.L., Riley J.M., 1974, MNRAS 167, 31P
Fanti C., Fanti R., Dallacasa D., et al., 1995, A&A 302, 317
Fassnacht C.D., Taylor G.B., 2001, AJ 122, 1661
Fazio G.G., 1970, nat 225, 905
Fehn K., 2014, Ph.D. thesis, Friedrich-Alexander-Universität, Erlangen-Nürnberg, Germany, in prep.
Fermi E., 1949, Physical Review 75, 1169
Ferrarese L., Merritt D., 2000, ApJ 539, L9
Finke J.D., 2013, ApJ 763, 134
Fitzpatrick E.L., 1999, PASP 111, 63
Fomalont E., 1981, NRAO Newsletter 3, 3
Fossati G., Maraschi L., Celotti A., et al., 1998, MNRAS 299, 433
Frail D.A., Scharringhausen B.R., 1997, ApJ 480, 364
Fritsch U., 2014, Ph.D. thesis, Friedrich-Alexander-Universität, Erlangen-Nürnberg, Germany, in prep.
Fujisawa K., Inoue M., Kobayashi H., et al., 2000, PASJ 52, 1021
Fukazawa Y., Hiragi K., Yamazaki S., et al., 2011, ApJ 743, 124
Fürst F., 2011, Ph.D. thesis, Friedrich-Alexander-Universität, Erlangen-Nürnberg, Germany
Gaensler B.M., Slane P.O., 2006, ARA&A 44, 17
Gambill J.K., Sambruna R.M., Chartas G., et al., 2003, A&A 401, 505
Gehrels N., Chincarini G., Giommi P., et al., 2004, ApJ 611, 1005
Gehrels N., Shrader C.R., 2001, In: Ritz S., Gehrels N., Shrader C.R. (eds.) Gamma 2001: Gamma-Ray Astrophysics, Vol. 587. American Institute of Physics Conference Series, p.3
Georganopoulos M., Finke J.D., Reyes L.C., 2010, ApJ 714, L157
Georganopoulos M., Kazanas D., 2003a, ApJ 594, L27
Georganopoulos M., Kazanas D., 2003b, ApJ 589, L5
Ghisellini G., Celotti A., Fossati G., et al., 1998, MNRAS 301, 451
Ghisellini G., Tagliaferri G., Foschini L., et al., 2011, MNRAS 411, 901
Ghisellini G., Tavecchio F., 2008, MNRAS 387, 1669
Ghisellini G., Tavecchio F., Chiaberge M., 2005, A&A 432, 401
Ghisellini G., Tavecchio F., Foschini L., et al., 2010, MNRAS 402, 497
Giommi P., Polenta G., Lähteenmäki A., et al., 2012, A&A 541, A160
Giroletti M., Giovannini G., Taylor G.B., Falomo R., 2004, ApJ 613, 752
GLAST Facility Science TeamGehrels N., Michelson P., 1999, Astroparticle Physics 11, 277
Gomez J.L., Marti J.M.A., Marscher A.P., et al., 1995, ApJ 449, L19
Goodger J.L., Hardcastle M.J., Croston J.H., et al., 2010, ApJ 708, 675
Grandi P., Malaguti G., Fiocchi M., 2006, ApJ 642, 113
Grandi P., Palumbo G.G.C., 2004, Science 306, 998

Gregory P.C., Vavasour J.D., Scott W.K., Condon J.J., 1994, ApJS 90, 173
Greisen E.W., 2003, Information Handling in Astronomy - Historical Vistas 285, 109
Griffith M.R., Wright A.E., 1993, AJ 105, 1666
Griffith M.R., Wright A.E., Burke B.F., Ekers R.D., 1994, ApJS 90, 179
Grinberg V., Hell N., Pottschmidt K., et al., 2013, A&A 554, A88
Großberger C., 2014, Ph.D. thesis, Friedrich-Alexander-Universität, Erlangen-Nürnberg, Germany
Gubbay J., Legg A.J., Robertson D.S., et al., 1969, Nat 224, 1094
Gültekin K., Richstone D.O., Gebhardt K., et al., 2009, ApJ 698, 198
Halzen F., Hooper D., 2002, Reports on Progress in Physics 65, 1025
Halzen F., Klein S.R., 2010, Review of Scientific Instruments 81, 081101
Hanke M., 2011, Ph.D. thesis, Friedrich-Alexander-Universität, Erlangen-Nürnberg, Germany
Hardcastle M.J., Worrall D.M., Birkinshaw M., et al., 2002, MNRAS 334, 182
Hardcastle M.J., Worrall D.M., Kraft R.P., et al., 2003, ApJ 593, 169
Harris G.L.H., Rejkuba M., Harris W.E., 2010, Proc. Astron. Soc. Aust. 27, 457
Hartman R.C., Bertsch D.L., Bloom S.D., et al., 1999, ApJS 123, 79
Hartman R.C., Bertsch D.L., Fichtel C.E., et al., 1992, In: C. R. Shrader, N. Gehrels, & B. Dennis (ed.) NASA Conference Publication, Vol. 3137., p.116
Hasinger G., Miyaji T., Schmidt M., 2005, A&A 441, 417
H.E.S.S. CollaborationAbramowski A., Acero F., et al., 2013a, A&A 550, A4
H.E.S.S. CollaborationAbramowski A., Acero F., et al., 2013b, A&A 552, A118
Hirabayashi H., Hirosawa H., Kobayashi H., et al., 2000, PASJ 52, 955
Högbom J.A., 1974, A&AS 15, 417
Homan D.C., Kadler M., Kellermann K.I., et al., 2009, ApJ 706, 1253
Homan D.C., Ojha R., Wardle J.F.C., et al., 2002, ApJ 568, 99
Horiuchi S., Meier D.L., Preston R.A., Tingay S.J., 2006, PASJ 58, 211
Houck J.C., Denicola L.A., 2000, In: Manset N., Veillet C., Crabtree D. (eds.) Astronomical Data Analysis Software and Systems IX, Vol. 216. Astronomical Society of the Pacific Conference Series, p. 591
Hovatta T., Lister M.L., Kovalev Y.Y., et al., 2010, Int. J. Mod. Phys. 19, 943
Hovatta T., Tornikoski M., Lainela M., et al., 2007, A&A 469, 899
IceCube Collaboration 2013, Science 342
IceCube Collaboration, Abbasi R., Abdou Y., Abu-Zayyad T., et al., 2009, Physical Review Letters 103, 221102
Israel F.P., 1998 8, 237
Israel F.P., Raban D., Booth R.S., Rantakyrö F.T., 2008, A&A 483, 741
Jansky K.G., 1933, Nat 132, 66
Jones D.L., Tingay S.J., Murphy D.W., et al., 1996, ApJ 466, L63
Jorstad S., 2008, In: Proceedings of the Workshop on "Blazar Variability across the Electromagnetic Spectrum", Proceedings of Science.
Jorstad S.G., Marscher A.P., Larionov V.M., et al., 2010, ApJ 715, 362
Jorstad S.G., Marscher A.P., Mattox J.R., et al., 2001a, ApJ 556, 738
Jorstad S.G., Marscher A.P., Mattox J.R., et al., 2001b, ApJS 134, 181
Junor W., Biretta J.A., Livio M., 1999, Nat 401, 891
Kadler M., Ros E., Lobanov A.P., et al., 2004, A&A 426, 481
Kadler M., Ros E., Perucho M., et al., 2008, ApJ 680, 867
Kalberla P.M.W., Burton W.B., Hartmann D., et al., 2005, A&A 440, 775
Katz U.F., Km3NeT Consortium 2011, Nuclear Instruments and Methods in Physics Research A 639, 50
Kellermann K.I., Lister M.L., Homan D.C., et al., 2004, ApJ 609, 539
Kellermann K.I., Pauliny-Toth I.I.K., 1969, ApJ 155, L71
Kellermann K.I., Vermeulen R.C., Zensus J.A., Cohen M.H., 1998, AJ 115, 1295
Khangulyan D.V., Barkov M.V., Bosch-Ramon V., et al., 2013, ApJ 774, 113
Kharb P., Lister M.L., Cooper N.J., 2010, ApJ 710, 764

Kino M., Asano K., 2011, MNRAS 412, L20
Kino M., Ito H., Kawakatu N., Nagai H., 2009, MNRAS 395, L43
Kino M., Kawakatu N., Ito H., 2007, MNRAS 376, 1630
Komissarov S.S., 1994, MNRAS 266, 649
Königl A., 1981, ApJ 243, 700
Kovalev Y.Y., 2009, ApJ 707, L56
Kovalev Y.Y., Aller H.D., Aller M.F., et al., 2009, ApJ 696, L17
Kovalev Y.Y., Kellermann K.I., Lister M.L., et al., 2005, AJ 130, 2473
Kovalev Y.Y., Lister M.L., Homan D.C., Kellermann K.I., 2007, ApJ 668, L27
Kraft R.P., Forman W.R., Jones C., et al., 2002, ApJ 569, 54
Kraushaar W.L., Clark G.W., Garmire G.P., et al., 1972, ApJ 177, 341
Krauß F., 2013, *Master's thesis*, Friedrich-Alexander Universität Erlangen/Nürnberg, Germany
Krauß F., Kadler M., Mannheim K., et al., 2014, A&A 566, L7
Krauß F., Müller C., Kadler M., et al., 2013, In: Conference Proceedings of "11th European VLBI Network Symposium & Users Meeting". Proceedings of Science
Krawczynski H., Hughes S.B., Horan D., et al., 2004, ApJ 601, 151
Krichbaum T.P., Bach U., Graham D.A., et al., 2008, In: Conference Proceedings of "9th European VLBI Network Symposium & Users Meeting". Proceedings of Science
Krolik J.H., 1999, Active galactic nuclei : from the central black hole to the galactic environment, Princeton New Jersey, Princeton University Press, 1999
Kunert-Bajraszewska M., Labiano A., Siemiginowska A., Guainazzi M., 2014, MNRAS 437, 3063
Lauer T.R., Faber S.M., Currie D.G., et al., 1992, AJ 104, 552
Lawrence A., 1987, PASP 99, 309
Lenain J.P., Ricci C., Türler M., et al., 2010, A&A 524, A72
León-Tavares J., Chavushyan V., Patiño-Álvarez V., et al., 2013, ApJ 763, L36
Levenberg K., 1944, Quarterly of Applied Mathematics 2, 164
Lind K.R., Blandford R.D., 1985, ApJ 295, 358
Linford J.D., Taylor G.B., Romani R.W., et al., 2011, ApJ 726, 16
Lira P., Videla L., Wu Y., et al., 2013, ApJ 764, 159
Lister M.L., Aller H.D., Aller M.F., et al., 2009a, AJ 137, 3718
Lister M.L., Aller M., Aller H., et al., 2011, ApJ 742, 27
Lister M.L., Aller M.F., Aller H.D., et al., 2013, AJ 146, 120
Lister M.L., Cohen M.H., Homan D.C., et al., 2009b, AJ 138, 1874
Lister M.L., Homan D.C., 2005, AJ 130, 1389
Lister M.L., Piner B.G., Tingay S.J., 2000, In: Hirabayashi H., Edwards P.G., Murphy D.W. (eds.) Astrophysical Phenomena Revealed by Space VLBI., p.189
Lobanov A.P., 1998, A&AS 132, 261
Lyubarsky Y., 2011, pre 83, 016302
Malmrose M.P., Marscher A.P., Jorstad S.G., et al., 2011, ApJ 732, 116
Mannheim K., 1993, A&A 269, 67
Mannheim K., 1995, Astroparticle Physics 3, 295
Mannheim K., Biermann P.L., 1992, A&A 253, L21
Mannheim K., Stanev T., Biermann P.L., 1992, A&A 260, L1
Markowitz A., Takahashi T., Watanabe S., et al., 2007, ApJ 665, 209
Markowitz A.G., Krumpe M., Nikutta R., 2014, MNRAS
Marscher A., 2008, In: Proceedings of the Workshop on "Blazar Variability across the Electromagnetic Spectrum", Proceedings of Science.
Marscher A.P., 1980, ApJ 235, 386
Marscher A.P., 2006, Astronomische Nachrichten 327, 217
Marscher A.P., 2009, In: T. Belloni (ed.) The Jet paradigm - From Microquasars to Quasars, Lecture Notes in Physics, 794., p.175

Marscher A.P., 2014, ApJ 780, 87
Marscher A.P., Gear W.K., 1985, ApJ 298, 114
Marscher A.P., Jorstad S.G., Agudo I., et al., 2012, In: Ojha, R., Thompson, D. and Dermer, C. (ed.) Proceedings of the Workshop "2011 Fermi and Jansky - Our Evolving Understanding of AGN",.
Marscher A.P., Jorstad S.G., D'Arcangelo F.D., et al., 2008, Nat 452, 966
Marscher A.P., Jorstad S.G., Gómez J.L., et al., 2002, Nat 417, 625
Marscher A.P., Jorstad S.G., Larionov V.M., et al., 2010, ApJ 710, L126
Marshall H.L., Schwartz D.A., Lovell J.E.J., et al., 2005, ApJS 156, 13
Massardi M., Ekers R.D., Murphy T., et al., 2011, MNRAS 412, 318
Massaro E., Perri M., Giommi P., Nesci R., 2004, A&A 413, 489
Massaro F., D'Abrusco R., Ajello M., et al., 2011, ApJ 740, L48
Massaro F., D'Abrusco R., Tosti G., et al., 2012, ApJ 752, 61
Mattox J.R., Bertsch D.L., Chiang J., et al., 1996, ApJ 461, 396
Mauch T., Murphy T., Buttery H.J., et al., 2003, MNRAS 342, 1117
McConville W., Ostorero L., Moderski R., et al., 2011, ApJ 738, 148
Meegan C., Lichti G., Bhat P.N., et al., 2009, ApJ 702, 791
Meisenheimer K., Tristram K.R.W., Jaffe W., et al., 2007, A&A 471, 453
Meyer E.T., Fossati G., Georganopoulos M., Lister M.L., 2011, ApJ 740, 98
Meyer E.T., Fossati G., Georganopoulos M., Lister M.L., 2012, ApJ 752, L4
Mimica P., Aloy M.A., Agudo I., et al., 2009, ApJ 696, 1142
Mimica P., Aloy M.A., Müller E., Brinkmann W., 2004, A&A 418, 947
Mücke A., Protheroe R.J., Engel R., et al., 2003, Astroparticle Physics 18, 593
Müller C., 2010, Diploma thesis, Friedrich-Alexander-Universität, Erlangen-Nürnberg, Germany
Müller C., Böck M., Wilms J., et al., 2012, In: R. Ojha, D. Thompson & C. Dermer (ed.) Proceedings of Fermi & Jansky: Our Evolving Understanding of AGN, St. Michaels, MD, 2011. eConf Proceedings C1111101
Müller C., Kadler M., Ojha R., et al., 2010, In: Savolainen, T., Ros, E., Porcas, R.W. & Zensus, J.A. (ed.) Proceedings of the Workshop "Fermi meets Jansky - AGN in Radio and Gamma-Rays", Bonn: MPIfR., p.229
Müller C., Kadler M., Ojha R., et al., 2014a, A&A 562, A4
Müller C., Kadler M., Ojha R., et al., 2009, In: 2009 Fermi Symposium. eConf Proceedings C091122
Müller C., Kadler M., Ojha R., et al., 2014b, A&A 569, A115
Müller C., Kadler M., Ojha R., et al., 2011, A&A 530, L11
Müller C., Krauss F., Kadler M., et al., 2013, In: 11th European VLBI Network Symposium & Users Meeting. Proceedings of Science, arXiv:1301.4384
Murphy T., Mauch T., Green A., et al., 2007, MNRAS 382, 382
Murphy T., Sadler E.M., Ekers R.D., et al., 2010, MNRAS 402, 2403
Nandra K., 2006, MNRAS 368, L62
Napier P.J., 1995, In: J. A. Zensus, P. J. Diamond, & P. J. Napier (ed.) Very Long Baseline Interferometry and the VLBA. ASP Conf. Proc., 82, p. 59
Neronov A., Semikoz D., Taylor A.M., 2012, A&A 541, A31
Nesci R., Tosti G., Pursimo T., et al., 2013, A&A 555, A2
Neumayer N., 2010, Proc. Astron. Soc. Aust. 27, 449
Nolan P.L., Abdo A.A., Ackermann M., et al., 2012, ApJS 199, 31
Norris R.P., 1988, In: Reid M.J., Moran J.M. (eds.) The Impact of VLBI on Astrophysics and Geophysics, Vol. 129. IAU Symposium, p. 485
Nowak M.A., Neilsen J., Markoff S.B., et al., 2012, ApJ 759, 95
O'Dea C.P., 1998, PASP 110, 493
Ojha R., Fey A.L., Charlot P., et al., 2005, AJ 130, 2529
Ojha R., Kadler M., Böck M., et al., 2010, A&A 519, A45
Orienti M., Dallacasa D., Giovannini G., et al., 2011, In: "2011 Fermi Symposium". eConf Proceedings C110509
Ott J., Meier D.S., McCoy M., et al., 2013, ApJ 771, L41

Owsianik I., Conway J.E., 1998, A&A 337, 69
Page M.J., Symeonidis M., Vieira J.D., et al., 2012, Nat 485, 213
Panessa F., Giroletti M., 2013, MNRAS 432, 1138
Paragi Z., Reynolds C., Biggs A.D., et al., 2005, In: Romney J., Reid M. (eds.) Future Directions in High Resolution Astronomy, Vol. 340. Astronomical Society of the Pacific Conference Series, p. 611
Parsley S., 2004, In: Vandenberg N.R., Baver K.D. (eds.) International VLBI Service for Geodesy and Astrometry 2004 General Meeting Proceedings., p. 205
Peck A.B., Taylor G.B., 2000, ApJ 534, 90
Perley R.A., Chandler C.J., Butler B.J., Wrobel J.M., 2011, ApJ 739, L1
Perucho M., Lobanov A.P., Martí J., Hardee P.E., 2006, A&A 456, 493
Perucho M., Martí J.M., 2007, MNRAS 382, 526
Piner B.G., Mahmud M., Fey A.L., Gospodinova K., 2007, AJ 133, 2357
Piner B.G., Pant N., Edwards P.G., 2010, ApJ 723, 1150
Piner B.G., Pushkarev A.B., Kovalev Y.Y., et al., 2012, ArXiv e-prints
Plotkin R.M., Anderson S.F., Brandt W.N., et al., 2012, ApJ 745, L27
Potter W.J., Cotter G., 2013, MNRAS 431, 1840
Predehl P., Schmitt J.H.M.M., 1995, A&A 293, 889
Pushkarev A.B., Kovalev Y.Y., Lister M.L., Savolainen T., 2009, A&A 507, L33
Quillen A.C., Brookes M.H., Keene J., et al., 2006, ApJ 645, 1092
Readhead A.C.S., Taylor G.B., Pearson T.J., Wilkinson P.N., 1996, ApJ 460, 634
Richards G.T., Strauss M.A., Fan X., et al., 2006, AJ 131, 2766
Richter S., Spanier F., 2013, In: European Physical Journal Web of Conferences, Vol. 61. European Physical Journal Web of Conferences, p. 5010
Rigby E.E., Best P.N., Brookes M.H., et al., 2011, MNRAS 416, 1900
Rivers E., Markowitz A., Rothschild R., 2011, ApJ 742, L29
Rivers E., Markowitz A., Rothschild R., 2013, ApJ 772, 114
Roming P.W.A., Kennedy T.E., Mason K.O., et al., 2005, Space Sci. Rev. 120, 95
Rothschild R.E., Markowitz A., Rivers E., et al., 2011, ApJ 733, 23
Rybicki G.B., Lightman A.P., 1979, Radiative processes in astrophysics, New York: Wiley-Interscience
Ryle M., Elsmore B., Neville A.C., 1965, Nat 205, 1259
Ryle M., Hewish A., 1960, MNRAS 120, 220
Ryle M., Neville A.C., 1962, MNRAS 125, 39
Sahakyan N., Yang R., Aharonian F.A., Rieger F.M., 2013, ApJ 770, L6
Sambruna R.M., Barr P., Giommi P., et al., 1994, ApJ 434, 468
Savolainen T., Homan D.C., Hovatta T., et al., 2010, A&A 512, A24+
Scargle J.D., Norris J.P., Jackson B., Chiang J., 2013, ApJ 764, 167
Schawinski K., Thomas D., Sarzi M., et al., 2007, MNRAS 382, 1415
Schödel R., Ott T., Genzel R., et al., 2002, Nat 419, 694
Seyfert C.K., 1943, Contributions from the Mount Wilson Observatory / Carnegie Institution of Washington 671, 1
Shakura N.I., Sunyaev R.A., 1973, A&A 24, 337
Shaw M.S., Romani R.W., Cotter G., et al., 2013, ApJ 764, 135
Shepherd M.C., 1997, In: G. Hunt & H. Payne (ed.) Astronomical Data Analysis Software and Systems VI. ASP Conf. Proc. 125, p. 77
Shu X.W., Yaqoob T., Wang J.X., 2010, ApJS 187, 581
Siemiginowska A., LaMassa S., Aldcroft T.L., et al., 2008, ApJ 684, 811
Sikora M., Begelman M.C., Rees M.J., 1994, ApJ 421, 153
Skrutskie M.F., Cutri R.M., Stiening R., et al., 2006, AJ 131, 1163
Sokolovsky K.V., Kovalev Y.Y., Pushkarev A.B., Lobanov A.P., 2011a, A&A 532, A38
Sokolovsky K.V., Kovalev Y.Y., Pushkarev A.B., et al., 2011b, A&A 535, A24
Sowards-Emmerd D., Romani R.W., Michelson P.F., Ulvestad J.S., 2004, ApJ 609, 564

Spada M., Ghisellini G., Lazzati D., Celotti A., 2001, MNRAS 325, 1559
Springel V., White S.D.M., Jenkins A., et al., 2005, Nat 435, 629
Stawarz L., Ostorero L., Begelman M.C., et al., 2008, ApJ 680, 911
Steinle H., 2006, Chin. J. of Astron. and Astrophys. Supplement 6, 1
Steinle H., 2010, Proc. Astron. Soc. Aust. 27, 431
Steinle H., Bennett K., Bloemen H., et al., 1998, A&A 330, 97
Stevens J., Edwards P.G., Ojha R., et al., 2012, In: R. Ojha, D. Thompson & C. Dermer (ed.) Proceedings of Fermi & Jansky: Our Evolving Understanding of AGN, St. Michaels, MD, 2011. eConf Proceedings C1111101
Stickel M., Meisenheimer K., Kuehr H., 1994, A&AS 105, 211
Tadhunter C., Holt J., González Delgado R., et al., 2011, MNRAS 412, 960
Tavecchio F., Ghisellini G., 2008, MNRAS 385, L98
Tavecchio F., Ghisellini G., Bonnoli G., Ghirlanda G., 2010, MNRAS 405, L94
Tavecchio F., Maraschi L., Ghisellini G., 1998, ApJ 509, 608
Taylor G.B., Charlot P., Vermeulen R.C., Pradel N., 2009, ApJ 698, 1282
Taylor G.B., Fassnacht C.D., Sjouwerman L.O., et al., 2005, ApJS 159, 27
Taylor G.B., Healey S.E., Helmboldt J.F., et al., 2007, ApJ 671, 1355
Taylor G.B., Readhead A.C.S., Pearson T.J., 1996, ApJ 463, 95
Taylor G.B., Vermeulen R.C., Readhead A.C.S., et al., 1996, ApJS 107, 37
Tchekhovskoy A., Narayan R., McKinney J.C., 2011, MNRAS 418, L79
Tengstrand O., Guainazzi M., Siemiginowska A., et al., 2009, A&A 501, 89
Thompson A.R., Moran J.M., Swenson, Jr. G.W., 2001, Interferometry and Synthesis in Radio Astronomy, 2nd Edition, New York : Wiley
Thompson D.J., Bertsch D.L., Fichtel C.E., et al., 1993, ApJS 86, 629
Tingay S.J., Jauncey D.L., King E.A., et al., 2003, PASJ 55, 351
Tingay S.J., Jauncey D.L., Reynolds J.E., et al., 1998, AJ 115, 960
Tingay S.J., Lenc E., 2009, AJ 138, 808
Tingay S.J., Murphy D.W., 2001, ApJ 546, 210
Tingay S.J., Preston R.A., Jauncey D.L., 2001, AJ 122, 1697
Tombesi F., Sambruna R.M., Marscher A.P., et al., 2012, MNRAS 424, 754
Tornikoski M., Valtaoja E., Teraesranta H., et al., 1996, A&AS 116, 157
Trüstedt J., 2013, *Master's thesis*, Julius-Maximilians-Universität Würzburg, Germany
Urry C.M., 1996, In: Miller H.R., Webb J.R., Noble J.C. (eds.) Blazar Continuum Variability, Vol. 110. Astronomical Society of the Pacific Conference Series, p. 391
Urry C.M., Padovani P., 1995, PASP 107, 803
Urry C.M., Sambruna R.M., Worrall D.M., et al., 1996, ApJ 463, 424
Venturi T., 2010, In: 10th European VLBI Network Symposium and EVN Users Meeting: VLBI and the New Generation of Radio Arrays.
VERITAS CollaborationAcciari V.A., Aliu E., et al., 2009, Nat 462, 770
Vermeulen R.C., Ros E., Kellermann K.I., et al., 2003, A&A 401, 113
Verner D.A., Ferland G.J., Korista K.T., Yakovlev D.G., 1996, ApJ 465, 487
Véron-Cetty M.P., Véron P., 2000 10, 81
Véron-Cetty M.P., Véron P., 2006, A&A 455, 773
Vink J., Snellen I., Mack K.H., Schilizzi R., 2006, MNRAS 367, 928
Wagner S.J., Witzel A., 1995, ARA&A 33, 163
Wells D.C., Greisen E.W., Harten R.H., 1981, A&AS 44, 363
Wilkinson P.N., Henstock D.R., Browne I.W., et al., 2001, Physical Review Letters 86, 584
Wilks S.S., 1938, Ann. Math. Statist. 9, 60
Wilms J., Allen A., McCray R., 2000, ApJ 542, 914
Wilms J., Juett A.M., Schulz N.S., Nowak M.A., 2012, published at `http://pulsar.sternwarte.uni-erlangen.de/wilms/research/tbabs/`

Wootten A., Thompson A.R., 2009, IEEE Proceedings 97, 1463
Worrall D.M., Birkinshaw M., Kraft R.P., et al., 2008, ApJ 673, L135
Wright E.L., Eisenhardt P.R.M., Mainzer A.K., et al., 2010, AJ 140, 1868
Yaqoob T., Padmanabhan U., 2004, ApJ 604, 63

Acknowledgements

First of all, I would like to thank my advisors Jörn Wilms and Matthias Kadler, who gave me the opportunity to work in this field of astronomy. I deeply appreciate having two "Doktorväter" sharing their experience and knowledge with me. Thanks for your support, helpful feedback, for offering positive encouragement, and giving me the chance to present my work on international conferences and to travel to our collaboration members all around the world. The three years of doing research as a member of the joint astronomy groups of Bamberg and Würzburg were a great pleasure and I highly appreciate the interdisciplinary exchange, the fantastic and productive team work, and the everyday fun, which this collaboration brings along.

I gratefully acknowledge the funding through a PhD fellowship from the *Studienstiftung des Deutschen Volkes*, the funding by the *Deutsche Forschungsgemeinschaft* and by the *Erlangen Center for Astroparticle Physics* (ECAP), which made this work possible. This research was performed in the framework of the TANAMI program in close collaboration with the *Fermi*/LAT and ANTARES Collaborations. I want to thank all team members for their support, the excellent collaboration and their trust. In particular: Roopesh Ojha, who always gave me useful advise and had a sympathetic ear; Eduardo Ros – for his helpful comments and feedback; Greg Taylor – for his constructive contributions to the work on PMN J1603−4904; Clancy James and Kerstin Fehn – for the collaboration in the joint TANAMI-ANTARES project. Big thank you goes to all of my co-authors for their help on the papers, especially to Manel Perucho for his work and the interesting discussions on Centaurus A, to Fe for the great collaboration on PMN J1603−4904, and to all the observers. I want to thank Neil Gehrels at NASA's Goddard Space Flight Center (GSFC), and G. Taylor at the University of New Mexico (UNM) for providing financial support and hosting me. These stays abroad have been a valuable experience during my PhD time. I loved working together with the research groups at GSFC and UNM. A special thanks goes to Bill McConville and Mike Dutka for the great time and teamwork.

I want to thank my colleagues at the Remeis observatory, ECAP and the University of Würzburg for being such a great team! The abbreviation FRANCI[1] stands for "FRanconian Astronomy Neighborhood Collaboration Incentive", and effectively describes everything that I appreciate: a personal and scientific network, fruitful discussions on different astronomical topics, joint social activities and, of course, many new friends. To all Remeisen, a big thank you for the enjoyable time and the good cooperation over the past years: The Admins (Ingo, Fritz, Tommy and Matthias) – they do a wonderful job and are always willing to help; Fe, Tommy and Moritz – for their great support; Christoph – for his immense effort on setting up the simultaneous fitting with ISIS and Difmap; Alex Markowitz – for the helpful input while working on Cen A; Felix – for all the good conversations; Tobi, Basti, Eva and Eugenia – for always putting a smile on my face. As much, I would like to thank

[1] the title of the first collaboration and get-to-know meeting of the Franconian astronomers (in July 2013)

all colleagues of the Chair of Astronomy in Würzburg, for the warm welcome at the very beginning of the Bamberg-Würzburg-connection and giving me a “second scientific home”. Big thanks to the AG Kadler for the positive working and research environment, which is motivating every day – in particular to Robert, Annika, Till, Jonas and Katha for the great discussions and cooperation, for the support and the funny time. I am looking forward to continuing to work with you all!

A special thank you goes to my flatmate Katha and my fellow students Kora and Neli who supported me a lot in the last years, showed interest in this work and took my mind off things whenever necessary.

I would like to thank Sebastian for being there for me, for his patience and great encouragement. And last but not least, I would like to express my gratitude to my parents for their confidence and support.